Optomechanical energy conversion and vibrational coherence in biomimetic molecular photoswitches

Moussa Gueye

Moussa Gueye. Optomechanical energy conversion and vibrational coherence in biomimetic molecular photoswitches. Physics [physics]. Université de Strasbourg, 2016. English. NNT : 2016STRAE016 . tel-01391909v3

HAL Id: tel-01391909
https://theses.hal.science/tel-01391909v3

Submitted on 28 Aug 2017

Thèse de doctorat

en vue de l'obtention du grade de
Docteur de l'université de Strasbourg en Physique
delivré par
L'Ecole Doctorale de Physique et Chimie Physique de Strasbourg
(ED182)

Optomechanical energy conversion and vibrational coherence in biomimetic molecular photoswitches

---

Moussa Gueye

Directeur de Thèse: Dr. Jérémie Léonard
Rapporteur: Dr. Pascale Changenet-Barret
Rapporteur: Dr. Maciej Lorenc
Examinateur: Dr. Nicolas Ferré
Examinateur: Dr. Guy Buntinx
Rapporteur: Prof. Jean-Yves Bigot

Thèse soutenue le 05 Juillet 2016

Contents

Remerciements

Mes remerciements seront portés à l'égard de mes professeurs qui, durant tout mon cursus m'ont transmis les connaissances qui m'ont permis aujourd'hui d'arriver à ce stade. Je tiens à remercier Stefan Haacke en sa qualité de directeur de L'IPCMS, d'avoir accepté mon intégration au sein de l'équipe BIODYN dont il est le directeur. Je tiens à exprimer toute ma gratitude à mon super encadrant, Jérémie Léonard. Sa disponibilité ainsi que ses qualités humaines m'ont beaucoup aidé dans la réalisation de ce travail. Très sincèrement, je ne cesserai jamais de le remercier de m'avoir assisté dans tous les volets du travail, par les multiples compétences qu'il a mises à mon service et par la rigueur et la bonne humeur dont il a fait preuve tout au long de mes travaux de thèse. Je voulais adresser aussi mes remerciements à Olivier Crégut pour sa disponibilité précieuse en salle de manip. Je remercie également Jean-Pierre Vola, Michelangelo romeo, Emilie Couziné et Gautier Dekyndt pour leurs aides apportés pour la réussite de mes travaux de thèse. Je souhaite aussi remercier les doctorants et les post-doctorants de l'équipe BIODYN: Li Liu, Anastasia Ionna Skilitsi, Damianos Agathangelou, Youssef El Khoury et Vincent Kemlin qui m'ont apporté un soutien psychologique indispensable grâce à leur humour et à leur bonne humeur. J'adresse un remerciement spécial à mon épouse Fatou N'diaye pour le soutient et la compréhension dont elle a fait preuve tout au long de mes travaux de thèse. Pour finir, je voudrais remercier mes parents, mes frères et sœurs, mes amis, ainsi que toutes les personnes qui de près ou de loin ont contribué à la réussite de ces travaux.

Résumé en français

L'absorption d'un photon par un chromophore, permet de promouvoir celui-ci dans un état excité où une photoréaction peut avoir lieu. Lorsque ces réactions sont accompagnées par des changements structurels de grande ampleur, l'énergie lumineuse est convertie en un mouvement mécanique à l'échelle moléculaire. C'est le cas dans les systèmes que nous étudions où une photoisomérisation $C = C$ induit une transition électronique ultrarapide via une Intersection Conique (IC) entre les surfaces d'énergie potentielle électronique impliquées. Le mouvement photoinduit de rotation autour de la double liaison réalise une conversion d'énergie optomécanique qui est à l'origine du concept de photocommutateur moléculaire.
Les photocommutateurs produisent un travail mécanique à l'échelle moléculaire en réponse à une excitation optique. Ils modulent l'activité biologique de diverses protéines photosensibles. Le chromophore rétinal de la rhodopsine, le pigment visuel des animaux supérieurs constitue un exemple d'un photocommutateur naturel. En effet, dans la rhodopsine bovine, sous l'action de la lumière, la photoisomérisation du chromophore de la base de Schiff protonée du rétinal (PSBR) vibrationnellement cohérente, déclenche le cycle visuel en un temps très rapide (200 fs) via l'évolution d'un seul état excité (S_1) $\pi - \pi^*$ et d'une décroissance dans la l'état fondamental all-trans (S_0) du produit avec un rendement quantique de 67 % jamais égalé. Bien que ces propriétés font de la rhodopsine une parfaite référence pour concevoir des photocommutateurs synthétiques, l'irradiation du PSBR isolé en solution conduit à une photochimie différente, incluant une perte de ces propriétés remarquables de vitesse et d'efficacité.
Les informations limitées sur les mécanismes de changement de conformations ouvrent une large applicabilité de cette approche rendant une recherche sur des molécules artificielles pouvant imiter la photoréaction de la rhodopsine.
Suivant une approche dite biomimétique, une nouvelle classe de commutateur basée sur la structure alkylée d'indanylidène-pyroline (IP), inspirée par la photoisomérisation du chromophore rétinal dans la rhodopsine à été imaginée et synthétisée par Massimo Olivucci et *al.* (voir figure 0.1.A). Des investigations théoriques et expérimentales révèlent que, dans une solution de méthanol, le cation p-méthoxy-N-alkylé IP (MeO-NAIP) présente une surface d'énergie S_1 et une vitesse de photoisomérisation similaire à celle observée dans la rhodopsine.

Cette famille de molécules IP est le siège d'une photoisomérisation cohérente unique pour un photocommutateur synthétique en phase condensée. Il s'agit d'un mécanisme où l'énergie lumineuse est convertie en énergie mécanique délivrée de manière cohérente dans un nombre restreint de degrés de liberté vibrationnels à basse fréquence. Ce mouvement vibrationnel cohérent conduit le système à travers l'IC jusqu'à l'état fondamental. Une telle photoréaction, si son rendement pouvait être optimisé, pourrait être utilisée à la fabrication de machines moléculaires ou le contrôle par la lumière d'une fonction biologique.

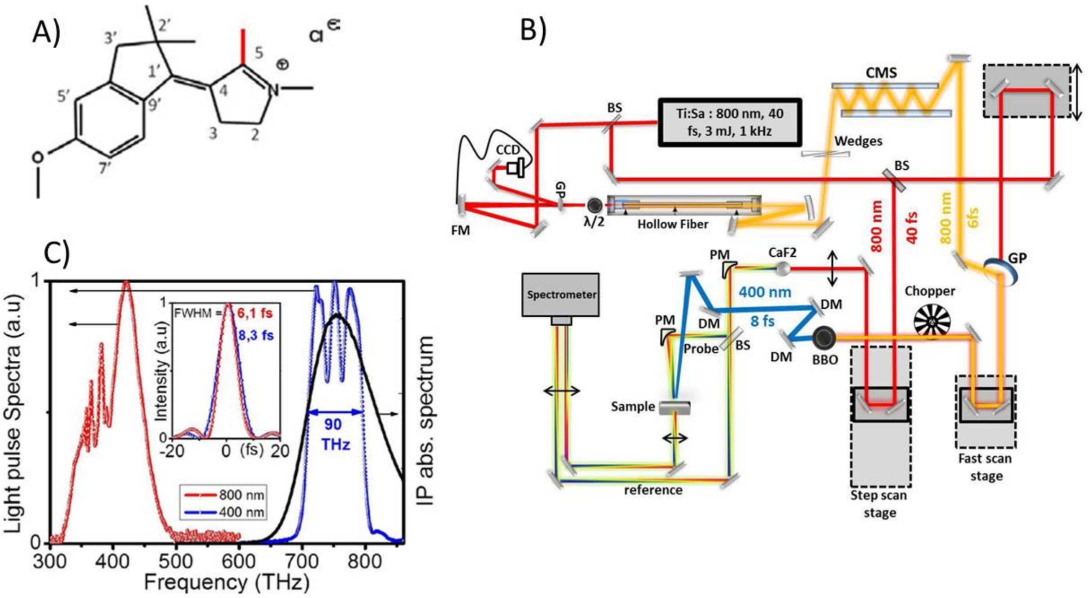

Figure 0.1.: A) Structure de la molécule MeO-NAIP B).Dispositif expérimental pour l'implémentation de la spectroscopie de cohérence vibrationnelle. C) Spectre des impulsions pompe rouge (fibre creuse) et UV (400 nm).

Ce travail de doctorat s'est déroulé dans l'équipe expérimentale BIODYN au Département d'Optique ultrarapide et Nanophotonique (DON) de l'Institut de Physique et Chimie des Matériaux de Strasbourg (IPCMS), en étroite interaction avec des partenaires théoriciens. Nous avons étudié le mécanisme de photoisomérisation à l'œuvre dans des photocommutateurs moléculaires, par spectroscopie d'absorption transitoire, afin de comprendre les paramètres qui régissent la dynamique et le rendement de ce type de photoréaction. Le principe de l'expérience consiste à exciter l'échantillon avec une première impulsion dite "pompe" afin de déclencher une photoréaction, ensuite après un certain délai par rapport à l'impulsion pompe, une deuxième impulsion dite ”sonde” est envoyé dans l'échantillon. Le changement d'absorption de la molécule induite par la pompe nous donne l'effet du processus photodéclenché dans l'échantillon à un instant t+t', où t' étant le délai entre la pompe et la sonde. Ce délai entre ces deux impulsions est contrôlé grâce à une ligne à retard (motorisée et contrôlée par ordinateur) permettant ainsi échantillonner la réponse temporelle du système mesuré. Une analyse des signaux obtenus permet de remonter à la dynamique réactionnelle.

Nous avons exploré l'origine du mécanisme de photoisomérisation vibrationellement cohérente à travers l'IC en comparant la photoréaction d'une variété de composé IP montrant différentes substitutions. Les indications d'une photoisomérisation cohérente ne sont observées que dans certains cas, où le durée de vie dans l'état excité est < 300 fs, et le rendement de photoisomérisation est décorrélé de la vitesse de réaction ou de la cohérence vibrationnelle du mouvement réactionnel.
Ainsi comprendre le mécanisme qui régit le rendement de ce type de photoréaction et aussi la possibilité de contrôler l'efficacité en manipulant optiquement la dynamique vibrationnelle, nécessite l'utilisation d'impulsions ultracourtes qui permettrons d'exciter l'échantillon sur des échelles de temps plus courtes que la période des mouvements vibrationnelles, générant des paquets d'onde à la fois dans l'état excité et dans l'état fondamental. Afin de mieux explorer le lien entre la dynamique vibrationnelle cohérente, la vitesse et le rendement de la photoréaction, nous avons développé au cours de cette thèse un nouveau montage expérimental utilisant des impulsions laser ultracourtes (<8 fs) permettant de générer des paquets d'ondes vibrationnels et de réaliser une spectroscopie Raman dans le domaine temporel aussi appelée spectroscopie de cohérences vibrationnelles (SCV) (voir Fig 0.1.B). Brièvement ce montage utilise une impulsion pompe issue d'un amplificateur Ti: saphir et élargie spectralement par propagation non linéaire guidée (fibre creuse) dans du gaz néon. La recompression temporelle et conversion de fréquence permet de générer une impulsion centrée à 400 nm de largeur spectrale correspondant à une durée de 8 fs (Fig 0.1.C). Une impulsion de lumière blanche UV-Vis générée dans un cristal de CaF2 est utilisée comme sonde. Un balayage rapide du délai entre la pompe et la sonde est mis en œuvre pour supprimer de manière efficace l'effet dominant du bruit à basse fréquence de l'intensité de la pompe sur les signaux d'absorption transitoire. Les performances de sensibilité de mesure de variation d'absorption (ΔA) de l'expérience sont comparables aux meilleurs montages existants. Des signatures vibrationnelles sont démontrées dans l'acétonitrile jusqu'à 3000 cm^{-1} avec une sonde UV et ce avec une sensibilité inférieure à 15 µOD. La signature des paquets d'onde se manifeste sous forme d'oscillations modulant ainsi les spectres d'absorption de l'état fondamental et de l'état excité.

Des résultats de SCV sur les composés IP ont pu être obtenus, permettant ainsi d'identifier des signatures vibrationnelles distincts (surtout dans les basses fréquences <500 cm^{-1}) pour divers composés IP.

Les résultats de spectroscopie d'absorption transitoire ont montré que les commutateurs IP affichent des caractéristiques spectro-temporelles qui dépendent de la structure des molécules. Par conséquent, deux types de photoréactions ont été observés et qualifiées comme une photoisomérisation cohérente ou non cohérente. Le premier scénario concerne les molécules qui affichent une photoisomérisation ultra-rapide (sub-200 fs), avec des indications de mouvement de paquet d'ondes sur la surface d'énergie potentielle (indiqué par un décalage spectrale et temporelle de la bande d'absorption) de l'état excitée S_1 vers l'IC, se produisant sur une échelle de temps entre 170 et 260 fs, suivant les molécules. La deuxième signature spécifique est la repopulation quasi-impulsive et décalée en temps dans l'état fondamental qui est attribuée à la signature du photoproduit. Ce signal impulsionnel conduit à des oscillations de basse fréquence (sub-100 cm^{-1}), reflétant le mouvement de paquet d'ondes sur la surface d'énergie potentielle de l'état fondamental. Le deuxième scénario concerne les molécules qui subissent une photoisomérisation qui peut être décrite par des cinétiques de réaction exponentielles avec des temps d'isomérisation > à 300 fs.

Les mesures de spectroscopie d'absorption transitoire sur les composés qui affichent la signature de paquet d'ondes observée au cours de la réaction indiquent que les photocommutateurs IP subissent une isomérisation où une partie de l'énergie lumineuse absorbée est efficacement canalisée dans un nombre restreint de modes vibrationnels de basse fréquence dans l'état fondamental, comme déjà observé au cours de l'isomérisation du rétinal dans la rhodopsine. Cependant, cet effet est sensible à la géométrie moléculaire à l'état fondamental, modulée par la présence d'un groupement méthyle sur le carbone C5 (voir fig 0.1.A). En effet, la production d'une réaction vibrationnellement cohérente nécessite une isomérisation rapide favorisée par une géométrie distordue causée par la présence du groupement méthyle sur le carbone C5.

Nous avons utilisé les molécules IP comme un système de référence pour s'investir de l'influence de la dynamique réactionnelle sur le rendement quantique de photoisomérisation. Plutôt que le rendement absolu, nous avons déterminé avec précision le rendement relatif des différents composés IP et leurs temps d'isomérisation correspondant. En comparant toutes les molécules ensemble, aucune corrélation est observé entre le temps d'isomérisation, l'observation de cohérence vibrationnelle et le rendement quantique de photoisomérisation contrairement à la rhodopsine.

En effet, la dynamique de ces photoréactions, ainsi que le rendement de photoisomérisation sont gravement influencés par la forme de la surface d'énergie potentielle des états impliqués, la topologie de l'intersection conique (elle-même influencée par l'interaction avec l'environnement en phase condensée) et la dynamique vibrationnelle du système à travers ces intersections. La configuration complexe de ces surfaces multidimensionnelles rend ces systèmes difficiles à explorer expérimentalement avec une expérience de spectroscopie d'absorption transitoire classique. Ainsi, il est possible d'explorer la dynamique vibrationnelle du système dans la surface d'énergie potentielle et au voisinage de l'CI grâce à la SCV.

Comme indiqué ci-dessus, durant la photoisomérisation ultrarapide du MeO-NAIP, des oscillations de basse fréquence ont été détectées dans l'état fondamental S_0 suivant une conversion interne à travers l'CI. Des investigations théoriques ont attribué ces oscillations comme étant originaires d'une déformation cyclique de basse fréquence accompagnant le mouvement de torsion autour de la double liaison $C = C$, déclenché par le mouvement réactif dans l'état excité S_1. En appliquant la SVC sur le MeO-NAIP, nous serons en mesure de répondre expérimentalement à la question à savoir, si ces modulations de basse fréquence découlent d'un mouvement réactif vibrationnellement cohérent, initié dans l'état excité et préservé à travers l'CI, ou cela résultent tout simplement de la signature de paquets d'onde déclenchée dans l'état fondamental par l'excitation laser. En excitant les molécules d'intérêt d'une manière résonante et non-résonante, nous avons été en mesure de distinguer les modes vibrationnels provenant de l'état excité et les modes vibrationnels originaires de l'état fondamental. L'analyse et l'interprétation des résultats ont confirmé que le photocommutateur MeO-NAIP isomérise dans un régime vibrationnellement-cohérent avec un transfert de l'activité cohérente de modes à basse fréquence de l'état excité à l'état fondamental du photoproduit, suivant une conversion interne à travers l'intersection conique. La comparaison à son homologue le dMe-MeO-NAIP où le groupement méthyle sur le carbone C5 est remplacé par un atome d'hydrogène, confirme que la présence du méthyle sur C5 est nécessaire pour déclencher et préserver l'activité cohérente qui accompagne la réaction de photoisomérisation du MeO-NAIP.
Ces résultats constituent une preuve définitive de l'existence d'un mouvement réactif vibrationnellement cohérent qui accompagne la réaction d'isomérisation de certains composés IP.

Démêler le mécanisme de ces processus de changement de conformation, ouvrirait une large applicabilité de molécules synthétiques qui pourront imiter la photoréaction de la rhodopsine. Dans le contexte de contrôler par la lumière la conformation d'un peptide afin d'activer ou d'inhiber des fonctions biologiques, des investigations théoriques effectuées sur un nombre de molécules bio-inspirées, montrent que certains molécules peuvent travailler comme photocommutateurs pouvant contrôler la conformation d'un peptide.

Nous avons étudié au cours de la thèse (en collaboration avec l'équipe théorique de D. Sampedro, Espagne), la dynamique du control de la conformation d'un peptide avec un commutateur basé sur la structure du benzylidène-pyrroline (BP) et du N-protoné benzylidène pyroline (NHBP). Nous avons présenté des détails expérimentaux et théoriques pour s'investir de la dynamique électronique et conformationnelle d'un peptide lié avec ce photocommutateur. En combinant des expériences de spectroscopie d'absorption transitoire en fonction de la température et des simulations, nous avons comparé la dynamique et le mécanisme de la photoisomérisation du photocommutateur isolé en solution ou lié de manière covalente au peptide. Nous avons conclu que la photoisomérisation se produit à travers une intersection conique après l'activation thermique d'une barrière d'énergie potentielle à l'état excité S_1, dont la hauteur dépend de la conformation du peptide à l'état fondamentale. Nous avons été en mesure de rationaliser l'effet de la liaison du peptide sur la dynamique de la photoisomérisation du commutateur. Ce travail peut être considéré comme une approche où, partant d'une molécule synthétique isolée, un chromophore biomimétique, nous avons considéré l'effet de la liaison avec le peptide sur la photodynamique. Ces résultats doivent être considérer avec soin en vue de concevoir des chromophores synthétiques destinés à commuter d'une manière efficace des fonctions moléculaires.

Enfin, nous avons également dégagé les propriétés spectroscopiques et le mécanisme réactionnel d'un nouveau commutateur moléculaire voisin des IPs, mais conçu comme un anion modèle du chromophore HBDI de la GFP, et de synthèse bien plus aisée. En collaboration avec les études théoriques de l'équipe de M. Olivucci, nous avons rapporté un travail pluridisciplinaire basé sur des des tâches complémentaires, combinant la théorie, la synthèse, la caractérisation de l'état photostationnaire et l'expérience d'absorption transitoire. Nous avons présenté la préparation d'un photocommutateur moléculaire anionique imitant la structure électronique du chromophore p-HDBI de la GFP. La synthèse facile du commutateur étudié permet une caractérisation en termes de spectroscopie, de photochimie et de la dynamique ultrarapide induite par laser, montrant que le système est photochromique et thermiquement stable à température ambiante et que sa forme anionique a des valeurs d'absorption maximales distinctes (351 nm pour la forme E et 359 nm pour la forme Z).

Les calculs et les investigations par spectroscopie d'absorption transitoire ont démontré que la dynamique de la réaction de photoisomérisation se produit par une rotation axiale comme dans les composés IP (cationiques), leurs propriétés stationnaires et électrostatiques sont très complémentaires. Cela s'explique par une structure voisine et une translocation de charge similaire dans l'état excité (une charge de signe opposé se déplace dans le sens opposé). Nous envisageons que les composés HBDI pourront être utilisés pour concevoir des dispositifs moléculaires avec des effets statiques ou électrostatiques opposés à ceux proposés par les composés IP.

En définitive, les résultats apportés au cours de cette thèse indiquent que ces photocommutateurs biomimétiques sont des systèmes modèles pour l'étude fondamentale des réactions de photoisomérisation en régime vibrationnellement cohérent et de la dynamique de paquet d'ondes au cours de la réaction. Ils sont également applicables au déclenchement de fonctions biologiques par contrainte stérique.

Part I.

General introduction

1. General introduction

In material science, the molecular level has become the relevant or target scale for controlling the physical properties of matter [1]. The interaction with light energy is a method of choice to study and or manipulate molecular properties in condensed phase during a chemical reaction. Ultrafast pump-probe transient absorption spectroscopy[2] is a powerful tool to experimentally investigate the molecular dynamical processes occurring typically on time scales of femtoseconds or picoseconds. In such an experiment, the photo-induced molecular reaction drives a molecule from a photo-excited electronic state to another excited electronic state (eg charge transfer in an organic molecules for photovoltaics [3]) or directly to the ground state (S_0) possibly in another geometry (eg C=C photoisomerization in a molecular switch or a molecular machine [4, 5]).

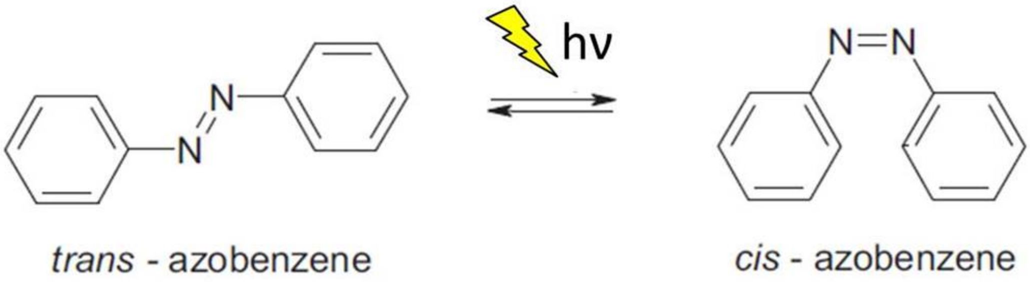

Figure 1.1.: Principle of photoisomerization. A molecule (here Azobenzene), is in a given structural conformation (trans in the present case). Upon light irradiation, it absorbs a photon and undergoes a large structural change towards another isomerical conformation (cis) and vis-versa.

Photoisomerization is a simple mechanism through which, a molecular system converts light energy into mechanical energy via a conformational change, in response to an optical excitation. This optomechanical energy conversion is the origin of the concept of molecular photoswitches, referred to as cis and trans (or Z and E) isomers.

The molecular photoswitches produce mechanical work at molecular level in response to an optical excitation. A typical example of this process is the photoinduced cis-trans isomerization of azobenzene (AB)[6]. As shown in Figure 1.1, by irradiation at UV wavelength, the trans conformation is converted into the cis form via a rotation around the central $N = N$ double bound, the process being reversible upon excitation in visible. These ultrafast electronic structural changes are often described by two (ground- and excited) electronic potential energy surfaces (PES) as a function of molecular coordinates [7], both crossing a region called conical intersection(CI)[8]. The latter is a consequence of the degeneracy of both excited and ground states. This hyper surface contains 3N-8 degrees of freedom and is a very effective pathway for nonadiabatic electronic transitions on the nuclear motion time scale (femtosecond). Thus, the mechanism of ultrafast isomerization can be explained as shown in Figure 1.2. Upon vertical excitation, the Franck-Condon (FC) region is fisrt populated, indicating that the transition between two electronic states is always much faster than nuclear motions. After vibrational relaxation out from the FC region, the excited state populations evolve on the PES along the reaction coordinate, toward the CI, which is either leading back to the reactant ground state (avorted isomerization) or to the formation of the photoproduct. The motion between the FC region and the CI reflects the isomerization time and the amount of photo-

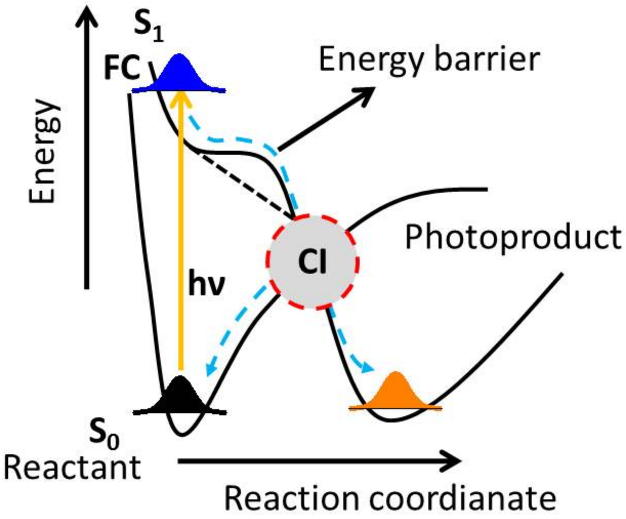

Figure 1.2.: Simplified model summarizing the photoisomerization dynamics. See text for details.

product formed compared to that of starting reactant defines the isomerization quantum yield (QY). As schematically illustrated in Fig. 1.2, the S_1 PES can be characterized by the presence of a barrier (i.e. a transition state). The height of the putative potential energy barrier, which can be overcome by thermal activation, influences the dynamics of the population on the S_1, thus the excited state lifetime.

The retinal chromophore of rhodopsin (Rho) constitutes an example of natural photoswitch witch undergoes an efficient (67%) photoisomerization through a CI characterized by a barrierless S_1 relaxation on a time scale less than 200 fs [10, 11]. Although these properties make rhodopsin a perfect reference to design photoswitches, the retinal chromophore loses its outstanding properties when taken in solution [12]. Thus the dynamics of these photoreactions are critically influenced by the topology of the electronic PES in the vicinity of the CI (topology itself influenced by the interaction with the environment in the condensed phase), and the vibrational dynamics of the system through these intersections.

Excitation of the molecular system with a coherent laser pulse, temporally short enough compared to the vibrational periods of the molecule, multiple vibrational eigenstates can be populated to create a coherent superposition of eigenstates wave functions, which can be written as:

$$\psi(r,t) \quad = \quad \Sigma_n c_n \psi_n(r) \exp -i(\omega_n t - \varphi_n), \tag{1.1}$$

where $\psi(r)$ and ω_n are the eigenfunctions and transition frequency of the n^{th} vibrational level, c_n and φ_n represent the amplitude and phase of the latter, with r being a nuclear coordinate. Such a superposition of eigenstates is called vibrational wavepacket which oscillates back and forth along the r reaction coordinate, with the period T_0 of molecular vibrational motion ($\omega_n = \frac{2\pi}{T_0}(n+\frac{1}{2})$ for harmonic oscillator). Figure 1.3 shows a schematic representation of a molecule, which is electronically-excited with an ultrashort laser pulse.

The vibrational coherence results in a collective behavior among an ensemble of molecules. It reflects the nonstationary wavepacket dynamics of individual molecules, describing the nuclear motion. This can lead to a better understanding of a reaction, as the wavepacket evolves from the initial state, through transient states, and towards final products. The vibrational coherences observed during the dissociation of the ICN molecule by Zewail *et al* [9] demonstrated the first experimental observation of wavepackets in molecular systems. The vibrational coherence reactive motion has been observed also during the ultrafast photoisomerization of the retinal chromophore in Rho. Such coherence initially produced in the S_1 excited state, persists throughout the reaction coordinate until the formation of the impulsive photoproduct, in a so-called vibrationally-coherent photoreaction [10].

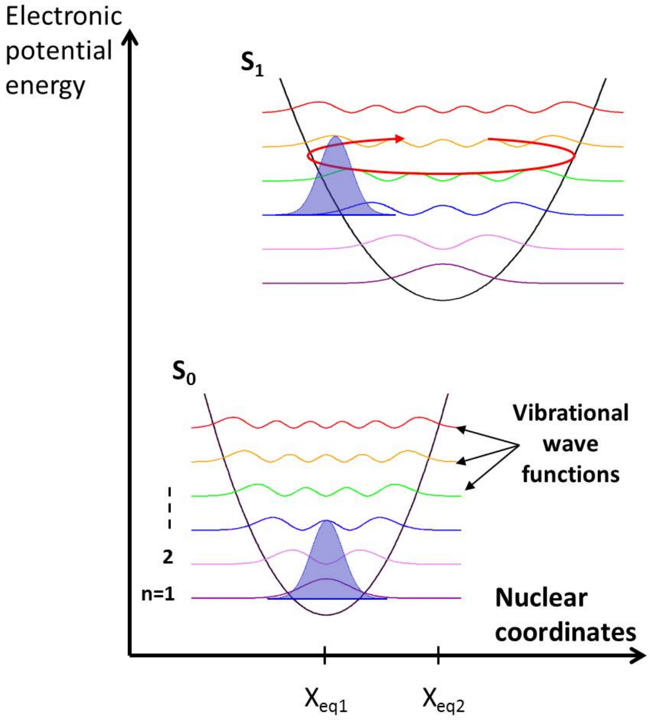

Figure 1.3.: Wavepacket generation principle. A laser pulse coherently excites multiple vibrational wavepackets in a molecule. The superposed eigenstates wave functions interfere to create a spatially localized wave function, referred to as a wavepacket.

The information about the mechanisms of isomerization open wide applicability of research on synthetic molecules that would mimic the photoreaction of Rho. In this approach, a class of molecules derived from the indanylidene-pyrroline (IP) expected to mimic the photoisomerization of the retinal chromophore in Rho has been designed and synthesized by Massimo Olivucci et *al* [13]. Fundamental investigations based on a combined theoretical and experimental approach show that the IP compounds undergo an ultrafast photoisomerization very similar to what is observed in Rho, except that their quantum yield is significantly lower [14]. These molecules undergo a vibrationally-coherent photoisomerization reaction [15, 16]. This is a conversion of light energy into mechanical energy impulsively delivered into a small number of vibrational degrees of freedom, in the electronic ground state before vibrational dephasing occurs due to the interaction with the thermal bath. Recent advances in quantum chemistry enabling the modeling of semi-classical trajectories with PES derived “on the-fly” from QM/MM computations [17] reveal the reactive motion along the photoreaction through the CI at the individual atomic level for molecules as complex as retinal in Rho or IP in a solvent, with very good agreement with observations[16].

Experimentally, understanding the mechanisms that govern the yield of such photoreactions, and the possibility to control the efficiency in handling optically the vibrational dynamics requires the use an excitation pulse whose duration is shorter than the periods for vibrational coherent reactive motion. Nowadays, the combination of computational technologies with ultrafast spectroscopy opens new opportunities towards understanding the physics of CI’s in general, including predicting the isomerization quantum yields. If the efficiency of such photoreactions could be optimized, it could be used to manufacture synthetic molecular machines or photoswitches to control molecular function, e.g peptide structures photocontrol [18, 19].

This PhD work takes place in the BIODYN experimental team of the Department of ultrafast Optics and Nanophotonics (DON) in close partnership with theoreticians via different collaborations (E.Gindensperger, Strasbourg; M. Olivucci, Italy; D. Sempedro, Spain). We study the photoisomerization mechanism of biomimetic molecular switches by transient absorption spectroscopy in order to understand the parameters witch govern the dynamics and the yield of this kind of photoreactions. In particular, we have explored the origin of the vibrationally coherent photoisomerization mechanism by comparing the photoreactions of a variety of IP compounds showing different substitutions. To further explore the link between the coherent vibrational dynamics, speed and efficiency of the photoreaction, we have developed during this thesis a new experimental setup using ultrashort laser pulses (< 8 fs) allowing us to generate vibrational wavepackets and to perform time-domain Raman spectroscopy also called Vibrational Coherence Spectroscopy (VCS). Then we exploit the opportunities of application of this mechanism to possible use of the photo mechanical energy conversion in these or similar photoswitches. This work is therefore organized as follows.

Chapter 2 introduces the principle of transient absorption spectroscopy measuring the dynamics of the electronics population during the photoreaction. We provide a description of the signals obtained by performing transient absorption measurement, including the data processing and analysis. The newly developed vibrational coherence spectrometer setup and its performances are presented in details in Chapter 3, together with the data that are acquired and the information that they provide. Note that the results disclosed in chapter 3 are the subject of an article already submitted.

Chapter 4 gives an exhaustive review of the experimental investigations of the IP biomimetic models of PSBR in Rho. After introducing the general biomimetic approach guiding this work, we present results obtained with unpublished members of the IP family to illustrate the two different types of photoisomerization reactions (coherent or non-coherent) generally observed. A systematic comparison of the photoisomerization dynamics, excited state lifetime and photoisomerization quantum yield is provided (article in preparation).
The results obtained of Vibrational Coherence Spectroscopy (VSC) on IP compounds that identify the distinct vibration signatures (especially in the low frequencies $> 500\ cm^{-1}$) are presented in Chapter 5. The combination off on- and off-resonant VCS schemes on the IP molecules, deciphers the vibrational modes which are signatures of the ground or excited state, or those which are excited optically or by the reactive motion itself and contribute to the reaction coordinate. Therefore, we provide a definitive proof of the occurrence of vibrationally-coherent photoisomerization in IP compounds as observed in Rho (article in preparation).

We have also explored in Chapter 6, the application of related compounds (also inspired by PSBR), to photoswitch the structure of a model peptide. We investigate, in collaboration with the academic team of D. Sampedro, Spain the influence of the cross-linked peptide on the photoreactivity of the molecular switch. In parallel, we also identify in Chapter 7 the spectroscopic properties and the reaction dynamics of a new biomimetic molecular switch, designed as a model anion of HBDI chromophore of GFP. Together with the theoretical studies of the Mr. Olivucci team, we have shown that the second generation of biomimetic photoswitches (anionic version) displays similar photoreaction dynamics of some IPs (cationic), which is explained by a nearby structure and similar charge translocation in the excited state (an opposite charge moves in the opposite direction). Finally, a summary and perspectives of this work are provided, while in the Appendix auxiliary calculations for Chapter 3 are given.

Part II.

Experimental methods

2. Tansient Absorption Spectroscopy of photoisomerizing compounds

Throughout this thesis, two experimental setups are used to characterize the photodynamics of the samples of interest, a conventional 70 fs temporal resolution, pump-probe transient absorption spectroscopy (TAS) system (historical setup) [15] for electronics dynamics populations characterization and a vibrational coherence spectroscopy (VCS) system for both electronics and vibrational dynamics characterization of the investigated samples.

In this chapter, we describe the main techniques relevant for measuring the electronic populations kinetics of isomerizing molecules, including data processing and analysis.

In many case a molecular system contain a mixture of components (isomers mixture, different populated states, solvent contribution), the spectroscopic signatures of these different contributions overlap and make the direct interpretation of the obtained data not straightforward. To relate an exhaustive quantitative description of the systems, the samples of interest should be characterized in order to determine the isomeric contents before performing pump-probe measurement. The latter provides data (containing rich informtions about the electronics state population dynamics) which have to be post-processed before quantitative analyses. In particular, the transient signals generated in the solvent and the quartz flow cell has to be subtracted from the data. The group velocity dispersion in the probe beam should be compensated so as to define accurately the time zero at all wavelengths. Also, because in general case the sample over which we perform transient absoption (TA) may contain a mixture of isomers, we have to extend the TA signal in Eq 2.9 in order to retrieve the pure isomer contributions.

Finally, a parameterized kinetic model for the temporal evolution of population is used to extract the quantitative properties, which means that the dynamics are modelled with a predefined analytical rate-equation model.

This procedure is adopted on the data obtained by performed TAS on the compounds presented in Chapter 4, 6 and 7. However, the analysis and the interpretation of the VCS (Chapter 3) data are different because the pump pulse used to trigger the photoreaction is very short and thus we detect both electronic and vibrational contributions.

2.1. Broadband transient absoprtion spectroscopy

2.1.1. Steady state absorption spectrsocopy

In order to investigate the photoreaction of molecules, it is essential to measure their ground state absorption spectrum. This measurement provides informations about the energy differences for transitions from the ground state (S_0) to the excited states (S_n) and also about the dipole moment and oscillator strength of the probed $S_0 - S_n$ transitions.

To start with, by definition of the *absorption cross section* σ, the number $\delta n/dt$ of photons absorbed per time unit by a UNIQUE absorber is equal to the product of the cross section by the incident flux of photons. With I the intensity of the incident light beam, and $h\nu$ the photon energy:

$$\frac{\delta n}{\delta t} = \sigma \times \frac{I}{h\nu}.$$

Hence, a medium of thickness dz, section S, and density ρ of absorbing (scattering) particles absorbs

$$\frac{\delta N}{\delta t} = \sigma \times \frac{I}{h\nu} \times \rho S dz$$

photons per time unit. The intensity of a light beam of section S traveling through this medium is then decreased by:

$$\begin{aligned} dI &= -\frac{\delta N}{\delta t} \times \frac{h\nu}{S} && (2.1) \\ dI &= -\sigma \times \frac{I}{h\nu} \times \rho S dz \times \frac{h\nu}{S} && (2.2) \\ \text{hence} \quad dI &= -I\sigma\rho dz. && (2.3) \end{aligned}$$

Within the *linear regime*, i.e if the intensity I is *small enough*, then the absorption cross section is *independent* of the intensity (say I smaller than the saturation intensity, see for instance the 2-level model), and Equation (2.3) can be integrated in a simple exponential law:

$$I(z) = I_0 \exp(-\sigma\rho z).$$

This is the Beer-Lambert Law. The wavelength-dependent steady-state absorbance *absorbance* A of a medium is defined as:

$$A(\lambda) = -\log_{10}(I(\lambda)/I_0(\lambda)) = \varepsilon(\lambda)cz,$$

where ε is the *extinction coefficient* (independent of I, within the linear regime), and c is the concentration (in Mol.L^{-1}) of the absorber particles. Then the following relation holds:

$$\sigma = \ln 10 \frac{\varepsilon}{N_A}.$$

2.1.2. Determination of the ground state isomeric content and the pure isomer steady state absorption

The molecular conformations are referred to as E and Z (or cis and trans) isomers, according to their ground state structure. The solution that we use to perfrom TAS is usually a mixture of both related isomers. The isomers have different steady state absorption according to their photochromism properties. The latter is the light induced reversible conversion in the absorption spectrum of molecules. The thermally activated interconversion may be very slow due to the high ground state energy barrier between E and Z -isomers, therefore the solution are sometimes a mixture of both isomers. Thus it is important to determine the proportion of each isomers and their pure steady state absorptions, before performing experiment.

For this purpose, two types of measurement are necessary, firstly a measurement of the absorption spectra of molecules in solution before and after illumunation with a laser beam by using a UV-Vis spectrometer (U-3000 spectrophotometer, Hitachi) and secondly Nuclear Magnetic Resonance (NMR) spectroscopy measurement of the isomeric composition of these solutions using a 300-MHz ^{1}HNMR spectrometer (Avance 300 MHz, Bruker). The first step allows also determining an important feature of the molecules, the isosbestic point which is a wavelength where both isomers have the same extinction coefficient.

To illustrate this procedure, we consider the Ch-MeO-NAIP sample (See Chapter 3). It is in the pure E isomer when freshly prepared in the dark at room temperature. The Z isomer may be accumulated upon illumination at 350 nm in CD_3OD until reaching the photostationary state, which depends to illumination conditions. The spectra of the dark and illuminated solutions are plotted in Figure 2.1.A. Notice that, here, the *light-adapted* (LA) and *dark-adapted* (DA) samples refer respectively to the fresh solution kept in the dark (with dominating E form) and to the illuminated sample (which is most likely a mixture of E and Z).

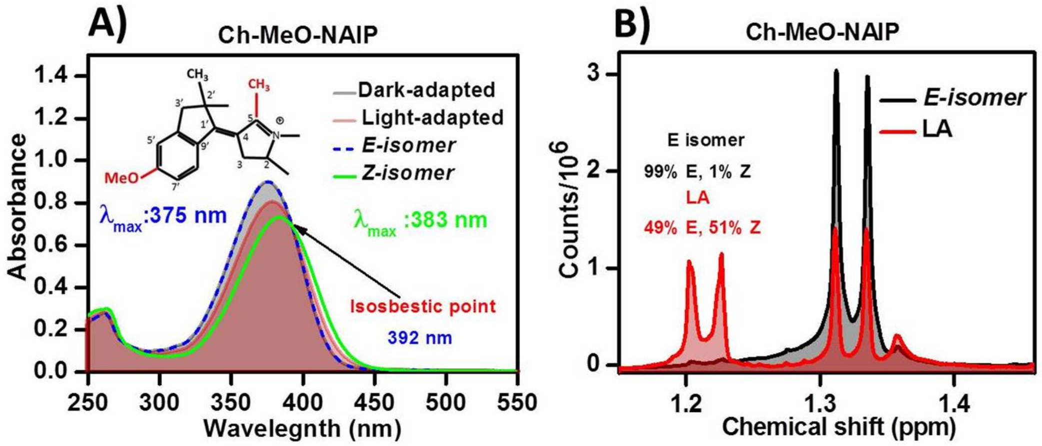

Figure 2.1.: A) DA (balck), LA (red) *E isomer* (dashed blue and *Z isomers* (green) absorption spectra for Ch-MeO-NAIP. The inset displays the structure of the molecule. B) NMR spectrum in the 1.15 to 1.46 ppm region. The area below these signals helps to determine the *Z*:*E isomer*ratio.

NMR peaks-shift measurement on the sample related above is displayed in Figure 2.1.B, where we can find two specific proton signatures. The local environment of the proton changes depending on whether the molecule is in E or Z conformation which leads to different chemical shifts when exposed in a magnetic field. Thus NMR is a quantitative isomer-sensitive tool, since the signals areas are proportional to the number of protons involved in the E or Z conformations. The computations of the areas of the two measured spectra allows us to determine the percentage of E and Z species present in the DA and LA solutions. In one case (E isomer black curves), the sample was carefully kept in the dark. The E isomer form represents more than 99% of the molecules. The other signal (LA sample, red curves) is the NMR spectra obtained after irradiation with a laser at 350 nm. The photostationary state isomeric content is then 49% E /51% Z.

Finally, by knowing the absorption spectra and the isomeric contain of both DA and LA solutions, we can determine the pure absorption spectra of both isomers following the linear combination of the two spectra:

$$A_{DA} = \alpha_1 A_0^E + \beta_1 A_0^Z \tag{2.4}$$

$$A_{LA} = \alpha_2 A_0^E + \beta_2 A_0^Z \tag{2.5}$$

where α_1, β_1, α_2 and β_2 represent respectively the corresponding percentage of each isomer in the DA and LA solutions. By linear combination, we obtain the pure A_0^E and A_0^Z absorption spectra of the two isomers:

$$A_0^E = \frac{\beta_2 A_{DA} - \beta_1 A_{LA}}{\alpha_1\beta_2 - \alpha_2\beta_1} \tag{2.6}$$

$$A_0^Z = \frac{\alpha_2 A_{DA} - \alpha_1 A_{LA}}{\alpha_2\beta_1 - \alpha_1\beta_2} \tag{2.7}$$

The result is plotted in Figure 2.1.A, with the spectra of the pure *E isomer* (absorption maximum at 375 nm) and the pure *Z isomer* (λ_{max}= 383 nm) red shifted compared to the *E isomer* one. The isosbestic point is at 392 nm.

2.1.3. Transient absorption signal

The main principle of the TAS technique is illustrated in Figure 2.2.A.
An ultrafast TAS consists in exciting resonantly the sample with a laser pulse called pump pulse, in order to bring the population into an excited state, and trigger a photo-reaction process in the solute. Then after an adjustable time delay t, a second broadband weak and ultrafast pulse (continuum or white light pulse) called probe pulse is sent through the sample. The pump-induced transient absorption change of the sample i (i standing for e.g LA or DA solution) can be writen:

$$\Delta A_i(\lambda, t) = A_i(\lambda, t)_{P_{on}} - A_i(\lambda, t)_{P_{off}} \tag{2.8}$$

where P_{on} and P_{off} meaning the pump is "on" or "off". Thus according the description related in Pollard *et al* [20], the TAS can be understood as a third order nonlinear interaction ($P^{(3)}$), with two-order interactions with the pump pulse to create the populations and a third-order interaction with the probe to interrogate the perturbed system. However, in their work the authors concluded that, because the excitation and the probe steps have been separated, the probe pulse can now be considered to measure the first-order linear absorption spectra of the nonstationary ground and excited state. According this validity, we can write:

$$\Delta A_i(\lambda, t) = \Delta c_i \times \sum_{k=1}^{N_i} n_k^i(t)\varepsilon_k^i(\lambda, t) \times l \tag{2.9}$$

where the Δc_i is the pump-induced initial change in concentration of solute i in its ground state, $n_k^i(t)$ are the (normalized) electronics population kinetics of the species k which are formed upon excitation of solute i, and the $\varepsilon_k^i(\lambda, t)$ the corresponding transient extinction coefficients. The $\{n_k^i(t)\}$ do not depend on the Δc_i provided the molecular dynamics are governed by processes of individual molecules.

Consider the case in which the excitation brings part of the population in the first excited state S_1, the same part is lacking in the S_0 ground state which reduces the absorption of the sample. This resultes in ΔA, a negative contribution called Ground State Bleach (GSB) with the same spectral signature as the steady state absorption. The population of molecules that have been promoted to S_1 by the pump may return to S_0. This also resultes a negative contribution in ΔA called Stimulated Emission (SE) with a spectral signature related to the static fluorescence. Excited State Absorption (ESA) and Photoproduct Absorption (PA) are both induced absorptions and concern transitions between new (excited or photoproduct) states and higher laying electronics states. Both signals provide positive contributions to ΔA signal. Figure 2.2.B schematizes the 4 majors transient absorption signal introduced above.

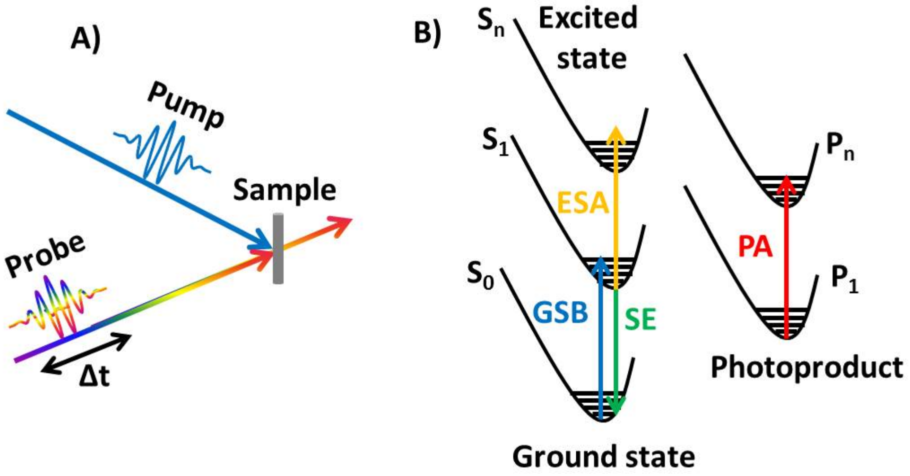

Figure 2.2.: A) Scheme representing the transient absorption spectroscopy: A strong, resonant excitation pulse triggers dynamical process in the sample. After an adjustable delay time, another probe pulse is sent through the sample. Comparison between the probe pulses when the pump is on and off gives the pump-induced absorption changes at a given delay time. B) Assignments of the different measured signals according the electronic energy levels: GSB, ground state bleach; ESA, excited state absorption; SE, stimulated emission; PA, photoproduct absorption.

2.1.4. Excitation probability

The transient absorption experiment can be considered as a spectroscopic study of an excited molecular state. Hence the signal depends primarily on how many molecules are brought to this excited state by the pump beam. Thus checking the linearity of the ΔA signal with respect to the excitation density is relavant to avoid the saturation of the transient absorption signal. To evaluate the excitation density, let's consider a pump laser pulse (frequency ν_p, section S, energy per pulse $\mathcal{E}_p$) traveling over a distance l through a solution containing different solutes at concentrations c_i, with extinction coefficients $\varepsilon_i(\nu_p)$. The total absorbance of the solution at the pump wavelength is $A_p = \sum_i \varepsilon_i(\nu_p)c_i l$. We define $a = A_p/l$ and $a_i = c_i\varepsilon_i(\nu_p)$, with $a = \sum_i a_i$. According to the Beer-Lambert law, the energy $\delta\mathcal{E}_i$ absorbed by each solute i within a slice of thickness dz after propagation over z inside the solution is given by:

$$\begin{aligned} \delta\mathcal{E}_i &= \ln(10)\mathcal{E}(z) \times \varepsilon_i c_i dz \\ &= \mathcal{E}_p \times 10^{-az} \times a_i \ln(10) dz \end{aligned} \tag{2.10}$$

Over the full solution thickness (integration over z from 0 to l), the light energy absorbed by solute i is:

$$\begin{aligned} \Delta\mathcal{E}_i &= \int_0^l \mathcal{E}(z) \times \varepsilon_i c_i \ln(10) dz = a_i\mathcal{E}_p \int_0^l \exp(-\ln 10\, az)\ln(10)dz \\ &= \frac{a_i}{a}\mathcal{E}_p \times (1 - 10^{-al}) \end{aligned} \tag{2.11}$$

The number of photons absorbed over the entire column of solution (thickness l) is $\Delta\mathcal{E}_i/(h\nu)$ and is equal to the number of molecules of solute i excited in a linear regime of absorption. Hence we may define an initial pump-induced change of "column-averaged" concentration of solute i over the full solution thickness by:

$$\Delta c_i = -\frac{\Delta\mathcal{E}_i}{h\nu_p N_A S l} = -\frac{\varepsilon_i(\lambda_p)\, c_i}{N_A}\,\frac{\mathcal{E}_p}{h\nu_p S}\,\frac{1 - 10^{-A_p}}{A_p} \tag{2.12}$$

and the relative change of the concentration of solute i, hence the column-averaged excitation probability is:

$$\frac{\Delta c_i}{c_i} = -\frac{\varepsilon_i(\lambda_p)}{N_A}\,\frac{\mathcal{E}_p}{h\nu_p S}\,\frac{1 - 10^{-A_p}}{A_p} \tag{2.13}$$

orders of magnitude

In the limit of very thin or very dilute sample, the absorbance A_p vanishes, and all molecules in the sample "see" the same light intensity. Note that, in the case where $A_p = 0$, the quantity $(1 - 10^{-A_p})/A_p$ has a maximum value of $\ln(10) \simeq 2.3026$. In this limit, exciting the molecules within the linear regime means that $\Delta c_0/c_0$ remains small (say 1% for instance). With typical values: $\varepsilon(\nu_p) = 10^4$ L.Mol^{-1}cm^{-1}, $\nu_p = c/(400\text{ nm})$, we get the energy density required for a 1% excitation probability, i.e. an order of magnitude of the maximum pump intensity compatible with the linear regime (i.e. the saturation intensity):

$$\frac{\mathcal{E}_p}{S} = \frac{N_A}{\varepsilon_0(\nu_p)} \times h\nu_p \times \frac{1\%}{\ln(10)} \simeq 0.13\text{ mJ/cm}^2$$

The lower the extinction coefficient, or the photon wavelength, the larger the saturation intensity. Typically for a given pump diameter of ~ 100 µm and 36 nJ in pulse energy (180 µW at 5 kHz repetition rate), a extinction coefficient of ~ 23000 /M/cm, the maximum excitation probability is therefore 5%. The experimental determination of the saturation of the pump-probe signal as a function of pump intensity shows the onset of saturation (say a typical 10% less than expected if linear) at approximately 2 times the excitation density determined here for 5% excitation probability.

2.1.5. Pump-probe stup

The overview of the transient absorption spectroscopy set-up used to perform measurement have been described previously[15]. Briefly, it is based on a Ti:sapphire generative amplifier laser system, delivering 800 nm, 40 fs pulses at a repetition rate of 5 kHz. A beam splitter divides the initial pulse into two pulses. The first one is either injected in a TOPAS (Optical Parametric Amplifier from “Light Conversion”) to generate a 290 nm-20 μm pump beams, or it is used for second harmonic generation (SHG in a BBO crystal) to generate a 400-nm pump beam. The second pulse is used to generate the white light probe pulse (supercontinuum generation in CaF_2) covering a spectral range from 290 nm to > 950 nm. The time delay between pump and probe pulses are adjusted by a stepper motor (“delay line”). The experimental time resolution is ~ 70 fs determined by fitting with a Gaussian profile the stimulated Raman scattering signal from the methanol C-H stretch. Both pump and probe beams are focused into a 0.2-mm thick flow cell containing the sample in solution. We will discuss in more detail most of these elements and their functional principles in the following chapter, where we address a similar transient absorption setup different with the related one by the pump pulse duration. The actual ~ 70 fs time resolution transient absorption setup is expected to provide information about the dynamics of the electronic populations and thus provides information about the photo-processes of the investigated sample.

2.2. Data processing and correction

The data recorded using TAS need to be corrected by removing some unwanted contributions. Indeed, the solvent response which is only occurring during the pump/probe temporal overlap, determines the time zero at all wavelengths. As Cleary seen in Figure 2.3 .A and .B, time zero is wavelength-dependent, due to group velocity dispersion (GVD) which affects the white-light continuum, and thus the transient absorption signal. The absolute zero delay should be defined accurately before the analysis of the data. Analyzing the data in order to extract information about the populations dynamics required general data processing techniques [21].

2.2.1. Solvent response correction

Within the first 100 fs, the so-called ”coherent artefact” appears as a pump-induced signal while resulting from an interaction between the pump and probe pulses in the solvent. This signal, is mostly due to pump-probe cross-phase modulation (XPM) and two-photon absorption (TPA), possibly appearing on the whole wavelength range, and to Raman contributions, giving signals at solvent-dependent specific wavelengths [22], [23]. This coherent ultrafast signal is presented in Figure 2.3 .A and .B in the case of methanol with a pump central wavelength of 400 nm. These contributions are measured in the very same experimental conditions as for the sample of interest, by performing a transient absorption experiment with the solvent only, for delays close to time zero. These solvent contributions can be subtracted from the sample data, in order to have only transient absorption contributions from the investigated molecule. Usually, when the pump is resonant with the absorption of the molecule of interest, its average intensity is absorbed by the molecule in the excited volume, somewhat attenuating the solvent contribution in the sample data. The correction is done by subtracting the solvent dataset from the sample one by using a multiplication factor α (always $\leqslant 1$) which takes into account the sample absorption at the pump excitation wavelength, as shown in Eq 2.14.

$$\Delta A(\lambda, t)_{corrected} = \Delta A(\lambda, t)_{sample\ in\ solvent} - \alpha \Delta A(\lambda, t)_{solvent} \tag{2.14}$$

2.2.2. Group velocity Dispersion (GVD) correction

The supercontinuum probe beam is generated inside a crystal (CaF_2 or Sapphire) and spans over a large range of wavelengths 300-800 nm. As a result of the dependence of the refractive index as a fuction of wavelength, Group Velocity Dispersion (GVD) induces a chirp in the white ligth (see Fig.2.3. A). The low

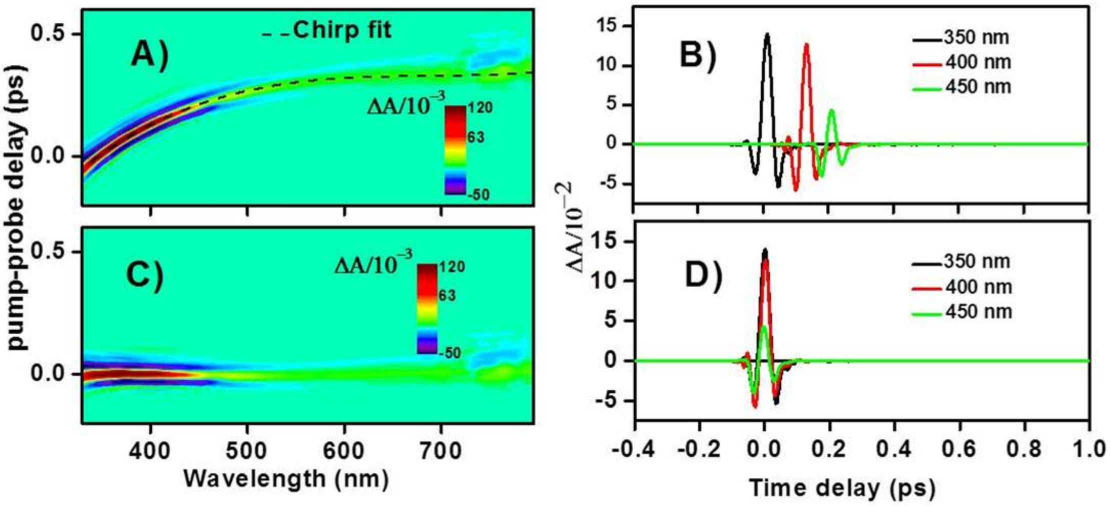

Figure 2.3.: A) Transient absorption change (ΔA) data of methanol, together with the polynomial fit (dashed) defining the GVD curve. B). Transients at 340, 400 nm and 450 nm, showing prominent TPA, XPM processes and temporal shifts. C), D) Same as A) and B) respectively after GVD compensation.

energy part of the probe pulse travels faster than the high energy part, and thus interacts with the pump at different delays that can span over 200 fs. Although the GVD has been minimized by thin optics. At each individual probe wavelength, time zero is defined within ± 20 fs as being the time-axis mid-point of the coherent solvent signal (see Fig.2.3. A). In order to characterize the GVD, a fifth-order polynome is used to fit the location of the wavelength-dependent time zero. A representative example is introduced in Figure.2.3. B to illustrate the GVD compensation in methanol. A home-implemented Scilab routine time-shifts the data for the different wavelengths according to the determined GVD polynome. Figure 2.3 .C and D show the signal of the solvent (methanol) after the GVD correction.

2.2.3. Reconstruction of pure isomers transient absorption signal

As discussed above, the investigation of photoisomerization by TAS may suffer from the presence of both isomers if the solution is not pure. Deciphering isomer specific kinetics is thus necessary to investigate each isomer reaction dynamics. For this purpose we perform two TAS experiments on two solutions of different know isomer content (e.g LA and DA solutions), and we compute the isomer-specific data set according to the procedure detailed below.

Consider a solution of two isomers E and Z with a total concentration c_0 and a fraction x of Z isomer. Its absorbance at the pump wavelength is:

$$A_p(x) = c_0 l \left(x\varepsilon_Z(\lambda_p) + (1-x)\varepsilon_E(\lambda_p) \right).$$

We perform two transient absorption experiments $\Delta A_1(\lambda, t)$ and $\Delta A_2(\lambda, t)$ on the same solution in the very same conditions, but with two values x_1 and x_2 of x, and we want to infer the transient absorption maps of pure E and Z molecules. We define:

$$\begin{aligned}
\Delta A(\lambda,t,x)/l &= \Delta c_E(x) \times \sum_{k=1}^{N_E} n_k^E(t)\varepsilon_k^E(\lambda,t) + \Delta c_Z(x) \\
&\quad \times \sum_{k=1}^{N_Z} n_k^Z(t)\varepsilon_k^Z(\lambda,t) && (2.15) \\
\Delta A_E(\lambda,t)/l &= \Delta c_E(x=0) \times \sum_{k=1}^{N_E} n_k^E(t)\varepsilon_k^E(\lambda,t) && (2.16) \\
\Delta A_Z(\lambda,t)/l &= \Delta c_Z(x=1) \times \sum_{k=1}^{N_Z} n_k^Z(t)\varepsilon_k^Z(\lambda,t) && (2.17) \\
\text{with} \quad \Delta c_{E,Z}(x) &= -\frac{\varepsilon_{E,Z}(\lambda_p)\, c_{E,Z}}{N_A} \frac{\mathcal{E}_p}{h\nu_p S} \frac{1-10^{-A_p(x)}}{A_p(x)} < 0 && (2.18)
\end{aligned}$$

With the following notations:

$$\boxed{\begin{aligned}
c_Z(x) &= x c_0 \\
c_E(x) &= (1-x)c_0 \\
A_p(x) &= c_0 l \left(x\varepsilon_Z(\lambda_p) + (1-x)\varepsilon_E(\lambda_p) \right) \\
g(x) &= \tfrac{1-10^{-A_p(x)}}{A_p(x)}
\end{aligned}} \qquad (2.19)$$

One may write:

$$\Delta A(\lambda,t,x) = \frac{(1-x)g(x)}{g(0)} \times \Delta A_E(\lambda,t) + \frac{x g(x)}{g(1)} \times \Delta A_Z(\lambda,t) \qquad (2.20)$$

And thus:

$$\begin{aligned}
&\frac{g(0)}{(1-x_1)g(x_1)}\Delta A(\lambda,t,x_1) - \frac{g(0)}{(1-x_2)g(x_2)}\Delta A(\lambda,t,x_2) \\
= &\frac{g(0)}{(1-x_1)g(x_1)}\frac{x_1 g(x_1)}{g(1)} \times \Delta A_Z(\lambda,t) - \frac{g(0)}{(1-x_2)g(x_2)}\frac{x_2 g(x_2)}{g(1)} \times \Delta A_Z(\lambda,t) \\
\text{and} \quad &\frac{g(1)}{x_1 g(x_1)}\Delta A(\lambda,t,x_1) - \frac{g(1)}{x_2 g(x_2)}\Delta A(\lambda,t,x_2) \\
&\frac{g(1)}{x_1 g(x_1)}\frac{(1-x_1)g(x_1)}{g(0)} \times \Delta A_E(\lambda,t) - \frac{g(1)}{x_2 g(x_2)}\frac{(1-x_2)g(x_2)}{g(0)} \times \Delta A_E(\lambda,t)
\end{aligned}$$

that is:

$$\begin{aligned} &\frac{\Delta A(\lambda,t,x_1)}{(1-x_1)g(x_1)} - \frac{\Delta A(\lambda,t,x_2)}{(1-x_2)g(x_2)} = \frac{x_1-x_2}{(1-x_1)(1-x_2)g(1)}\Delta A_Z(\lambda,t) \\ \text{and} \quad &\frac{\Delta A(\lambda,t,x_1)}{x_1 g(x_1)} - \frac{\Delta A(\lambda,t,x_2)}{x_2 g(x_2)} = \frac{x_2-x_1}{x_1 x_2 g(0)}\Delta A_E(\lambda,t) \end{aligned} \tag{2.21}$$

In the end, the followig equations are used:

$$\boxed{\begin{aligned} \Delta A_Z(\lambda,t) &= \tfrac{g(1)}{x_1-x_2}\left(\tfrac{1-x_2}{g(x_1)}\Delta A(\lambda,t,x_1) - \tfrac{1-x_1}{g(x_2)}\Delta A(\lambda,t,x_2)\right) \\ \Delta A_E(\lambda,t) &= \tfrac{g(0)}{x_2-x_1}\left(\tfrac{x_2}{g(x_1)}\Delta A(\lambda,t,x_1) - \tfrac{x_1}{g(x_2)}\Delta A(\lambda,t,x_2)\right) \end{aligned}} \tag{2.22}$$

Here $\Delta A_Z(\lambda,t)$ and $\Delta A_E(\lambda,t)$ are respectivelly the TAS signal of the pure Z- and E-isomer respectively. This computation is valid if the excitation density used by performing TAS on the LA and DA solutions is exactelly the same with also the same initial concentration c_0 of both solutions. Therefore to apply this formula, we need only to know the absorbance, the isomeric content of both LA and DA solutions and the excitation coefficients of both isomers.

About photoreaction quantum yield determination.

The differential absorption spectrum ΔA reaches a stationary spectral shape, which overlaps with the difference between E and Z extinction coefficients, showing the completion of the photoreaction. These final ΔA spectra are reached after a typical 50 to 100 ps, during which complete equilibration with the solvent proceeds, and are the signature of reaction of the initial isomer to produce the other one. For each isomer, the relative amplitude of the final difference spectrum to that of the initial GSB, would allow us to determine the photoisomerization quantum yield. However, generally, the ESA overlaps with and is stronger than the GSB, preventing accurate absolute QY determination by this method. Instead, relative isomerization yields of two compounds (e.g. two isomers) can be accurately determined from the relative intensities of the final spectra, provided the extinction coefficient of both compounds is accurately known, and that the experiments are performed in identical conditions on both compounds. The computation of the relative QY is described as the following.

If the photoreaction is finished at the end of the observation time window, the ”final” transient absorption change of the Z (resp. E) species is the contribution of the initial bleach refilled by the non-reactive formation of Z (resp. E) and of the reactive formation of E (resp. Z) :

$$\Delta A_Z(\lambda, t=\infty)/l \;=\; \Delta c_Z(x=1) \times (1-(1-\eta_Z)\varepsilon_Z(\lambda) - \eta_Z\varepsilon_E(\lambda)) \quad (2.23)$$
$$\Delta A_E(\lambda, t=\infty)/l \;=\; \Delta c_Z(x=0) \times (1-(1-\eta_E)\varepsilon_E(\lambda) - \eta_E\varepsilon_Z(\lambda)) \quad (2.24)$$

where $\Delta A_Z(\lambda, t)$ and $\Delta A_E(\lambda, t)$ are given by Eq 2.22, and η_Z and η_E are the photoisomerization quantum yields of species Z and E respectively. Using Eq 2.12, one gets:

$$\Delta A_Z(\lambda, t=\infty)/l \;=\; -\frac{\varepsilon_Z(\lambda_p)\, c_0}{N_A}\, \frac{\mathcal{E}_p}{h\nu_p S}\, g(1) \times \eta_Z(\varepsilon_Z(\lambda) - \varepsilon_E(\lambda)) \quad (2.25)$$
$$\Delta A_E(\lambda, t=\infty)/l \;=\; -\frac{\varepsilon_E(\lambda_p)\, c_0}{N_A}\, \frac{\mathcal{E}_p}{h\nu_p S}\, g(0) \times \eta_E(\varepsilon_E(\lambda) - \varepsilon_Z(\lambda)) \quad (2.26)$$

There the ratio between the photoisomerization quamtum yield (QY) in both directions is given by:

$$\boxed{\frac{\eta_Z}{\eta_E} = -\frac{\Delta A_Z(\lambda, t=\infty)}{\varepsilon_Z(\lambda_p) g(1)} \times \frac{\varepsilon_E(\lambda_p) g(0)}{\Delta A_E(\lambda, t=\infty)}} \quad (2.27)$$

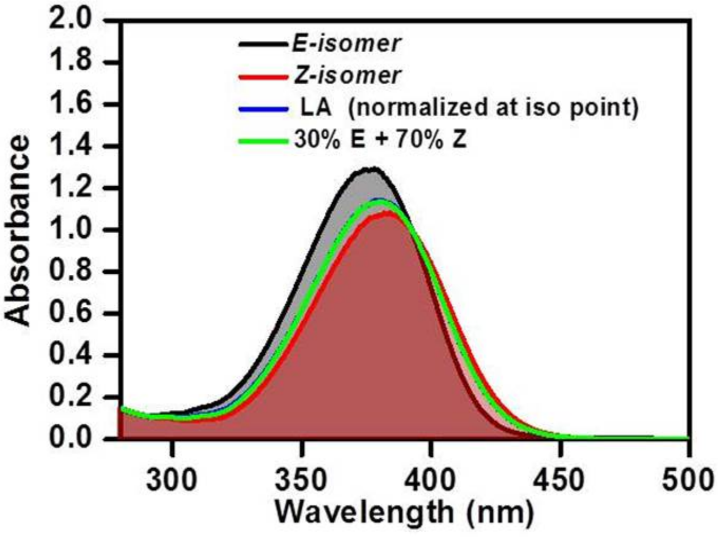

Figure 2.4.: textitE (balck), Z (red),normailzed-LA (blue) and linear combinaison of E and Z (green) absorption spectra for Ch-MeO-NAIP.

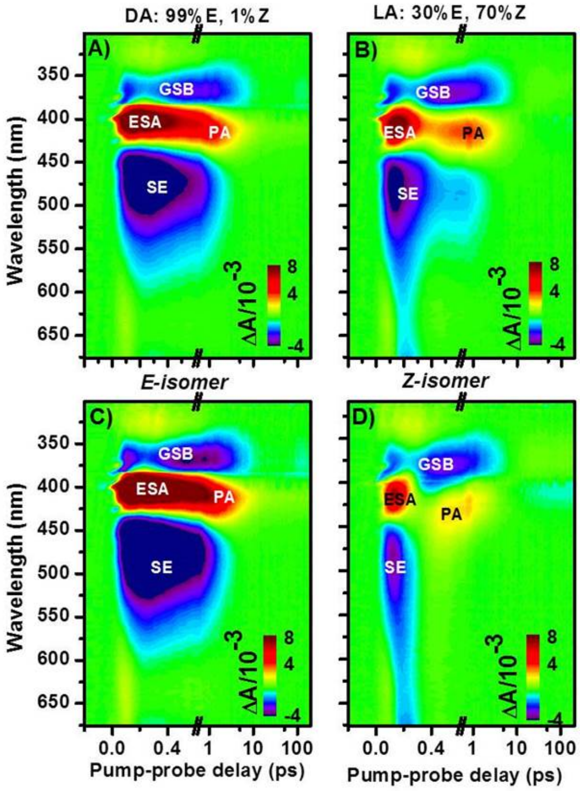

Figure 2.5.: A) 2D Transient absorption change ΔA in methanol after excitation at 400 nm, as function of wavelength (in nm) and time delay between excitation and probe pulse (in ps) of DA A) and LA B) solutions of Ch-dMe-MeO-NAIP. C) and D) Reconstructed transient absorption data for the pure E-isomer and pure Z-isomer of Ch-MeO-NAIP respectively.

As an example, we illustrate this technique on the Ch-MeO-NAIP molecular switch. In the dark at room temperature, the composition of Ch-MeO-NAIP DA solution used in this experiment is dominated by the stable E isomer witch accumulates up to $> 99\%$. Upon irradiation at 333 nm, a photostationary state is obtained. In order to determine the isomer contents of this latter, we normalize the absorption of the corresponding solution at the isosbestic point, with respect to the absorption of the pure E and Z solutions determined above by NMR. The spectrum resulting from the linear combinaison of both pure E and Z absorption spectra ($30\%\ E + 70\%\ Z$) is in good agreement with the LA absorption spectrum (see Fig 2.4).
It is immediately seen in Figure 2.5 that the TAS signature of the majority Z-isomer is clearly distinct from that of the minority E-isomer in the LA solution of Ch-MeO-NAIP (Fig 2.5.B). Quantitative comparison between both isomer-

ization directions requires extraction of the pure isomer contributions from the TAS data of the mixture. The application of the Eq 2.22 on the raw TAS 2D-maps obtained for the DA and LA solutions allows us to recover the TAS signal of pure *E* and *Z* isomer, as shown in Figure 2.5.C and D.

2.2.4. Data fitting

In order to perform quantitative analysis of the population dynamics, the datas have to be adjusted with a model function. If the model provides the good fit convergence, we can use the fitting parameters to describe the molecular photoreaction. The most common model is a rate equation. Here we give a short illustration considering a very simple model system in which a number N_0 of molecules are promoted to the first S_1 excited state upon impulsive excitation. The vibrationally hot S_1 population decay into an relaxed S_{1R} state with a rate constant k_{12} due to fast intramolecular vibrational relaxation. Then the population decays to S_0 with a rate constant k_{20} as represented in the Figure 2.6). The time evolution of the population on the different states can be written as follows:

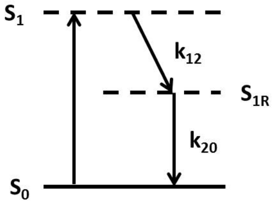

Figure 2.6.: Model photoreaction

$$\begin{aligned} \frac{dN_1(t)}{dt} &= -k_{12}N_1(t) \\ \frac{dN_2(t)}{dt} &= -k_{20}N_2(t) + k_{12}N_1(t) \\ \frac{dN_0(t)}{dt} &= k_{20}N_2(t) \end{aligned} \tag{2.28}$$

It assums that the dynamics can be described by rate constants corresponding to the transitions between the involved states.

Thus, by solving the equations 2.28, we obtain the concentration of the populations in the different states:

$$\begin{aligned} N_1(t) &= N_0 \exp^{-k_{12}.t} \\ N_2(t) &= \frac{N_0 k_{12}}{k_{12}-k_{20}}(\exp^{-k_{20}.t} - \exp^{-k_{12}.t}) \\ N_0(t) &= \frac{N_0}{k_{12}-k_{20}}(k_{20}\exp^{-k_{12}.t} - k_{12}\exp^{-k_{20}.t}) + N_{tot}, \end{aligned} \tag{2.29}$$

with $N_{tot} = \sum_{i=0}^{2} N_i(t)$ is the total concentration of the sample. The steady state absorbance of the sample of thickness l at $t = 0$ is given by:

$$A_0(\lambda) = N_{tot}\epsilon_0(\lambda)l, \tag{2.30}$$

and the absorption at a given time $t > 0$ is given by:

$$A(\lambda, t) = [N_1(t)\epsilon_1(\lambda) + N_2(t)\epsilon_2(\lambda) + N_0(t)\epsilon_0(\lambda)]l \tag{2.31}$$

Thus the differential absorption as function of time and wavelength becomes (cf Eq 2.9):

$$\begin{aligned} \Delta A(\lambda, t) &= A(\lambda, t) - A_0(\lambda) \\ &= [N_1(t)\epsilon_1(\lambda) + N_2(t)\epsilon_2(\lambda) + (N_0(t) - N_{tot})\epsilon_0(\lambda)]l \\ &= [(N_1(t)(\epsilon_1(\lambda) - \epsilon_0(\lambda)) + (N_2(t)(\epsilon_2(\lambda) - \epsilon_0(\lambda))]l \end{aligned} \tag{2.32}$$

Replacing the $N_i(t)$ by theirs expected expressions (Eq 2.29), we can we rationalize the Eq 2.32 with exponentials as common factors, and it becomes:

$$\begin{aligned} \Delta A(\lambda, t) &= (N_0\epsilon_1 - \frac{N_0 k_{12}}{k_{12}-k_{20}}\epsilon_2 + \frac{N_0 k_{20}}{k_{12}-k_{20}}\epsilon_0)\exp^{-k_{12}.t} \\ &+ (\frac{N_0 k_{12}}{k_{12}-k_{20}}\epsilon_2 - \frac{N_0 k_{12}}{k_{12}-k_{20}}\epsilon_0)\exp^{-k_{20}.t} \end{aligned} \tag{2.33}$$

The Eq.2.33 shows that $\Delta A(\lambda, t)$ evolves in term of exponentials decay.
Therefore the differential absorption can be written as a sum of exponentials decays:

$$\Delta A(\lambda, t) = \sum A_i e^{-k_i.t}, \tag{2.34}$$

where A_i are constants. Thus, according to this model, the data can be effectively adjusted with a sum of exponential terms, convoluted by the response function $R(t)$ of the experimental set-up:

$$\Delta A(\lambda, t) = \left\{A_0 + H(t) \times \left(\sum A_i e^{-t/\tau_i}\right)\right\} \otimes R(t - t_0) \tag{2.35}$$

Here, A_0 accounts for a possible offset at negative delays, $H(t)$ is the Heaviside function ($H(t) = 0$ it $t < 0$; $H(t) = 1$ if $t \geq 0$. To each decay constant $\tau_i = 1/k_i$ an amplitude A_i is assigned. In case the different decays would start after a time delay t_i, one can write:

$$\Delta A(\lambda, t) \;=\; \left\{A_0 + H(t-t_i) \times \left(\sum A_i e^{-(t-t_i)/\tau_i}\right)\right\} \otimes R(t-t_0) \qquad (2.36)$$

Assuming a normalized Gaussian function for the response function:

$$R(t) = \frac{1}{\sigma\sqrt{2\pi}}\ \exp\left(-\frac{t^2}{2\sigma^2}\right),$$

the analytical expression of Eq 2.36 is:

$$\begin{aligned}\Delta A(\lambda, t) = A_0 \ + \sum_i \Bigg[\frac{A_i}{2}\ \exp\left(\frac{\sigma^2}{2\tau_i^2}\right)\ \exp\left(-\frac{t-t_0-t_i}{\tau_i}\right) \\ \times\ \left(1 + \ \operatorname{erf}\left(\frac{t-t_0-t_i-\sigma^2/\tau_i}{\sigma\sqrt{2}}\right)\right)\Bigg],\end{aligned} \qquad (2.37)$$

where erf designates the error function and σ is the standard deviation of the response function $R(t)$.

Assuming a time constant τ_G is faster than the experimental time resolution σ: $\tau << \sigma$. The convolution yields the nearly unaltered shape of the Gaussian. The exponential function takes non vanishing values over an interval of a few τ' around $t' = 0$ (or $t' = \tau_G$). On that interval, the IRF varies very little and may be approximated by its Taylor development. We must therefore add to the adjustment function 2.37 the term A_g multiplied by the term of the instrumental response function $R(t)$):

$$\tilde{\Delta A}(\lambda, t) = \frac{A_G}{\sigma\sqrt{2\pi}} \exp\left(-\frac{(t-t_0)^2}{2\sigma^2}\right) + \Delta A(\lambda, t), \qquad (2.38)$$

where A_G is the amplitude of the non resolved component.

2.2.5. Singular values decomposition and global analysis

In order to reveal the whole molecular dynamics, global analysis is performed by adjusting all the kinetics traces with the same time constants. Singular Value Decomposition (SVD) gives the possibility to filter and decompose any 2D matrix in a set of singular transients associated with singular spectra and characterized by their relative weight, i.e. the singular values (SV). Global fitting is then performed by the simultaneous fitting of the singular kinetics characterized by the dominant few singular values. The information contained in the other terms of the decomposition (weaker singular values and singular kinetics) are disregarded as being representative of the noise in the data.

Time-resolved spectroscopy data are matrices (functions of wavelength λ_i and time delay t_i) of the kind: $Data_{ij} = D(\lambda_i, t_j)$. Here i denotes the line number (i.e. a time evolution at a given wavelength), j the column number (i.e. a spectrum at a given time delay). The SVD is a mathematical decomposition of the Data matrix of the kind:

$$Data_{ij} = \Sigma_{mn} U_{im} S_{mn} W_{nj} = \Sigma_n U_n(\lambda_i) s_n W_n(t_j), \tag{2.39}$$

where wavelength and time variables are separated. In this decomposition, $S_{mn} = \delta_{mn} s_n$ is a diagonal matrix composed of the (sorted) singular values (SV) s_n. The U_{im} matrix contains $n = m$ columns representing n "singular" spectra associated with the singular values. The W_{nj} matrix contains n lines representing n "singular" transients (ST). Assuming the whole data set can be modeled by a sum of N decaying exponential functions with wavelength-independent time constants, and time-independent amplitudes, we may write each of the singular transients as a linear combination of all these time constants:

$$s_n W_{nj} = s_n W_n(t_j) = \Sigma_{\alpha=1}^{N} A_{n\alpha} e^{t_j/\tau_\alpha}. \tag{2.40}$$

Hence, we may rewrite the data set:

$$\begin{aligned} Data_{ij} &= \Sigma_n U_{in} \times \Sigma_{\alpha=1}^{N} A_{n\alpha} e^{-t_j/\tau_\alpha} && (2.41)\\ &= \Sigma_{\alpha=1}^{N} \left[\Sigma n U_{in} A_{n\alpha}\right] e^{-t_j/\tau_\alpha}. && (2.42)\end{aligned}$$

We thus can define the so-called Decay-Associated Spectra DAS:

$$\begin{aligned} DAS_{i\alpha} &= \Sigma_n U_{in} A_{n\alpha} && (2.43)\\ &= \Sigma_n U_n(\lambda_i) A_{n\alpha}. && (2.44)\end{aligned}$$

Here A is a matrix which contains n lines, with n the number of singular transients taken into account, and α column, with α the number of exponential decaying functions used to model the whole time dependence. Notice that this method is limited if the processes display a wavelength dependent time evolution which break the reparability of time and wavelength.

As an example a typical outcome of this procedure applied on HBDI-like molecular switch presented in Chapter 6. The 2-D maps map obtained after excitation at 350 nm is displayed in Figure 2.7.A. In the present case, the SVs are illustrated in the inset of Figure 2.7, and we fit “globally” the 4 first singular transients (see Figure 2.7.B). This global fitting means that the same function is used to fit simultaneously all 4 STs, while sharing the same time constants in all 4 traces, but enabling the fitting routine (non-linear least-square minimization, "Origin" software) to adjust independently the corresponding pre-exponential factors in each individual ST.

The global fitting, using the function introduced in Eq 2.38 of TAS data is illustrated in Figure 2.7.B. Importantly, in the present case where the signal rise is non-instantaneous, the component $A_gR(t)$) may not account for a non-resolved signal, but may advantageously enable the fitting of that delayed onset. In this case the result of the fitting for the parameter σ, is also affected by this molecular time scale over which dynamic spectral shifts may occur, and is no longer strictly representative of the time resolution.

The same function is used to fit simultaneously the four dominant singular transient, with shared values for the parameters t_0, σ, the three finite time constants τ_i $(i = 1, 2, 3)$, and one infinite time constant (τ_4) which accounts for the long-lived photoproduct signature and is not a free parameter). Only the 5 corresponding amplitudes A_i and A_G are optimized independently for the four SVs.

Figure 2.7.C displays the 4 residuals obtained by this global fitting and shows that they all have amplitudes smaller than the first neglected singular transient (SV5). Noticeably the latter displays an oscillatory behavior at early times which can obviously not be fitted by a sum of exponential functions and a gaussian function. This is characteristic of a data set where all kinetics do not start simultaneously, as is the case here with dynamic spectral shifts, where e.g. the SE signal rises on a time scale which increases while probing further and further to the red.

We conclude that even if the fitting function $\Delta\tilde{A}(t)$ is not optimum (it cannot fit singular values which are above the noise level), it works remarkably well in the present case on non-exponential early dynamics.

Using the same SVD mathematical transformation, one can reconstruct the so-called decay associated spectra from the set of A_i obtained as a result of the fitting routine for the four singular transients. These DAS are displayed in Figure 2.7.D. they represent the wavelength dependent weight of each decaying component τ_i throughout the data set. With the present choice of fiiting function, the wavelength dependence of the non-resolved component may be retrieved similarly in the form of a Gaussian-associated spectrum which is also displayed in Figure 2.7.B. Further analysis and interpretation of this data set is found in Chapter 7.

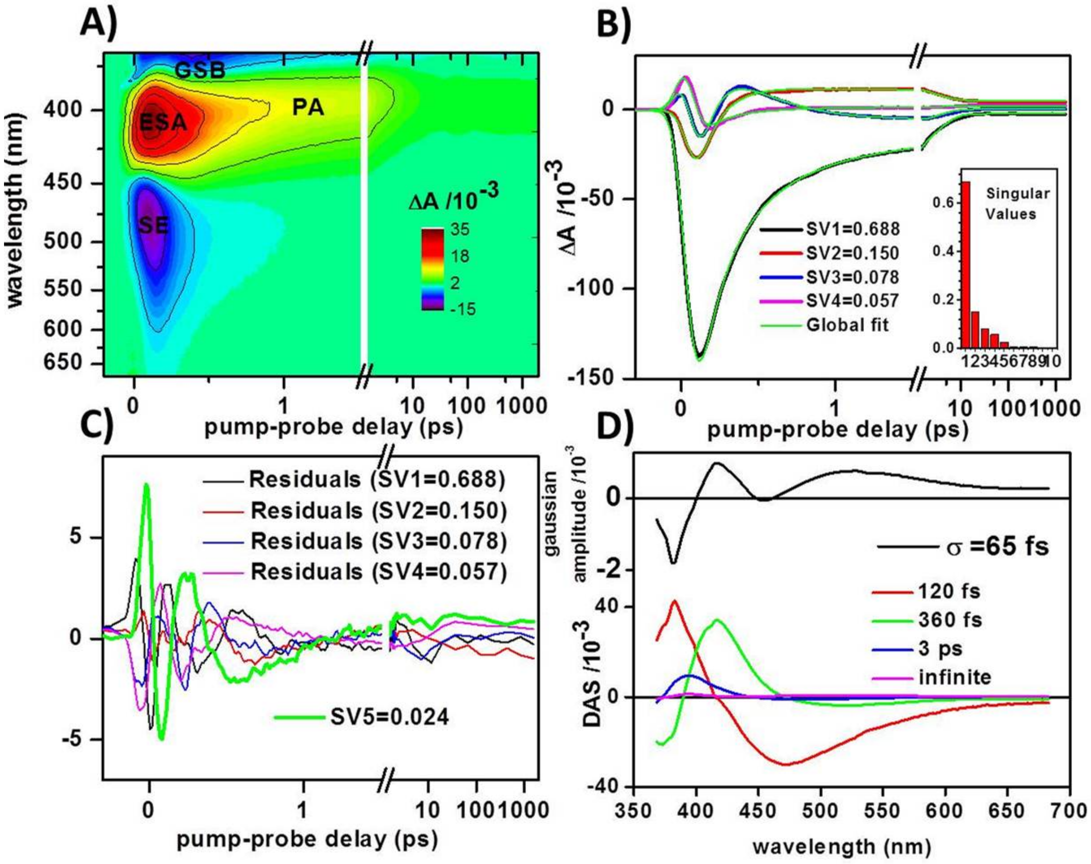

Figure 2.7.: Global analysis of the entire 2D map: A) 2D transient absorption data (in color code) as a function of wavelength (nm) and pump-probe time delay (ps). B) The four dominant singular transients and their fit by the fitting function introduced above. The inset displays th values of the first ten dominant singular values. C) The residuals corresponding to the simultaneous fitting of the four singular kinetics of panel A, compared to the first neglected singular transient corresponding to the fifth singular value SV5. D) Gaussian-associated and Decay-Associated Spectra obtained for the global analysis of the TAS data.

2.3. Conclusion

The aim of this chapter was to describe the main application of the trensient absorption spectroscopy on the photoisomerizing compounds, including the illustration of the data processing allowing obtaining the pure information arising from the photoreaction. It has been shown that TAS provides informations about the electronics dynamics in the ultrafast photoisomerization reaction by performed global analysis using a fitting function described in section 2.2.4.
In the following chapter, we will present transient absorption technique allowing to probe in addition to the electronic contributions, the vibrational contributions resulting to an excitation with a short laser pulse.

3. Time domain vibrational coherence spectroscopy

This Chapter has been submitted to the Rewiew of Scientific Instruments as an article.

3.1. Introduction

Photoreactions of organic molecules mostly occur via conical intersections, which are intersections between electronic potential energy surfaces, where electronic degrees of freedom are coupled to and controlled by the vibrational degrees of freedom, in a non-Born-Oppenheimer regime. Therefore, there is strong interest in investigating vibrational dynamics in excited electronic states to decipher the mechanisms of ultrafast photoreactions. Since the advent of femtochemistry with short enough laser pulses, the spectroscopic signatures of vibrationally coherent dynamics induced both in the ground and excited molecular states by resonant impulsive laser excitation, have been recorded in the time domain [24, 25, 26, 20, 27, 28, 29]. Thus, depending on the resonance conditions of the pump pulse, vibrational coherence (VC) can be produced in the excited state. It can also persist along the reaction path and be observed in the photoproduct ground state [10]. It may also be initiated by Resonant Impulsive Stimulated Raman Scattering (RISRS), which creates coherent vibrational motion on the reactant ground state potential energy surface [30].

Transient absorption spectroscopy can be described by three field interactions with the molecule [20]. Figure 3.1 shows the different cases leading to VC on the excited state and the ground state according to the matrix density formalism. A first resonant pump field interaction creates a coherence that is brings the initial ket wavepacket into the S_1 PES, where it begins to evolve. A second resonant pump field interaction promotes the bra wavepacket on the S_1 PES (see figure 3.1.A), thus creating a population in S_1. Thus within the perturbative expansion, the first two interactions (pumps) create a non-stationary state and the subsequent interaction with the probe (third order responsible for $P^{(3)}$ polarization) can then be understood as a linear absorption of this non-stationary state [20] as already discussed in chapter 2. The third interaction with the probe

electric field brings the ket wavepacket on the S_n (n=1,2...) PES, leading a electronic coherence between the S_1 and the S_n excited state. The dynamics of the wavepackets created on the excited state by the pump manifest itself in form of oscillations and thus modulate the ESA signal. Since the SE reflects the dynamics of populations on the excited state, the interpretation is the same exept that the third interaction bring the bra wavepacket in the ground state, leading a third order coherence between the S_0 and the first excited state. Ground state oscillations are generated when the first interaction with the pump field promotes the initial ket wavepacket on the excited state, where it evolves until it is projected back to the ground state by a second field interaction on the ket side, thus creating a non-stationary population in S_0. Hence the wavepacket dynamics modulate the GSB spectrum (see Fig 3.1.B).
Resolving the wavepacket dynamics requires high enough temporal resolution to record common vibrational frequencies for organic molecules which are up to 3000 cm^{-1} frequency, corresponding to a period down to 10 fs.

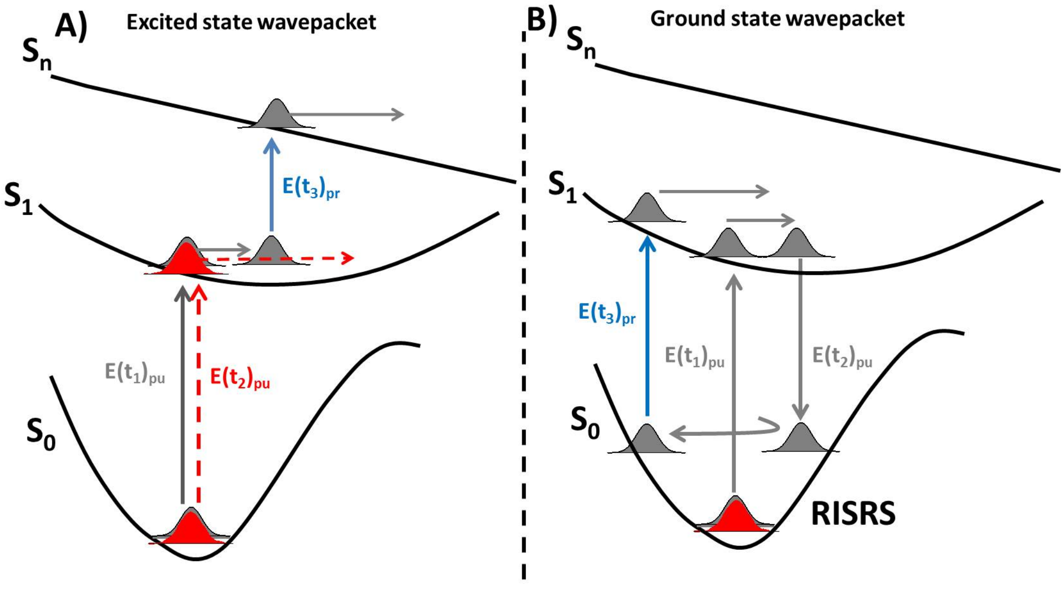

Figure 3.1.: Generation of excited and Ground state wavepacket: A) Bra and ket wavepacket dynamics for the excited state absorption. B) Bra and ket wavepacket dynamics for the Ground state bleach. Vertical arrows mark the transitions between electronics state and horizontal arrows mark the propagation on the PES. Solid and dashed lines indicates a single field interaction, respectively with the ket and bra side of the density matrix elements.

Time resolving the Raman signatures of a molecule along its photoreaction from the ground to excited and photoproduct states has been implemented by first triggering the photoreaction with an actinic pump pulse, and subsequently probing the molecular vibrational signatures either in the frequency domain as in Femtosecond Stimulated Raman scattering (FSRS) [31, 32, 33, 34, 35] or in the time domain via vibrational coherence spectroscopy (VCS) implemented by impulsive vibrational spectroscopy (IVS) [36, 37] or equivalently degenerate four wave mixing (DFWM)[38]. All these approaches give in principle access to identical information about vibrational dynamics [38, 39], with the advantage that IVS (and variants like "pump-IVS"[24] or "population-controlled IVS"[40]) can be performed with a broadband probing employing a chirped, supercontinuum light pulse, which enables optimum time resolution [37, 41, 42], and simultaneously gives more insight into the underlying electronic dynamics. Indeed, as in all transient absorption experiments in condensed phase, a very broad spectral coverage facilitates the identification of the electronic states contributing to the signal [43]. This and the ability to perform off- and on- resonant IVS experiments enable disentangling ground- from excited-state VC and following the time evolution of the vibrational dynamics along the photoreactive channel even without employing a preceding actinic pump pulse [43, 44].

The development of non-collinear optical parametric amplification (NOPA) for the production of sub-10 fs pulses and their applications to transient absorption spectroscopy has fostered the use of VCS as a time domain version of Raman spectroscopy [45]. However due to the difficulties associated with the generation of ultrashort blue to UV ($\sim$ 10 fs) laser pulses, little advancement has been made in the improvement of VCS on systems which absorb around 400 nm.

alternativelly, the development of the hollow fiber based compression leads to the generation of short, down to few cycle, pulses of high energy [46, 47]. With this method, laser pulses are spectrally broadened by Self Phase Modulation (SFM) in a gas contained within a long (1 m) hollow fiber waveguide [48]. Sub-8-fs UV pulses have been generated by a hollow fiber compressor and were used for the ultrafast pump-probe spectroscopy [49, 50]. Recently, tunable sub-10 fs UV pulses were generated by sum-frequency generation (SFG) between a broadband visible pulse, and a narrowband pulse spanning from the visible to the near-infrared [51]. Such broadband visible and UV pulses provide tools for high-time resolution in ultrafast spectroscopy.

Transient signatures of VC are weak oscillations on the top of the electronics population dynamics. Obtaining reproducible results from molecular vibrational modes is not straightforward and requires high signal stability. Stability issues are related to the long term fluctuations in the laser intensity (due to the fluctuation in humidity, temperature, air flow around the system etc...) during the experiment, and thus mask the VC contributions [52]. Generally, the oscillatory signals are weak and thus require high signal-to-noise (S/N) ratio and stability. However, fast acquisition in the time scale shorter than the long term fluctuations can improve the S/N ratio and thus the quality of the VC signal.

In this thesis, we built an ultrafast VCS setup starting from a dedicated 1 kHz amplified Ti:Sa laser. The setup uses a 6 fs Vis to IR pulse generated by non-linear propagation in a hollow fiber. A broadband UV pulse is obtained by SFG of the 6 fs pulse. Broadband detection in the UV-Vis spectral range using super continuum whitelight generation is implemented. We also implemented a fast scanning which significantly improves the S/N ratio as compared to the conventional step-scanning.

3.2. Femtosecond laser pulse generation

3.2.1. Experimental Ti: Sapphire system

The experimental transient absorption (pump-probe) setup is based on a Ti:Sapphire regenerative amplifier laser system (Amplitude Technologies, France) which delivers 800-nm, 3-mJ, 40-fs pulses a at 1 kHz repetition rate, with a pulse-to-pulse energy fluctuations of 0.2% rms. Figure 3.2 shows the system global design and its main characteristics.

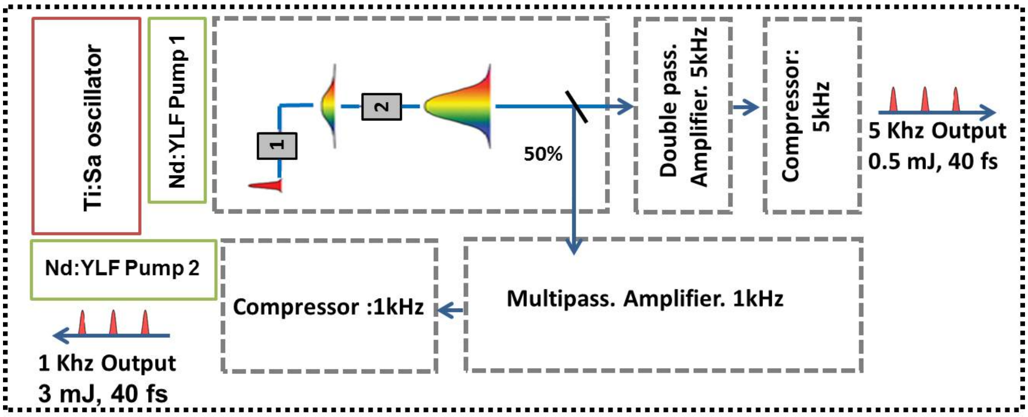

Figure 3.2.: Simplified design of the amplified laser system and its main characteristics. 1: Stretcher; 2:"Regen" amplifier

Briefly, we use a femtosecond pulses obtained by pumping an oscillator with a diode pumped solid state DPSS Nd:YAG laser (Opus 2W, Laser Quantum Ltd). This oscillator is a Ti:Sapphire (Femtosource Synergy 20, FEMTOLASER) producing ∼ 20 fs short pulses at 63 MHz, and centered around 800 nm. Those pulses then enters an amplifier pumped by another DPSS, Nd:YLF laser, generating 200 ns pulses at 5kHz (at 527 nm, 27 W). The amplifier uses the principle of the Chirped Pulse Amplification (CPA)[53], that consists of stretching the pulse before amplification (so the peak power in the amplifying medium is less intense), and then recompressing it. The amplification itself is obtained using a regenerative amplifier producing approximately 0.5 mJ per pulse. A portion (50%) of the latter is selected and sented in a double pass amplifier, giving a 5 kHz output. This output is used for the "historitical" pump probe setup as in chapter 4. The other portion passes a multipass amplifier stage using another DPSS Nd:YLF pump, giving a 1 kHz output, 3 mJ per pulse. The latter is used here to develop the VCS setup described in this chapter.

3.2.2. Ultrashort pump pulse generation

Sub-6 fs Visible pulse from hollow fiber

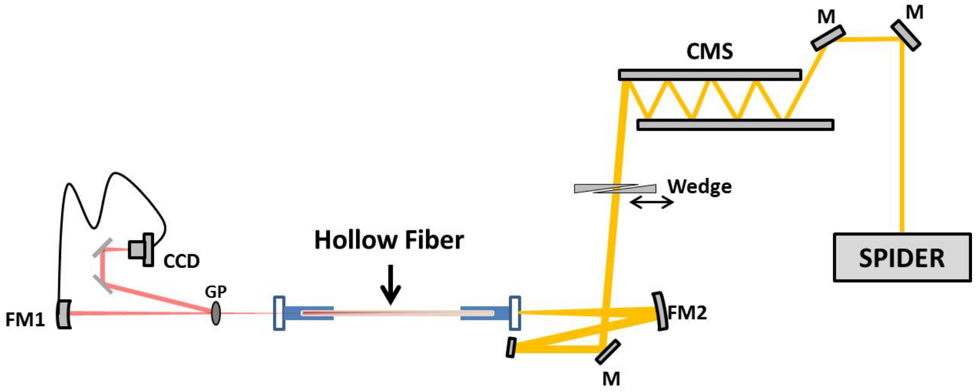

Figure 3.3.: Hollow fiber system: FM1,2: focusing and recollimating mirrors respectively; CMs: Chirped mirrors..

A scheme of the hollow fiber layout used to generate a short visible pulse is shown in Figure 3.3. A portion of the fundamental beam (∼ 1 mJ) is coupled into a 240 µm inner diameter, neon filled, hollow fiber (commercial system by

Imperial College Consultants), by a 1 m focusing mirror. An active beam pointing stabilization is used to compensating slow position drift on the laser beam and allowing for the reproducible performance with minimal user adjustment. The fiber output beam is recollimated using a 75 cm focal length mirror. Nonlinear, guided propagation in the rare gas generates a spectrally broadened pulse which is temporally recompressed by a pair of chirp mirrors at the fiber output (Each chirped mirror bounce pair imposes a negative chirp on the pulse and compensates for 40 fs^2 of positive chirp) and through fine-tuning of the group delay dispersion with fused silica wedges. The maximum output energy reaches 0.59 mJ by corresponding to fiber transmission of $\sim$ 50%. The hollow fiber

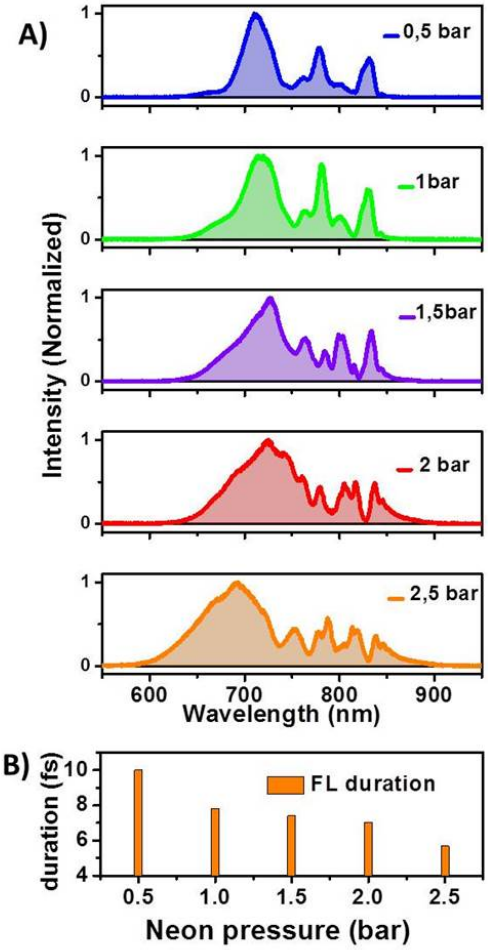

Figure 3.4.: A) Normalized spectra acquired after broadening in a statically filled hollow fiber for different values of pressure. B) Transform limited pulses duration after compressed the output fiber as function of the neon gas pressure for an input fiber energy pulse of 1.23 mJ.

chamber is optimized for maximum transmission in the vacuum and spectral broadening was measured at the output of the fiber for neon pressures of 0-2.5 bar. The spectrum broadens as function of the gas pressure. At higher energy (1.23 mJ), spectra spanning 600-900 nm are achieved when the gas pressure was increased to 2.5 bar (see 3.4.A). These spectra can support transform-limited pulse duration of 5-10 fs range (see Fig 3.4.B). This technique allows generating pulses of tunable duration with constant energy and alignement by a simple variation of the gas pressure. At higher pressures (> 2.5 bar), spectra begin to reduce in bandwidth due to the reduced energy throughput at these pressures, attributed to ionization defocusing at the fiber entrance, which causes an increase in the focal spot size and beam aberrations and consequently a reduced coupling efficiency [54].

A commercial APE'FC-SPIDER apparatus was used to measure spectral phase of the fiber output pulse after recompression. This technique provides a direct and rapid algebraic field reconstruction. The reconstructed pulse (RP) amplitude and phase in the time domain are shown in Figure 3.5. The spectrum can support about 5.06 fs transform limited pulse duration and the measured pulse duration is 6.09 fs. At the fiber output, pulse-to-pulse energy fluctuation is measured to be $\sim 0.4\%$, and the low-frequency power drift is limited to 2% rms.

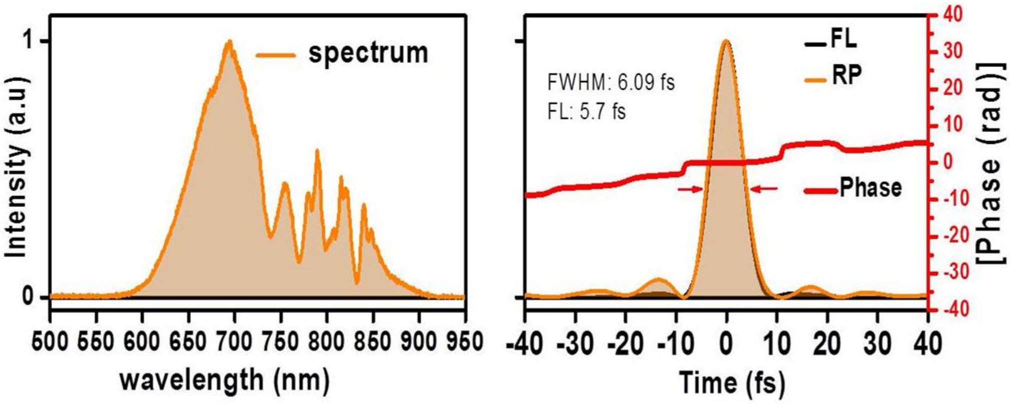

Figure 3.5.: Left: Normalized spectrum acquired after broadening in the hollow fiber for an input energy of 1.23 mJ and gas pressure of 2.5 bar. Right: FC-SPIDER temporal profile reconstruction of the shortest Hollow fiber compressed pulse (red curve) together with the Fourier limited pulse (black curve) and the temporal phase (green curve).

Sub-8 fs UV pulse from broadband sum frequency generation

We are interested in using very short pump pulses ($\sim$ 10 fs and below) with 400 nm wavelength. These blue 400-nm pulses will be generated from a short, red 800-nm pulses. As both the red and the blue pulses are to be as short as possible, they will possess large spectra. This creates a need for broadband frequency conversion. Assuming the validity of some simplifications (cf. Appendix A), it is possible to deduce a compact expression for the calculation of the efficiency of sum-frequency generation (SFG) along a propagation axis z in second order nonlinear materials:

$$I_3(z) \quad = \quad \frac{1}{2\varepsilon_0 c^3}\frac{|\chi^{(2)}|^2}{n_1 n_2 n_3}\omega_3^2 I_1 I_2 z^2 sinc^2\left(\frac{\Delta k z}{2}\right), \tag{3.1}$$

The conversion efficiency thus depends in particular on the thickness of the crystal ($I_3 \propto z^2$) and is severely limited by the phase mismatch $\Delta k = k_3 - k_1 - k_2$. To calculate the phase mismatch explicitly, one has to substitute the different k_i by the appropriate values for

$$k_1 = \frac{2\pi n_{e2}(\lambda_1,\theta)}{\lambda_1}$$

$$k_2 = \frac{2\pi n_{01}(\lambda_2)}{\lambda_2},$$

and

$$k_3 = \frac{2\pi n_{e2}^2(\lambda_3,\theta)}{\lambda_3}$$

depending on the favoured type of phase matching. In the case where all other parameters are fixed, we can for reasons of convenience define the relative conversion efficiency η as:

$$\eta = sinc^2\left(\frac{\Delta k L}{2}\right) \tag{3.2}$$

The different parameters effect on the SFG spectral acceptance is visualised in Figure 3.6. If the angle θ of the nonlinear crystal is adjusted approximately to the values which allow perfect type-II phase matching for a collinear layout, i.e. 42 ° for BBO, fixed crystal thickness L and wavelengths around 800 nm, we observe a high conversion efficiency in this region of the spectrum (cf.Fig. 3.6. A). As in Fig.3.6. B, the conversion efficiency curve typically exhibits two lobes of which only the left lobes are visible in Fig.3.6. A, whose maxima mark the wavelengths of perfect phasematch.

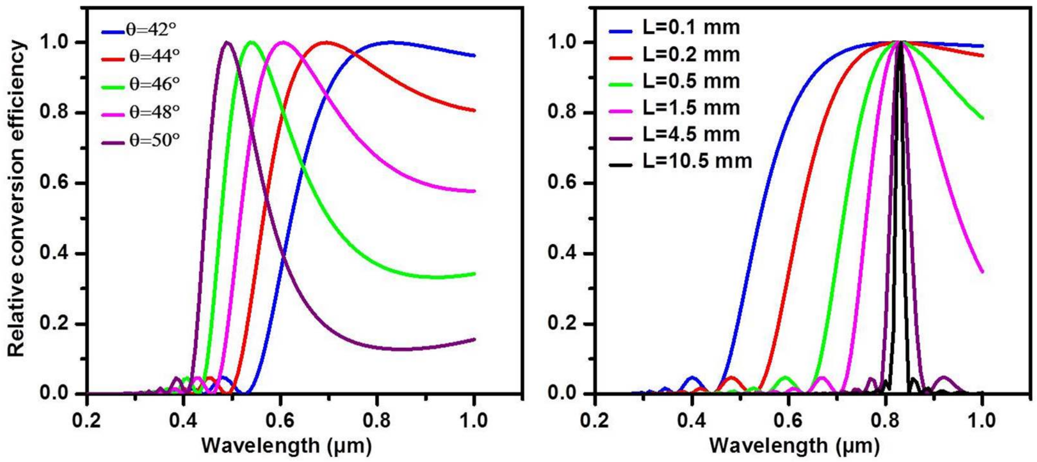

Figure 3.6.: The relative conversion efficiencies $\eta(\lambda_2)$ for type-II SFG in BBO. Left: Relative conversion efficiency for different angles θ in BBO with $\lambda_1 = 800$ nm and crystal thickness $L = 200\ \mu m$. Right: Relative conversion efficiency for different crystal thicknesses L of BBO with $\lambda_1 = 800$ nm, and 42°.

By varying the internal phase matching angle θ, it is possible to modify the distance between the two maxima and thus reach a larger spectral acceptance, if we accept a decrease of conversion efficiency midway between the maxima. It is therefore necessary to seek a compromise between the width of spectral acceptance and the homogeneity of conversion efficiency, which is e.g. found at θ around 42°. In the collinear case, it is particularly easy to choose the optimum cutting angle Θ of the crystal (angle between crystal face and optical axis). To minimize losses due to reflexions, the wavevector should at its best be perpendicular to the crystal face. In this special case, however, the optimum cutting angle simply equals the optimum internal phase matching angle, $\Theta \equiv \theta$.

Also concerning the thickness L of the crystal a compromise is to be found: As we see in Fig.3.6 .B, the spectral acceptance increases for reduced L. On the other hand, the absolute conversion efficiency is $\propto L^2$ according to Eq. A.8, this means we have to trade off the spectral acceptance against the absolute intensity of converted light.

The experimental principle for the broadband UV pulse generation is displayed in Figure 3.7.A. Around 152 µJ of the hollow fiber beam is collinearly overlapped with $\sim$ 145 µJ of the fundamental beam in the nonlinear medium, using a beam splitter reflecting the s-polarized 6 fs pulse and transmitting the p-polarized fundamental beam. Type II phase matching with the broadest 6 fs pulse polarized along the ordinary axis enables very broad acceptance band-

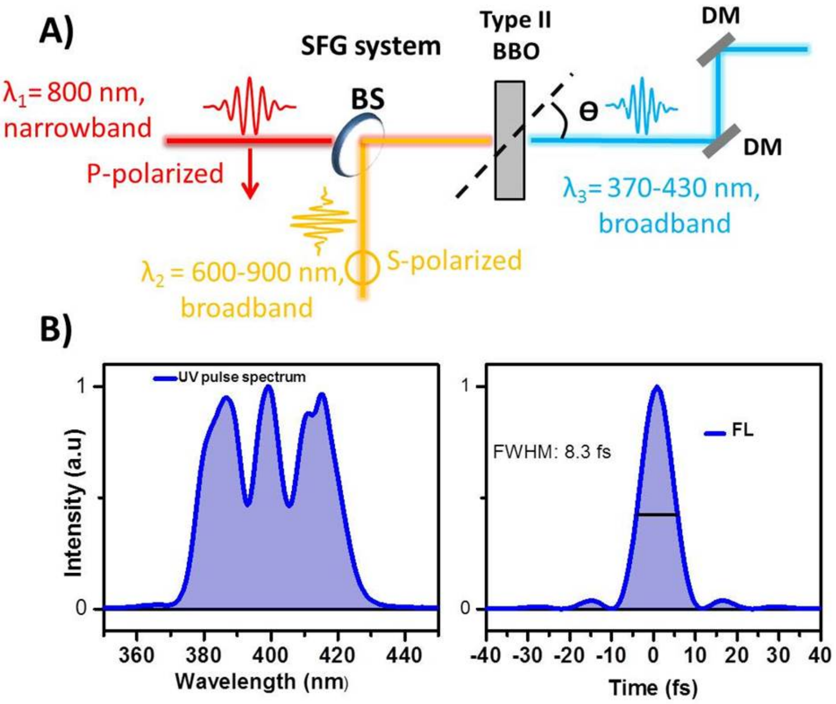

Figure 3.7.: Schematic and performance of the broadband sum-frequency generation: A Experimental SFG layout: BS, beam splitter; DM, dichroic mirrors. B) Normalized spectrum acquired after SFG between the fundamental beam and the broadband hollow fiber beam together with it corresponding temporal profile.

width for the 400 nm pulse along the extraordinary axis of the 80 μm thick, type II, barium borate (BBO) crystal [51]. The choice of thin crystal thickness is required to improve the yield of the SFG, because as already shown (Fig. 3.6.B), a thick crystal reduces the spectral acceptance. However, due to the different refractive indices (no resp. ne) the two fundamental beams travel at different speeds and therefore overlap only over a limited distance. This effect knowing as group velocity mismatch (GVM) tends to limit the efficiency of the SFG (see Appendix A and [51]).

The spectrum and the temporal intensity profile of the blue light pulse obtained after filtering the fundamental beams by using UV dielectric mirrors are displayed in figure 3.7.B. The collinear SFG layout provides broadband 400 nm pulses with energy up to 2.5 μJ. The resulting spectrum extends from 372 to 430 nm (90 THz), corresponding to 8.3 fs TL pulse duration. The pulse to pulse stability is $\sim$ 0.7%.

3.3. UV-Vis whitelight probing

In order to produce a broad spectral range in a single pulse, one can generate a wavelength continuum in a transparent medium via third order non-linear effect. Crystals such as sapphire (Al_2O_3) or calcium fluoride (C_aF2) are commonly used to generate supercontinuum whitelight. They are transparent in the visible, have inversion symmetry and a relatively large non-linear susceptibility $\chi^{(3)}$. Pumped at 800 nm, they produce broadband continua extending from UV up to near-IR [55].

3.3.1. Whitelight generation

Figure 3.8 illustrates supercontinuum generation in C_aF2 plate used in the experimental setup, and a set of portions of the white-light continuum, defining the spectral regions experimentally accessible with our setup. A supercontinuum white light pulse spanning from 300 nm to $>$ 900 nm is generated by focusing 1.4 µJ of the fundamental pulse into a 2-mm thick calcium fluoride crystal (C_aF2), with a 100 mm focal length lens. To avoid crystal damage, the CaF2 plate is translated vertically and periodically ($\sim$ 1Hz frequency) by the 1- to 2-mm-amplitude motion of the membrane of a small loud-speaker placed horizontally and carrying the CaF2 plate mount. The diverging continuum is recollimated with a first parabolic mirror (PM) and divided into probe and reference beams using a metallic-coated, fused silica neutral density filter (OD = 0.3) as a beam splitter (spectrally flat over the entire UV-Vis range). Under the appropriate (large) incidence angle, the reflected and transmitted beams respectively used as probe and reference, have nearly identical intensity.

3.3.2. Whitelight detection

The probe beam is focused with a parabolic mirror into the sample (which is supported by a mechanical xyz stage) and recollimated, before being focused on the vertical slit of a commercial (Stresing), home-improved,fused silica prism spectrometer (Fig 3.9.A). The reference beam is focused a few mm below through the same slit with a small vertical angle, such that after dispersion in the prism both beams can be reflected and imaged by separate mirrors on 2 separate CCDs line detectors (S7030, Hamamatsu, Japan). The CCD are made of 512x58 square pixels, where the vertical pixels are binned together to form a unique potential trap. The manufacturer announces a maximum number of electrons per pixel of 1000 ke^-, coded on 16 bits (from 0 to 65535). The thermal noise is negligible: 100 to 1000e^-/pixels/s announced at 25°; we acquire at 1 kHz so we should have 0 or $< 1e^-$ per pixel! and per laser shot. Spectral calibration was done with

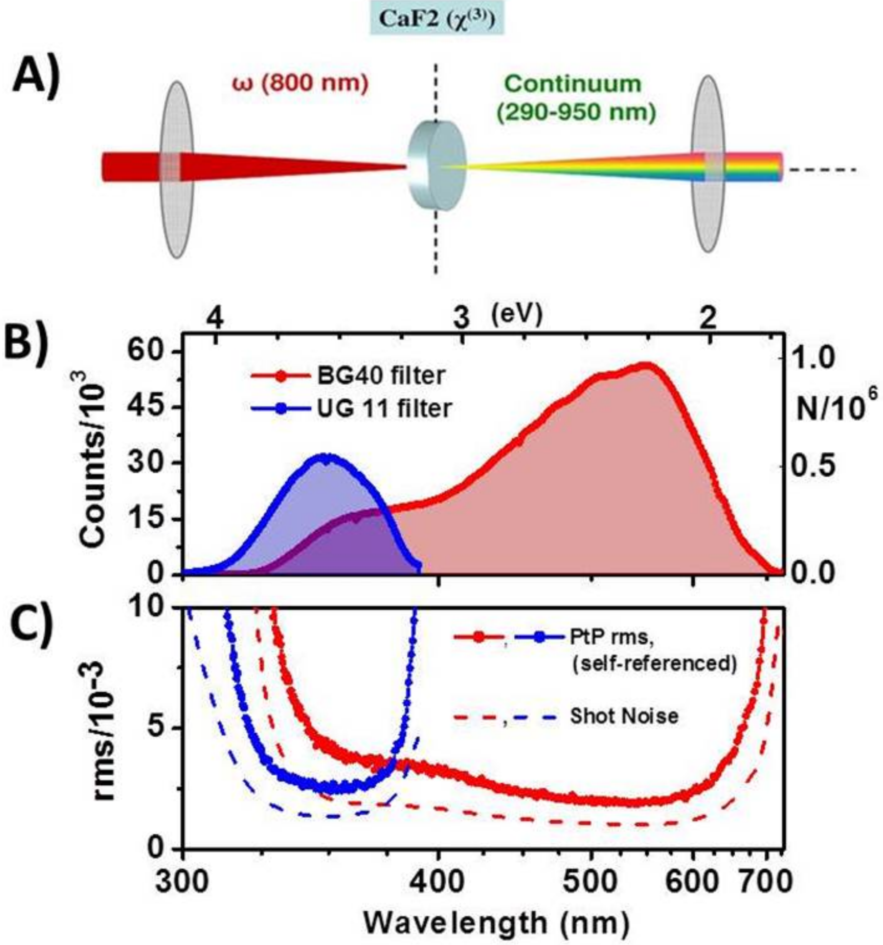

Figure 3.8.: A) White-light generation principle. A femtosecond pulse train (in this example at 800 nm) is focused into $\chi^{(3)}$ material which creates a broadband continuum. Both pictures were taken with 40-fs, 800-nm pulses focused into a 2-mm CaF2 crystal. B) Probe spectrum recorded through BG40 or UG11 color filters. The corresponding number N of electrons detected per pixel is given on the right axis (measured to be 17 electrons per count). C) Measured pulse-to-pulse relative rms noise (see text) of the self-referenced signal $s_k = p_k/r_k$ (lines+circles), compared to the single spectrum shot-noise (dashed lines) computed as $1\sqrt{N}t$, for both color filters.

a Neon-mercury lamp (From UVP) that has very specific and well known rays. The wavelengths of the distinctive rays are plotted as a function of the pixel number where they were detected and fitting to a 5^{th} order polynomial function in order to obtain the wavelength axis (see fig 3.9.B. We also use the 800 nm passing through the CaF_2 for the calibration in 800 nm. For fast adjustment, a

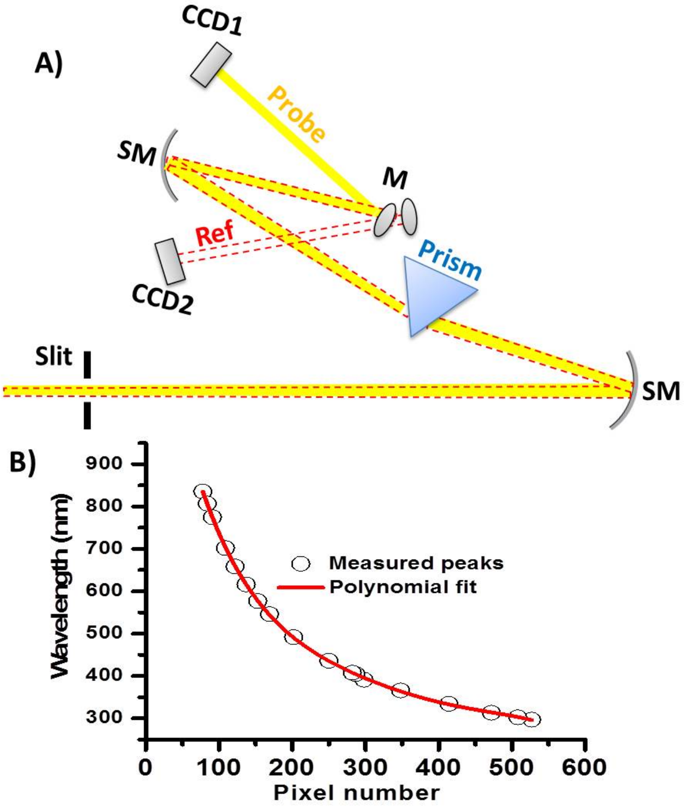

Figure 3.9.: A) the prism spectometer: SM, Spherical mirror. The pump and the probe are imaged on the two CCD sensors B) calibration using the prominent peaks of Neonmercury spectral lamp. The given empirical fit function (red line) is used for later pixel-number-wavelength calibration.

FGB67 filter (Thorlabs) may be useful too.

3.4. Pump-Probe setup performance

The setup is implemented both with the sub-8 fs, 400 nm pulse or 800 nm pulses. In both cases, the supercontinuum pulse of white light will be used as a probe to perform broadband transient absorption spectroscopy and detect the signatures of vibrational dynamics. Figure 3.10 shows a schematic of the experimental pump-probe layout. The pump pulses are modulated by an optical chopper (MC1000, Thorlabs, Munich, Germany), which is synchronized to the repetition rate of the laser pulses such that it selectively blocks one out of two pulses. We actually use two delay lines to control the pump-probe delay. A 30 cm long motorized translation stage (LS-110, PI miCos, Germany) is on the supercontinuum probe path and a 500 µm-travel piezo stage (P-625.1CD, PI, Germany) on the pump beam path. The first delay line may be used for ”step” scanning, and the second de for ”fast” scanning, which allow for mapping the temporal evolution of the system under investigation. The pump is focused into a 0.2 mm-thick quartz flow cell containing the sample in solution using 30 cm focal spherical mirror. The probe beam is focused with a second parabolic mirror into the sample, recollimated and focused on the vertical slit of a prism spectrometer. A peristaltic pump is used to circulate the sample so as to refresh it between successive excitation laser shots.

3.4.1. Whitelight stability and referencing

The probe spectra detected at time t_k can be written as:

$$p_k = \alpha I_k (T_k + \Delta T_k)(1 + \varepsilon_k^d) \tag{3.3}$$

where I_k is the probe light intensity, T_k the sample transmission, ΔT_k the pump-induced transmission change, ε_k^d the relative detection noise including pixel shot noise and read-out-noise. α is a factor accounting for the photoelectron conversion efficiency and signal digitalization. All quantities $X = I, T, \Delta T$ are characterized by an expectation value $\overline{X}$ and a (small) relative noise:

$$\begin{aligned} I_k &= \overline{I}(1 + \varepsilon_k^{pr}) \\ T_k &= \overline{T}(1 + \varepsilon_k^{T}) \\ \Delta T_k &= \overline{\Delta T_k}(1 + \varepsilon_k^{pu}) \end{aligned}$$

where ε_k^{pr},ε_k^{T} ,ε_k^{pu} account for the relative noise distributions of the probe pulse intensity, sample transmission (e.g. due to sample scattering), and pump light intensity, respectively. Since experiments are done in the linear regime of excitation, the fluctuations in pump light intensity ε_k^{pu} are also those of the pump-induced change in transmission ΔT_k.

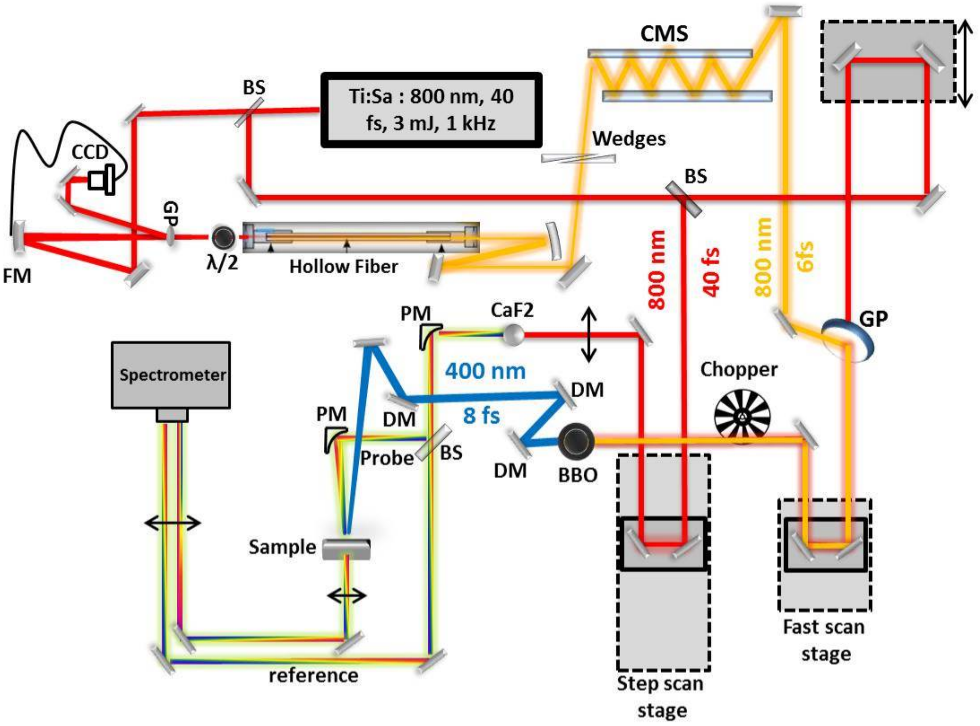

Figure 3.10.: Schematic of the experimental pump/probe layout. BS: beam splitter; FM: focusing mirrors; CMs: Chirped mirrors; GP: Glass plate; PM: parabolic mirrors; DM: dichroic mirrors..

The chopper is switching on and off every second pump pulse (i.e. odd shots are with $\Delta T_{(2k+1)} = 0$), such that two successive probe spectra may be used to compute at a 500 Hz frequency a measurement of the differential absorbance:

$$\Delta A_k \quad = \quad log_{10}\left(\frac{p_{2k}}{p_{2k+1}}\right) \tag{3.4}$$

At the lowest order in the different noise contributions, we can write ΔA_k as a function of its expectation value $\overline{\Delta A}$:

$$\begin{aligned} \Delta A_k \quad = \quad & \overline{\Delta A} + \frac{1}{ln10}\{(\varepsilon^{pr}_{2k+1} - \varepsilon^{pr}_{2k}) + (\varepsilon^{d}_{2k+1} - \varepsilon^{d}_{2k}) \\ & +(\varepsilon^{T}_{2k+1} - \varepsilon^{T}_{2k}) - \frac{\overline{\Delta T}}{T}\varepsilon^{pu}_{2k}\} \end{aligned} \tag{3.5}$$

We first note that the pump intensity noise only appears as a second order term since it is multiplied by $\frac{\overline{\Delta T}}{T} >> 1$. All other noise contributions appear at the first order, but as differences of two successive realizations of the same noise probability distribution.

In the absence of pump pulse (or at negative time delays) odd and even spectra have identical expectation value $\overline{p_{2k}} = \overline{p_{2k+1}} = \overline{p}$, and the standard deviation of the noise distribution on ΔA_k is the limit in sensitivity, or noise floor (NF), of the set-up, which is controlled by the relative shot-to-shot rms noise of the probe:

$$NF \quad = \quad \frac{\sigma_{StS}}{\ln 10} \tag{3.6}$$

with $\sigma^2_{StS} = (\overline{(p_{2k+1} - p_{2k})^2}/\overline{p} = \overline{\left((\varepsilon^{pr}_{2k+1} - \varepsilon^{pr}_{2k}) + (\varepsilon^{d}_{2k+1} - \varepsilon^{d}_{2k}) + (\varepsilon^{T}_{2k+1} - \varepsilon^{T}_{2k})\right)^2}$.

Detection and scattering noise may not be correlated from the one shot to the next and their variances add up. Instead a shot-to-shot intensity correlation is usually quite high in kHz amplified systems [56, 57], such that we get, in the limit of no sample scattering:

$$\sigma^2_{StS} \quad = \quad 2\sigma^2_{pr}(1 - c_{pr}) + 2\sigma^2_{SN} + 2\sigma^2_{RO}, \tag{3.7}$$

where $c_{pr} = \varepsilon^{pr}_{2k+1}\varepsilon^{pr}_{2k})/\sigma^2_{pr}$ is the shot-to-shot intensity correlation of the probe beam, σ^2_{pr} the variance of the noise distribution ε^{pr}_{k}, and σ^2_{SN} and σ^2_{RO} respectively the variances of the shot noise and the read-out noise distributions. Since here the probe is generated in a constantly moving CaF_2 plate, the shot-to-shot probe intensity fluctuations may be enhanced, weakly correlated and exceed the detection noise. In that case, single-shot referencing may be implemented by normalizing each probe spectrum by the reference spectrum recorded simultaneously from the same laser pulse. Very high probe-to-reference correlation may be achieved for each individual laser pulse [58], therefore efficiently cancelling the probe intensity fluctuations. Individual differential spectra are then computed as:

$$\Delta A_k = -\log_{10}\frac{s_{2k}}{s_{2k+1}},$$

with $s_{2k} = p_k/r_k$, the ratio between probe (p_k) and reference (r_k) spectra. The noise floor NF_{ref} for the single-shot referenced case is:

$$\frac{\sigma_{StSref}}{\ln 10},$$

with

$$\sigma^2_{StSref} \quad = \quad 2\sigma^2_{s}(1 - c_s) + 4\sigma^2_{SN} + 4\sigma^2_{RO}, \tag{3.8}$$

where σ^2_s and c_s are respectively the variance and the shot-to-shot correlation of the intensity ratio s_k. Simultaneously, since a single ΔA_k spectrum results from the measurement of two probe and two reference spectra, the detection-related contributions are doubled. Finally, in our case, a 4-fold reduction in NF is achieved by implementing single-shot referencing (see figure 3.8. C).

The detection related contribution to the NF is measured in both cases by detecting the spectrum of a cw flash light (LED's) powered with a 1.5-volt battery. The observed rms noise does increase by $\sqrt{2}$, in the single-shot referenced case. We conclude that the dominating contribution to the NF is the detection noise. Finally by averaging M individual ΔA_k differential spectra, at a 0.5 kHz rate, we expect to reduce the NF by $\sqrt{M}$, meaning NF=15 μOD after 20 s integration time at a fixed pump-probe time delay, as verified experimentally.

3.4.2. Pump intensity fluctuations and referencing

We see that the NF is controlled by the detection and probe pulse intensity fluctuations and gives the minimum detectable pump-induced ΔA_k with the set-up. Instead the signal-to-noise ratio (S/N) of a large (e.g. few 10 mOD) ΔA_k signal may be affected by the pump pulse intensity fluctuations, although they appear only at second order in the computed differential spectrum. Pump intensity fluctuations may also be self-referenced by recording simultaneously the intensity of a reflection. In order to illustrate the pump fluctuation self-

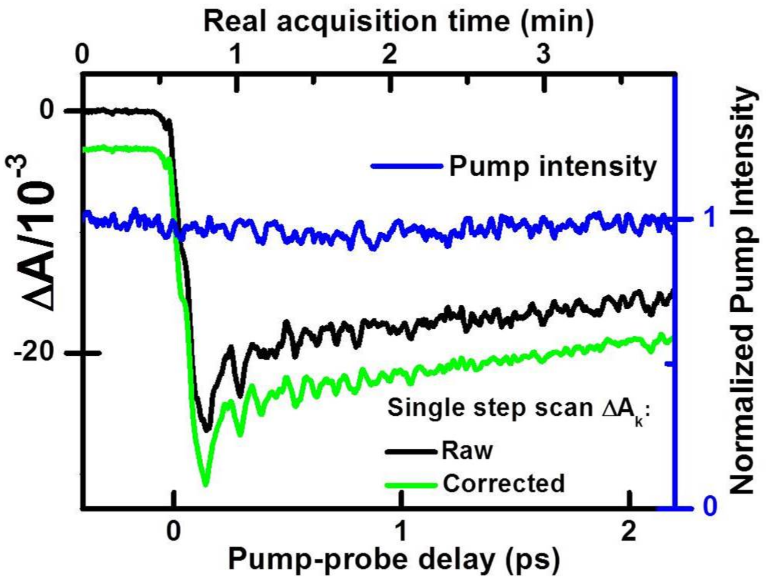

Figure 3.11.: Time-resolvedΔA signals of coumarin 307 at 445 nm obtained after excitation at 400 nm, using step scan experiment without (black curve) and with (green curve) pump intensity self-referencing. The blue curve is the pump pulse fluctuations recorded during the acquisition. There is a clear correlation between the pump intensity fluctuations and the oscillations of the black kinetic trace.

referencing, we perform measurement on coumarin 307 in ethanol upon excitation with the 400 nm pump pulse. Figure 3.11 displays the kinetic trace recorded at a probe wavelength of 445 nm, where the long-lived, ground-state bleach signal is observed, overlapped with oscillatory signal attributed to VC induced by the short pump pulse (see 3.5).

The step scan experiment is made by averaging the signal over 100 ms at each step (i.e. averaging over M = 50 differential spectra per time step) using a 30-cm-long motorized translation stage (LS-110, PI miCos, Germany), and scanning the pump-probe delay stepwise over 3 ps in steps of 4 fs. We evidence a strong correlation between the fluctuations of the pump pulse intensity recorded simultaneously and those of the signal, but normalizing the transient absorption signal by the pump light intensity (i.e. pump intensity self-referencing) helps correcting for these fluctuations.

However, a more efficient alternative is to implement fast scanning, where data are acquired by averaging M rapid scans of the pump-probe delay, rather than step scanning, where M individual ΔA_k spectra are averaged at the fixed pump-probe delay, before realizing another time delay (moving the motor to the next position)[59, 52].

3.4.3. Fast-scanning method

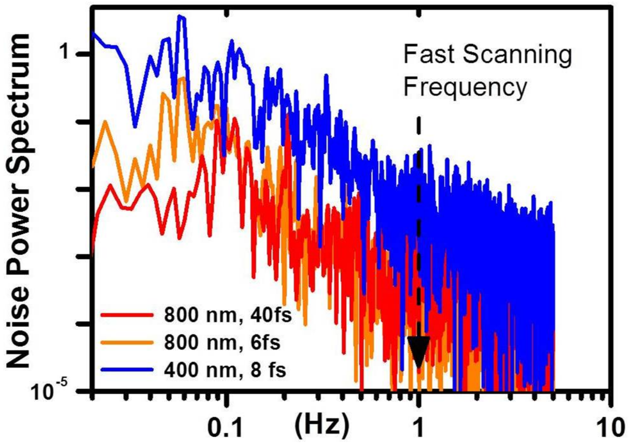

Figure 3.12.: Noise power spectral density of the laser intensities recorded at the amplifier output (red; fundamental beam), at the hollow fiber output (orange), after SFG at the sample location (blue; pump pulse).

The superiority of rapid scanning comes from the fact that pump power intensity fluctuations are dominated by low frequency components, i.e. drifts on the several-second to minute time scale as illustrated in Figure 3.12. By recording the laser intensity with an integration time of 100 ms over 10 minutes, and computing the corresponding noise power spectrum, we evidence that in the present set-up, low frequency noise dominate in the fundamental laser beam (amplifier output), especially in the 0.1-Hz region, corresponding to the 10 to 12 s cycling period of the chiller feedback loop for water temperature control. Then, enhanced noise is detected, especially at even lower frequencies, at the hollow fiber output (800 nm, 6 fs), and after SFG (400 nm, 8 fs FL), most likely due to beam pointing instabilities at the fiber input, and after long propagation distances of both fundamental and 6 fs beams until generation of the 400 nm pulse close to the sample.
The use of fast scanning requires displacement of the piezo delay. The method detailed below was used to calibrate the temporal scale.

calibration of the fast scanning delay line

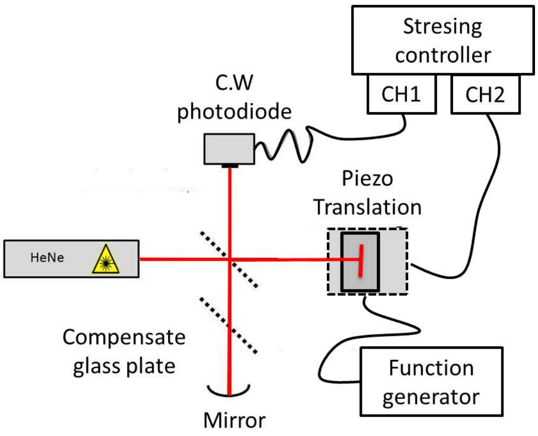

Figure 3.13.: Sketch of the Michelson interferometer applied for the piezo stage calibration. The piezo position is recorded ”on the fly” in synchronicity with the laser pulses

The piezo delay line was calibrated using a narrow-spectrum HeNe laser ($\lambda = 632.8nm$, Model 1101P, JDS Uniphase, Milpitas, CA, USA) in a Michelson interferometer as drafted in figure 3.13. For the voltage output of the function generator, a triangular shape with amplitude of 10.0 V (peak-to-peak) was chosen, thus taking advantage of the full piezo range (∼ 3 ps). A special BNC output of the servo controller is read out with the Stresing digital-analog converter and allows recorded ”on the fly” the piezo stage position in synchronicity with the laser pulses (see Fig 3.14.A) and in the joint focus of the mirrors was placed a photodiode to record the sinusoid interference pattern (see Fig 3.14.B). The position accuracy of the piezo positioning system was determined by fitting the data with a polynomial function (see Fig 3.14.A) and the analysis of the fit residual reveals a standard deviation of 10 counts (see Fig 3.14.C), due to the marked 50 Hz oscillation (see Fig 3.14.D). Thus the accuracy of the piezo position signal is limited neither by the function generator nor by the digitalization process, but by a residual 50-Hz electrical noise in the capacitive sensor voltage (see Fig 3.14.D). Figure 3.15.A shows the sinusoid interference

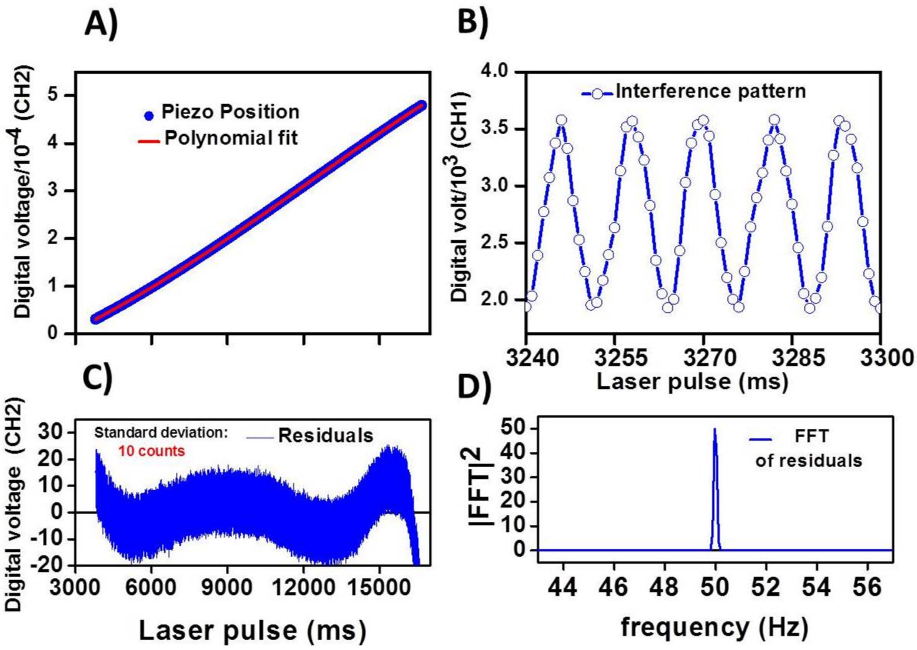

Figure 3.14.: A)Piezo position delivered by the digital-analogue. The red curve is a polinomial fit. B) Detail of the interference pattern of the HeNe laser. C) Residuals from the polinomial fit of the piezo position. D) Fourier transform of the residuals showing the 50-Hz electrical noise in the capacitive sensor voltage.

patter (recorded in CH1) as function of the polynomial fit of the piezo position (50 Hz filtered out) and Figure 3.15 displays the calibration curve showing the linear relationship between the piezo time delay and the voltage delivered by the analogue-digital converter (ADC) with a slope of 0.06635 fs. We note that the 50 Hz noise (accounting for 10 counts) induces a 0.66 fs uncertainty on the actual piezo position.

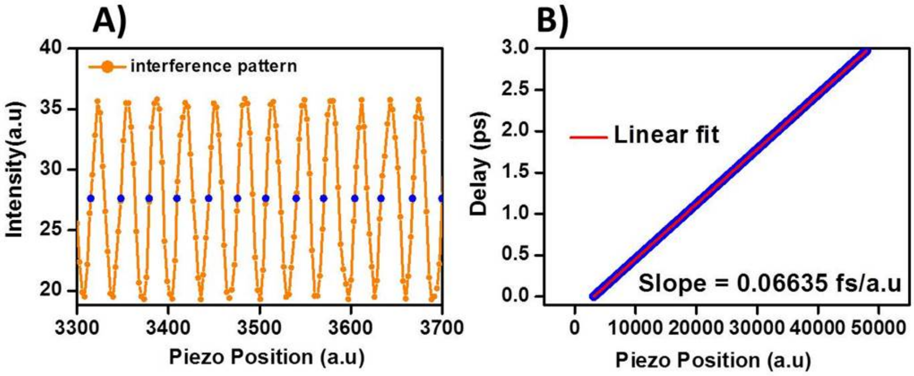

Figure 3.15.: A) Interference pattern of the HeNe laser as function of piezo position. Calibration of the fast scan delay line. The red curve is fit showing the linear relationship between the piezo time delay and the voltage delivered by the digital-analogue.

Implementation for transient absorption setup

For the implementing fast-scanning in the pump-probe setup, the digitalized voltage encoding the piezo position (embedded capacitive sensor) is acquired on-the-fly in synchronicity with each pump laser pulse. Hence for each individual differential spectrum the corresponding pump-probe delay is measured with 0.06 fs accuracy, but a 0.66 fs precision due to the residual 50-Hz electrical noise. The overall 3 ps time range scanned by the piezo displacement is decomposed in arbitrarily small time bins (e.g. 2 fs) and each ΔA_k spectrum is stored in its corresponding time bin. After minutes of continuous acquisition, up to millions of ΔA_k spectra may be distributed almost uniformly along the 3 ps time window and finally averaged within each time bin.

3.4.4. Fast scanning versus step scanning methods

Transient absorption measurement were performed on ethanol coumarin-307 solution in order to evaluate the performance of the fast scanning method compared to the conventional step scan pump-probe method in the same experimental conditions. In figure 3.16, we then compare the kinetic trace obtained by averaging of 5 such step scanning with pump intensity referencing to that obtained by fast scanning without pump intensity referencing. In the latter case, a time bin of 4 fs is also defined, and the total acquisition time is set such that the same overall number of individual spectra is recorded in both data sets. A better signal-to-noise ratio is demonstrated in the case of fast scanning since the low-frequency noise in the pump pulse power does no longer affect the signal. In addition, the overall acquisition time is 3 times faster (nearly 7 min continuous acquisition for fast scanning instead of 20 minutes for 5 step scanning) since in the step scanning procedure, two third of the time is exclusively spent at interrupting the acquisition to move the motorized delay line.

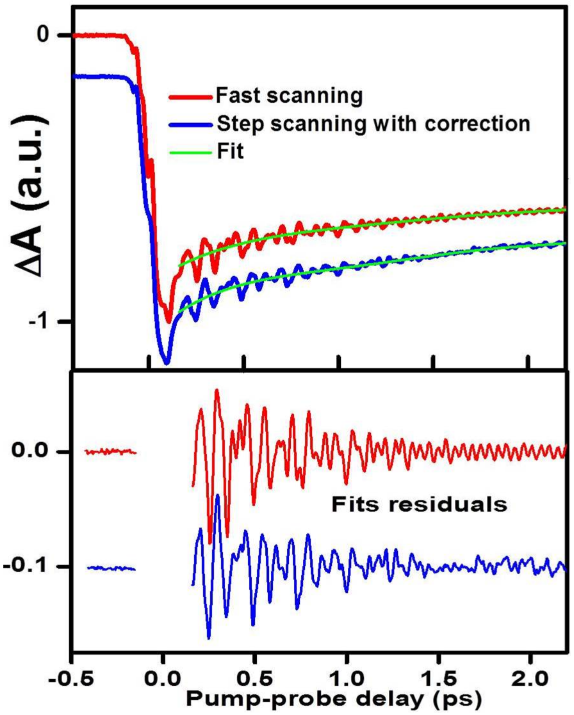

Figure 3.16.: Time-resolved ΔA signals of coumarin 307 at 445 nm and residuals of a biexponential fit: red fast scanning, blue: step scanning with correction of the pump intensity fluctuations. The signal at negative time is shown to compare the the amplitude of the signal to the NF.

From now on, we will implement fast scanning with no referencing of the pump power fluctuations, and a 2 fs time bin to sample the kinetics.

3.5. From raw data to Fourier spectra

We now illustrate the data proceesing using an example of resonant VCS on coumarin-307 in ethanol. The excitation pulse is resonant with the $S_0 - S_1$ electronic transition of the molecule, and thus VC is created both on the excited and the ground state potential energy surfaces.

The transient absorption map obtained in the 323-760 nm spectral windows, after excitation with the 400 nm, 8 fs FL pump pulse is shown in figure 3.17.A.

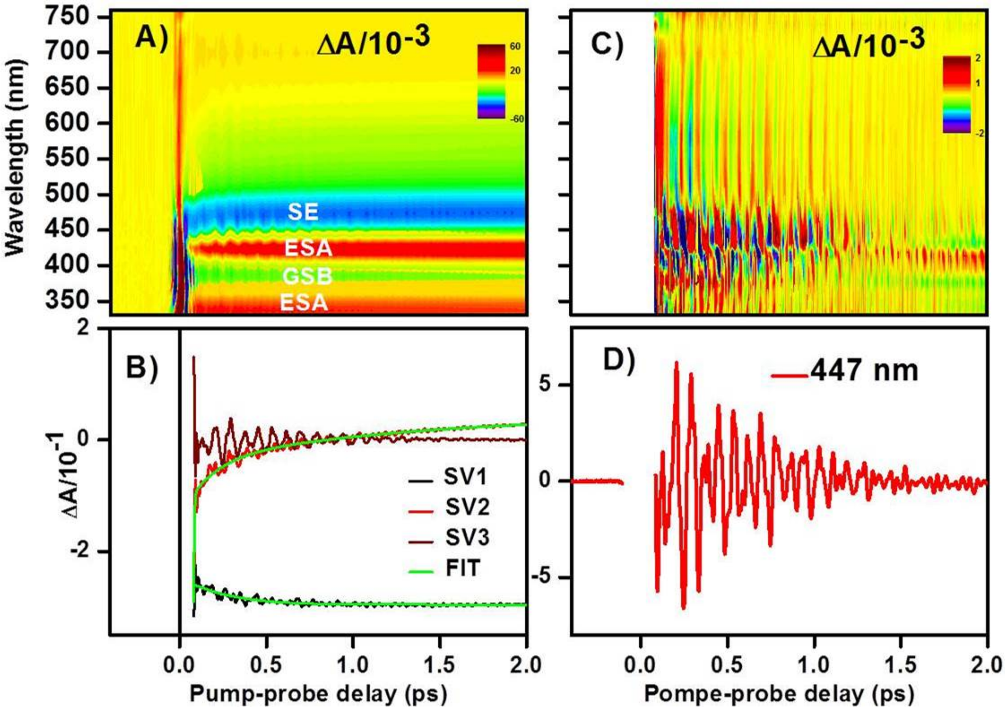

Figure 3.17.: A) 2-D transient absorption map recorded for coumarin 307 using a 8fs pulse centered at 400 nm. B) The 2 first singular transient and their fit, compared to the first neglected singular transient which not contains electronic contribution. C) Residuals coherence 2D-map obtained after subtraction of the electronic part by global fitting the raw 2D-map. D) Cut at 447 nm showing the vibrational coherence.

Coherent artifacts around time zero are observed, followed by spectroscopic signature of the exited (ESA and SE) and ground (GSB) states. Oscillatory patterns are visible in the transient absorption signal as result of the high temporal resolution. After correction of the wavelength dependent time zero caused by the chirped whitelight probe (see section 2.2.2), the first step in the data processing is to truncate the 2-D map after the coherent artifact (after ∼ 80 fs) and globally fit the electronics kinetics by the sum of exponential decaying function as discuting in 2.2.4. In the present case, we fit the 2 singular transients (see figure3.17.B). Here global fitting means that the same function (but not necessarily the same time constant) is used to adjust one by one all the singular

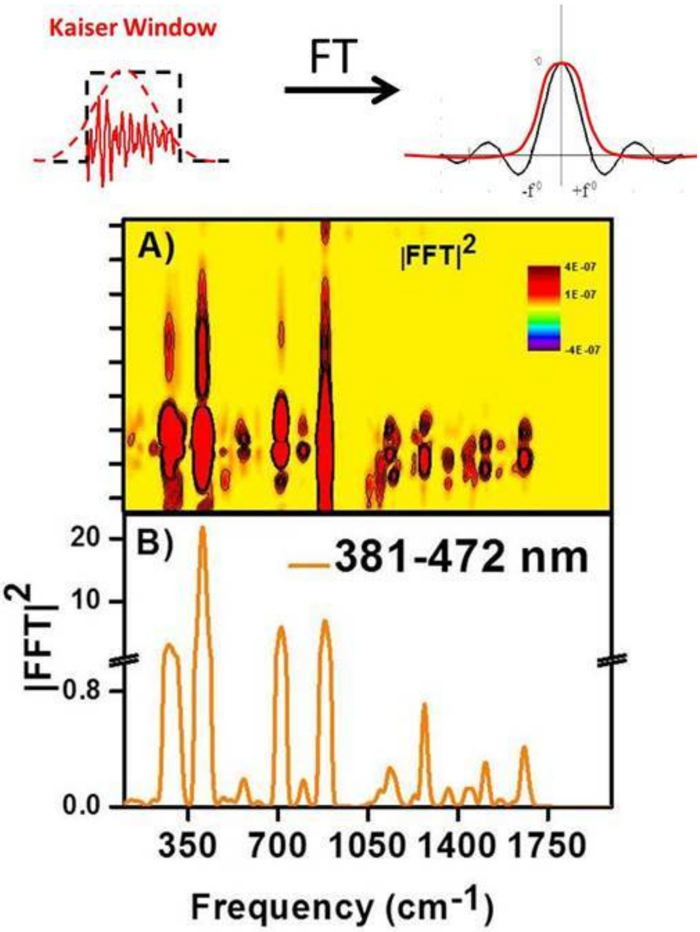

Figure 3.18.: A) Fourier amplitude 2D-maps obtained by Fourier transformation the vibrational coherence 2-D map. B) Vibrational spectra obtained by spectral average from 390-400 nm.

transients in order to follow as well as possible the electronic kinetics. As discuting in section 2.2.5, we assum that each of singular transients may write as: $s_n W_n(t_j) = F_{nj}$. Hence, we may write the electronic contributions as:

$$FitData_{ij} \quad = \quad \sum_{i=1}^{n} U_{in} F_{nj} \tag{3.9}$$

As shown in figure 3.17.C and .D. we isolate the pure VC activity by substrating the electronics contribution in the raw 2-D map according the following formula.

$$VC_{ij} \quad = \quad Dataij - FitData_{ij} \tag{3.10}$$

The final step is to apply one-dimensional Fourier transformation (FT) on a wavelength by wavelength base in order to obtain the 2-D maps witch shows the wavelength dependent vibrational spectra (see Figure 3.18.A and .B). FT is performed after zero padding (to improve the sampling) and a multiplication with a window function (Kaiser-Bessel window) [44]. (Figure 3.17.E and .F). Because the FT of rectangle function yields a spectrum consisting of a sinc function, a performance filter is obtained by multiplying the data with a Gaussian window function (see Fig 3.18). The result is a passband filter in the frequency domain. Notice that imperfection of the fit can cause spectral distortion in the low frequency vibrational spectrum ($< 100\ cm^{-1}$). To overcome this imperfection, it is necessary to record long pump-probe time delay to aid the fit convergence.

3.6. Probing vibrational coherences at high temporal resolution

Here we test the performance of the set-up at exciting and probing VC in pure liquid acetonitrile upon off-resonance interaction with the 800 nm, 6 fs pulse or the 400 nm, 8 fs FL pulse. Both pulses trigger acetonitrile ground state vibrational modes via a non-resonant Raman process.

Figure 3.19 displays the 2D-map obtained with the 400nm pump pulse and broadband UV-Vis probing. The non-linear, coherent interaction between the chirped probe and the pump pulse produces a strong signal evidencing the wavelength dependence of the pump-probe temporal overlap [41]. Figure 3.20 shows the kinetic traces at specific UV probing wavelengths observed upon off-resonant interaction of acetonitrile with either pump pulse. The early intense signal has vanished after ~ 100 fs and is followed by oscillatory modulations of ΔA. While the former is disregarded, the Fourier transfor of the later yields the same vibrational spectrum for both pump pulses. It is in good agreement with the

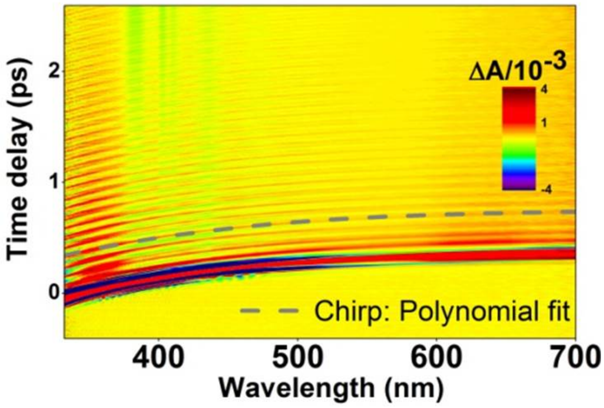

Figure 3.19.: Transient absorption 2D-map of acetonitrile after impulsive, non-resonant interaction with with the 400 nm, 8 fs FL pump pulse. The dashed grey line is a polynomial fit of the chirp in the WL probe pulse.

expected vibrational spectrum of ground state acetonitrile [60], within less than 10 cm^{-1}, in line with the 8 cm^{-1} spectral sampling allowed by the 2 ps observation time window. The ability to excite high-frequency vibrational modes and to time-resolve the corresponding oscillatory signals are intrinsically controlled respectively by the pump pulse duration and the probe supercontinuum spectral width [44]. However in practice, the chirp in the probe pulse, defined here as the slope β (in fs/nm) of the polynomial displayed in fig.3.19, results in an effective wavelength-dependence of the phase of the oscillatory signals. In combination with the finite resolution $\Delta\lambda$ of the spectrometer which spectrally averages of the signal over $\Delta\lambda$, this results in a significant attenuation factor of the frequency components higher than $(\beta\Delta\lambda)^{-1}$. In the present experiment implementing a prism spectrometer, the spectral resolution depends on the detection wavelength. At 400 nm, where the chirp is as large as $\beta \sim 2.9$ fs/nm and $\Delta\lambda = 1.2$ nm FWHM, the cut-off frequency is 2800 cm^{-1}.

We see that our system is able to detect impulsively generated vibrational wave packets at frequencies up to 2940 ± 8 cm^{-1} corresponding to a period of 11 fs.

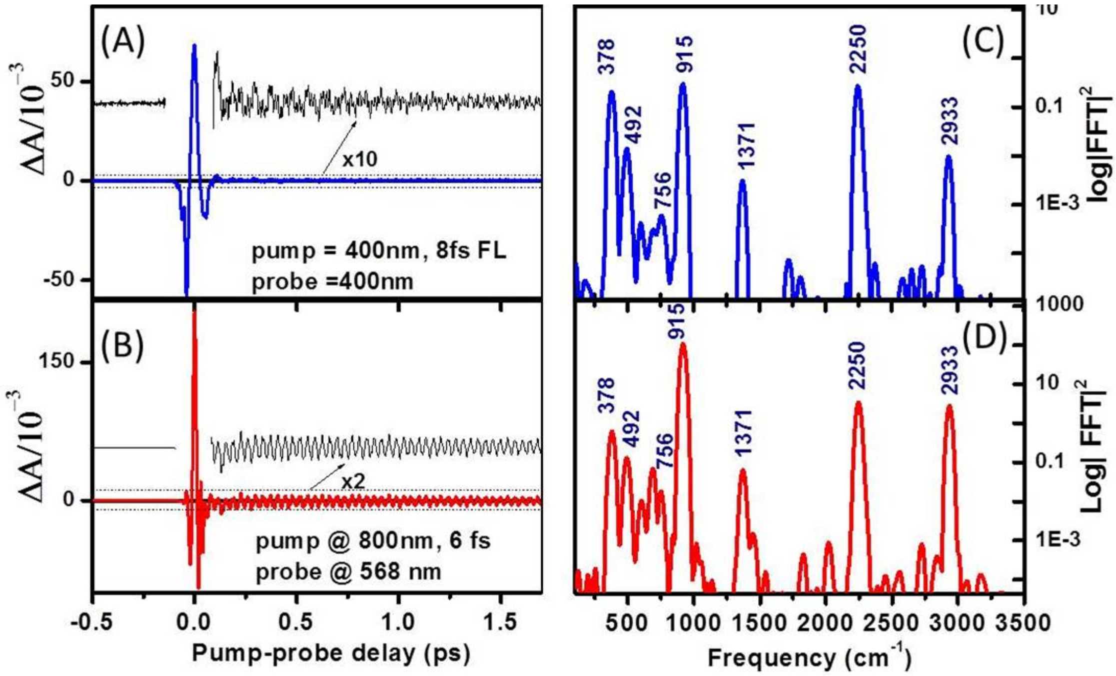

Figure 3.20.: A) and B) Kinetics trace at 400 nm and 563 nm obtained after excitation at 400 and 800 nm respectively, showing the oscillations behavior. C) and D) Fourier transform of the coherent signals showing the vibrational modes of acetonitrile obtained after excitation with the 400 and 800 nm pump pulse respectively.

3.7. Conclusion

In conclusion, we have presented the new developed experimental set-up recording time-domain Raman spectroscopy by so-called VCS, with broadband UV-Vis detection or sub-8 fs excitation pulse centered at 400 nm and at 800 nm enabling resonant and non-resonant excitation of the compounds of interest. Implementing probe intensity self-referencing, the apparatus reaches a shot-noise limited noise floor. Rapid scanning of the pump-probe delay is implemented to suppress very efficiently the dominating effect of low-frequency pump intensity noise on the transient absorption kinetics. Up to 3000 cm^{-1} vibrational signatures are demonstrated in pure acetonitrile at UV and Vis probing wavelengths, with < 15 μOD noise floor. Upon Fourier transformation of the oscillatory residuals, vibrational coherence of both the ground and the excited (Franck-Condon) states of the samples of interest is recovered. This set-up will be used in Chapter 5 to investigate the vibrational dynamics of IP molecular switches.

Part III.

N-alkylated indanylidene-pyrroline: An ultrafast biomimetic molecular photoswitch

4. Ultrafast photoisomerization dynamics in biomimetic molecular switches

This Chapter is presently being formatted for submission as a mini-review article.

4.1. Introduction

The conversion of light energy into mechanical motion at molecular level including $C = C$ double bond photoisomerization is the origin of the concept of molecular photoswitches. Molecular photoswitches produce mechanical work in response to an optical excitation. They modulate the biological activity of various photosensitive proteins or synthetic molecular motors. The retinal chromophore of rhodopsin (Rho) constitutes a natural example of photoswitch. Indeed, in the membrane protein rhodopsin, the photo-isomerization of the protonated Schiff base of rhodopsin (PSBR) 11-cis-retinal triggers the visual cycle in a very short time (200 fs) via evolution in a singlet $\pi - \pi^*$ excited state S_1 followed by a decay to the product all-trans ground state S_0 with a quantum yield of 67% [11] and a 100% 11-cis to all-trans selectivity. Most remarkably, in Rho and nowhere else the PSBR reactive motion appears to be vibrationally coherent. Indeed, a vibrational wavepacket is thought to be triggered by the impulsive population of low-frequency modes during the very fast reactive motion on the excited state S_1 potential energy surface. The vibrational wavepacket propagates through the conical intersection [42] between S_1 and the ground S_0 and further evolves on the electronic ground state as evidenced by the low-frequency oscillations observed in the transient absorption signature of the photoproduct [10]. Such a photoreaction appears as a very effective scheme for optomechanical energy transduction at the molecular scale since the mechanical energy is directed into the vibrationally coherent, reactive motion on a time scale faster than energy dissipation to the environmental thermal bath. Although these properties make rhodopsin a perfect reference to design photoswitches, the PSBR loses its outstanding proprieties when taken in solution. Indeed, in solution its photoisomerization is about 1 order of magnitude slower, the selectivity is lost with the production of several isomers and an overall quantum yield in the range of 15 to 20 % [61]. In a so-called ”biomimetic approach”, a molecular photoswitch based on the indanylidene-pyrroline (IP) skeleton has been synthesized [13] such that the π electron system of IP in solution would mimic that of retinal in Rho. Realistic QM/MM computational model including the 10 π electrons of the IP backbone at the ab initio CASSCF or CASPT2 level (QM, Quantum Mechanics) and the solvent at the Molecular Mechanics (MM) level have been developed which allow accurate modeling of the electronic structure and photoreaction dynamics of the IP's in solution [13, 14, 18, 62, 63]. The photoisomerization of the so-called “parent” Methoxy-N-alkylated IP (MeO-NAIP) was shown to occur on a time scale similar to that of Rho [14]. Remarkably, the same spectroscopic signatures of vibrational coherent motion as in Rho were also observed in several representatives of the MeO-NAIP family [15, 16] which thus are the first synthetic molecular switches displaying a vibrationally coherent $C = C$ photoisomerization. However, although several features of the Rho photoreaction are reproduced in the IP's, the photoisomerization quantum yield does not reach that of Rho, which remains a major opened question raised by the biomimetic approach. The IP molecules thus appear as a very good model system for both experimental and computational investigations of the mechanism that controls the photoreaction properties and the occurrence of the vibrationally coherent reactive motion. In addition, chiral IP compounds have also been synthesized. In these compounds, mirror image symmetry breaking is expected to yield unidirectional rotary motion [64, 65], the fundamental property to achieve the functionality of a rotary molecular motor, potentially turning the IP compounds into effective photomechanical transducers at the single molecule level.

This chapter is an exhaustive review of the experimental investigations of the IP biomimetic molecular switches. After discussing the general biomimetic approach guiding this work, we present results obtained with unpublished compounds to illustrate the so-called vibrationally-coherent photoisomerization and the vibrationally-non-coherent photoisomerization scenario generally observed. A systematic comparison of the photoisomerization speed, quantum yield and the occurrence of vibrational coherence reactive motion is provided.

4.2. The biomimetic design of the IP molecular switches

A variety of IP compounds displayed in Figure 4.1. A have been synthesized and their photoreaction dynamics investigated experimentally and theoretically.

In all IP compounds, the positively charged N atom and the π electron system of the sp^2 carbon backbone featuring 5 double bonds mimic a PSBR-like electronic structure. However, unlike in PSBR, only one central $C1' = C4$ double bond can undergo isomerization in the IP compounds since other double bonds are locked inside ring structures. This ensures the facto the photoisomerization selectivity around a unique double bond, as is observed for PSBR inside the protein cavity in retinal proteins.

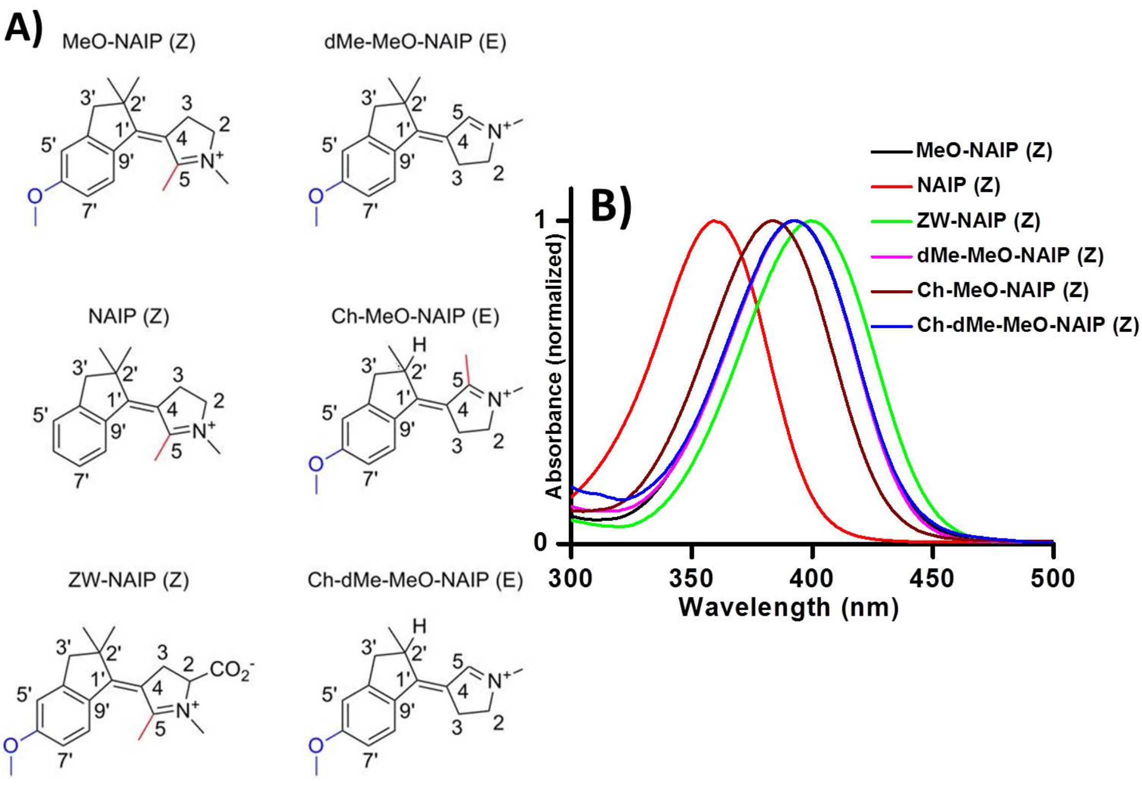

Figure 4.1.: A) Chemical structure of the 6 investigated molecular photoswitches in the most stable isomer and B) their normalized steady state absorption spectra.

As a very general rule driving their early photophysics, the S_1 state of the N^+ terminated polyene IP molecules is expected to feature a charge transfer character [66]. In theIP compounds, the positive charge located on N in S_0 translocates across the isomerizing bond towards the indanylidene moiety in S_1 [13]. A similar photoinduced charge translocation occurs in retinal models [67], PSBR [68, 7], Rho [69] or bacteriorhodopsin [70, 71]. As a consequence, in the IP compounds like in Rho [68] and all PSBR-like systems, the bond length alternation (BLA) mode of the sp^2 carbon backbone is strongly coupled to the optical excitation, as confirmed by the strong Raman signature of this mode at 1575 cm^{-1} in MeO-NAIP (see chaapter 5). In addition, the BLA mode is shown to contribute predominantly to the early nuclear motion away from the FC region. Indeed in the IP compounds the mid-IR signature of the $C1' = C4$ stretching mode is lost instantaneously upon excitation to S_1 [15], indicating that the bond loses its double bond character. This unlocks the torsional motion around the bond and opens the path towards the CI which is predicted to occur for a $C1' - C4$ angle of approximately $80\,^{\circ}$ [14]. The decay to S_0 through the CI and reformation of the exocyclic double bond is evidenced by the recovery of the $C = C$ stretch mid-IR signature on the 0.2-ps time scale.

Because of the charge transfer character of the S_1 state, a major parameter influencing the photophysical properties of PSBR in proteins is the counterion neutralizing its positive charge [72]. In Rho, a complex involving the Glu113 aminoacid acts as the counterion of PSBR [73], and it has been argued that the electrostatic environment of the protein pocket rather shields the interaction of PSBR with Glu113, while in solution, the solvent hardly affects the strong interaction between PSBR and a solvated chloride counterion [69, 74]. A zwitterionic IP compound, ZW-NAIP, was synthesized [15, 18] in which a carboxylic acid group is substituted on C2 (see Figure 4.1.A). Its photoreaction dynamics [15] is essentially identical to that of the parent MeO-NAIP chloride ion pair in solution [16], confirming the absence of shielding effect of the solvent in the latter case.

In the parent MeO-NAIP molecule, beside the effect of the counterion, the electron-donating MeO group on C6’ as well as the inductive effect of the methyl substitution on the sp^2 C5 atom also affect the S_0 and S_1 charge distributions along the molecule backbone. As a global result, the light induced charge translocation of MeO-NAIP in solution with its counterion mimics very well that of PSBR in Rho [13]. In addition, the charge transfer character of the S_1 state of MeO-NAIP is predicted to be preserved all along the barrierless path from the Franck Condon (FC) state to the Conical intersection (CI) with S_0 [14], as a consequence of the relatively large energy gap and weak state mixing with the higher lying S_2 state, very much in accordance with the 2-state model invoked for PSBR in Rho [7]. The result is that the photoreaction dynamics of MeO-NAIP resembles very much that of Rhodospin [16].

The MeO group on C6’ stabilizes the positive charge on the indanylidene moiety in the IP S_1 state. Its influence has been tested in NAIP compound which features no MeO group (see Figure 4.1. As we will report in section 4.4.1, the photoreaction dynamics of the NAIP compound turns out to be similar and even faster than that of the parent MeO-NAIP, including marked signatures of vibrational coherence along the reaction path. This is in spite of a strong blue shift of the ground state absorption indicating a significant destabilization of the S_1 charge distribution [13].

Also the effect of the Me substitutions has been explored in so-called "demethylated" IP compounds which feature no Me on C5 (see Fig 4.1.A). In the case of PSBR in solution, it has been shown that Me substitutions along the sp^2 backbone strongly affect the excited state lifetime and the photoisomerization selectivity and quantum efficiency [75, 61]. In the IP compounds, besides inductive effects affecting the potential energy topology, the Me group on C5 also yields steric hindrance responsible for the S_0 pretwist of the isomerizing double bond. A similar pretwist of the isomerizing bond is also present in PSBR inside Rho [13] and held responsible for the enhanced photoreaction speed and yield [76, 77] in the protein. As a matter of fact, in dMe-MeO-NAIP, the ground state structure is more planar and the photoreaction dynamics appears qualitatively different with a slightly longer excited state lifetime, no evidence of vibrational coherence, but similar quantum yield [78].

4.3. The chiral IP compounds

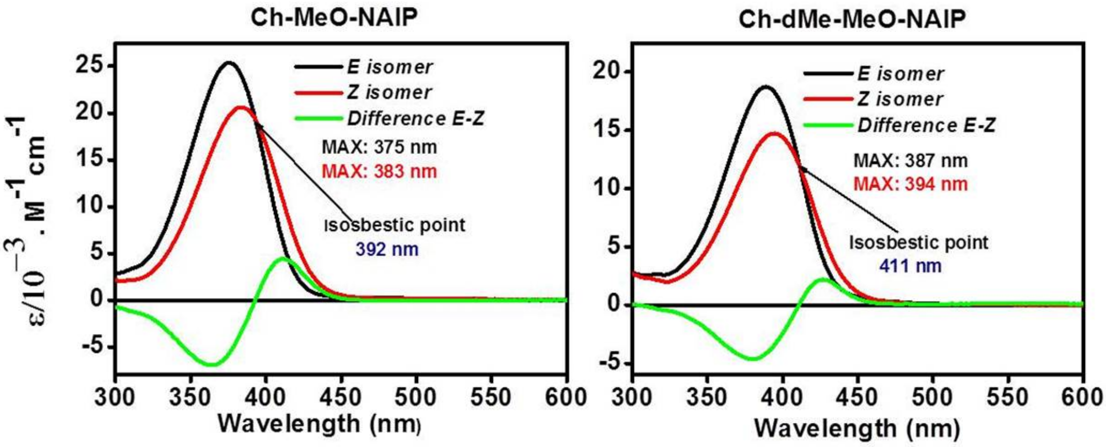

Figure 4.2.: Right: Steady-state absorption spectra of the ch-MeO-NAIP pure E isomer (black) and pure Z isomer (red) in MeOH together with their difference (green). Left: The same for the ch-dMe-MeO-NAIP.

Photoisomerizing molecules capable of converting light energy in continuous unidirectional rotary motion are suited for light-driven molecular rotors applications. In this approach, chiral, newly synthesized IP analogues are available to investigate a unidirectional direction of rotation. We use pump-probe TAS to study the photoisomerization dynamics in methanol of chiral (Ch) NAIP compounds (see Fig 4.1) in which a H atom replaces one of the two methyl groups carried by the C2' atom in the previous, non-chiral NAIP's. Forward E to Z and backward Z to E reactions are investigated and compared for both chiral switches.

The steady state absorption spectra of both switches are presented in Figure 4.2. H-NMR spectroscopy allows us to determine the relative E and Z content for each solution used in the transient absorption experiment (see chapter 2). Typically, in the dark at room temperature, the composition of both "dark-adapted" (DA) solutions is dominated by the stable E isomer witch accumulates up to $> 95\%$. Upon irradiation at 333 nm, a photostationary, so-called light-adapted (LA) solution (stable aver more than 24 hours, in the dark at room temperature) is obtained with a composition of 38% E and 62% Z for the Ch-dMe-Meo-NAIP and 30% E and 70% Z for the Ch-MeO-NAIP. Transient absorption data acquired successively on both the DA methanol solution and on the LA solution immediately after producing the photostationary state allows us to retrieve the TAS data of pure E and pure Z compounds, by computing the appropriate linear combination of both TAS data sets (see Chapter 2 for details).

As we will see, all IP compounds displayed in Figure 4.1 exhibit a sub-ps excited state lifetime. However two qualitatively different types of transient absorption signatures are observed, which are attributed either to a vibrationally coherent photoisomerization, or to a vibrationally non-coherent scenario. In section 4.4, we illustrate the vibrational coherent scenario with the unpublished NAIP switch. After, we introduce the chiral compounds by using one of them to illustrate the second scenario where no signature of vibrational coherence photoreaction is observed. These two photoisomerization scenarios are compared with the example of a recently synthesized chiral version of the parent MeO-NAIP. This molecule is a particular case since it is so far the only member of the family for which one isomer (Z) displays signatures of vibrational coherence while the other (E) does not. In section 4.5, we introduce the molecular origin of vibrational coherence in the IP compounds. Finally in section 4.6, we summarize and compare the isomerization dynamics and quantum yield of all investigated IP compounds.

4.4. Photoisomerization dynamics revealed by transient absorption spectroscopy

In this chapter, the transient absorption spectroscopy (TAS) set-up used is the ”historical setup” described previously [15]. It is based on the combination of an ultrabroad probe pulse (300-750 nm) and a 400 nm pump pulse, with a resolution of 70 fs. The relative linear polarizations of pump and probe beams are set to magic angle (54.7°). The pump intensity is kept in the linear regime of excitation in order to promote the sample to its first excited state (S_1) with a few-percent probability. Both pump and probe beams are focused into a 0.2-mm thick flow cell containing the sample in solution. A peristaltic pump circulates the sample to refresh it between two excitation laser shots. The sample optical density (OD) at the excitation wavelength (400 nm) is ~ 0.6. All UV-VIS data presented here are post-processed in order to compensate for the group velocity dispersion in the probe beam so as to define accurately the time zero at all wavelengths. Also, the transient signals generated in the solvent and the quartz flow cell are subtracted from the data as explained in chapter 2.

4.4.1. NAIP: Illustration of vibrationally-coherent

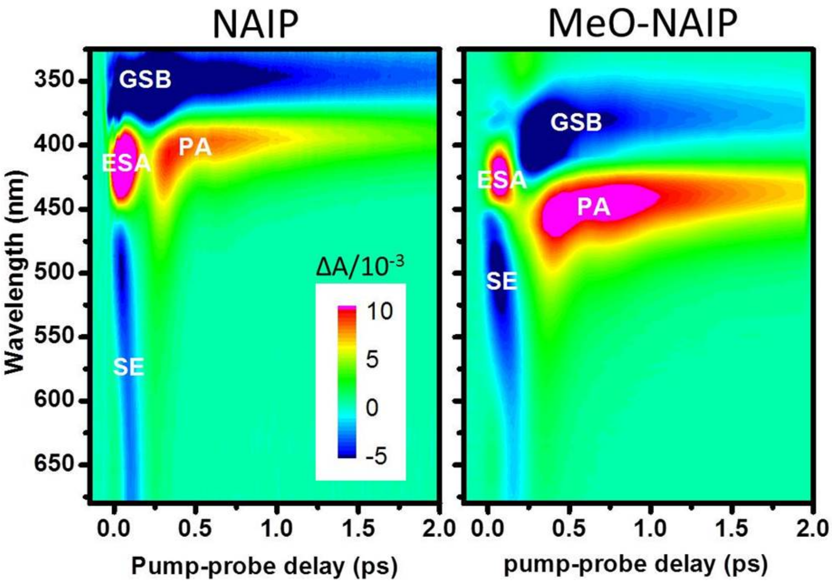

Figure 4.3.: Transient absorption 2D maps for te Z isomers of NAIP (left) and of the parent MeO-NAIP (right) as a function of wavelength (nm) and time delay (ps) after excitation at 400nm.

Figure 4.3 displays the TAS data of the *Z* isomer of NAIP and the parent MeO-NAIP in methanol (MeOH). Despite a 30-nm blue-shift of the ground state absorption of the former, both molecules display very similar transient spectra at early times (< 0.3 ps), with the spectroscopic signature of the excited state absorption (ESA) and stimulated emission (SE) at wavelengths < 450 nm and > 450 nm respectively. At the same time we detect the signature of the ground state contribution composed of ground state bleach (GSB) < 400 nm and photoproduct absorption (PA) > 400 nm for both compound. In the following, we describe specifically the photoreaction kinetics of NAIP, which turns out to be very similar to and representative of that of MeO-NAIP [16] and ZW-MeO-NAIP [15]. Figure 4.4 presents selected spectra from the same data set. The time-zero transient spectrum shows the spectroscopic signature of the S_1 state. It is essentially composed of SE producing a negative contribution ($\Delta A < 0$) from 450 nm to above 650 nm, and of ESA producing a positive contribution ($\Delta A > 0$, in red) from 450 nm down to 387 nm. The latter signal is overlapped with the ground state bleach (GSB, ($\Delta A < 0$) between 325 and 387 nm). The

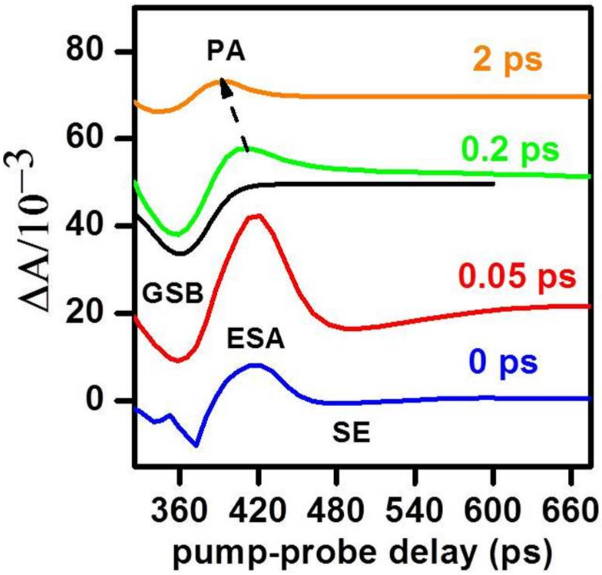

Figure 4.4.: Transient spectra at different delay between the pump and the probe. Along the 0.2-ps spectrum, the opposite of the ground state absorbance is shown (black line). In the 0.2 ps spectrum the positive signal (390 to > 660 nm is attributed to the early signal of the photoproduct.

apparent spectral evolution of SE from 0 to 50 fs is due to the presence of a fast decaying excited-state absorption (ESA), most clearly seen (fig 4.3) from 600 to > 650 nm. The spectroscopic signatures of the S_1 state are very short-lived (< 200 fs). Like in the case of MeO-NAIP, they are followed by a very broad photoproduct absorption band (PA, $\Delta A > 0$) which emerges impulsively around 0.2 ps from 400 nm to 700 nm, and rapidly narrows and blue-shifts into the 390 nm band seen to last from ~ 0.2 ps to 2 ps and beyond.

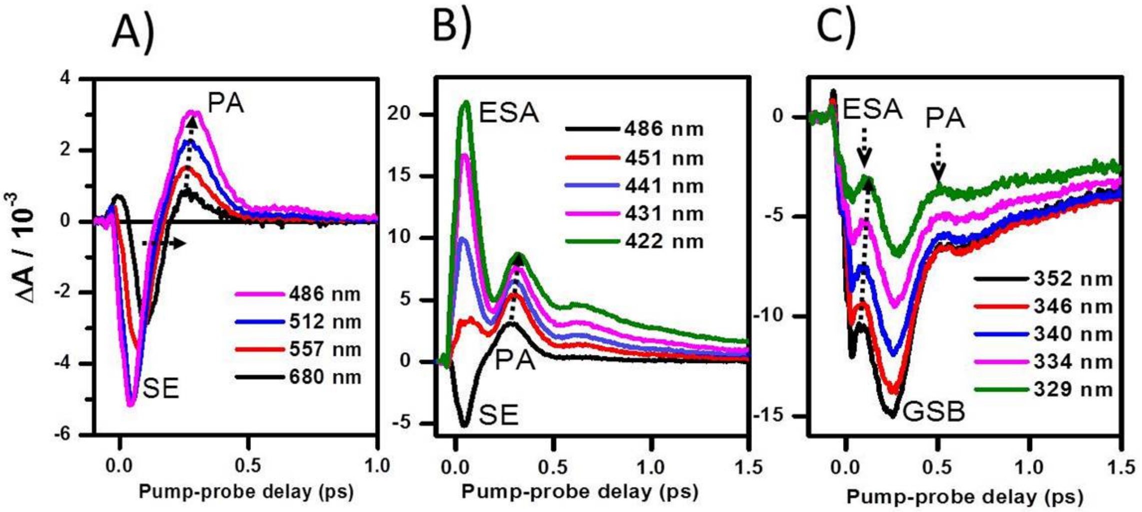

Figure 4.5.: TAS of NAIP. Selection of kinetic traces illustrating A) the rapid red shift of the SE and blue shift of the PA in the red part of the observation window (> 486 nm), B) the impulsive rise of the PA signature and its further blue shift, following the S1 state signatures (SE and ESA) after ~ 200 fs, in the range 420-490 nm, C) the dynamic blue shift of the delayed ESA signature in the GSB spectral region (330-350 nm), followed by the impulsive recovery of the GSB and PA signal onset.

Figure 4.5 displays kinetic traces at a selection of wavelengths. A characteristic feature of the NAIP TAS data is the very broad SE extending to wavelengths > 650 nm, which decays on a time scale shorter than 200 fs and is followed by a weak, positive, equally broad absorption band. The latter is attributed to the earliest signature of the photoproduct, by analogy with the case of MeO-NAIP and ZW-MeO NAIP where the same spectroscopic signatures are observed and time-resolved Mid-IR spectroscopy showed in addition that the central $C = C$

is reformed on the same 200 fs time scale, indicating the decay to the ground state [15]. The rapid cross-over between the SE and subsequent photoproduct absorption (PA) band is illustrated in Figure 4.5.A. It clearly reveals that with increasing wavelengths the zero-crossing between the negative SE and positive PA signals occurs at later time delays while the maximum of the PA signal is reached at earlier times (see arrows in figure 4.5 A). This temporal behavior is assigned to the signature of a vibrational wavepacket, that is a population which remains focused in the configurational space while evolving along the reaction coordinate on the S_1 PES towards the CI (red shift of the SE), impulsively arrives on the S_0 PES via the CI, and further evolves towards the S_0 minimum (blue shift of the PA). A similar TAS signature was also observed in Rho [79] and other IP compounds [15, 16] and interpreted the same way. Figure 4.5.C illustrates the dynamic spectral shift observed in the ESA signal, which appears instantaneously around 352 nm, but with a delayed onset in the UV most part of the observation window (329 nm). The large ESA spectral shift (from 352 nm to 329 nm) over 160 fs and the non-exponential character of the blue-most traces are indicative of a wavepacket, which remains relatively focused in the configurational space during the motion away from the initial Franck-Condon (FC) region. Similarly the impulsive onset of the PA signature can be followed temporally and spectrally from the red part of the observation window (Fig. 4.5.A) to the blue range, where it follows the SE and ESA signatures of S_1 after ~ 200 to 250 fs (Fig.4.5.B), and until the UV range where it causes the impulsive GSB recovery at time delays between 250 and 400 fs (Fig.4.5.C). This is interpreted as further ground state dynamics of the wavepacket which rapidly evolves from the CI region towards the S_0 minimum of energy. Like in other IP compounds [15] [16], subsequent low-frequency oscillations are observed in the range 320-450 nm which further support the interpretation. Noticeably, unlike the case of exponential dynamics which can be well modeled by non-retarded, (multi) exponential kinetics as described in chapter 2, the dynamics are here essentially non-exponential, and required a more elaborated fitting function [16].

Figure 4.6 displays the oscillations observed at 425 nm and 335 nm. The oscillatory behavior is isolated by fitting the S_0 transient kinetics traces by a multiexponential decaying function, and plotting the corresponding fit residuals. The inset of Fig.4.6 displays the two residuals together with the kinetic trace observed at 680 nm. The latter shows the earliest signature of the wavepacket in the ground state (arrow 1), soon after passing through the CI. Then, arrows number 2 and 3 in Fig 4.6 pinpoint the passage of the wavepacket through different spectral observation windows around 425 nm and 325 nm successively. Subsequent oscillations are clearly distinguishable from the noise, and appear out-of-phase in the 425 nm and 335 nm traces which are respectively in the red and blue sides of the PA absorption spectrum. This is reminiscent of sim-

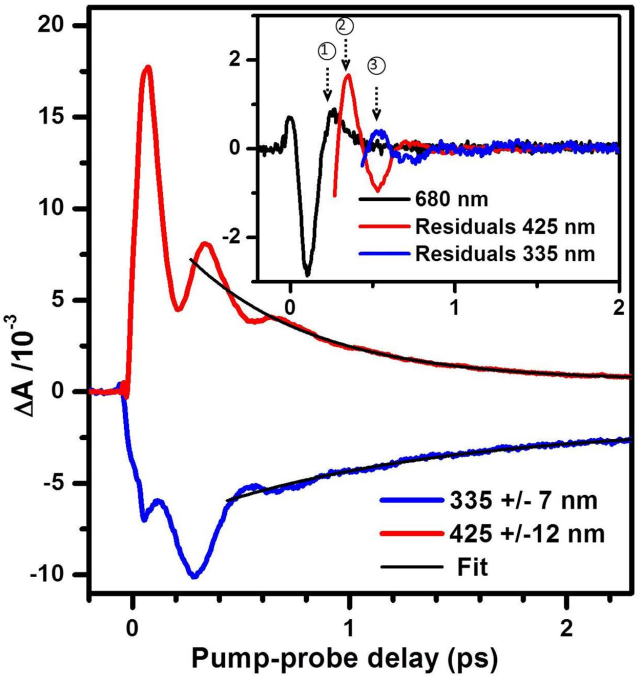

Figure 4.6.: TAS of NAIP displaying oscillatory behavior after decay to the ground state. Inset: The residuals of the (multi)exponential fit exhibit oscillations which are compared to the transient absorption signal observed at 680 nm.

ilar, low-frequency oscillations observed in Rhodopsin [10], and is indicative of further oscillatory motion of the wavepacket around its equilibrium position in the ground state. Fourier transform (FT) of both residuals yields a vibrational period of 400± 50 fs (80 cm^{-1}) with a damping time constant at 200 fs.

Summary of the signature of vibrationally coherent photoisomerization

The NAIP data presented above show a slightly different distinct coherent signatures discussed for MeO-NAIP and ZW-NAIP:

1) The dynamic shift of the excited-state absorption band from ∼ 420 nm to 300 nm on a 160 fs time scale, and the red shift of the short live stimulated emission signal from ∼ 450 nm to > 650 nm reflecting fast reactive motion (out of FC) on the excited-state potential energy surface.

2) The delayed and quasi-impulsive arrival of the wave packet-like population in the ground state observed with the photoproduct absorption band peaking at 260 fs on the red-most edge of the spectrum (SE/PA "crossover").

3) The oscillations in the ground state, with a period of 400 fs and 200 fs damping time constant (for NAIP). The low-frequency modes are in the range

of torsional modes, in particular ring distortion [16].

The data reported above for the NAIP photoswitch show that the molecules isomerize in a vibrationally-coherent fashion. Thus, the well-focussed population can be tracked in time, leading to the scenario depicted in figure 4.7. Immediately after photoexcitation, ESA and SE are observed. The ESA band spectrally and temporally shifts (160 fs), reflecting motion along the torsional coordinate. After a spectroscopically dark period of ~ 160 fs, associated with the passage through the conical intersection, the molecules populate the ground state in both isomer conformations in form of an oscillating, rapidly damped wavepacket with a ~ 400 fs period (80 cm^{-1}).

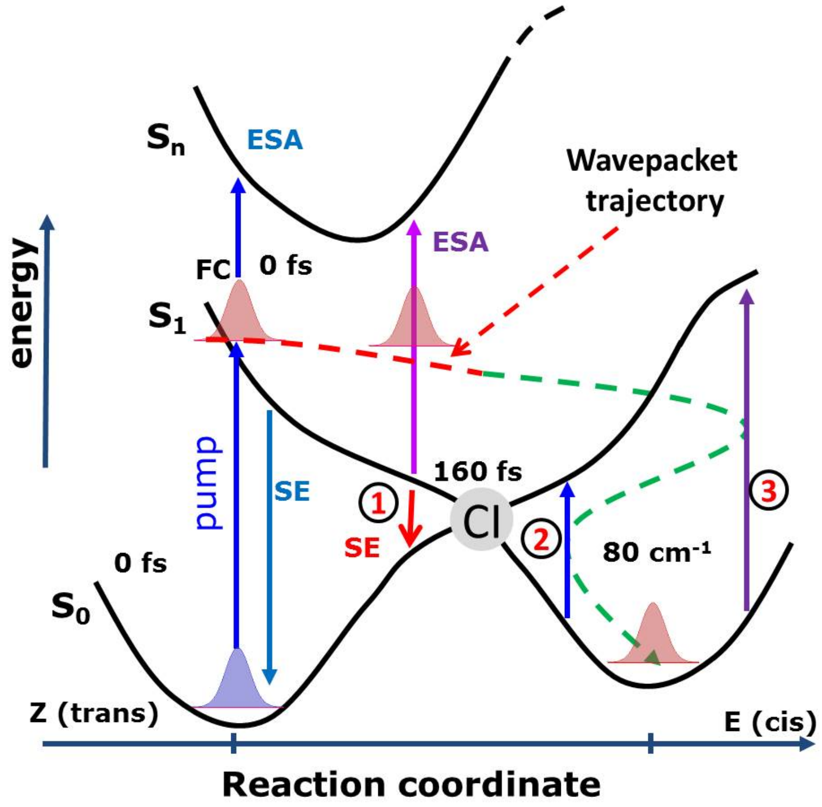

Figure 4.7.: Illustration of vibrationally-coherent photoisomerization scenario and timing for NAIP. Number 1 to 3 refer to the successive spectral windows through which the wave packet is observed in line with arrows 1 to 3 in Fig 4.6. The dashed arrow represent schematically the wave packet trajectory in S_1 (red) and in S_0 (green).

4.4.2. The Ch-dMe-MeO-NAIP: illustration of non-coherent photoisomerization scenario

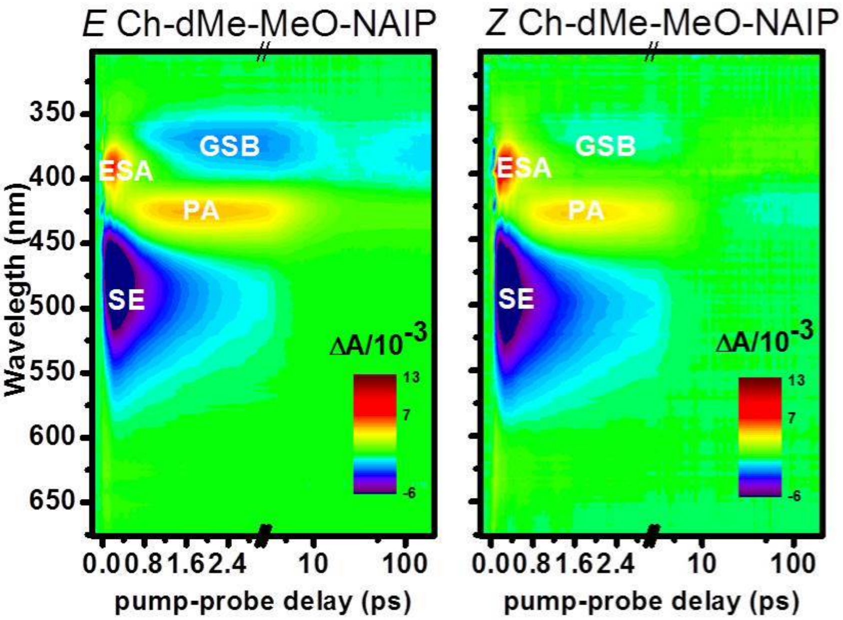

Figure 4.8.: Pump-induced absorption change ΔA as function of probe wavelength (in nm) and time delay (ps) between pump (400nm) and probe pulses of (Right) the pure E and (Left) the pure Z isomers of Ch-dMe-MeO-NAIP in MeOH.

Figure 4.8 displays the transient absorption data for the pure *E*- (right) and pure *Z*- (left) isomers of Ch-dMe-MeO-NAIP in MeOH, as reconstructed from the TAS data recorded with the DA and LA samples. Both 2D-map are very similar indicating a nearly identical photoreaction dynamics in both isomerization directions. For both isomers, we observe at short time delays, the spectroscopic signature of the S_1 excited state essentially composed of stimulated emission (SE, negative signal in the 430-580 nm range) and excited state absorption (ESA, positive signal in the range 370 nm to 420 nm). Concomitant of the decay of ESA and SE, the spectroscopic signature of the photoproduct absorption (PA) emerges after ~ 0.5 ps and further rises in the range 410 to 450 nm. The intense ESA band overlaps with the less intense ground state bleach (GSB) which is thus non apparent at very short time delays, but is detected as a weak negative signal between 350 and 400 nm at later time delays (> 0.5 to 1 ps), when the

ESA signature has decayed. After $\sim$ 30 ps, a quasi-static, vibrationally-relaxed spectrum is observed up to 100 ps for both molecules (hardly seen in Fig . 4.8, better shown in Fig 4.9.C).

Figure 4.9. A and .B display a selection of transient spectra for both isomers. At early times (160 fs), the S_1 signatures are the ESA, maximum at 390 nm for E and 400 nm for Z, and the SE, maximum at 470 nm or 480 nm for both isomers. The (negative) GSB is not seen because it is hidden by the more intense (positive) ESA signal in the same wavelength range. On the 0.5 ps time-scale, the ESA and SE signatures decay and the PA band rises with a maximum at $\sim$ 425 nm (E) and $\sim$ 430 nm (Z). After 2 ps, the GSB clearly appears (negative signal around 370 nm for both isomers) due to the significant decay of the overlapping ESA. At the same time delay, SE has also significantly decayed but is still detectable. After complete decay from S_1, further vibrational relaxation occurs in the vibrationally hot ground state on the several ps time scale until a quasi-stationary spectrum is observed ($>$ 50 ps). The latter overlaps with the difference between E and Z static absorption spectra, thus evidencing the formation of Z when exciting E and vice versa (see Fig 4.9.C). The photoreaction kinetics are essentially identical for both isomers.

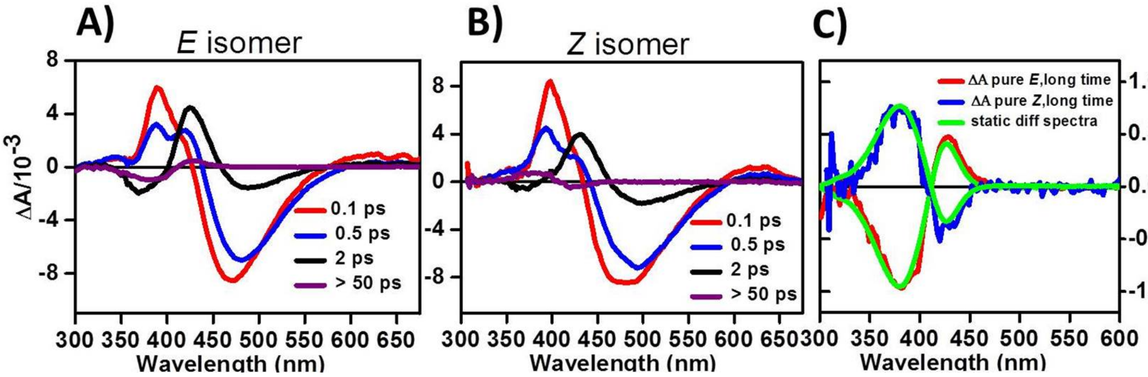

Figure 4.9.: Transient Absorption data on the E and Z isomers of the chrial dMe-MeO-NAIP in MeOH. Selection of transient spectra for A) the pure E and B) the pure Z compounds. C) Quasi-static transient spectra at long time overlaped with the steady state difference spectra (green curve) for both isomers.

In particular, Figure 4.10. C and .D show the kinetics traces indicative of the photoreaction dynamics of both isomers. A quantitative analysis of the photoreaction kinetics is made by fitting some kinetic traces with a sum of exponential functions convoluted with the instrument response function (IRF) of the experimental setup as described in Chapter 2. Interestingly, for both isomers, the SE signals rises beyond 0.1 or 0.15 ps with a somewhat reduced slope until they reaches their maximum at ∼ 250 fs. This rise time is not limited by the experimental resolution and is indicative of excited state vibrational relaxation on the same time scale. As illustrated in Figure 4.10. C and .D, for both isomers, the decay of the ESA (plotted at 374 nm) is synchronous to the rise of the PA (at 427 nm). For both isomers, a rise time is also clearly resolved in the ESA signal (373 nm) which becomes maximal after ∼ 250 (± 30) fs. Then, the 373 nm (ESA decay and GSB recover), 427 (PA formation) and 491 (SE decay) nm traces are fitted simultaneously with a bi-exponential function while seeking identical time constants in the three traces (global fitting). The same analysis is repeated independently on both isomers and yields exactly the same time constants as seen in table 4.1. The first time constant $\tau_1 = 0.7$ ps is common to the decay of the SE and ESA and the rise of the PA. It is thus attributed to the excited state population decay and photoproduct formation. The second time constant $\tau_2 = 4$ ps is common to further relaxation of the PA signal (observed at 427 nm after the PA rise) and of the GSB (observed at 373 nm after the ESA decay). Hence the 4 ps time must be attributed to ground–state vibrational relaxation and cooling.

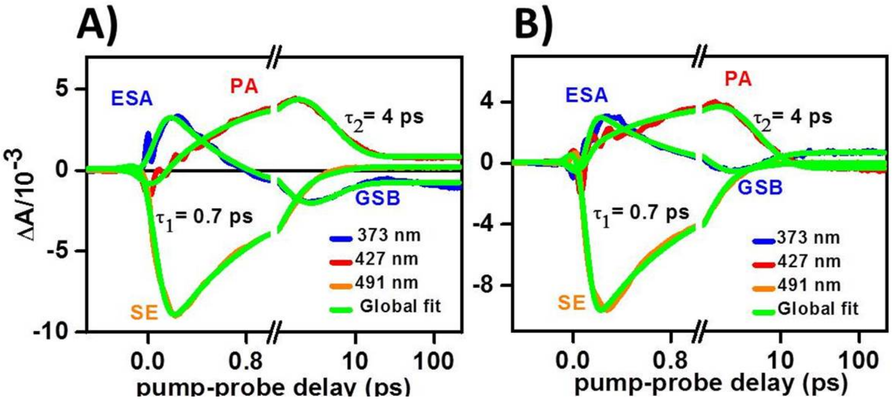

Figure 4.10.: A) Temporal evolution of ESA + GSB signal at 373 (blue curve), PA signal at 427 nm (red curve) and SE signal at 491 nm (orange trace), togather with a global fit (green curve) for the Ch-dMe-MeO-NAIP *E*-isomer. B) The same for the *Z* compound.

Finally, we note that the traces at 427 nm display oscillatory behavior in the wavelength range of 400-420 nm corresponding to the ESA and GSB spectral region during the first ps. A very preliminary analysis indicates that the period of oscillation is $\sim$ 150 fs (220 cm^{-1}), that is about three times shorter than the $\sim$ 500 to 600 fs period of the oscillations attributed to ground state vibrational coherence in the MeO-NAIP or the ZW-NAIP. In addition, here they die out before the PA is formed. The slightly irregular rise of the kinetic trace (SE) of both isomers in Fig **??** .A and .B may be a signature of similar, much weaker oscillation in the SE signal or in the far red wing of the ground state bleach...). For the time being, we are not able to speculate that they could possibly be attributed to ground state oscillations produced by Resonant Impulsive Stimulated Raman Scattering (RISRS) or attributed to excited state. This question will be addressed in the chapter 5.

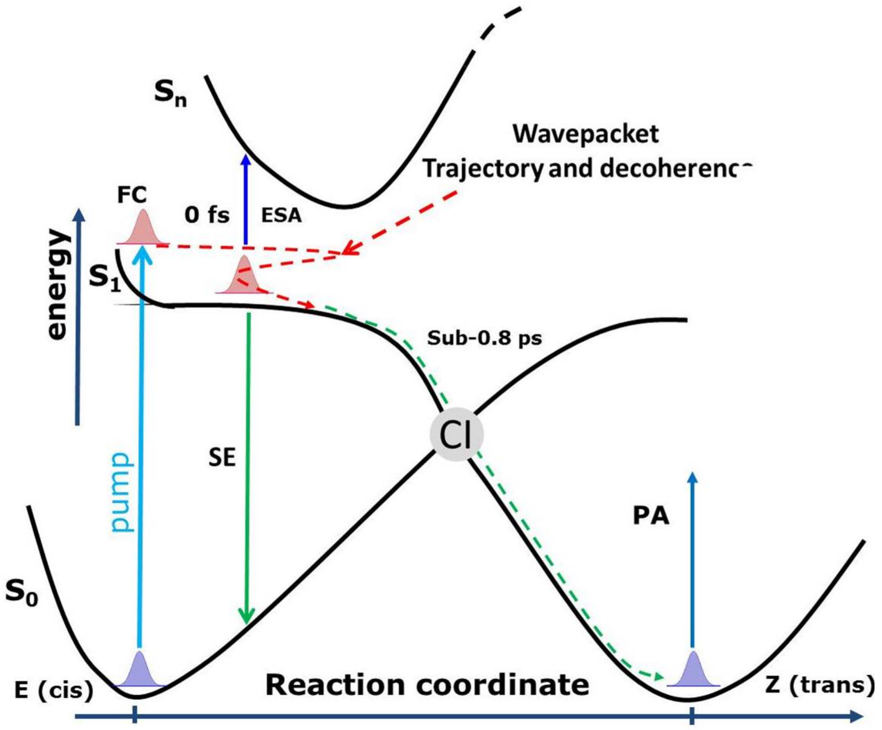

Figure 4.11.: Illustration of the vibrationally non-coherent photoisomerization scenario and timing for E Ch-dMe-MeO-NAIP. Red dashed line represents schematically the wavepacket trajectory and the decoherence in S_1. The green arrow represents schematically the non-coherent decay scenario.

The scenario depicted in figure 4.11 illustrates the non-coherent photoisomerization scenario. Immediately after photoexcitation, wavepackets are generated in FC region. After vibrational relaxation out from the FC region, ESA and SE witch reflect the motion on the S_1 PES toward the CI, are observed. Due to the long excited state lifetime ($\sim$ 0.8 ps for the Ch-dMe-MeO-NAIP), the coherence is lost before crossing the CI. Thus the populations populate the ground state in form of exponential dynamics.

	373 nm, 427 nm, and 491 nm *E*	373 nm, 427 nm, and 491 nm *Z*
Rise	250 ± 30 fs (373 and 491 nm)	250 ± 30 fs (373 and 491 nm)
$\tau 1$	780 fs	800 fs
$\tau 2$	4.2 ps	4.4 ps

Table 4.1.: Table summarizing the fitting results from the isomerization dynamics of both isomers of Ch-dMe-MeO-NAIP.

The overall photoreaction dynamics is actually very similar to that of the non-chiral dMe-MeO-NAIP [78], that is in contrast to the vibrationally-coherent scenario described for the parent MeO-NAIP which carries a Me on C5. we will come back for this comparaison with different IP compounds.

4.4.3. The case of Ch-MeO-NAIP

The Ch-MeO-NAIP which is unique in the IP compound family since each isomer exhibits a different photoreaction scenario. The TAS data displayed in Figure 4.12, where the isomer-specific signature have been isoletad using the procedure introduced in chapter 2 after performing two TAS experiment on a DA and LA sample. On the one hand, *Z* Ch-MeO-NAIP displays a TAS 2D map very similar to that of the above NAIP and of the non-chiral, parent MeO-NAIP. In particular the SE spectrum extends to large wavelengths and is impulsively followed by an early PA band rapidly blue shifting. On the other hand, *E* Ch-MeO-NAIP displays a much longer-lived, comparatively narrower SE, which is not follow by and red-detuned signature of the PA, somewhat similar to the Ch-dMe-MeO-NAIP (see above). Figure 4.13 illustrates the difference between the photoreaction characteristics of both isomers of Ch-MeO-NAIP. Fig. 4.13. A displays the transient signals observed at 500 nm, close to the maximum of the SE band for both isomers. For the *Z* isomer, the rapid cross

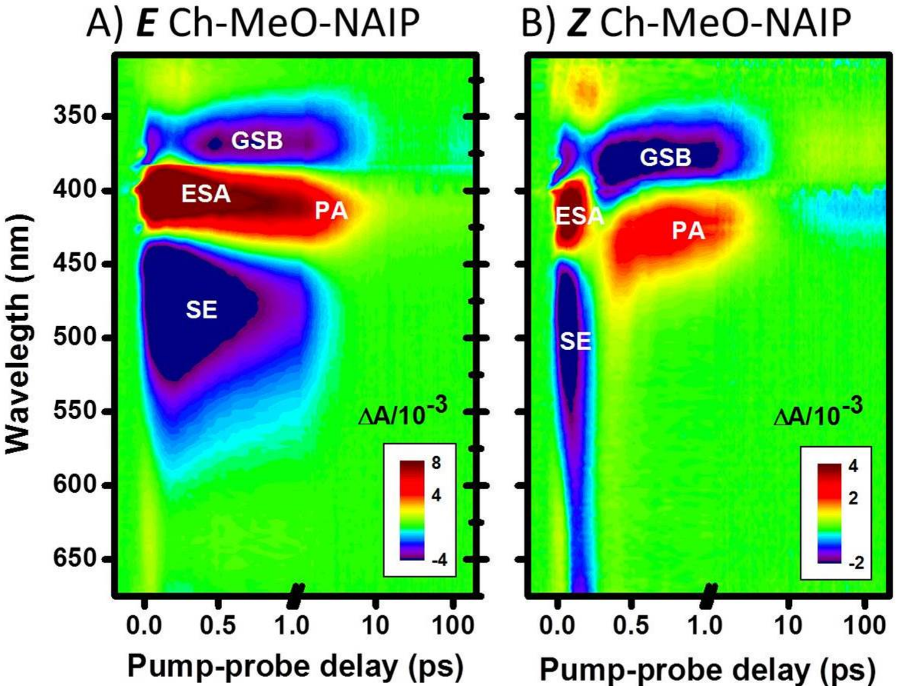

Figure 4.12.: Transient absorption (ΔA) 2D maps for Ch-MeO-NAIP in the E (A) and Z (B) isomers, as a function of wavelength (nm) and time delay (ps) after excitation at 400nm.

over from SE to PA occurs at 500 nm after ∼ 260 fs, and is again attributed to the signature of the excited state vibrational wavepacket travelling through the conical intersection (CI). Instead, no such signature is observed for the *E* isomer, where the SE is much longer lived, comparatively narrow-band, and not followed by any positive signature of the PA. In the latter case, the signal is seen to rise on a (wavelength-dependent) time scale of ∼ 200 fs (at 500 nm) as a consequence of either a dynamic Stocked shift of the SE, or of the decay of a very short-lived overlapping ESA (better seen in the range 580 nm to 670 nm in fig. 4.12 left). This signal rise is anyway indicative of motion out of the FC region on the 100-fs time scale. Then the SE signal is seen to decay bi-exponentially with time scales (and amplitudes) of 440 ± 70 fs (60%) and 1.4 ps (40%). Fig. 4.13.B displays the long-delay (t > 30 ps) TAS data both *E*- and *Z*-isomer: a very good overlap is observed with the static *Z*-*E* and *E*-*Z* difference spectra, showing that the reverse isomerization reaction occurs in both cases.

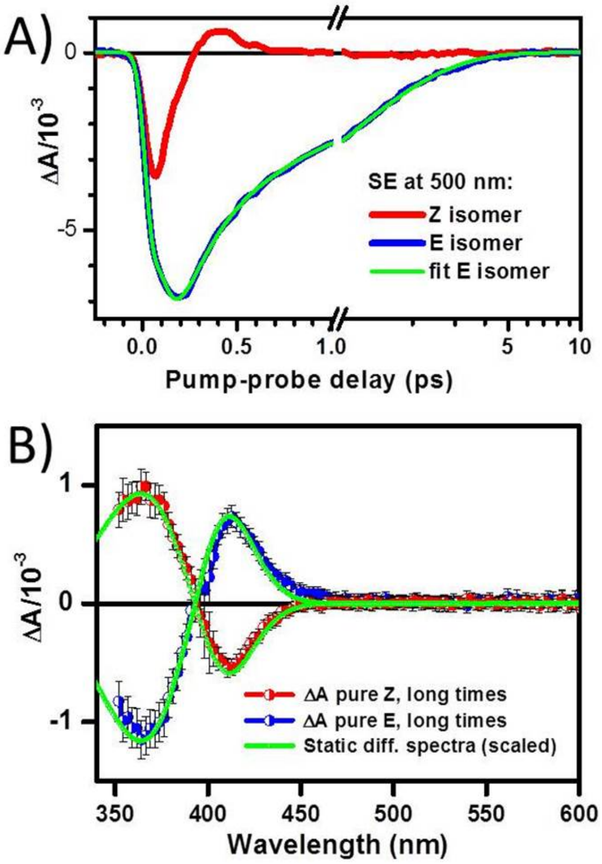

Figure 4.13.: Comparison of the TAS signatures of the *Z* (red) and *E* (blue) isomers of Ch-MeO-NAIP. A) transient kinetics at 500nm. B) Stationary transient spectra at long time delays (> 50ps).

4.5. The molecular origin of the vibrational coherence in IP compounds

To rationalize the backbone modification effect on the isomerization dynamics of the IP photoswitches, it is useful to consider the ground state geometries of these molecules. Figure 4.14 displays the Newman projections of the IPs structures.

Since the photoreaction dynamics are influenced by the topology of the PES, the difference of the photisomerization dynamics in IP molecules can be rationalized as the difference of the excited state plateau witch can be assigned to the "geared" *E* conformation present in the ground state structure of some and absent for others IP molecules (see Fig 4.14). The hydrogen atom (H) of C8' can fit in between both H atoms on C3. This conformation would provide a greater stability of the structural configuration (see Chapter 7).

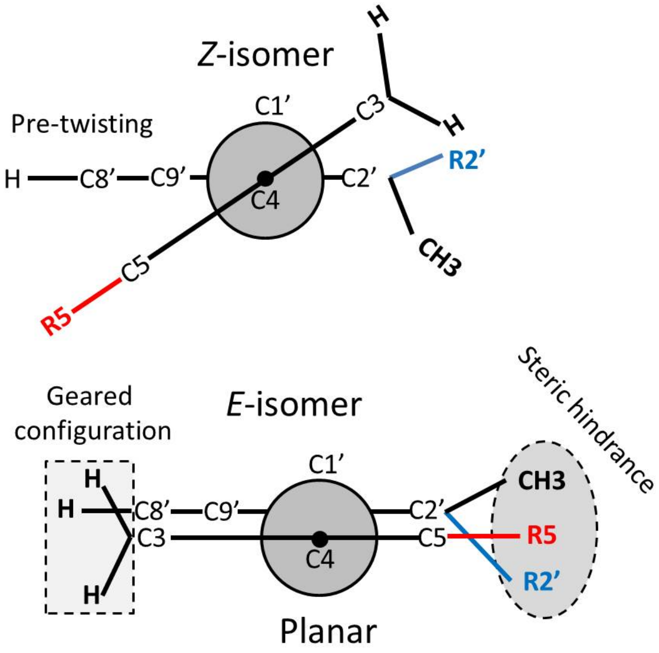

Figure 4.14.: Perspective representation and Newman projections of the IP structures: R2' = H = chiral; R2' = CH3 = non chiral; R5 = H = "demethylated"; R5 = CH3 otherwise. Top: *Z* isomer "skewed" and pre-twisted; Bottom: *E* isomer in the "geared" arrangement.

Within our investigated compounds, vibrationally coherent reactive motion is observed only in those compounds which carry a methyl group on the sp^2 hybridized C5 atom of the pyrrolinium moiety (see table4.2). The photoreactions speed are very fast (< 300 fs). As displayed in Figure 4.15, it appears that removing one methyl substituent in C5 washes out all signatures of vibrationally coherent reactive motion as observed in both isomerization directions (Z to E and E to Z) in the parent MeO-NAIP.

The effect of the C5-methylated on the photoreaction dynamics can be qualitatively related by considering the equilibrium geometry difference between the MeO-NAIP and dMe-MeO-NAIP for example. The Z isomer of MeO-NAIP (R5 = CH3 and R2' = H) is the more stable isomer. This arise from the steric hindrance between the methyl group at C5 and the two methyl group attached to C2' (in the E conformation) which causes a destabilization of the geared arrangement. Therefore, the most stable conformer becomes the Z isomer in S_0, which is distorted, with a pre-twist along the C1'-C4' bond (see Fig 4.14). The presence of the methyl group on the sp^2 hybridized C5 provides to the MeO-NAIP a pre-twisting geometry more than 15° [78], due to a steric hindrance caused

Compound	R5	R2’	Vibrationally-coherent
NAIP(Z)	CH3	CH3	Yes
MeO-NAIP(*Z*)	CH3	CH3	Yes
MeO-NAIP(*E*)	CH3	CH3	Yes
ZW-NAIP(*Z*)	CH3	CH3	Yes
ZW-NAIP(*E*)	CH3	CH3	Yes
Ch-MeO-NAIP(*Z*)	CH3	H	Yes
Ch-MeO-NAIP(*E*)	CH3	H	No
dMe-MeO-NAIP(*Z*)	H	CH3	No
dMe-MeO-NAIP (*E*)	H	CH3	No
Ch-dMe-MeO-NAIP(*Z*)	H	H	No
Ch-dMe-MeO-NAIP(*E*)	H	H	No

Table 4.2.: Comparison of the photoisomerization dynamics of various IP compounds.

by this groupement. This geometrical arrangement results in the fast photoisomerization in MeO-NAIP and in the vibrationally-coherent reactive motion scenario.

Instead when the methyl group on C5 is removed, the geared *E* geometry is not destabilized and remains more stable than the *Z*. As a consequence, the dMe-MeO-NAIP (R5 = H and R2’ = CH3) adopts the *E* stable structure on the ground state. The planar geometry can be responsible for slower ESL of the C5-non-methylated compounds compared to the C5-methylated compounds and thus the lack of coherence activity upon photoisomerization.

Interestingly to the Ch-MeO-NAIP (R5 = CH3 and R2’ = H) and the Ch-dMe-MeO-NAIP (R5 = H and R2’ = H), like in dMe-MeO-NAIP structural

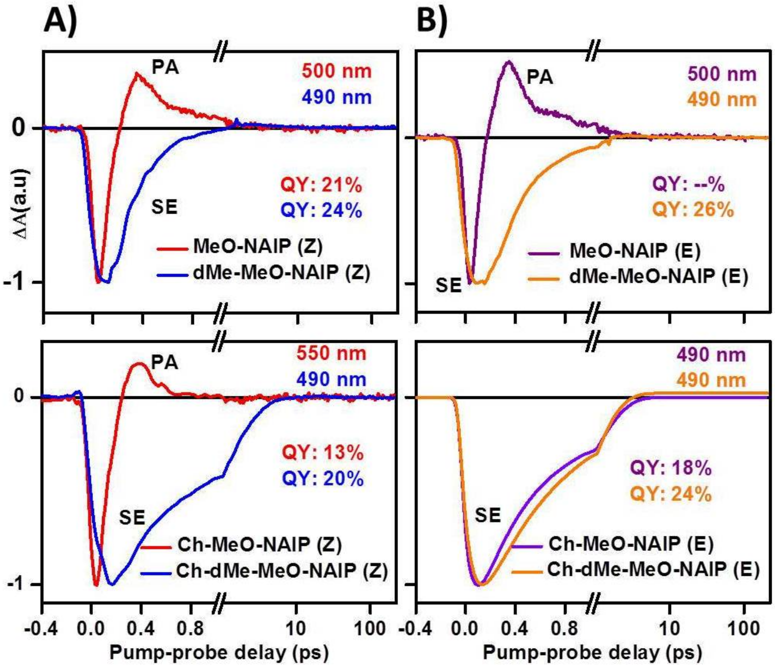

Figure 4.15.: Influence of the demethylation on the photoreaction dynamics. A) and B) Transient absorption kinetics at selected wavelengths showing the SE decay in the red part of the observation window, followed (*Z*- and *E*-MeO-NAIP, *Z*-Ch-MeO-NAIP) or not (the other compounds) by the impulsive PA signature. The sudden cross-over between SE and PA observed at around 230 fs for *Z*-MeO-NAIP and 260 fs for the *E*-MeO-NAIP and the *Z*-Ch-MeO-NAIP is the signature of a vibrationally coherent reactive motion through the conical intersection.

configuration, the geared arrangement is preserved for both chiral compounds. This explains the non-coherent behavior displayed by the *E* chiral molecules and the *Z* Ch-dMe-MeO-NAIP (”non-skewed”), since the excited state decay is long. However in the case of *Z* Ch-MeO-NAIP, the observed vibrationally-coherent photoisomerization signature suggests a faster photoreaction, which is a consequence of a possible pre-twisted configuration of the *Z* isomer.

In summary, the photoisomerization dynamics in IP compounds seems to be controlled by the ground state structure of the molecule. Vibrationally-coherent photoisomerization scenario is observed only in those compounds where the geared arrangement is strongly destabilized. This destabilization is due to the presence a steric hindrance causing a distortion along C1’-C4 isomerizing bond. Thus the molecule in this configuration adopts a pre-twisting initial geometry, required for fast decay and thus preservation of the vibrational coherence activity upon photoisomerization. This approach is supported by recent theoretical investigations of isomerization dynamics of IP compounds by on-the-fly Tully surface-hopping methods at the semi-empirical OM2/MRCI level [80]. The results show that from MeO-NAIP to dMe-MeO-NAIP, demethylation takes more time to move out of the plateau towards the CI, making more difficulty for the dMe-MeO-NAIP to reach the S_0/S_1 CI. As the result, the ESL is slower.

4.6. Discussion

The outstanding photoreaction dynamics of PSBR in Rhodopsin was proposed as a paradigm for barrierless excited-state reactivity, in which the high photoisomerization quantum yield is a consequence of the very high reaction speed, both resulting from the fast reactive motion in S_1 [81]. The model was introduced in the framework of the Landau-Zener Theory for non-adiabatic transitions, and supported by the observation of vibrational coherence in the photoproduct since they are induced by the fast excited state reactive motion. With this picture in mind, we analyze here the results obtained on several NAIP representatives by systematically comparing the excited lifetimes (indicative of the photoreaction speed), the observation or not of vibrationally coherent reactive motion, and the photoreaction quantum yields. The results are summarized in table 4.3.

4.6.1. Excited State Life time (ESL) determination

The photoreactions of all IP compounds are either similar to the vibrationally coherent photoreaction, or to the so-called "non-coherent" behavior discussed above. While in the first case the photoreaction displays the rapid crossover from SE to PA characteristic of the passage of a vibrational wavepacket through the CI, a longer-lived SE decay (which is not followed by any >0, red-detuned PA signature) is observed for the second case, and is correctly fitted by exponential decaying functions as is expected for a vibrationally non-coherent photoreaction which would obey a rate-equation type of kinetics.

Because the kinetics are so different, the quantitative comparison of the excited state lifetimes is not straightforward. Indeed, when the signature of a vibrational wavepacket travelling through the CI is observed, the time at which the system passes through the conical intersection may be identified to the crossover time between SE and PA as it is observed experimentally in the red part of the visible spectrum [79] or in the near IR [15], and is thus considered as a measurement of the ESL. This estimate of the passage through the CI is readily comparable to the hoping time obtained theoretically with semi-classical trajectories computed along on-the-fly QM/MM potential energy surfaces. Instead, no such signature

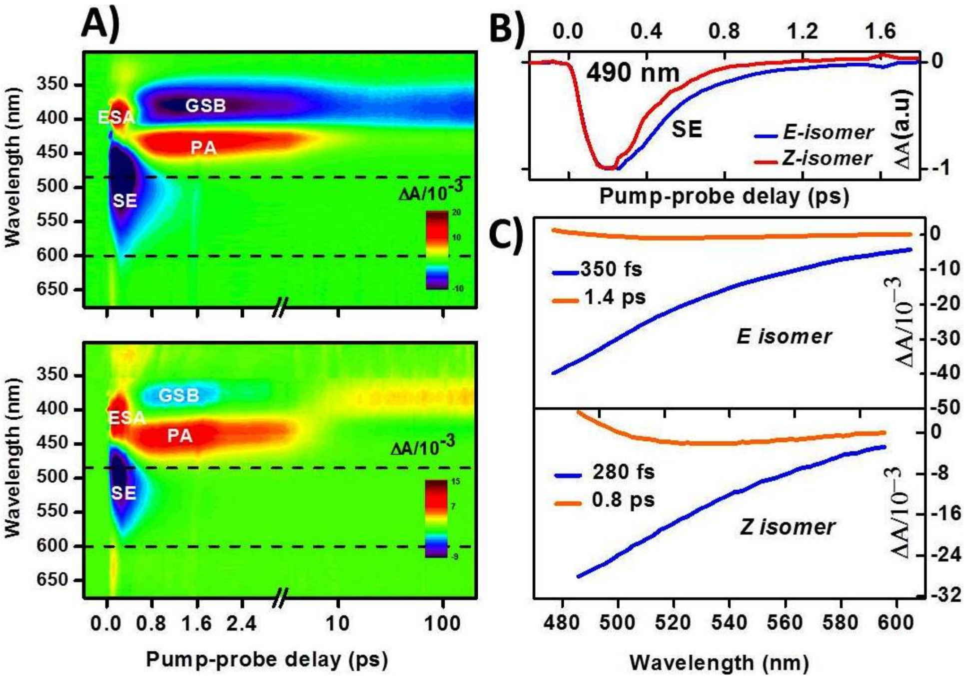

Figure 4.16.: A) Pump-induced absorption change ΔA as function of probe wavelength (in nm) and time delay (ps) between pump and probe pulses of (top) the *pure* E and (bottom) the pure Z isomers of dMe-MeO-NAIP in MeOH. B) Time evolution of the SE signal at 490 nm of both isomers. C) Decay Associated Spectra obtained after global optimization within th SE band of both isomers.

of a vibrational wavepacket is observed for the E-chiral molecules excited in the same conditions, and not either for the non-chiral dMe-MeO-NAIP [78]. What is more, the SE kinetic traces of the chiral compounds are nicely fitted by a biexponential decay. Interestingly, in the coherent molecules such a biphasic behavior may not be observed in the SE signal since the latter is rapidly followed by the PA signal which may overlap and mask a putative longer-lived SE compound. However, we notice that time resolved fluorescence (measured by the up-conversion technique) instead did reveal a biphasic fluorescence emission of the non-chiral MeO-NAIP ($<$ 40fs and $\sim$ 300fs [14]) and ZW-NAIP (140fs and 1 ps [15]) although on a much shorter time scale.

Therefore, for the vibrationally non-coherent photoreaction, due to the strong overlap between the ESA and the GSB signal (see Fig 4.16, a determination of the excited state lifetime may be obtained by performing global analyses withing the pure SE band which reflects the dynamics of populations on the excited state. For illustration, Figure 4.16 displays the results obtained by performed TAS on both isomers of dMe-MeO-NAIP molecular switch. The photodynamics observed here resemble very much that of Ch-dMe-MeO-NAIP (See Fig 4.16.A and .B). We perform quantitative analysis by fitting the SE band (485-600 nm) via a global optimization routine. Typical kinetic traces showing the temporal evolution of the SE at 490 nm for both isomers are shown in 4.16.C. Here, the photoreaction dynamics could be ajusted by a bi-exponential decay function. The Decay Assiociated Spectra (DAS) obtained from the global optimization are displayed in Fig 4.16.C for both dMe-MeO-NAIP isomers. We find a more dominant component which decay on time scale ranging from 350-280 fs and less dominant component which decay on the time scale ranging from 1.4-0.8 ps respectively for both *E*- and *Z*-isomer. The ESL is evaluated as the average time resulting to the bi-exponential decay along the SE band, determinated as a DAS weighted average of the decay time constant and the relative value of the amplitude. Thus the dynamics of all non-coherent compounds could be described like here, to estimate the ESL, see Table 4.3.

4.6.2. On the relation between photoreaction dynamics and quantum yield

Understanding the key parameters controling the dynamics and efficiency of isomerization reaction would enable designing efficient biomimetic molecular devices. The intra-molecular parameters, controlling the efficiency of the photoisomerization reaction is a relevant question. It has been argued that the high QY is a consequence of the high reaction speed [10]. In contrast, the recent investigation of a variety of backbone-substituted RPSB compounds in solution reveals an anti-correlation between the ESL and the QY [61].

We propose here to compare the isomerization quantum yield of all IPs molecules from the transient absorption in order to draw a relationship between the photoisomerization dynamics and the QY. The results of the photodynamics processes of the investigated compounds are reported in Figure 4.17.

To determine the absolute QY, we compare the QYs of compounds two by two by performing several TA experiments in a row on different IP compounds in methanol solutions of known absorbance at the pump wavelength, and keeping the exact same excitation conditions by following the procedure described in details in chapter 2. We finally scale all the obtained QY's to that of the *Z*-isomer of the MeO-NAIP, measured to be 0.21±0.03 by two independent experiments [13, 14]. The results are gathered in table 4.3.

The correlation between vibrationally-coherent reactive motion, photoisomerization quantum yield and the photoreaction speed or ESL in the IP biomimetic molecular family is systematically investigated. The IP undergo an isomerization reaction as fast as 0.2–1 ps depending on substitutions on either moiety

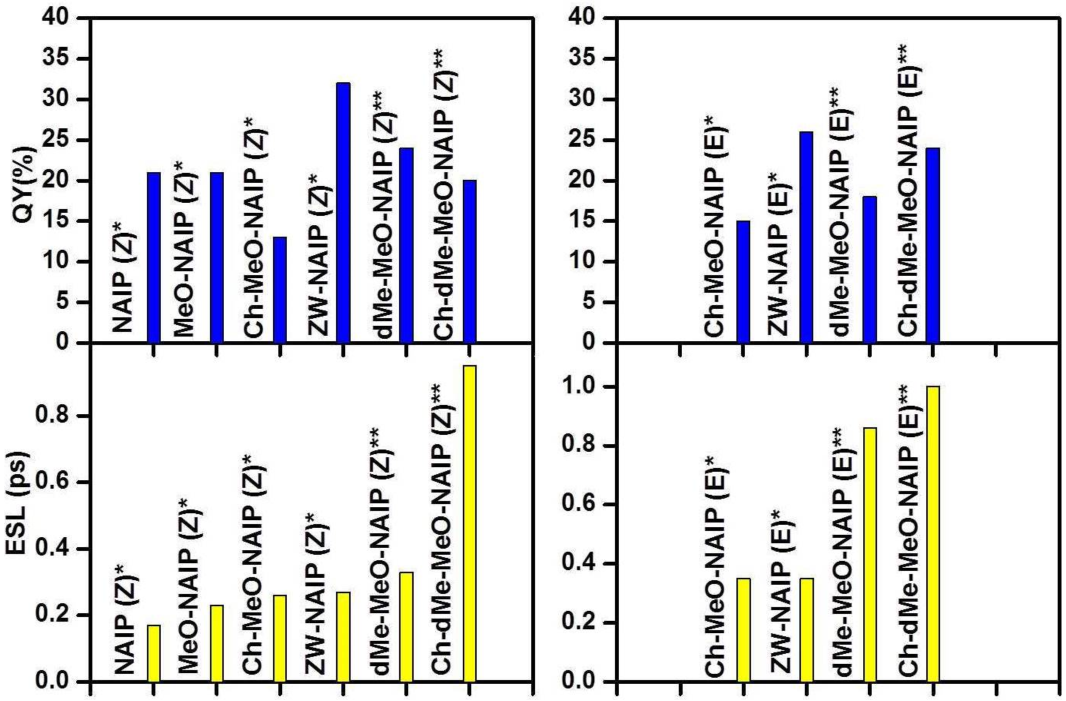

Figure 4.17.: Excited state lifetimes and isomerization QY of different NAIP isomers in MeOH. $*$ Coherent photoisomerization; $**$ incoherent. photoisomerization

across the central $C = C$ isomerizing bond, with quantum yields in the range of 0.15–0.35 significantly lower than that of rhodopsin (0.67). Comparing the isomerization dynamics and effiency of all IPs switches together, it appears that there is no correlation between the occurrence of vibrational coherences along the reactive motion and the photoisomerization QY (see Fig 4.17). Thus we are not able to draw general rules by which the excited state dynamics would control the photoisomerization QY in this set of compounds, unlike what was obseved for Rho and its mutants. Instead, we notice that the QY may also be influenced by further dynamics on the ground state potential soon after the decay through the CI as was suggested by recent theoretical developments including dynamic electron correlations in the computation of the ground state PES of a retinal model system [82].

Compound	SE/Fluo‡	ESL(fs)	QY($\pm$2%)	QY(Ref)
NAIP(Z)	–	170*	21	14-21
MeO-NAIP(*Z*)	40 fs(–) ; 300fs (–)	230*	21	21 [16]
MeO-NAIP(*E*)	–	260*	–	34 [13]
ZW-NAIP(*Z*)	140 fs (87%); 1ps (13%)	270*	32	35 [15]
ZW-NAIP(*E*)	–	350*	15	15 [62]
Ch-MeO-NAIP(*Z*)	–	260*	13	–
Ch-MeO-NAIP(*E*)	500fs (60%); 1.4 ps (40%)	860**	18	–
dMe-MeO-NAIP(*Z*)	280fs (90%); 0.8 ps (10%)	330**	24	–
dMe-MeO-NAIP (*E*)	340 fs (99%); 1.4 ps (1%)	350**	26	25 [78]
Ch-dMe-MeO-NAIP(*Z*)	590 fs(40%); 1.5 ps (60%)	950**	20	–
Ch-dMe-MeO-NAIP(*E*)	650 fs (40%); 1.7 ps (60%)	1000**	24	–

Table 4.3.: Comparison of the photoisomerization dynamics properties of IP compounds. ‡ biexponential fit of the SE in case of incoherent photoreactions or of the femtosecond fluorescence (up-conversion set-up) in the vibrationally coherent cases. * time at which the crossover between SE and Pa signature are observed in the red part of the visible spectrum (>650 nm). ** Average decay time from a bi-exponential fit of the SE signal in the cases of incoherent reactive motion.

4.7. Conclusion

Photoisomerization in molecular photoswitches is a key process which the light energy is converted into mechanical motion at molecular level, with fundamental questions to be further investigated, such as the parameters governing the dynamics, the efficiency or the vibrationally-coherent properties sometimes observed.

For this purpose, supplementary studies of the photoisomerization dynamics of new synthetic IP photoswitches has been achieved using a femtosecond transient absorption spectroscopy, in order to relate the keys process which govern such photoreaction.

The results shows that the IP switches display different spectro-temporal features depending to the structure of the molecules. Therefore two photoreactions scenario were observed and described as coherent or non-coherent photoisomerization. The first scenario concerns the molecules which shows faster, sub-200 fs isomerization times, with indications of vibrational coherence reactive motion on the S_1 PES (followed through the spectral and temporal shift of the ESA signal) toward the CI, measured to occur on the 170-260 fs time scale depending on the sample. The second specific signature is the observed SE spectrum extending far in the red and is followed by a spectrally very broad, far red detuned band attributed to the earliest signature of the PA absorption. The rapid crossover from SE to PA in the red part of the spectrum the signature of a vibrational wavepacket travelling through the conical intersection (CI). Finally, this impulsive signal leads to low frequency (sub-100 cm^{-1}) oscillations, reflecting wavepacket motion on the ground state PES as described in section 4.4.
The second scenario concerns the molecules which undergoes an mostly rate-equation-like, isomerization dynamics where instead the SE is much longer lived (still sub-1 ps time scale), comparatively narrow band, and is not followed by any red-detuned signature of the PA.

Together with the results of coherent-like molecule as the NAIP, the MeO-NAIP, the ZW-NAIP and the Ch-MeO-NAIP, the IP switches undergo a photoisomerization which a part of the absorbed photon energy is effectively funneled into specific low-frequency S_0 modes as already observed in the reference isomerization of retinal in Rho. However this effect is sensitive to the molecular structural ground state conformtion modulate by the presence of methyl group in C2' (chiral molecules) or in C5 (so-called "demethylated").
Deeper investigations to understand the photophysics of the IP familly is however necessary. Based on the same TAS configuration, coherence vibrational spectroscopy, using an impulsive excitation laser pulse whose duration is shorter than the periods of vibrational coherence reactive motion in both the excited and the ground state, can be a powerful direction to understand the dynamics of internal conversion through a CI like photoisomerization. To this end, this procedure is applied on two representatives IP molecules in the following chapter.

5. Vibrational Coherence Spectroscopy of Biomimetic Molecular Switches

5.1. Introduction

As described in detail in Chapter 4, during the ultrafast photoisomerization of the MeO-NAIP switch, low-frequency vibrational coherence in S_0 ground state have been detected after internal conversion through the CI as observed in Rho [10] and others IP switches [15]. State-of-art non-adiabatic trajectory modelling assigned the oscillatory signal to a low-frequency ring distortion triggered by the reactive motion on S_1 and futher observed after decay to S_0 in the photoproduct spectroscopic signature [16].

In this chapter, we present the first results of time-domain Raman spectroscopy obtained with the setup devolepped during this PhD work and described in Chapter 3.

In particular, by applying VCS to MeO-NAIP, wa are able to address experimentally the question whether, the low frequency vibrational coherence results from vibrationally-coherent reactive motion initiated in S_1 excited state and preserved through the CI, or wether the S_0 ground state vibrational coherence could have been produced impulsively by the pump in S_0, according the RISRS mechanism.

Upon Fourier transformation of the oscillatory residuals of the TAS signal obtained with the high temporal resolution with this setup, we recover the Raman spectrum of the ground state and of the transient, excited (Franck-Condon) state.

We investigate the vibrational dynamics of the parent MeO-NAIP and the "demethylated" dMe-MeO-NAIP where the methyl group on C5 is replaced by a hydrogen atom [78]. While dMe-MeO-NAIP does not exhibit the impulsive, red-detuned onset of the photoproduct absorption band as already described for MeO-NAIP [16], it does not either show the low-frequency vibrational mode already evidenced in the ground state of MeO-NAIP.

Time-domain Raman spectroscopy performed by impulsive vibrational coherence excitation revealed that the low-frequency vibrational coherence observed in the MeO-NAIP ground state (S_0) is not Raman active, but is observed only after populating the excited (S_1) state. This is the definitive proof for vibrationally-coherent photomechanical energy conversion in the synthetic IP compounds, a unique mechanism to be explored for molecular photoswitching applications.

Besides the major results, the data disclosed here reveal signature of many other vibrational modes, the assignement of which is still very preliminary and would require theoretical support, hopefully triggered by the present work.

5.2. Results

In order to probe the vibrational coherence on MeO-NAIP and dMe-MeO-NAIP, we excite both compounds with the 400 nm, 8 FL fs pump pulse and generate wavepackets in all Frank Condon (FC) active modes coupled to the optical transition. The generated S_0 ground state wavepacket oscillates around its equilibrium point, while in S_1 the wavepacket moves out from the FC region following the S_1 slope and thus modulates the excited state absorption spectra. (Figure 5.1).

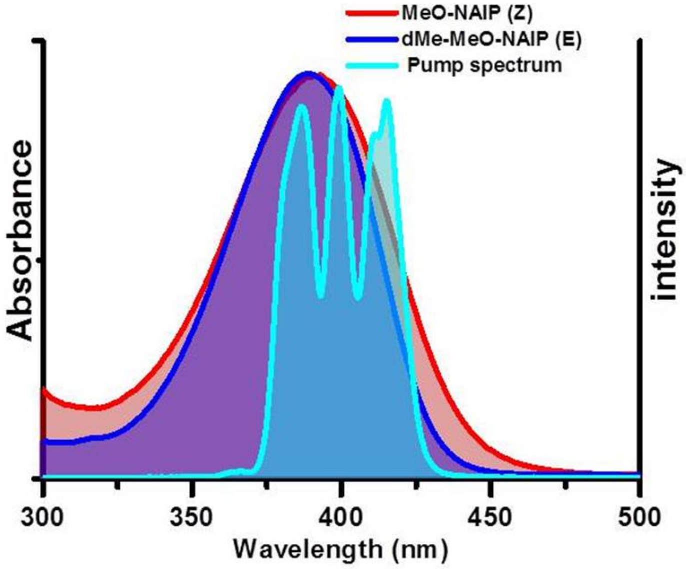

Figure 5.1.: Absorption spectrum of MeO-NAIP and dMe-MeO-NAIP together with the spectrum of the 8 fs excitation pulse.

5.2.1. Experimental evidence of vibrationally-coherent isomerization of MeO-NAIP

The results of VCS upon resonant excitation of MeO-NAIP in methanol are displayed in Figure 5.2.A. The corresponding TAS signal shows, after the coherent artifacts around time zero, the same electronic populations dynamics as already evidenced in Chapter 4, i.e. a red-shifting SE followed by the impulsive onset of the PA in the red part of the probing window ($>$ 600 nm), which blue shifts to the final absorption maximum at 444 nm. This is attributed to the signature of the electronic population decay driven by a vibrationally-coherent motion along the reaction coordinate through the S_1 to S_0 CI (see Chapter 4). As shown in Figure 5.2.B, large oscillations modulating the electonic signal are best seen in the blue (380 nm) and the red (446 nm) edges of the ground state absorption (392 nm), corresponding to the ground state vibrational wavepacket already identified (Chapter 4). As shown in Fig 5.2.C, we isolate the wavelength dependent vibrational coherence by globally-fitting the underlying electronic populations kinetics (see chapter 3), where we see a most pronounced vibrational activity in the 360-500 nm spectral region, close to the ground state absorptions of both reactant and photoproduct. The large oscillatory patterns of the vibrational coherence at 380 and 446 nm appear antiphased as already discussed (see Figure 5.2.D). Lower-amplitude oscillations are also now revealed.

The intensity distrubutions of all vibrational modes obtained by FFT of the residuals reveal high-frequency modes up to 1575 cm^{-1} (Figure 5.3.A). As displayed in Figure 5.3.B, the average of 370-500 nm spectral windows shows intense contributions in the low frequency region ($<$ 500 cm^{-1}), with the most dominant component at 73 cm^{-1} (corresponding to a period of 456 fs). The three dominating peaks in the 1000-1800 cm^{-1} frequency region have been observed by resonance Raman (RR) spectroscopy of MeO-NAIP [63]. These peaks are assigned to ground state vibrational modes activated by RISRS (see Chapter 4) and are the signatures of isomerizing $C = C$ double bond stretch mode at 1575 cm^{-1}, as well as the modes at 1411 and 1261 cm^{-1} attributed to the indanylidene moiety [63].

Notice that due to the very similar absorption spectra of both isomers (see Fig 5.3.A), the signature of the vibrational coherence of the photoproduct (E-isomer) “hot” ground states and of the reactant (Z-isomer) are overlapped. Hence, the spectral overlap of the spectroscpic signatures complicates the identification of modes $<$ 1000 cm^{-1} (which are the main goal in this work), where no RR spectra nor theoretical prediction have been reported so far.

VCS using a sub-6 fs pulse now centered at 800 nm and hence non-resonant

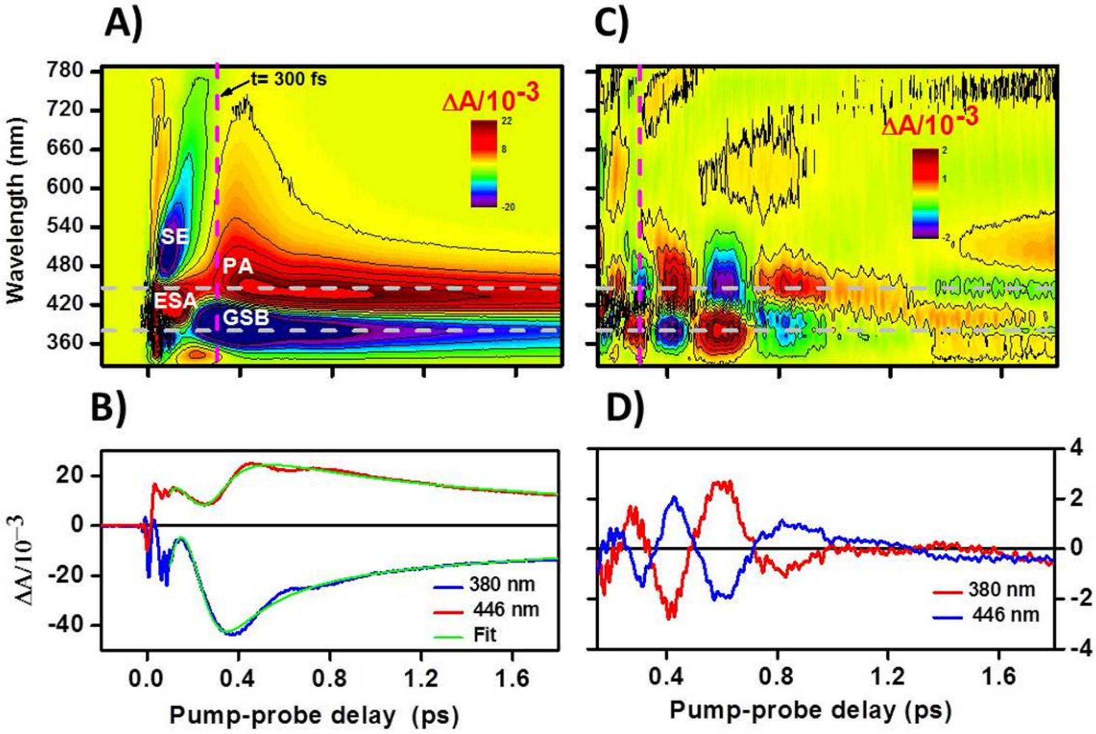

Figure 5.2.: Uv-Vis transient electronic and vibrational spectroscopy of MeO-NAIP after resonant excitation at 400 nm. A) ΔA 2D-map of MeO-NAIP exhibiting a coherent artifact at early time delay. B) Selected kinetic traces on the blue (380 nm, blue curve) and red (446 nm, red curve) sides of the S_0 MeO-NAIP absorption, together with their corresponding the electronic kinetics fit. C) Vibrational coherence 2D-map obtained after subtraction of the electronic part by global fitting the ΔA 2D-map. D) Cut at 380 and 446 nm showing the anti-phased oscillations associated to coherent vibrational motion in the ground state.

with the $S_0 - S_1$ transition, triggers exclusively ground state vibrational coherence in both methanol and the solute. This yields, the vibrational coherence activity shown in Figure 5.3.C. We perform an average of the 370-500 nm spectral region to reveal the ground state vibrational spectrum of the investigated sample (see orange curve in Fig 5.3.D). A comparison with the vibrational spectrum recorded under the same experimental conditions but on neat methanol is shown (see black curve in Fig 5.3.D). The coherence activity obtained under off-resonant experiment over the 370-500 nm spectral range (see Figure 5.3.D) is in agreement with the related ground state RR spectra of MeO-NAIP with the expected 1575 cm^{-1} $C = C$ isomerizing mode, as well as the mode at 1261

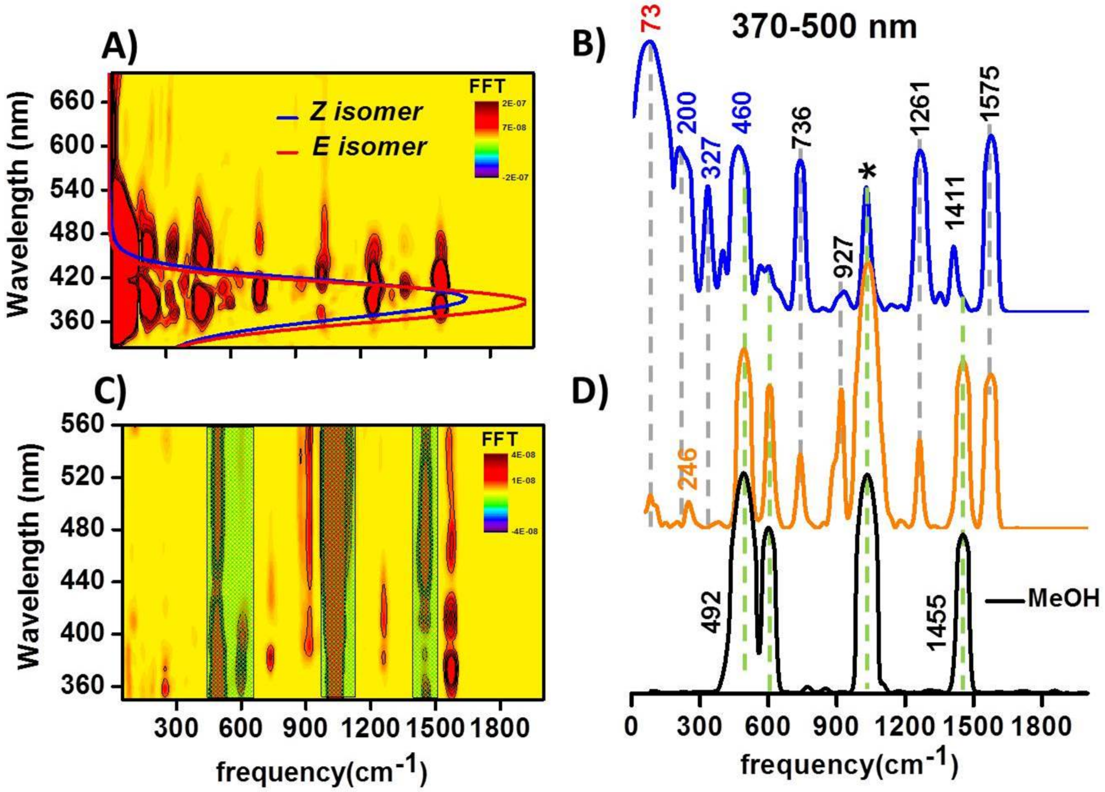

Figure 5.3.: Fourier transform 2D-map and vibrational spectra of MeO-NAIP under on and off resonance excitation plotted in semi-log scale. A) Vibrational mode 2D-maps following resonance excitation at 400 nm. B) Vibrational spectra obtained by spectral average from 370-500 nm GS spectral range (blue curve). C) Vibrational mode 2D-maps in methanol obtained under off-resonance excitation at 800 nm. D) Spectra obtained by averaging the 370-500 nm spectral region under off-resonant conditions for MeO-NAIP (orange curve) and for methanol (black curve). Peaks due to the solvent are denoted by asterisks.

cm^{-1}. The mode at 1411 is likely hidden by the MeOH mode at 1455 cm^{-1}. The modes at 246, 927, and 763 cm^{-1} also appear as vibrational signature of S_0, which have never been reported so far.

The major differences between the vibrational signatures of MeO-NAIP upon on- and off-resonant impulsive interaction actually appear below 500 cm^{-1}. Most strikingly, the prominent 73 cm^{-1} mode observed upon resonant excitation is clearly absent in off-resonant experiment. Comparing the results of on- and off-resonance experiments, allows us to determine which modes should be assigned to RISRS (i.e. those also abserved with the off-resonant 800 nm pulse) and which mode should be attributed to the photoreactive motion (either in S_1 or S_0 photoproduct). Upon resonant excitation, additional low-frequency mode are seen at 460, 327, 200 and 73 cm^{-1}. We may not exclude that the 460 cm^{-1} is present in the off-resonance vibrational spectrum but hidden by the intense 492 cm^{-1} MeOH mode. Thank to this comparison, we confirm that all the vibrational modes detected in the resonant spectrum below 500 cm^{-1} (327, 200 and 73 cm^{-1}) must be triggered in S_1 by the reactive motion.

While the 73 cm^{-1} was already cleary assigned to the photoproduct ground state, the electronic state origin of the 327 and 200 cm^{-1} modes remains to be determined. The question is whether the vibrational coherence activity of the modes is preserved upon internal conversion through a CI, in which case they are detected on the photoproduct ground state, or whether they are transient signatures of the S_1. To address this question, we truncate the vibrational coherence 2D-map at t = 300 fs to avoid the contribution of the excited state which decays at ~ 250 fs. Figure 5.4 compares the averaged Fourier intensity spectrum in the 370-500 nm spectral region to the one plotted in Fig 5.3.B, in the low frequency region, and reveals the signature at 460, 327 cm^{-1} but not the signature at 200 cm^{-1}. This means that the vibrational coherence activity of the latter initially generated in the S_1 excited state is lost upon crossing the

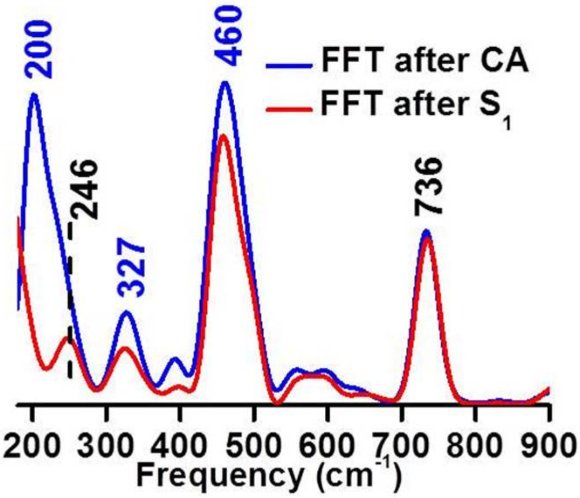

Figure 5.4.: Comparaison of Fourier spectra in low frquency region, obtained after the coherent artifacts (blue curve) and after (red curve) the decay of the excited state contribution. The 246 cm^{-1} is a ground state vibrational mode as shown in off-resonant experiment.

CI. However, the presence of the mode at 327 cm^{-1} (in addition to the expected mode at 73 cm^{-1}) after the decay suggests that vibrational coherence in multiple degrees of freedom is transferred from S_1, through the CI, into the S_0 ground state. This result definitively proves that coherent nuclear motion on the MeO-NAIP S_1 excited state is transferred to the S_0 ground state through the CI, in the so-called vibrationally-coherent photoisomerization as already observed in Rho.

5.2.2. Vibrational coherence spectroscopy of dMe-MeO-NAIP

The *E* dMe-MeO-NAIP compound has been identified as a so-called "non-coherent" molecular switch in chapter 4. The transient absorption 2-D map obtained after resonance photoexcitation of dMe-MeO-NAIP in methanol is shown in Figure 5.5.A. Coherent artifacts around time zero are observed followed by the spectroscopic signature of S_1 essentially composed of SE and ESA. The ESA spectrum almost perfectly overlaps the GSB which is thus non apparent at short time delays, but is detected as a weak negative signal between 350 and 400 nm at later time delays ($>$ 0.3 ps). Following the decay of the excited state contribution, the spectroscopic signature of the PA emerges in the 400-450 nm spectral range. Figure 5.5.C shows the isolated oscillations pattern 2-D map extracted from transient absorption data, by globally fitting the electronics dynamic (as illustrated in Fig 5.5.B for probe wavelength at 430 nm) of the populations. The vibrational coherent activity is most pronounced in the 350-500 nm spectral range, corresponding to *E* and *Z* ground state absorption spectra. As example cut at 430 nm (close to the photoproduct absorption band) shows oscillations which contain high and low-frequency components lasting for more than 1.8 ps (see fig 5.5.D).

Unlike with the MeO-NAIP, here the coherent activity in the visible range ($>$ 500 nm) corresponding to the excited state spectroscopic signature, is detected, in line with the longer excited lifetime of the dMe-MeO-NAIP. Instead the strong spectral overlap between the ESA and the ground state contributions (GSB and PA) in the UV, suggests that the UV vibrational coherence contains both S_0 and S_1 signatures, while in the visible, where the SE is well separated from the ground state contributions, vibrational coherence are dominated by the contribution of S_1.

FFT of the oscillatory compounds over the entire detection window leads to the 2-D maps in figure 5.6.A. Figure 5.6.B displays the vibrational spectrum integrated over the all 350-500 nm probe wavelength region (blue curve). First we note that, as already discussed in Chapter 4, the prominent 73 cm^{-1} mode

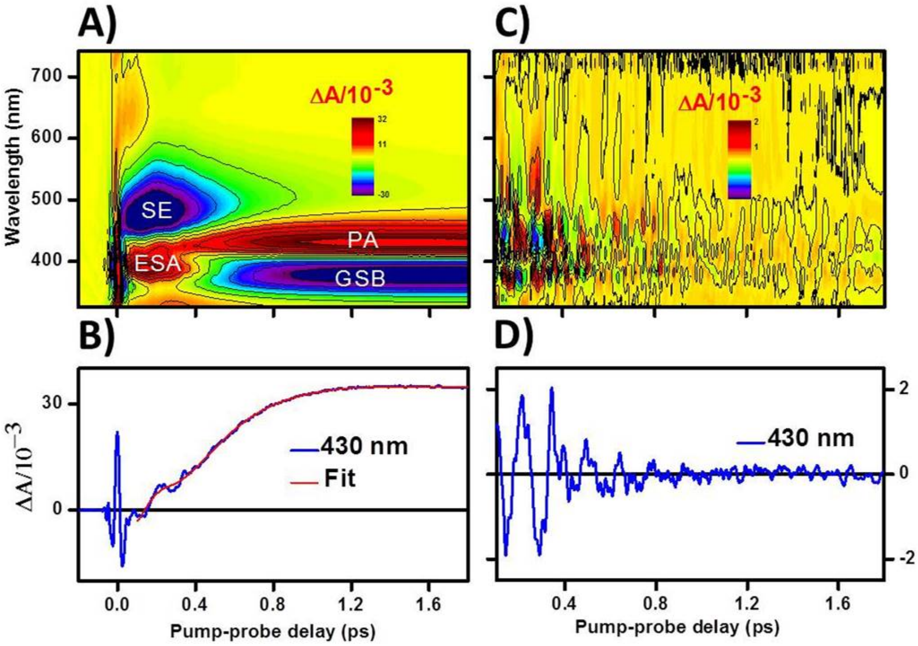

Figure 5.5.: Uv-Vis transient electronic and vibrational spectroscopy of dMe-MeO-NAIP after resonant excitation at 400 nm. A) ΔA 2D-map of dMe-MeO-NAIP exhibiting a coherent artifact at early time delay. B) Kinetics traces at 430 (witch illustrates the growth of the photoproduct absorption) plotted together with it corresponding fits (red curve). C) Vibrational coherence 2D-map obtained after subtraction of the electronic part by global fitting the ΔA 2D-map. D) Cut at 430 nm showing the vibrational coherence activity close to the PA absorption band.

observed in the parent MeO-NAIP switch is completely absent here. The high frequency peaks have been observed by RR on the MeO-NAIP and assigned to ground state vibrational modes. In addition the never-reported 736 cm^{-1} mode is also observed as in the MeO-NAIP.

Pronounced vibrational coherence activity is obseved in the visible region, mostly including low-frequency modes below 700 cm^{-1}, with a dominant mode at 227 cm^{-1}. The higher frequency ground state vibrational modes are absent from the spectrum. Averaging the 520-650 nm pure S_1 spectral region of the FFT maps (see the red curve in Fig 5.6.B) and comparing with the vibrational spectrum integrated in the UV region allows us to identify the vibrational activity originating from S_1. Although we are confident that these low-frequency vibrational modes detected in the visible arise from the excited state, the overlap between the ground and the excited state vibrational coherence complicate the identification of low frequency mode in the UV spectral region.

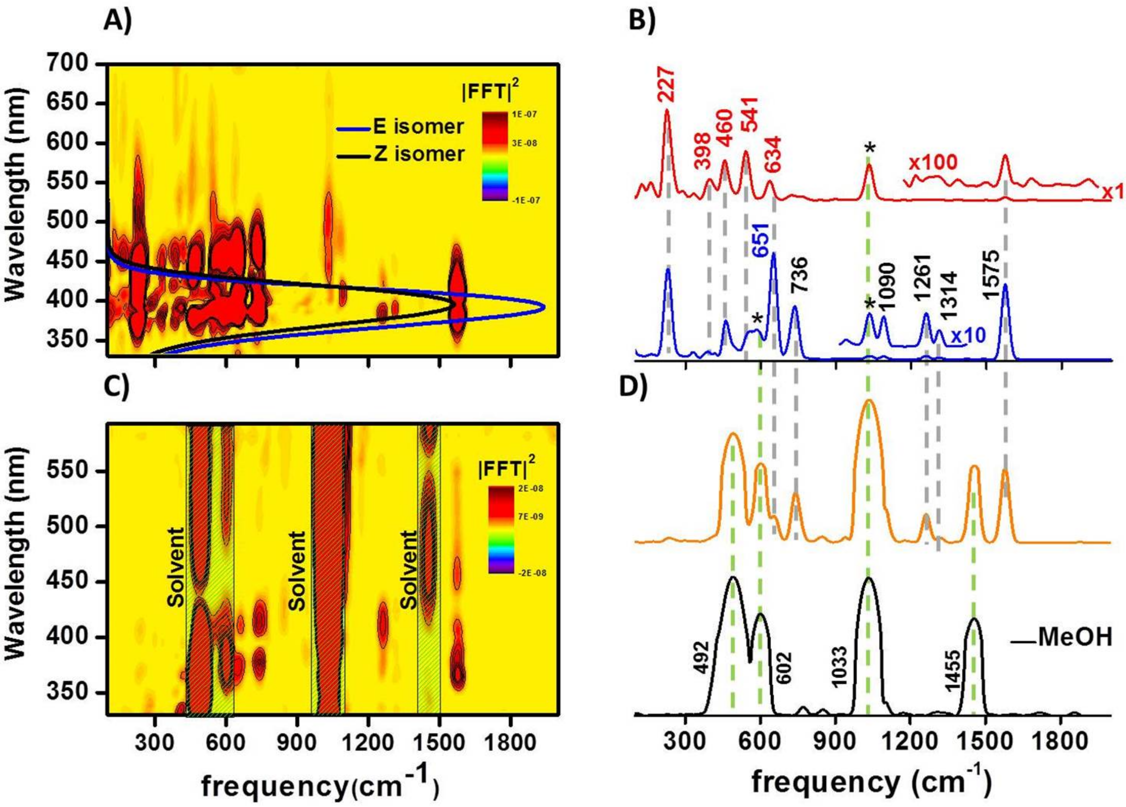

Figure 5.6.: Fourier transform 2D-map and vibrational spectra. A) Vibrational mode 2D-maps following resonance excitation at 400 nm for dMe-MeO-NAIP in methanol together with the corresponding isomers ground state (GS) absorbance. B) Vibrational spectra obtained by spectral average from 350-500 nm GS spectral range (blue curve) and from 520-650 nm pure SE spectral range (red curve). C) Vibrational mode 2D-maps for dMe-MeO-NAIP in methanol obtained under off-resonance excitation at 800nm. D) Spectra obtained by averaging the 350-500 nm spectral region under off-resonant conditions for the dMe-MeO-NAIP (orange curve) and for methanol (black). Peaks due to the MeOH are denoted by asterisks.

To rationalize the electronic state origin of the vibrational coherence, we also perform Off-resonance VCS measurement using the sub-6 fs pulse centered at 800 nm, in order to record specifically the reactant ground state vibrational spectrum as shown in Figure 5.6.C. By comparing the vibrational spectra obtained under off-resonance and on-resonance interaction, we find a good agreement between the high frequency region of both spectra which allows us to confirm that the

1575, 1314, 1261 and 736 cm^{-1} modes should be attributed to S_0 signatures. The 1090 cm^{-1} mode is likely hidden by the intense MeOH mode at 1033 cm^{-1} mode in the off-resonance experiment. We also note that the mode at 651 cm^{-1} (not seen in MeO-NAIP) is also present in the off-resonant experiment as a shoulder of the more pronounced 602 cm^{-1} mode of MeOH, and is therefore attributed to the reactant S_0.

Although we already argued in Chapter 4 that *E* dMe-MeO-NAIP photoisomerizes according to a "non-coherent" scenario, we have now the opportunity to try and investigate the fate of the S_1 vibrational coherence observed along the photoreaction. To that end, like for MeO-NAIP case, we perform FFT after different delays. The results is shown in Figure 5.7. While the 651 and 736 cm^{-1} already assigned to S_0 still detectable after 1 ps, the amplitude of the 227 cm^{-1} mode decays much slower, on the 0.5 ps time scale in line with the 350 fs ESL of *E*-dMe-MeO-NAIP (see table 4.3 in Chapter 4). We conclude that the 227 cm^{-1} vibrational coherence is lost upon decay to S_0 through th CI, likefor the 200 cm^{-1} mode of MeO-NAIP. The weaked vibrational activity in the

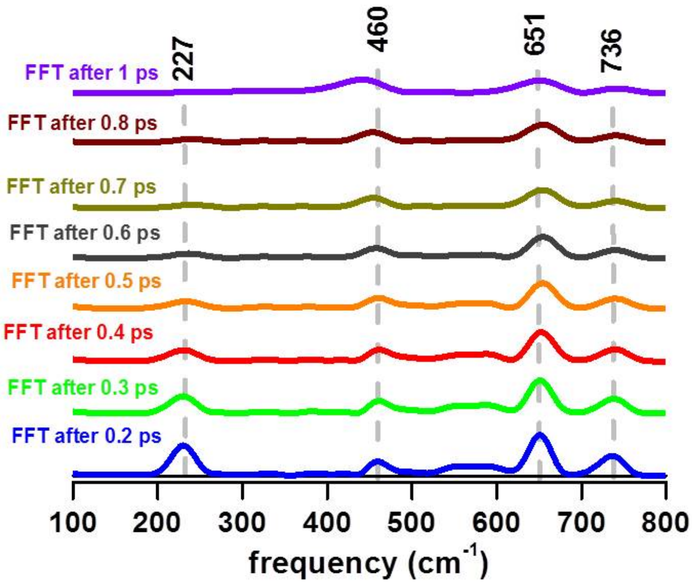

Figure 5.7.: Comparaison of vibrational spectra in the low-frequency region obtained by performing FFT after different delay for the dMe-MeO-NAIP. These spectra are obtained by averaging over the 350-500 nm spectral region.

530-600 cm^{-1} range also disappear upon decay to S_0. The 460 cm^{-1} mode also seen in MeO-NAIP seem to survive longer, in both compounds. As discussed in the case of MeO-NAIP, we cannot exclude that this mode is a signature of S_0 (hidden by the MeOH mode at 492 cm^{-1} in the off-resonance experiment) and would therefore undergoes decoherence on a time scale similar to the 651 and 736 cm^{-1} modes. The fact that the 460 cm^{-1} mode is also observed in the SE band would mean that both S_0 and S_1 state could display the same 460 cm^{-1} mode. Thus, the results plotted in Fig 5.7, suggests that, due to the long excited state lifetime (reflecting the motion from the FC toward the CI), the coherence activity of the low-frequency S_1 vibrational modes are lost upon decay to the ground state through the CI, in line with the non-coherent isomerization scenario already discussed for dMe-MeO-NAIP.

5.3. Discussion

Upon photoexcitation with femtosecond laser pulses, oscillatory signals attributed to vibrational coherence are easily created in ultrafast isomerizing molecular systems both in the excited as well as in the ground state. In most cases, ground state vibrational coherence results from RISRS. In retinal, vibrational coherence in the range of 500-1600 cm^{-1} were observed and assigned to originate from the electronic ground state [30]. In the case of rhodopsin, the 60 cm^{-1} vibratonal mode (corresponding to a vibrational period of 555 fs) observed in the photoproduct all-trans electronic state was not reported to be Raman active, but associated with backbone torsion mode involved in the reaction coordinate [10, 83]. The MeO-NAIP switch displays the same ground and excited electronic structure as the 11-cis retinal in Rho. Similarly, we conclude that by comparing on- and off-resonance measurement, the low frequency oscillations observed in the MeO-NAIP ground state after internal conversion through the CI are not produced by RISRS, but arise from the signature of a wave packet initially created in the excited state, which survives in the photoproduct after crossing the CI, in so called coherent photoisomerization.
The vibrational coherences transfer from the excited to the photoproduct state, during the primary visual event has been investigated previously by Kukura *et al* [83]. The difference between the coherence activity upon internal conversion and the RR spectrum provide informations about the CI topology. Indeed in Rho the separation of both reactant and photoproduct absorptions help the identification of the ground, excited and photoproduct vibrational modes, unlike in MeO-NAIP where the absorptions of both isomers are overlapped.

By comparing the vibrational spectra obtained in the resonant and non-resonant experiments of MeO-NAIP, we classify the coherent activities into three categories: those that, initially populated in S_1, survive after crossing the CI (73 and 327 cm^{-1}), those that lost their coherence activities upon internal conversion (200 cm^{-1}) and those are present both in the resonant and non-resonant Raman spectrum (736-1575 cm^{-1}), assigned to S_0 reactant and or photoproduct vibrational modes.

For the low frequency vibrational modes such as the 73 cm^{-1} (vibrational period of 456 fs) previously attributed to ring deformations in the electronic photoproduct ground state, the excited state lifetime ($\sim$ 250 fs) being shorter than the decoherence time scale, rapid crossing through the CI projects impulsively the low-frequency wave packet in the ground state, leading to large nuclear motion on the photoproduct PES.

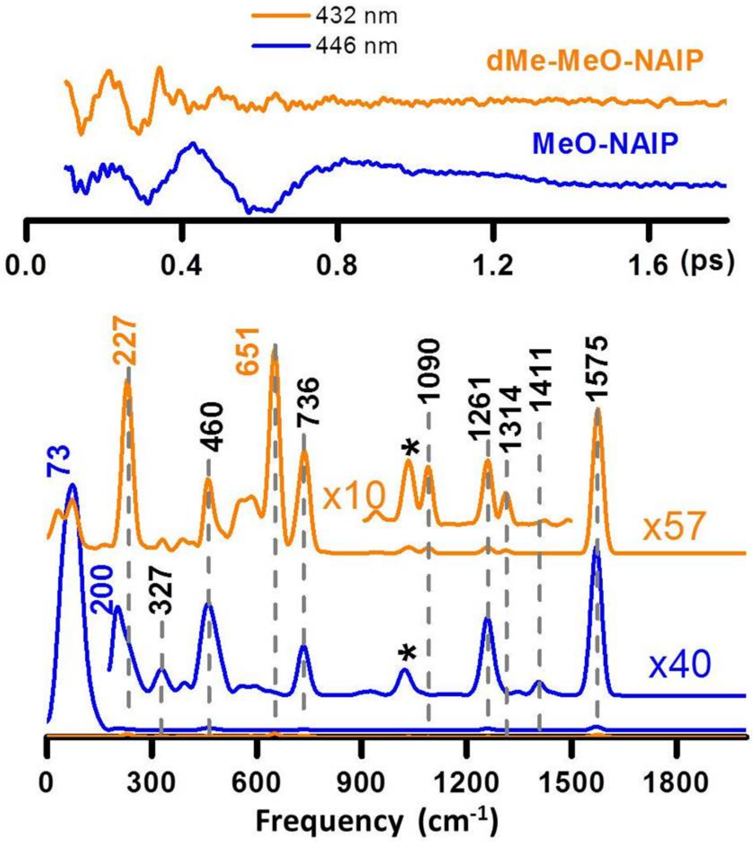

Figure 5.8.: Comparison of vibrational signature of MeO-NAIP and dMe-MeO-NAIP: A) Vibrational coherence close to the PA for both molecules. B) Corresponding Fourier intensity spectra for the MeO-NAIP (blue curve) and for the dMe-MeO-NAIP (orange curve)

In addition, we compare the vibrational dynamics of the parent MeO-NAIP and the dMe-MeO-NAIP. The results reported above show that the dMe-MeO-NAIP displays a vibrational dynamics different from that the parent MeO-NAIP. As shown in Figure 5.8.A, the vibrational coherence activities close to the PA absorption reveal similar high frequency modes ($> 1200\ cm^{-1}$) in both compounds. The major differences between the vibrational signatures of both compounds upon resonant impulsive excitation actually appear below 700 cm^{-1} (see Fig 5.8.B). Most strikingly, the prominent low-frequency oscillation observed in MeO-NAIP corresponds to the sub-73 cm^{-1} vibrational mode previously attributed to ring deformations in the electronic photoproduct ground state. This mode is clearly absent in dMe-MeO-NAIP. The 227 cm^{-1} mode was attributed to excited state vibrational coherence which does not survive by crossing the CI. This mode corresponds to the same mode observed in Ch-dMe-MeO-NAIP observed with the 70 fs time resolution TAS in Chapter 4.

These results provide strong support to previous theoretical investigations of similar molecules, including retinal in Rho, which do predict that optical excitation initially triggers $C = C$ stretch relaxation which acquires a single bound character thus enabling torsion [14, 7, 69]. We note here that in Rho, the phase of the high frequency ($\sim 900\ cm^{-1}$) hydrogen-out-of-plane (HOOP) modes have been predicted to control the branching ratio between reactant and photoproduct at the conical intersection [84]. In the IP switches, no such HOOP mode exists since both carbons involved in the isomerizing $C = C$ double bond are connected to two other carbon atoms of the rings. We propose that low-frequency ring deformations instead could play a role similar to that of the HOOP modes in Rho at controlling photoisomerization yield in IP biomimetic molecular switches.

5.4. Conclusion

We have performed VCS by combining on- and off-resonant light interaction to investigate the coherent nuclear motion along photoisomerization through the CI on the IP molecular switches. When comparing the coherence spectrum obtained upon on- and off-resonant excitation, we shows that the parent MeO-NAIP molecule isomerizes in a vibrationally-coherent regime with observation of low frequency vibrational modes according to a coherent motion first on the excited state, then in the ground state through the CI. This behavior is in line to that observed during the photoisomerization of the retinal chromophore in Rho. The major difference between the coherence activity of the MeO-NAIP and the “demethylated” dMe-MeO-NAIP upon resonant impulsive excitation (where the methyl group on C5 is replaced by a hydrogen atom) appear in the low frequency range where the 73 cm^{-1} mode previously attributed to the photoproduct ground state of MeO-NAIP is clearly absent for the dMe-MeO-NAIP. While in MeO-NAIP there is indication of vibrational coherence transfer from S_1 to S_0, there is no such indication in dMe-MeO-NAIP where S_1 vibrational coherence does not seem to survive the CI.

This work should motivate further theoritical work to assign the observed modes and possibly validate their contribution at controlling the photoreactivity and quantum yield.

Part IV.

toward triggering biological functions by steric constraints

6. Peptide Conformation Photocontrol With a Retinal-Like Molecular Switch

Photocontrolling peptides conformations and therefore biological functions requires efficient photoswitches and substantial conformational change to drive functional changes in a biomolecule. Several works have been reported on how ultrafast photoisomerization of a molecular switch triggers structural dynamics and ultimately conformational change of model peptides appropriately linked to the switch [85, 86, 87]. With this aim, we present in this chapter an experimental and computational study, in collaboration with the theoretician team of D. Sampedro (Universidad de la Rioja, Spain.) to analyze how the photochemistry of a molecular switch changes when it is covalently linked to a peptide as compared to unbound in solution.
We focus here on a recently reported, retinal-like molecular switch linked to alpha-helical peptide [87]. We perform transient absorption spectroscopy as a function of temperature, and use molecular dynamics and hybrid quantum mechanics/molecular mechanics (QM/MM) methods to rationalize the effect of the peptide on the photoreaction by comparing the photoisomerization dynamics and mechanisms of the molecular switch free in solution or covalently bound to the peptide. We observe that the peptide-linked switch in water exhibits a bi-exponential decay of the excited-state compared with the mono-exponential one found for the free switch in methanol (MeOH). This is explained in terms of heterogeneity of the ground state structure as found by molecular dynamics, which in turn leads to different excited state energy barriers along the photoisomerization pathway, as calculated by ab initio multiconfigurational QM/MM methods for representative peptide structures.

This work is the subject of an article published in the Physical Chemistry Chemical Physics Journal (PCCP) and presented below. All the transient absorption spectroscopy results presented here were obtained by me at IPCMS, and i performed the corresponding data analysis.

PCCP

PAPER

View Article Online
View Journal | View Issue

Cite this: *Phys. Chem. Chem. Phys.*, 2016, **18**, 6742

A biomimetic molecular switch at work: coupling photoisomerization dynamics to peptide structural rearrangement†

Cristina García-Iriepa,[ab] Moussa Gueye,[c] Jérémie Léonard,*[c] David Martínez-López,[a] Pedro J. Campos,[a] Luis Manuel Frutos,[b] Diego Sampedro*[a] and Marco Marazzi‡*[d]

Received 9th December 2015,
Accepted 3rd February 2016

DOI: 10.1039/c5cp07599h

www.rsc.org/pccp

In spite of considerable interest in the design of molecular switches towards photo-controllable (bio)materials, few studies focused on the major influence of the surrounding environment on the switch photoreactivities. We present a combined experimental and computational study of a retinal-like molecular switch linked to a peptide, elucidating the effects on the photoreactivity and on the α-helix secondary structure. Temperature-dependent, femtosecond UV-vis transient absorption spectroscopy and high-level hybrid quantum mechanics/molecular mechanics methods were applied to describe the photoisomerization process and the subsequent peptide rearrangement. It was found that the conformational heterogeneity of the ground state peptide controls the excited state potential energy surface and the thermally activated population decay. Still, a reversible α-helix to α-hairpin conformational change is predicted, paving the way for a fine photocontrol of different secondary structure elements, hence (bio)molecular functions, using retinal-inspired molecular switches.

Introduction

Molecular machines, such as switches and motors, are becoming essential components for biochemistry and materials science.[1,2] This prompts the synthesis and characterization of a great variety of derivatives to tailor their properties for specific applications. Among them, molecular switches (especially when photoactive) are the most studied devices due to their simple mechanism and immense applications.[3]

Therefore, the photophysics and photochemistry of the most known photoactive molecular switches have been extensively investigated,[4] and their efficient application and inclusion into real systems is the next step, which is now an emerging and challenging task. One of the most important fields where photoswitches are being applied is biochemistry, in terms of the photomodulation of biological properties.[5–7] Azobenzenes are the largest family of switches used for the control of biomolecules. They have been incorporated into nucleic acids, receptors, channels, peptides, *etc.*[8–10] Stilbenes,[11–13] hemithioindigos[14,15] and the retinal protonated Schiff base (PSB) derived chromophores[16–18] have been used in similar applications but to a lower extent.

The ability of molecular photoswitches to control the structure by using a convenient external stimulus allows us to envisage fascinating applications in which the function of complex systems could be easily turned on and off. Attractive targets for this approach are proteins and peptides. In these compounds, the function and the structure are strongly linked and they mediate in a huge number of biologically relevant processes. From enzymatic catalysis to ligand recognition, proteins are involved in diverse physiological actions.[19] Also, a good number of diseases (Parkinson's and Alzheimer's diseases, among others) are linked to structural changes in proteins.[20,21] In this regard, different model peptides cross-linked with azobenzene have been studied by circular dichroism or IR spectroscopies together with molecular dynamics (MD) simulations to understand the peptide conformational change after photoisomerization.[22–27] Recently, the first example of a retinal-like switch linked to a peptide has

---

[a] *Departamento de Química, Centro de Investigación en Síntesis Química (CISQ), Universidad de La Rioja, Madre de Dios 53, E-26006 Logroño, Spain. E-mail: diego.sampedro@unirioja.es*
[b] *Unidad Docente de Química Física, Universidad de Alcalá, E-28871 Alcalá de Henares, Madrid, Spain*
[c] *Institut de Physique et Chimie des Matériaux de Strasbourg & Labex NIE, Université de Strasbourg, CNRS UMR 7504, 23 rue du Loess, Strasbourg 67034, France. E-mail: leonard@ipcms.u-strasbg.fr*
[d] *Department of Theoretical Chemical Biology, Institute of Physical Chemistry, KIT, Kaiserstrasse 12, 76131 Karlsruhe, Germany. E-mail: marco.marazzi@univ-lorraine.fr*

† Electronic supplementary information (ESI) available: Computational details; MD analysis; details about the simulated absorption spectra; additional MEPs, including CASPT2 single-point energy corrections; Cartesian coordinates of the most relevant structures. See DOI: 10.1039/c5cp07599h

‡ Present address: Théorie-Modélisation-Simulation, Université de Lorraine – Nancy, SRSMC & CNRS, Boulevard des Aiguillettes, Vandoeuvre-lès-Nancy, France.

been reported. The photoisomerization of the switch causes a large change in its end-to-end distance, which in turn modifies the peptide secondary structure.[17] The advantages of this type of switch for that application are its high photoisomerization quantum yield,[17,28] photostability[29] and large end-to-end distance change.[17]

Using this approach, it could be possible to modify to a great extent the secondary structure (and consequently the function) of any given peptide or protein. While the α-helix is the most abundant structure in proteins, its formation is strongly dependent on the number and types of aminoacids, the solvent and the presence of ions in solution. From the Zimm–Bragg model[30] to the work of Baldwin *et al.*[31–33] much effort has been made in the last few decades to learn how the proteins achieve their secondary structure both from the theoretical and experimental points of view. In those studies, the content of the α-helix is determined by the intrinsic properties of the proteins (sequence of amino acids). Alternatively, this helicity could also be altered by an external stimulus such as light. For instance, the dynamics of helix formation was studied after the photolysis of disulfide bridges.[34,35] However, while this contributes to a deeper understanding of the folding process, it lacks the ability to control it.

Moreover, few studies focus on how the photochemistry of the switch itself is affected upon linkage to the peptide. Yet this is a very fundamental question towards effective molecular function switching, especially when using PSBs, since the linkage of the switch may strongly affect its photoreactivity, as exemplified *e.g.* by the very different photoreaction of retinal in rhodopsins as compared to a homogeneous solvent.[36–40]

Here, we report on a combined experimental and computational study of the photoisomerization dynamics of a protonated retinal-like molecular switch covalently linked to a recently reported[17] α-helical peptide. We disclose a detailed comparative study of the molecular switch photochemistry linked to the peptide with respect to a homogeneous solvent environment. Moreover, we analyze the structural modification of the cross-linked peptide from an α-helix to an α-hairpin upon photoisomerization. The model system is illustrated in Fig. 1.

tert-Butyloxycarbonyl (BOC) protected (*E*)-4-(4-(4-aminobenzylidene)-3,4-dihydro-2*H*-pyrrol-5-yl)aniline is the molecular photoswitch investigated both in solution, compound ***E*-1**, and linked to the peptide, forming compound **2**. The peptide is a Marqusee and Baldwin type of peptide, with a high content of alanine residues favoring an α-helical structure.[31,32] By implementing UV-vis transient absorption spectroscopy, MD and hybrid quantum mechanics/molecular mechanics (QM/MM) methods, we show that photoisomerization occurs through a conical intersection after thermal activation over an excited-state (S_1) potential energy barrier for both compounds, with very similar time-resolved spectral signatures. While the S_1 decay kinetics is monoexponential for compound **1** (*i.e.* homogeneous solvent environment), it appears multiexponential for compound **2**, due to the structural heterogeneity of the cross-linked peptide. We conclude that the main influence of the peptide linkage on the photoreactivity of the switch is the increase in the S_1 energy barrier to a magnitude that depends on the ground state (S_0) conformation of the cross-linked peptide. We are able to rationalize the effect of the peptide linkage on switch photoisomerization, and propose the underlying mechanism, including the subsequent effect on the peptide conformation.

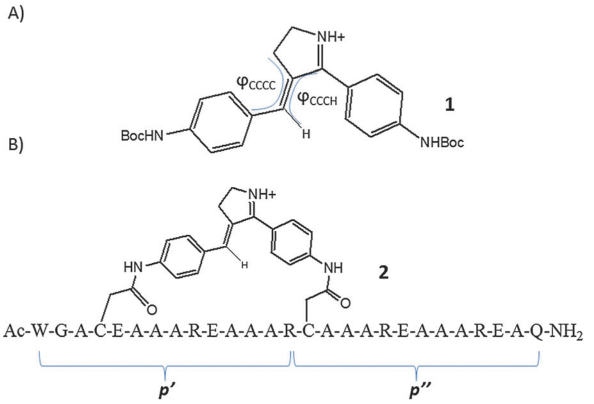

Fig. 1 (A) Structure of compound ***E*-1**, studied in MeOH. The dihedral angles φ_{CCCC} and φ_{CCCH} are introduced to describe the photoreactive motion of the switch. (B) Compound ***E*-2**, studied in water. The switch is linked to the cysteine residues of the peptide. The two halves of the peptide are labeled ***p′*** and ***p″*** as illustrated.

Methods

Experimental techniques

Compounds **1** and **2** were synthesized and purified as previously reported.[17] Transient absorption spectroscopy (TAS) is performed with a 400 nm pump pulse, and reveals the time evolution of the pump-induced absorption changes in the UV-VIS spectral range, with a 70 fs time resolution, at temperatures of 10 °C, 24 °C and 50 °C. The experimental set-up and data analysis by global fitting (assuming multiexponential kinetics) have been described previously[41] and are briefly recalled in the ESI.†

Computational strategy

A multi-scaling approach was adopted, considering the different tasks to be performed: classical MD was employed for the peptide conformational study, while hybrid QM/MM methods were applied to calculate photophysical and photochemical properties related to electronic absorption and photoswitching mechanisms.

Peptide conformations were evaluated by MD simulations (10 MD simulations of 50 ns (100 ns for ***Z*-2**)) where the peptide was represented by the AMBER99SB force field[42] and the molecular switch by the generalized AMBER force field (GAFF,[43] see the details in the ESI†).

The electronic vertical transitions were calculated for the optimized ***E*-1** and 50 MD snapshots of ***E*-2** and ***Z*-2** at the (TD-)DFT/MM level of theory, calibrated with the MS-CASPT2//SA-2-CASSCF/MM level of theory.[44] In all models, the photoswitch was included in the QM region, resulting in an active space of 12 electrons in 12 orbitals. *E*-to-*Z* minimum energy paths (MEPs) were calculated on S_1 at the SA-2-CASSCF level of theory and single point MS-CASPT2 corrections were performed along with them to quantitatively determine vibrational excess energies and excited state energy barriers. Moreover, on-the-fly non-adiabatic molecular dynamics were computed[45] at the CASSCF/MM level from the Franck–Condon point and from the S_1 transition state (see ESI† for details).

All MD trajectories were simulated using Gromacs 4.6;[46] MM parameters for the photoswitch were generated using the Antechamber program as part of AmberTools14.[47] MS-CASPT2//SA-2-CASSCF/MM calculations were performed using the Molcas 8 program[48] interfaced to Tinker 6.3.2,[49] TD-DFT/MM calculations were run with the M062X functional[50] using the Gaussian 09[51]/Tinker 4.2 interface, while MP2/MM calculations were performed using the Gaussian 09 ONIOM method.[52] The 6-31G(d) basis set was employed in all CASSCF and CASPT2 calculations, while the 6-311+G(d,p) basis was used for TD-DFT calculations.

Experimental results

When freshly dissolved in MeOH in the dark at room temperature, compound **1** is in the pure *E* isomer form (***E*-1**).[17] The *Z* isomer may be accumulated by illumination at 400 nm. Fig. 2A displays the steady state absorption spectra of the dark and illuminated samples in acidic (HCl in excess) MeOH solution. A buffer solution was used in all the experiments to ensure the protonated nature of the retinal-like switches. This allows for the use of visible light to activate the switch, as we have previously described.[17] The UV-vis steady state absorption of ***E*-2** in 2-(*N*-morpholino)ethanesulfonic acid (MES) buffer solution at pH = 4.3 is displayed in Fig. 2B. Irradiating the ***E*-2** solution at 400 nm yields a photo-stationary state (PSS) which was reported to be a 93/7 *Z*/*E* isomer mixture.[17]

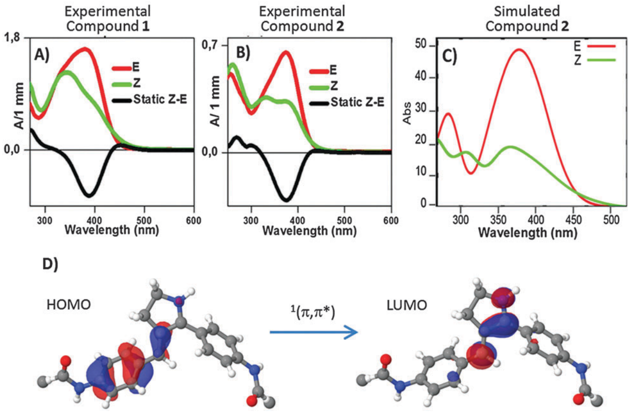

Fig. 2 Absorption spectra of (A) ***E*-1** (red line) and ***Z*-1** (green line) in acidic MeOH and (B) ***E*-2** (red line) and ***Z*-2** (green line) in buffer solution at pH = 4.3. The *Z*–*E* difference spectra (black curves) are useful for the interpretation of transient absorption data below. (C) Simulated absorption spectra of the protonated ***E*-2** and ***Z*-2** in water at the TD-DFT/MM level of theory. (D) Molecular orbitals involved in the $S_0 \rightarrow S_1$ electronic transition, showing the charge transfer character along the backbone.

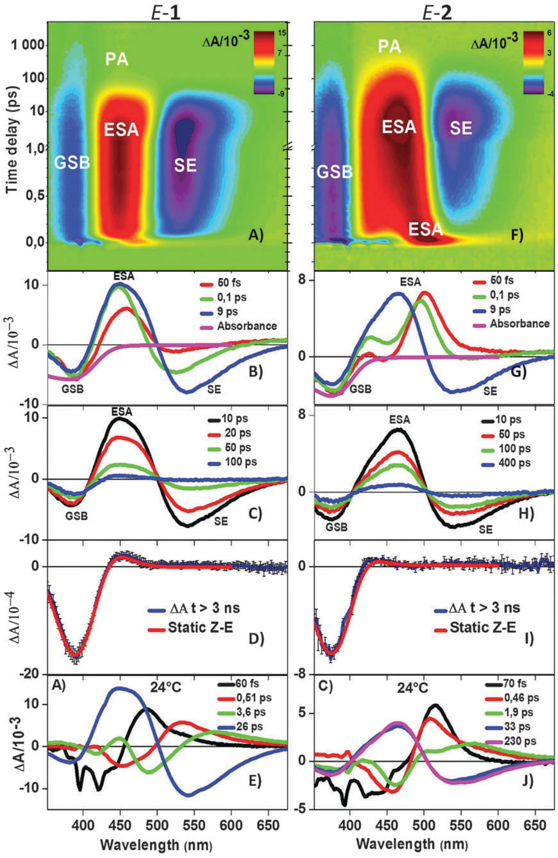

Fig. 3 (A and F) Room-temperature (24 °C) 2D transient absorption data (Δ*A* in color code) as a function of wavelength (nm) and pump–probe time delay (ps) for the dark-adapted solutions of ***E*-1** in acidic MeOH and ***E*-2** in aqueous buffer solution at pH = 4.3, respectively. (B and G) Transient spectra at early time delays (S_1 relaxation kinetics): the magenta curves are the opposite of the steady-state absorbance, proportional to the pure GSB signature. (C and H) Transient spectra at intermediate time delays (S_1 decay). (D and I) Quasi-static spectra obtained at a time delay >3 ns (blue) overlapped with the *Z*–*E* steady-state difference spectra (red). (E and J) Decay-Associated Spectra (DAS) obtained by global analysis of the 24 °C TAS data.

Fig. 3 compares the transient absorption changes (*i.e.* differential absorption Δ*A*) of compounds ***E*-1** and ***E*-2** under acidic conditions after excitation at 400 nm and at 24 °C (see the experimental details in the ESI†). In the Δ*A* 2D-maps (Fig. 3A and F) negative Δ*A*, coded in blue, is due to the ground state bleach (GSB) or stimulated emission (SE), while positive, red-coded Δ*A* represents the excited-state absorption (ESA) or photoproduct absorption (PA) bands. Both compounds display similar TAS spectral signatures dominated by several 10- to 100 ps- long-lived GSB at wavelengths <410 nm, ESA from ∼415 nm to ∼500 nm, and SE from ∼500 nm to >600 nm. Noticeably, at very early times the ESA signatures appear to be red-shifted, especially in ***E*-2** where it is seen to extend until >600 nm and where the initial negative signal at around 440 nm is attributed to an initially blue-shifted stimulated emission (see the spectrum at 50 fs in Fig. 3G). Fast spectral relaxation characterized by the concomitant blue shift of the ESA and/or red shift of the SE occurs on the 100 fs time scale in both molecules, although it is more pronounced in ***E*-2** (see Fig. 3B and G). This is indicative of reactive motion out of the Franck–Condon (FC) region on this time scale. A further rise or a red-shift of the SE band occurs within several ps in both compounds and is accompanied by the ESA blue shift on the same time scale in the case of ***E*-2**. This may be attributed to further structural molecular and (polar) solvent relaxation and thermalization in S_1. Subsequently, all TA signatures decay with no further change in the spectral shapes within a few 10 ps for ***E*-1** and a few 100 ps for ***E*-2** (Fig. 3C and H), indicative of the decay to the ground state (S_0) on these time scales. After complete spectral relaxation over the ns time scale, a quasi-static spectrum is observed for both compounds (see Fig. 3D and I), which overlaps perfectly with the *Z*–*E* steady state difference spectra, evidencing the formation of the *Z* isomer in both cases. Possibly, the *Z* isomers are formed earlier, presumably upon decay to S_0, but their final thermally relaxed forms characterized by the steady-state difference spectra are observed only after complete vibrational relaxation and thermalization.

When changing the temperature from 24 °C to 10 °C or 50 °C, similar TAS signals are observed, but kinetics time scales change. The results of the global analysis (see ESI†) are disclosed in the form of decay-associated spectra (DAS) displayed in Fig. 3E and J for both compounds at 24 °C and in Fig. S1 (see ESI†) at 10 °C and 50 °C. Table 1 summarizes all time constants revealed by the global analysis for both compounds, as a function of temperature.

For both compounds at any temperature, the DAS corresponding to the shortest 3 time constants (black, red and green curves in Fig. 3E and J) have dispersive-like shapes with negative amplitudes at shorter wavelengths and positive amplitudes at longer wavelengths. These are the signatures of the dynamic spectral shift discussed above (Fig. 3B and F) caused by excited state vibrational relaxation and solvation, which most likely obey non-exponential dynamics. The present data analysis, however, postulates multiexponential decay kinetics, and therefore yields 3 time constants which should be considered as typical time scales over which such non-exponential dynamics and corresponding spectral shifts occur in S_1. The fastest of these times constants, $\tau 1$, in the range of 60 to 90 fs (*i.e.* close to the experimental time resolution and therefore uncertain, possibly shorter) is essentially the same for both compounds and temperature-independent (see Table 1). It is attributed to the early reactive motion, along high frequency modes, out of the Franck–Condon region. Such motion is triggered by the initial slope of the (displaced) S_1 PES, and possibly releases a vibrational energy much larger than thermal energy, as confirmed by the minimum energy path computations below.

Table 1 Time constants associated with each DAS as a function of temperature for compounds ***E*-1** and ***E*-2**[a]

	10 °C		24 °C		50 °C	
	***E*-1**	***E*-2**	***E*-1**	***E*-2**	***E*-1**	***E*-2**
$\tau 1$ (fs)	90	90	60	70	90	60
$\tau 2$ (ps)	0.63	0.57	0.61	0.46	1.09	0.25
$\tau 3$ (ps)	3.8	2.7	3.6	1.9	3.8	0.8
$\tau 4$ (ps)	32	47 (50%)	28	33 (50%)	15	16 (65%)
$\tau 5$ (ps)	—	330 (50%)	—	230 (50%)	—	94 (35%)

[a] Time constants $\tau 1$, $\tau 2$, and $\tau 3$ are associated with vibrational and solvation relaxation kinetics in S_1, while $\tau 4$ and $\tau 5$ are attributed to S_1 population decay kinetics. The percentages in parentheses are the relative weight of both decay components in the biexponential decay.

The next two time constants $\tau 2$ and $\tau 3$ in the range of 0.2 to 4 ps are attributed to further vibrational relaxation involving lower-frequency modes, towards the minimum of the S_1 potential surface (PES) and possibly also solvent equilibration on the few ps time scale. While they are temperature-independent for ***E*-1**, they decrease when temperature increases for ***E*-2** (see Table 1). We tentatively attribute this temperature dependence of S_1 relaxation in ***E*-2** to the signature of a temperature-dependent population of various S_0 conformers having different S_1 vibrational relaxation pathways and kinetics. Further evidence of conformational heterogeneity of ***E*-2** is given below. Finally we note that at 50 °C, both $\tau 2$ and $\tau 3$, hence the overall S_1 equilibration, are significantly faster in ***E*-2** than in ***E*-1**, which we attribute to the enlarged number of intramolecular degrees of freedom available upon linkage to the peptide, enabling faster vibrational energy dissipation.

The longer-lived DAS have the same shapes as the spectra displayed in Fig. 3C and H, and characterize the S_1 decay. For ***E*-1**, this decay is monoexponential, with a temperature-dependent time constant $\tau 4$ ranging from 15 ps at 50 °C to 32 ps at 10 °C. This is the signature of an S_1 energy barrier to be overcome by thermal activation before effective decay to the ground state. Noticeably, for ***E*-2**, the S_1 decay is well fitted by a biexponential function with both time constants $\tau 4$ and $\tau 5$ depending on temperature. The faster time constant $\tau 4$ is very similar to that of the bare photoswitch while $\tau 5$ is systematically about 7 times slower. Hence the excited state lifetime is influenced by the peptide linkage and the biexponential decay is likely due to structural heterogeneity in the peptide, that is a distribution of (at least two) populations of conformers corresponding to different energy barrier heights on the S_1 PES. We note also that the relative weight for the fast decay component $\tau 4$ increases at 50 °C (see Table 1). This would indicate that higher temperature increases the population of a (less stable) S_0 conformer which would be characterized by a faster S_1 decay, as well as a faster S_1 equilibration (see above discussion on $\tau 2$ and $\tau 3$), as clearly illustrated by the comparison of the kinetic traces observed for various temperatures in Fig. S2 in the ESI.†

The temperature dependence of the S_1 lifetime of ***E*-1** ($\tau 4$) and ***E*-2** ($\tau 4$ and $\tau 5$, possibly characterizing the decay of two distinct sub-populations) is analyzed by Arrhenius plots (see Fig. S3 and Table S1 in the ESI†) seeking for an exponential dependence of the form: $1/\tau_{4,5} = Ae^{-E_A/k_BT}$, with E_A being the activation energy and A being a pre-exponential factor. They reveal that (i) the activation energy for the free switch in solution (3.5 kcal mol^{-1}, see ESI†) is slightly lower than for the cross-linked peptide (by a factor of 1.4 to 1.7 for the decay channels corresponding to $\tau 4$ and $\tau 5$, respectively), and (ii) the pre-exponential factors A appear to be significantly larger for compound **2**. In particular, the $\tau 4$ decay time constant is very similar for both compounds, although it corresponds to a larger activation energy (by a factor of ∼1.4) for ***E*-2**. Under local equilibrium conditions where thermodynamic quantities are defined, the transition state theory relates *A* to the activation entropy,[53,54] which includes intramolecular as well as solvent (environment) contributions, the latter one being of major influence.[55–59]

Recently, the temperature dependence of the excited state lifetimes of a bilin chromophore covalently linked to a structurally heterogeneous phytochrome protein was analyzed similarly to conclude that distinct protein conformers yielded significantly distinct prefactors *A*.[60] Here, on the one hand the peptide linkage increases the number of intramolecular degrees of freedom, but on the other hand the structural relaxation of the peptide is much slower than the photoisomerization and therefore restricts the accessible volume of the configurational space of the isomerizing subsystem. The detailed investigation of the change in activation entropy upon peptide linking is beyond the scope of the present paper. Instead, we focus below on the effect of the peptide linkage and peptide conformation on the S1 potential energy barrier height.

Computational results

Excited state pathways of *E*-1 in MeOH

The calculation of the absorption spectrum was performed at the CASPT2/MM level of theory. The optically bright state is found to be the first singlet excited state (S_1), with a S_0–S_1 excitation energy of 3.09 eV for the S_0 optimized geometry, in good agreement with the experimental value of 3.18 eV. Moreover, the electronic transition exhibits a high oscillator strength of *ca.* 1.0 and corresponds to a monoexcitation from a π orbital (centered on one phenyl ring and the photoisomerizable double bond) to its corresponding π* orbital, as illustrated in Fig. 2D.

The MEP computed on S_1 from the Franck–Condon (FC) geometry first evidences an abrupt energy loss of *ca.* 10 kcal mol^{-1} along the bond length alternation mode of the sp^2 carbon backbone, meaning that the stretching mode is activated, as is expected for such protonated Schiff bases.[7] Afterwards, a potential energy minimum is reached upon a very small torsion (*ca.* 2 degrees) around the isomerizing bond as illustrated in Fig. 4A and Fig. S13 (see ESI†).

A S_1 transition state (TS) is then located, corresponding to an energy barrier of *ca.* 3 kcal mol^{-1} at the CASPT2 level of theory, which connects the S_1 minimum to the conical intersection with the ground state (S_1/S_0 CI). The corresponding reaction coordinate mainly implies torsion around the isomerizing double bond. The torsion angle is φ_{CCCH} = 30 degrees at the TS. After decay to the ground state, two paths are possible, which are reversion or photoisomerization (see Fig. 4B). In the ground state, the *Z* photoisomer is predicted to be less stable than the *E* isomer (by 10.3 kcal mol^{-1} at the CASPT2 level), as observed experimentally, with a S_0 energy barrier high enough to prevent thermal ground state isomerization at room temperature.[17]

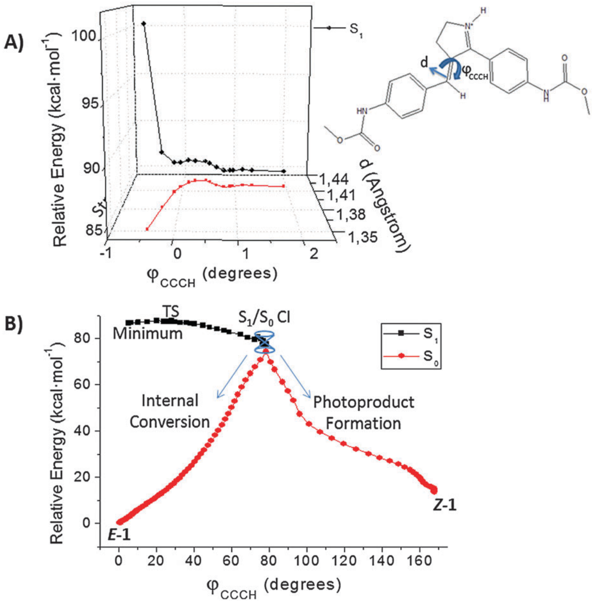

Fig. 4 Overall MEP of ***E*-1** in MeOH at the CASSCF level of theory: (A) on the S_1 state from the FC structure to the S_1 minimum. The stretching and torsion modes are depicted. (B) MEP from the excited transition state (TS) as a function of the torsional coordinate, φ_{CCCH}. The critical points are depicted, including the S_1 minimum and the S_1/S_0 conical intersection (CI). On the ground state, the internal conversion pathway back to ***E*-1** and the formation of ***Z*-1** as a photoproduct are shown.

Ground-state dynamics and characterization of *E*-2 and *Z*-2

The distance between the two sulfur atoms (SS distance) of the cysteine residues was analyzed as a measure of the switch end-to-end distance, which gives direct and crucial information about the effect of the switch linkage on the peptide structure. We first compare the average value of the SS distance along the MD simulations for the free peptide, ***E*-2** and ***Z*-2** in water. It was found to be 15.3 ± 2.2 Å, 13.7 ± 2.0 Å and 6.2 ± 1.7 Å, respectively (see Fig. 5A). Hence, we can conclude that the SS average distance of ***E*-2** is in the range of the one found for the free peptide, and that the peptide secondary structure should be maintained when linking the *E* isomer of the switch. Instead the SS average distance is reduced by *ca.* 7.5 Å in ***Z*-2**, that is upon photoisomerization, a value larger than the end-to-end distance change for azobenzene in similar applications.[61]

Moreover, the length of the α-helix was analyzed for the three systems in order to understand the effect of the switch linkage and photoisomerization on the peptide secondary structure. We obtain average α-helix lengths of 25.4, 26.8 and 23.4 Å for the free peptide, ***E*-2** and ***Z*-2**, respectively. First we note that the helicity percentage predicted by MD simulations for the free peptide (65%) is relatively high, as is expected for such a peptide where the high content of alanine residues is known to stabilize the α-helix content.[31,32] In addition, the predicted length of the α-helix is larger in ***E*-2** than in the free peptide indicating a stabilization of this secondary structure when the switch is attached. This observation is in line with the percentages of helical content found for the free peptide (65%) and ***E*-2** (69%) and their CD spectra.[17] Interestingly, this is one of the few examples where the cross-linking enhances the peptide helical content.[26,62,63]

Upon *E* to *Z* photoisomerization, the percentage of helical content is found to decrease slightly, as indicated both by the MD simulations (***E*-2** (69%) and ***Z*-2** (61%)) and the measured CD spectra (***E*-2** (79%) and ***Z*-2** (60%)[17,64]). This indicates that some amino acids of ***Z*-2** loose the helical arrangement. In order to further characterize the conformational change, we divided the peptide into two halves – ***p′*** from W1 to R14 (including the C4 switch linking site) and ***p″*** from C15 (the other linking site) to Q27, see Fig. 1B – and calculated the α-helix length for each half. It was observed that the helix length of ***p″*** is almost invariant for the free peptide (15.9 Å), ***E*-2** (15.6 Å) and ***Z*-2** (15.8 Å) (see Fig. 5B). Instead, the ***p′*** helix length is significantly different for the three models, namely 9.5, 11.3 and 7.9 Å for the free peptide, ***E*-2** and ***Z*-2**, respectively (see Fig. 5C). We conclude comparing the free peptide and ***E*-2** that the switch attachment does not affect the ***p″*** helix half but does stabilize the α-helix in the ***p′*** half. Moreover, the photoisomerization affects almost exclusively the helical content of the ***p′*** helix half where the loss of helicity from ***E*-2** to ***Z*-2** is located.

Furthermore, this partial loss of helical content observed for ***Z*-2** is mainly located in the region of A13 to R18 (see coil, bend and turn events for these amino acids between α-helical regions in Fig. 6). These structural modifications result in an α-hairpin secondary structure, as observed in seven out of ten ***Z*-2** trajectories (see Fig. 6 and movie in the ESI†). The remaining three trajectories also exhibit a helix bending in the same

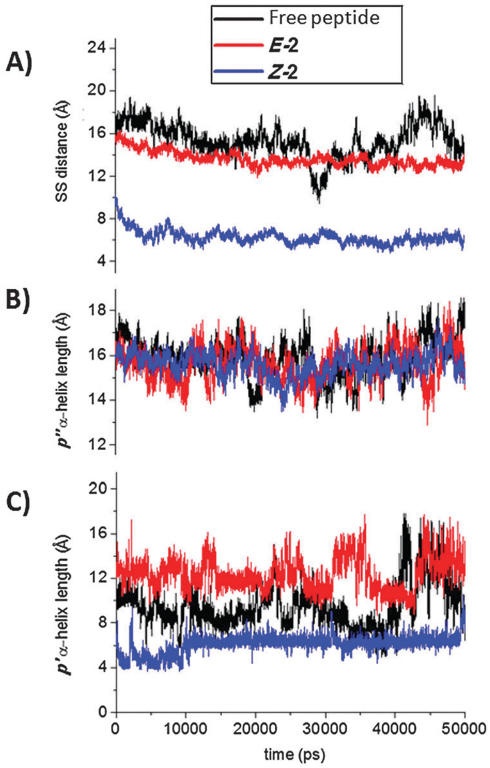

Fig. 5 Peptide structure characterization. (A) SS distance, and (B) ***p″*** and (C) ***p′*** helix length along the MD simulation time for the free peptide (black line), ***E*-2** (red line) and ***Z*-2** (blue line).

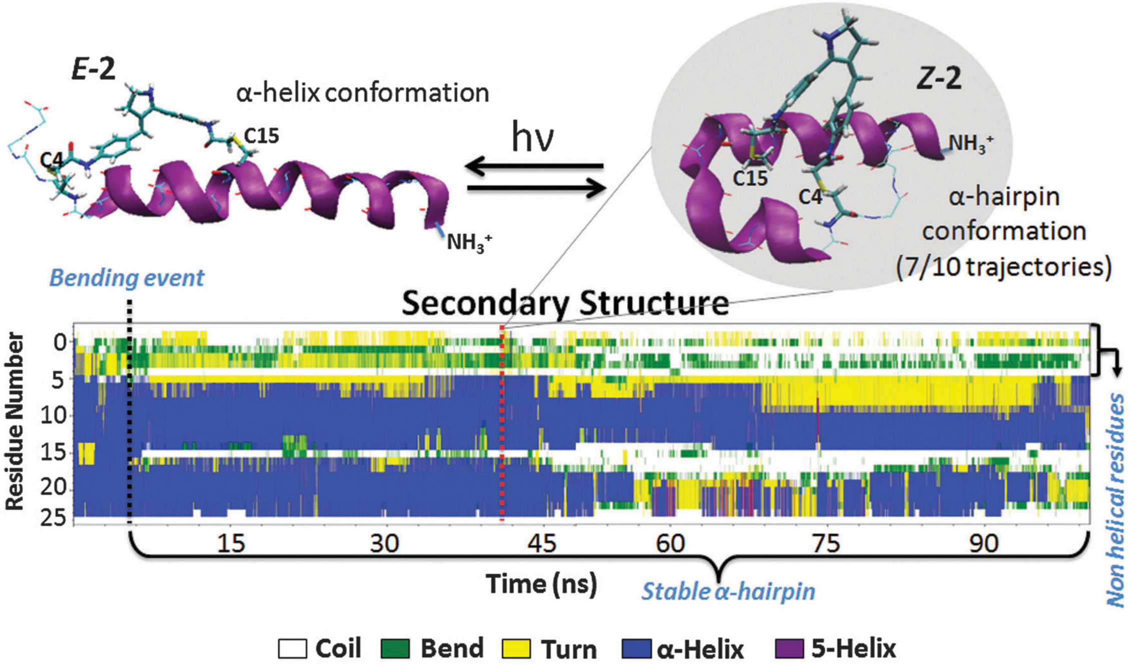

Fig. 6 (Top) Snapshots of the MD simulations representative of the conformational change triggered by the photoisomerization. (Bottom) Time evolution of the ***Z*-2** secondary structure using the DSSP (Define Secondary Structure of Protein) method.[65,66] Blue regions denote the α-helical structures. At around 5.5 ns a bending event promotes the formation of a stable α-hairpin (see the white region around residue 15 splitting the blue region in two different sides). The first five residues are highly fluctuating and never shape into an α-helix.

region of the peptide, and a higher simulation time would possibly result in the formation of an α-hairpin structure also in these cases. Hence, switch photoisomerization promotes a reversible peptide structural rearrangement, from the α-helix to the α-hairpin with a slight loss of helicity.

This reversible photo-conversion of the secondary structure predicted by the MD simulations agrees well and rationalizes the loss of helical content previously observed by circular dichroism spectroscopy on the same system[17] when forming ***Z*-2**. Moreover, the present MD results give detailed, atomistic-level insights into the peptide conformational change, which could not be revealed experimentally.

To further validate the MD simulation results we also computed the electronic absorption spectra of ***E*-2** and ***Z*-2** (see Methods) and compared them to the experimental data as shown in Fig. 2. For ***E*-2**, the optically bright state is also S_1 and its electronic nature is the same as for ***E*-1** (Fig. 2D). The calculated S_0–S_1 excitation energies are around 380 and 370 nm for ***E*-2** and ***Z*-2** at the TD-DFT/MM level of theory (see ESI†), which are in very good agreement (within less than 0.1 eV) with the experimental values. Moreover, the shapes of both simulated spectra are very similar to the experimental ones (see Fig. 2B and C). Hence, we conclude that the present MD study yields a suitable description of the system in the ground state.

Finally, beyond the above structural analysis in terms of average helical content, a cluster analysis (see ESI†) of the MD trajectories of ***E*-2** evidences conformational heterogeneity, which is of central importance for the interpretation of the transient absorption data described above. In particular two distinct dominating conformations of the peptide are predicted, which differ mainly in their SS distance: 50% of the geometries have an SS average distance of 14.7 Å, while 18% corresponds to a shorter SS distance of 11.5 Å (Fig. 7). Due to the peptide flexibility in water, several intermediate structures are predicted, each of them accounting for a proportion lower than 10%. We note here that the experimentally observed S_1 decay is fitted by a biexponential decay which may actually also account for a continuous distribution of exponentially decaying functions with intermediate lifetimes, and therefore does not exclude a distribution of more than two conformers.

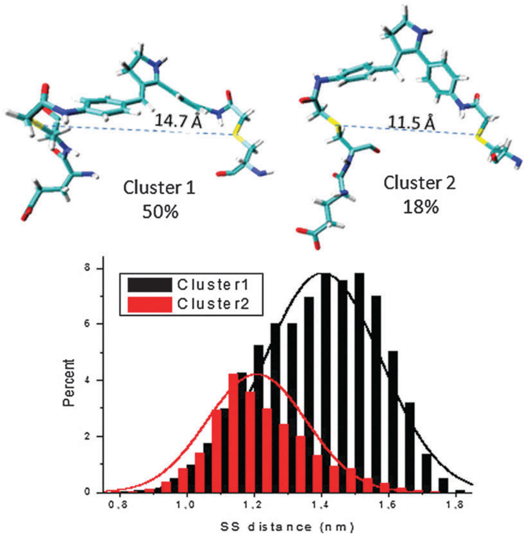

Fig. 7 Histograms of the SS distance distributions of the two most relevant conformers of ***E*-2**, as extracted by cluster analysis along the MD trajectory. The total percentage of occurrences is shown.

Noticeably, this conformational flexibility is not induced by the attached switch, but is an inherent property of this peptide sequence, as demonstrated by the clustering analysis of the free peptide, which shows almost the same results as for ***E*-2** (see ESI†). Nevertheless, the two identified clusters cannot be distinguished spectroscopically, since their absorption spectra do overlap, as predicted at the CASPT2 level of theory (see Fig. S8 in the ESI† for details).

Excited-state dynamics and pathways of *E*-2

In order to understand the effect of the peptide on the switch photoreactivity, the *E*-to-*Z* photoisomerization mechanism of the cross-linked peptide was investigated by calculating the excited-state pathway for a representative structure of each of the two clusters illustrated in Fig. 7: two snapshots, named ***E*-2-C1** (from cluster 1) and ***E*-2-C2** (from cluster 2), were selected and optimized at the MP2/MM level to refine their FC geometry, followed by a calculation of the S_1 MEP for each conformer (see Methods).

Similar to ***E*-1** in MeOH, after excitation to S_1, the bond length alternation due to stretching relaxation and a slight torsion of the double bond drive the system to a potential energy minimum (see Fig. S10 in the ESI†). To find the transition states (TSs) connecting the S_1 PES minimum to the CI, the PES is mapped by a double scan around φ_{CCCH} and φ_{CCCC}, which are the most relevant coordinates to describe the torsion around the central isomerizing bond in retinal-like molecular switches.[67] For ***E*-2-C1** a high energy region is found to connect the S_1 minimum and the CI *via* a saddle point that we identify as the TS, characterized by $\varphi_{\mathrm{CCCH}} = 45°$ and $\varphi_{\mathrm{CCCC}} = 35°$ (Fig. 8).

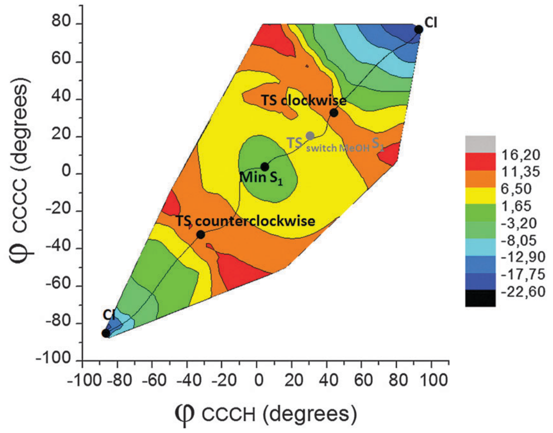

Fig. 8 Energy map as a result of the double scan around φ_{CCCH} and φ_{CCCC} for ***E*-2-C1**. The critical points are depicted: TS, S_1 minimum, S_1/S_0 conical intersections (CIs) and, for geometrical comparison, the TS of the switch in MeOH. The MEP connecting the TS with the minimum and the CI is shown in black.

The energy barrier calculated at the CASPT2 level is ≈13 kcal mol^{-1}. From the TS geometry, a MEP is computed toward the S_1 PES minimum and toward the CI. The rotation around the double bond from the S_1 minimum in the opposite sense (*i.e.* counterclockwise) was also evaluated. A similar CASPT2 energy barrier of ≈14 kcal mol^{-1} is found indicating that both clockwise and counterclockwise paths are almost equivalent.

Applying the same methodology, the TS geometry for **_E_-2-C2** was identified at $\varphi_{\text{CCCH}} = 20°$ and $\varphi_{\text{CCCC}} = 40°$, corresponding to an S_1 energy barrier of ≈5 kcal mol^{-1} at the CASPT2 level of theory. Again, the MEPs from the TS to the S_1 minimum and the CI are computed.

We can therefore conclude that both conformers minimize the energy from the TS along the torsion coordinate until reaching the S_1/S_0 CI. From there, the system decays to the ground state completing the photoisomerization or recovering the starting isomer. These two possible paths have been calculated for both conformers, **_E_-2-C1** and **_E_-2-C2** (Fig. S11 in the ESI†).

In the case of **_E_-2-C1**, non-adiabatic molecular dynamic trajectories were performed on S_1, in order to gain insights into the photoisomerization mechanism. Because of the high S_1 energy barrier and the rather long excited-state lifetime (of the order of hundreds of ps), a dynamical study describing the whole process is computationally unfeasible. Hence, we calculated trajectories with zero initial kinetic energy (i) from the Franck–Condon region toward the S_1 minimum, (ii) from the TS toward the S_1 minimum and (iii) from the TS to the ground state, either isomerizing or reverting back to the initial switch conformation. This allowed for a direct comparison with the calculated MEP. The results are illustrated in Fig. 9 and show that the overall trajectory (from the FC geometry to the formation of the photoisomer) describes the relation between C═C stretching and torsion in agreement with the calculated MEP. In particular, a complete decoupling between the two coordinates is never observed. Instead, in the excited state the C═C bond lengthening is firstly observed to be coupled to a slight torsion. Once the carbon–carbon bond becomes completely a single bond, the hydrogen-out-of-plane mode drives the reaction towards the intersection with the ground state, finally allowing the formation of the *Z* isomer while recovering the double bond character of the C═C central bond.[67] Noticeably, along these excited state trajectories and as also found through the MEP, the structural changes of the peptide moiety are limited to subtle rearrangements (*ca.* 2.0 Å) of the amino acids in the vicinity of the switch, and in the peptide region which is going to bend, especially W1, A6, A7, A8, E10, A11, A12, A13, R14 and C15. Indeed, these amino acids form a sort of pocket around the switch and their move favors the geometrical displacements required to afford the *E*-to-*Z* isomerization (see Fig. S12 in the ESI†). The actual, larger scale peptide bending of the A13 to R18 segment, and hairpin formation occur only after the decay to the ground state, on a much longer time scale.

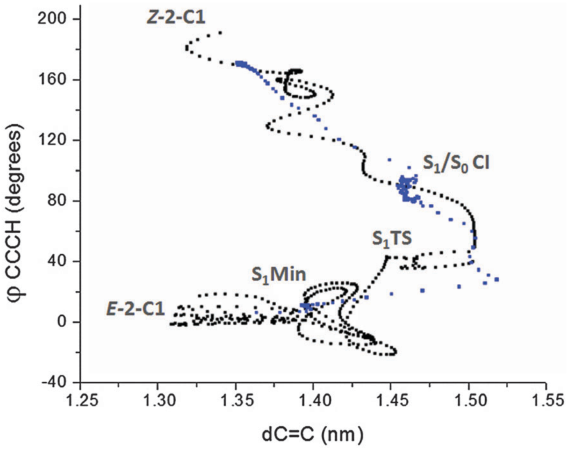

Fig. 9 Non-adiabatic MD simulation (black) and MEP (blue) of **2-C1** *E*-to-*Z* photoisomerization, as a function of the two most relevant coordinates: stretching and torsion around the central C═C bond.

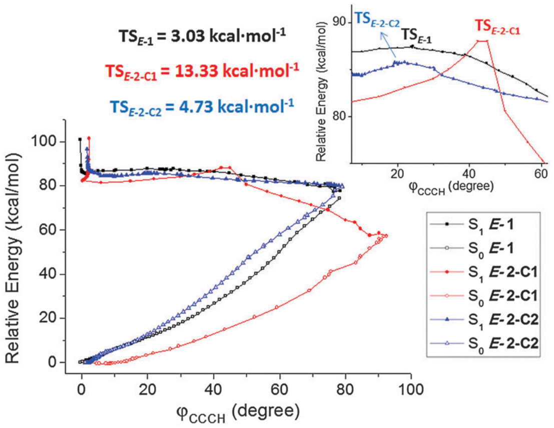

Fig. 10 CASSCF excited state pathways of **_E_-2-C1** (red lines), **_E_-2-C2** (blue lines) and **_E_-1** (black lines), as a function of the torsion around the photoisomerizable C═C bond. The inset shows the position and CASPT2 corrected energy barrier for each S_1 transition state (TS).

Summarizing, Fig. 10 shows all investigated photoisomerization pathways as a function of the central C═C bond torsion. **_E_-1** and **_E_-2-C2** appear to have similar S_1 topologies, characterized by a transition state located between 20 and 30 degrees of torsion and a S_1 energy barrier between 3 and 5 kcal mol^{-1}. On the other hand, **_E_-2-C1** shows a transition state above 40 degrees of torsion, associated with a higher S_1 energy barrier (*ca.* 13 kcal mol^{-1}). Moreover, the S_1/S_0 intersection region is lower in energy (17 kcal mol^{-1} at the CASPT2 level) and located at *ca.* 15 degrees higher torsion in the case of **_E_-2-C1**, when compared to **_E_-2-C2** and **_E_-1**.

Discussion

The overall mechanism from photon absorption to formation of the photoisomer can be summarized by three main steps: vibrational relaxation from the Franck–Condon region to the S_1 minimum; excited state population decay to the electronic ground state; conformational changes involving switch relaxation and peptide secondary structure reorganization.

The non-exponential S_1 vibrational and solvation dynamics evidenced by TAS and documented with three time scales spanning from sub-100 fs to a few ps is fully rationalized by the MEP calculations and non-adiabatic molecular dynamics. Indeed the latter evidence the excitation and early relaxation out of the FC region along (high-frequency) stretching modes which cause partial bond length alternation in the chromophore. This confers, at least partially, a single bond character to the central isomerizing carbon–carbon bond and enables the subsequent contribution of lower frequency modes to the reaction coordinate, and in particular the slower torsion motion around the isomerizing C–C bond. As a matter of fact, for all models the corresponding φ_{CCCC} torsion angle (see Fig. 1A) is twisted at the S_1 minimum (see below). Also the reorganization of the polar solvent (MeOH in compound **1** or water in compound **2**) and of the peptide (compound **2** only) around the chromophore is expected to occur on the sub-ps to ps time scale, given the charge transfer character of the S_1 electronic state, described by partial migration of the positive charge from the five-membered ring to the phenyl moiety (see Fig. 2D).

The main difference observed by TAS between ***E*-1** and ***E*-2** is in the S_1 population decay kinetics, being monoexponential (τ4) for ***E*-1** and biexponential (τ4 and τ5) for ***E*-2** (see Fig. 3). The QM/MM study of ***E*-1** predicts a 3 kcal mol^{-1} S_1 energy barrier between the S_1 minimum and the CI, which is in line with the thermally activated S_1 decay observed experimentally. For ***E*-2**, the MD simulations predict structural heterogeneity with, in particular, two main conformers of ***E*-2**, **C1** and **C2**. The QM/MM calculations conclude that both conformers influence differently the S_1 PES topologies and in particular the S_1 energy barriers. The 5 and 13 kcal mol^{-1} energy barriers predicted for **C2** and **C1**, respectively (see Fig. 8 and 10), should be considered as upper boundaries for the S_1 energy barriers since they result from the 2D exploration of a multidimensional PES. Still, the identification of different conformers exhibiting different S_1 energy barriers is in agreement with the experimental observation of a temperature-dependent biexponential S_1 decay, indicating the presence of (at least) two populations undergoing thermally activated population decay along distinct pathways. In addition, the predicted similarity of the PES topologies of compounds ***E*-1** in MeOH and ***E*-2-C2** in water is in line with the similar values observed for τ4 in both compounds, while the expected properties of ***E*-2-C1** are in line with the larger value of τ5.

We now discuss the mechanism by which the peptide linkage alters the PES topology and therefore the photoreactivity of the switch. First, we note that although both ***E*-2-C1** and ***E*-2-C2** are characterized by a significantly distinct average SS-distance (see Fig. 7) and S_1 energy barrier (see Fig. 10), the degrees of freedom primarily involved in the photoswitch reaction coordinate have ground state values very similar in both conformers and not either very different from ***E*-1** (see Table S4 in the ESI†). Interestingly, only in ***E*-2-C2** the φ_{CCCC} pretwist increased to about 11°, but this is apparently not affecting significantly the S_1 properties of ***E*-2-C2** with respect to ***E*-1**. This is in contrast to the photophysics of retinal proteins where 10 to 15° initial pretwist of the isomerizing bond is argued to be of major influence on the retinal photoreactivity (see below). We conclude that in the present case of thermal-activation in S_1, the initial FC geometry (and peptide constraint) is less critical in influencing the photoreactivity than in a nearly ballistic (sub-picosecond) reaction as observed in retinal proteins.

Instead, the comparison between the ***E*-2-C1** and ***E*-2-C2** geometries at the S_1 minimum and the TS suggests a structural explanation for their difference in the S_1 energy barriers. At the minimum of S_1, the bond length alternation is not completed for both conformers (*i.e.* the isomerizing bond still has a partial double bond character). Therefore, some energy is required in order to proceed with the isomerization process which requires torsion around that bond. In the case of ***E*-2-C1** however, the bond length alternation and the φ_{CCCC} torsion are even less advanced than for ***E*-2-C2** (see details in Table S4 in the ESI†) thus explaining by the electronic structure the presence of an enhanced excited state barrier in ***E*-2-C1**. This is also in line with the TS being characterized by (i) a larger value of the hydrogen-out-of-plane and (ii) a larger pyramidalization of the PSB nitrogen atom for ***E*-2-C1**, than for ***E*-2-C2** (see details in Table S4 in the ESI†). The structural parameters described for ***E*-2-C2** are instead closer to those of ***E*-1**, which has an even lower energy barrier since its bond length alternation at the S_1 minimum is almost complete.

Also consistent with the structural differences described above, the excited state charge transfer character of the TS is almost complete for ***E*-2-C1**, while only half of the charge migrated in ***E*-2-C2** or in ***E*-1** (see the details in Table S4 in the ESI†). Moreover, the charge transfer character is found to be related to the surrounding environment of the molecular switch. Indeed, a deprotonated C-terminus is expected considering the acidic experimental conditions (pH = 4.3) compared to the pK_a value of the W residue (2.46). We observe that the C-terminus tends to adopt two main arrangements along the trajectories, either placing the COO$^-$ group next to the switch six-membered ring directly bound to the photoisomerizable C=C bond, or exposing the COO$^-$ group to water. The former case enhances positive charge translocation along the switch and corresponds to ***E*-2-C1** (see Fig. S12 in the ESI†), while the latter case does not favor a notable charge transfer and corresponds to ***E*-2-C2**.

Hence we conclude that both, the electrostatic embedding and the mechanical force exerted at both ends of the switch by the covalently linked peptide, are responsible for the different S_1 energy barriers.

It is noteworthy to compare such a mechanistic and dynamic scenario (see Fig. 9 and 10) with previous studies performed on similar PSBs (especially retinal) in solution or as a rhodopsin chromophore: in all cases the photochemical pathway involves charge translocation, already in the FC region, which triggers the bond length alternation of the conjugated backbone followed by torsion and isomerization through a CI. In spite of a similar mechanistic description, the reaction kinetics can be largely different, depending on the environment. Indeed, a sub-ps photoisomerization is observed in retinal proteins,[68] where the opsin pocket induces (i) a pre-twisting of the isomerizing bond already in the ground state due to steric interaction[69] and (ii) an electrostatic field increasing the efficiency of the charge transfer driving the process.[70] Instead, the retinal PSB in solution behaves differently, since in this case the homogeneous environment does not either induce any specific pre-twist or enhance charge translocation along the backbone. In the latter case, a planar S_1 region or even a small energy barrier[71] slows down the isomerization process, reaching the ps time scale, as observed in **1**. On the other hand, in **2** the S_1 energy barrier can be even higher than in **1**, due to the different constraints imposed by the peptide attachment, that induces electrostatic interactions and forces at both sides of the switch. Moreover, the flexibility of the peptide creates different possible charge arrangements around the molecular switch (to a large extent sequence dependent).

Finally, when focusing the attention on the peptide, the extensive MD study of the free peptide, ***E*-2** (10 trajectories of 50 ns) and ***Z*-2** (10 trajectories of 100 ns) served to find out the switch linkage and photoisomerization effects on the peptide secondary structure. As the SS distance of the free peptide and ***E*-2** along the simulation time is very similar (see Fig. 5A), we do not expect a large secondary structural change upon switch linkage. Upon photoisomerization, a reversible secondary structural change from an α-helix (***E*-2**) to an α-hairpin (***Z*-2**) is observed. Moreover, the MD analysis of ***E*-2** allowed us to evince its intrinsic structural heterogeneity, thus rationalizing the observed photodynamics behavior.

Conclusions

Combining the state-of-the-art transient absorption spectroscopy and multiscale simulations, we were able to reveal the dynamical and mechanistic differences of the photoisomerization of a retinal-like, synthetic molecular switch in solution or cross-linked to a peptide. In the present case, we found that the polypeptide linkage modifies the excited state topology and therefore the reactivity of the switch, in a way that depends on the heterogeneous ground state peptide conformation. In particular, the excited state decay time increases up to one order of magnitude (at room temperature) when cross-linked to the polypeptide, nevertheless always enabling a successful isomerization, as proved by the photoisomerization quantum yield previously measured for these two compounds.[17] This is rationalized by evidencing, both experimentally and theoretically, the influence of the peptide linkage on the excited-state energy barrier. It has been concluded that different conformers, in particular ***E*-2-C1** and ***E*-2-C2**, exhibit different electronic and structural properties along their pathway from the FC region back to the ground state. In particular, ***E*-2-C2** behaves similar to ***E*-1**: the central C=C bond is significantly elongated after S_1 vibrational relaxation, and the transition state is characterized by a *ca.* 25° torsion and an energy barrier below 5 kcal mol^{-1}. Whereas, for ***E*-2-C1** the C=C bond has a significant character of the double bond leading to a higher energy barrier and a transition state retarded along the torsion coordinate (*ca.* 45°).

This work can be seen as a bottom-up approach for the investigation of the influence of the surrounding environment of a molecular switch on its photoreactivity where, starting from the bare synthetic chromophore, we have considered the effect of its linking to a peptide. This is a central issue (exemplified *e.g.* by the influence of the opsin pocket on the retinal photochemistry) which is to be carefully explored in the view of designing synthetic chromophores for the efficient photoswitching of molecular functions. In the specific case explored here, we show that combined transient absorption spectroscopy and extensive modeling are efficient tools to reveal the mechanism and ability of a retinal-like molecular switch to efficiently convert an α-helix into an α-hairpin in a process spanning from photon absorption to macromolecular conformational changes on time scales from the fs to μs time range.

Acknowledgements

This research was supported by the Spanish MICINN (grants CTQ2012-36966 and CTQ2014-59650-P), Universidad de Alcalá (grants CCG2013/EXP-089 and CCG2014/EXP-083), the French Agence Nationale de la Recherche (grant ANR-11-JS04-010-01 ''IPQCS'', Labex NIE, labex CSC), and the Région Alsace (contrat doctoral, convention 607-12-C31). C. G.-I. acknowledges the Spanish Ministerio de Educación y Ciencia for a doctoral fellowship. D. M.-L. thanks the Universidad de La Rioja for his doctoral fellowship. M. M. is grateful to the Alexander von Humboldt Foundation for a postdoctoral research fellowship.

References

1 *Molecular Machines*, [in: *Top. Curr. Chem.*, 2005, 262], ed. T. R. Kelly, Springer, 2005.
2 V. Balzani, *ChemPhysChem*, 2009, **10**, 21.
3 *Molecular Switches*, ed. B. L. Feringa and W. R. Browne, Wiley-VCH Verlag GmbH & Co. KGaA, Second, completely revised and enlarged edn, 2011, vol. 2.
4 C. Garcia-Iriepa, M. Marazzi, L. M. Frutos and D. Sampedro, *RSC Adv.*, 2013, **3**, 6241–6266.
5 W. Szymanski, J. M. Beierle, H. A. V. Kistemaker, W. A. Velema and B. L. Feringa, *Chem. Rev.*, 2013, **113**, 6114–6178.
6 I. Willner and B. Willner, *Photochemical biomolecular switches: The route to optobioelectronics*, Wiley Online Library, 2001.
7 S. Gozem, F. Melaccio, H. L. Luk, S. Rinaldi and M. Olivucci, *Chem. Soc. Rev.*, 2014, **43**, 4019–4036.
8 C. Renner and L. Moroder, *ChemBioChem*, 2006, **7**, 868–878.
9 A. A. Beharry and G. A. Woolley, *Neuromethods*, 2011, **55**, 171–184.
10 H. Janovjak and E. Y. Isacoff, *Neuromethods*, 2011, **55**, 233–266.
11 M. Erdelyi, A. Karlen and A. Gogoll, *Chem. – Eur. J.*, 2006, **12**, 403–412.
12 M. Erdelyi, M. Varedian, C. Skoeld, I. B. Niklasson, J. Nurbo, A. Persson, J. Bergquist and A. Gogoll, *Org. Biomol. Chem.*, 2008, **6**, 4356–4373.

13 N. J. V. Lindgren, M. Varedian and A. Gogoll, *Chem. – Eur. J.*, 2009, **15**, 501–505.

14 T. Cordes, C. Elsner, T. T. Herzog, C. Hoppmann, T. Schadendorf, W. Summerer, K. Rueck-Braun and W. Zinth, *Chem. Phys.*, 2009, **358**, 103–110.

15 N. Regner, T. T. Herzog, K. Haiser, C. Hoppmann, M. Beyermann, J. Sauermann, M. Engelhard, T. Cordes, K. Rueck-Braun and W. Zinth, *J. Phys. Chem. B*, 2012, **116**, 4181–4191.

16 T. Andruniow, S. Fantacci, F. De Angelis, N. Ferre and M. Olivucci, *Angew. Chem., Int. Ed.*, 2005, **44**, 6077–6081.

17 M. Blanco-Lomas, S. Samanta, P. J. Campos, G. A. Woolley and D. Sampedro, *J. Am. Chem. Soc.*, 2012, **134**, 6960–6963.

18 A. Sinicropi, C. Bernini, R. Basosi and M. Olivucci, *Photochem. Photobiol. Sci.*, 2009, **8**, 1639–1649.

19 J. A. McCammon and P. G. Wolynes, *Curr. Opin. Struct. Biol.*, 2002, **12**, 143–145.

20 C. D. Snow, H. Nguyen, V. S. Pande and M. Gruebele, *Nature*, 2002, **420**, 102–106.

21 *Protein and Peptide Folding, Misfolding, and Non-Folding*, ed. R. Schweitzer-Stenner, John Wiley & Sons, Inc., 2012.

22 P. H. Nguyen, Y. Mu and G. Stock, *Proteins: Struct., Funct., Bioinf.*, 2005, **60**, 485–494.

23 P. H. Nguyen, H. Staudt, J. Wachtveitl and G. Stock, *J. Phys. Chem. B*, 2011, **115**, 13084–13092.

24 G. A. Woolley, *Acc. Chem. Res.*, 2005, **38**, 486–493.

25 D. G. Flint, J. R. Kumita, O. S. Smart and G. A. Woolley, *Chem. Biol.*, 2002, **9**, 391–397.

26 A. M. Ali and G. A. Woolley, *Org. Biomol. Chem.*, 2013, **11**, 5325–5331.

27 J. Bredenbeck, J. Helbing, J. R. Kumita, G. A. Woolley and P. Hamm, *Proc. Natl. Acad. Sci. U. S. A.*, 2005, **102**, 2379–2384.

28 L. Rivado-Casas, M. Blanco-Lomas, P. J. Campos and D. Sampedro, *Tetrahedron*, 2011, **67**, 7570–7574.

29 D. Sampedro, A. Migani, A. Pepi, E. Busi, R. Basosi, L. Latterini, F. Elisei, S. Fusi, F. Ponticelli, V. Zanirato and M. Olivucci, *J. Am. Chem. Soc.*, 2004, **126**, 9349–9359.

30 B. H. Zimm and J. K. Bragg, *J. Chem. Phys.*, 1959, **31**, 526–535.

31 S. Marqusee and R. L. Baldwin, *Proc. Natl. Acad. Sci. U. S. A.*, 1987, **84**, 8898–8902.

32 S. Marqusee, V. H. Robbins and R. L. Baldwin, *Proc. Natl. Acad. Sci. U. S. A.*, 1989, **86**, 5286–5290.

33 S. Padmanabhan, E. J. York, L. Gera, J. M. Stewart and R. L. Baldwin, *Biochemistry*, 1994, **33**, 8604–8609.

34 M. Volk, Y. Kholodenko, H. S. M. Lu, E. A. Gooding, W. F. DeGrado and R. M. Hochstrasser, *J. Phys. Chem. B*, 1997, **101**, 8607–8616.

35 L. Milanesi, J. P. Waltho, C. A. Hunter, D. J. Shaw, G. S. Beddard, G. D. Reid, S. Dev and M. Volk, *Proc. Natl. Acad. Sci. U. S. A.*, 2012, **109**, 19563–19568.

36 P. Hamm, M. Zurek, T. Roeschinger, H. Patzelt, D. Oesterhelt and W. Zinth, *Chem. Phys. Lett.*, 1996, **263**, 613–621.

37 C. Punwong, J. Owens and T. J. Martinez, *J. Phys. Chem. B*, 2015, **119**, 704–714.

38 X. Li, L. W. Chung and K. Morokuma, *J. Chem. Theory Comput.*, 2011, **7**, 2694–2698.

39 K. Bravaya, A. Bochenkova, A. Granovsky and A. Nemukhin, *J. Am. Chem. Soc.*, 2007, **129**, 13035–13042.

40 O. Bismuth, N. Friedman, M. Sheves and S. Ruhman, *Chem. Phys.*, 2007, **341**, 267–275.

41 J. Briand, O. Braem, J. Rehault, J. Leonard, A. Cannizzo, M. Chergui, V. Zanirato, M. Olivucci, J. Helbing and S. Haacke, *Phys. Chem. Chem. Phys.*, 2010, **12**, 3178–3187.

42 V. Hornak, R. Abel, A. Okur, B. Strockbine, A. Roitberg and C. Simmerling, *Proteins: Struct., Funct., Bioinf.*, 2006, **65**, 712–725.

43 J. Wang, R. M. Wolf, J. W. Caldwell, P. A. Kollman and D. A. Case, *J. Comput. Chem.*, 2004, **25**, 1157–1174.

44 J. Finley, P.-A. Malmqvist, B. O. Roos and L. Serrano-Andres, *Chem. Phys. Lett.*, 1998, **288**, 299–306.

45 J. C. Tully, *J. Chem. Phys.*, 1990, **93**, 1061–1071.

46 See http://www.gromacs.org/.

47 R. Salomon-Ferrer, D. A. Case and R. C. Walker, *Wiley Interdiscip. Rev.: Comput. Mol. Sci.*, 2013, **3**, 198–210.

48 F. Aquilante, L. De Vico, N. Ferre, G. Ghigo, P.-A. Malmqvist, P. Neogrady, T. B. Pedersen, M. Pitonak, M. Reiher, B. O. Roos, L. Serrano-Andres, M. Urban, V. Veryazov and R. Lindh, *J. Comput. Chem.*, 2010, **31**, 224–247.

49 J. W. Ponder and F. M. Richards, *J. Comput. Chem.*, 1987, **8**, 1016–1024.

50 Y. Zhao and D. G. Truhlar, *Theor. Chem. Acc.*, 2008, **120**, 215–241.

51 M. J. T. Frisch, G. W. Trucks, H. B. Schlegel, G. E. Scuseria, M. A. Robb, J. R. Cheeseman, G. Scalmani and V. Barone, *et al., Gaussian 09 revision B.01*, Gaussian, Inc., Wallingford, CT, 2009.

52 T. Vreven, K. S. Byun, I. Komaromi, S. Dapprich, J. A. Montgomery, Jr., K. Morokuma and M. J. Frisch, *J. Chem. Theory Comput.*, 2006, **2**, 815–826.

53 E. V. D. Anslyn and A. Dennis, Transition State Theory and Related Topics, in *Modern Physical Organic Chemistry*, University Science Books, 2006.

54 K. J. J. Laidler, *J. Phys. Chem.*, 1983, **87**, 2657–2664.

55 J. Dokic, M. Gothe, J. Wirth, M. V. Peters, J. Schwarz, S. Hecht and P. Saalfrank, *J. Phys. Chem. A*, 2009, **113**, 6763–6773.

56 S. A. Kovalenko and A. L. Dobryakov, *Chem. Phys. Lett.*, 2013, **570**, 56–60.

57 D. A. Harris, M. B. Orozco and R. J. Sension, *J. Phys. Chem. A*, 2006, **110**, 9325–9333.

58 F. X. Vazquez, S. Talapatra, R. J. Sension and E. Geva, *J. Phys. Chem. B*, 2014, **118**, 7869–7877.

59 M. Strajbl, Y. Y. Sham, J. Villa, Z. T. Chu and A. Warshel, *J. Phys. Chem. B*, 2000, **104**, 4578–4584.

60 P. W. Kim, N. C. Rockwell, S. S. Martin, J. C. Lagarias and D. S. Larsen, *Biochemistry*, 2014, **53**, 2818–2826.

61 D. C. Burns, D. G. Flint, J. R. Kumita, H. J. Feldman, L. Serrano, Z. Zhang, O. S. Smart and G. A. Woolley, *Biochemistry*, 2004, **43**, 15329–15338.

62 J. R. Kumita, O. S. Smart and G. A. Woolley, *Proc. Natl. Acad. Sci. U. S. A.*, 2000, **97**, 3803–3808.

63 F. Zhang, O. Sadovski, S. J. Xin and G. A. Woolley, *J. Am. Chem. Soc.*, 2007, **129**, 14154–14155.

64 E. Lacroix, A. R. Viguera and L. Serrano, *J. Mol. Biol.*, 1998, **284**, 173–191.

65 W. Kabsch and C. Sander, *Biopolymers*, 1983, **22**, 2577–2637.

66 C. A. F. Andersen, A. G. Palmer, S. Brunak and B. Rost, *Structure*, 2002, **10**, 175–184.

67 I. Schapiro, M. N. Ryazantsev, L. M. Frutos, N. Ferre, R. Lindh and M. Olivucci, *J. Am. Chem. Soc.*, 2011, **133**, 3354–3364.

68 D. Polli, P. Altoe, O. Weingart, K. M. Spillane, C. Manzoni, D. Brida, G. Tomasello, G. Orlandi, P. Kukura, R. A. Mathies, M. Garavelli and G. Cerullo, *Nature*, 2010, **467**, 440–443.

69 L. M. Frutos, T. Andruniow, F. Santoro, N. Ferre and M. Olivucci, *Proc. Natl. Acad. Sci. U. S. A.*, 2007, **104**, 7764–7769.

70 K. Welke, J. S. Fraehmcke, H. C. Watanabe, P. Hegemann and M. Elstner, *J. Phys. Chem. B*, 2011, **115**, 15119–15128.

71 O. Valsson and C. Filippi, *J. Chem. Theory Comput.*, 2010, **6**, 1275–1292.

7. Photoisomerization dynamics of new HBDI-like photoswitch

In this chapter, in collaboration with Mr. Olivucci (Dipartimento di Biotecnologie, Chimica e Farmacia, Università di Siena, Italy), we report a pluridisciplinary work based on a complementary tasks, combining theory, synthesis, characterization of photostationary state and transient absorption experiment. We present the preparation of an anionic molecular photoswitch mimicking the electronics structure of the p-HDBI chromophore of the green fluorescent protein (GFP). The facile synthesis of the investigated swith allows for its characterization in terms of spectroscopy, photochemistry and laser induced ultrafast dynamics showing that the system is photochromic and thermally stable at room temperature and that its anionic form has distinct 351 nm (for the E form) and 359 nm (for the Z form) maximum absorption values. The computational and the transient spectroscopy studies demonstrate that the light-induced E/Z isomerization reactions dynamics occur on the sub-picosecond timescale. While the computed conical intersection structures and excited state trajectories of the HBDI-like photoswitch demonstrate that the isomerization occurs via an axial rotation as in the cationic IP photoswitch family, their stationary and transient electrostatic properties are highly complementary. Indeed, while in IP molecules a positive charge located on a five membered ring rotor gets translocated towards the bicyclic indanylidene stator during its excited state evolution [13], in HBDI-like systems it is a negative charge to be translocated away from the indanylidene rotor and to return upon ground state relaxation. We envision that a family of HDBI-like switches could be employed to engineer molecular devices with static or transient electrostatic effects opposite to those provided by NAIP switches.

This work is also the subject of an article published in the Journal of the American Chemical Society (JACS). All the experimental results and analysis revealed by transient absorption spectroscopy related in here (see pages > 8 in the article and page S4-S10 in the supporting information), was performed by myself.

JOURNAL OF THE AMERICAN CHEMICAL SOCIETY
Article
pubs.acs.org/JACS

Design, Synthesis, and Dynamics of a Green Fluorescent Protein Fluorophore Mimic with an Ultrafast Switching Function

Marco Paolino,*[†] Moussa Gueye,[‡] Elisa Pieri,[†,¶] Madushanka Manathunga,[§,¶] Stefania Fusi,[†] Andrea Cappelli,[†] Loredana Latterini,[∥] Danilo Pannacci,[∥] Michael Filatov,*[⊥] Jérémie Léonard,*[‡] and Massimo Olivucci*[†,§,#]

[†]Dipartimento di Biotecnologie, Chimica e Farmacia, Università di Siena, Via A. Moro 2, 53100 Siena, Italy
[‡]Institut de Physique et Chimie des Matériaux de Strasbourg & Labex NIE, Université de Strasbourg, CNRS UMR 7504, Strasbourg, France
[§]Chemistry Department, Bowling Green State University, Bowling Green, Ohio, United States
[∥]Dipartimento di Chimica, Biologia e Biotecnologie, Università di Perugia, Via Elce di Sotto, 8, 06123 Perugia, Italy
[⊥]Department of Chemistry, School of Natural Sciences, Ulsan National Institute of Science and Technology (UNIST), Ulsan 689-798, Korea
[#]University of Strasbourg Institute for Advanced Studies, 5, allée du Général Rouvillois F-67083 Strasbourg, France

S *Supporting Information*

ABSTRACT: While rotary molecular switches based on neutral and *cationic* organic π-systems have been reported, structurally homologous *anionic* switches providing complementary properties have not been prepared so far. Here we report the design and preparation of a molecular switch mimicking the anionic *p*-HBDI chromophore of the green fluorescent protein. The investigation of the mechanism and dynamics of the *E*/*Z* switching function is carried out both computationally and experimentally. The data consistently support axial rotary motion occurring on a sub-picosecond time scale. Transient spectroscopy and trajectory simulations show that the nonadiabatic decay process occurs in the vicinity of a conical intersection (CI*nt*) between a charge transfer state and a covalent/diradical state. Comparison of our anionic *p*-HBDI-like switch with the previously reported cationic *N*-alkyl indanylidene pyrrolinium switch mimicking visual pigments reveals that these similar systems translocate, upon vertical excitation, a similar net charge in the same axial direction.

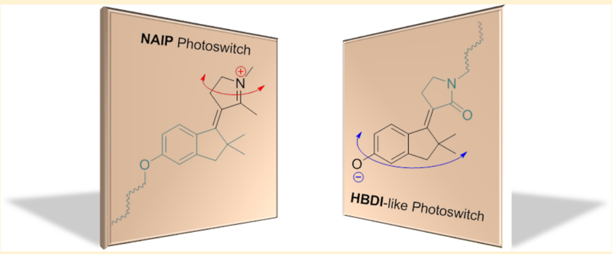

INTRODUCTION

The conversion of light energy into molecular motion is at the basis of the development of light-driven molecular devices such as molecular switches and motors.[1,2] Among these systems, single-molecule rotary devices are capable of funneling the energy of a photon into double bond isomerization modes and setting a *rotor* moiety in motion with respect to a *stator* framework.[3] Such a functionality has been employed in a number of prototype applications showing that it is possible to control ion complexation,[4,5] catalysis,[6] folding/unfolding of oligopeptides,[7] and other properties.[8−11]

While most of the above applications employed unnatural chromophores such as azobenzene, stilbene, and imine derivatives, during the past years, we have shown that mimicking closely the photoisomerization of biological chromophores represents a viable strategy for achieving alternative light-driven rotary devices. Indeed, we have reported the synthesis of several positively charged N-alkylated or N-protonated indanylidene pyrroline Schiff bases (NAIPs and NHIPs, respectively).[12−18] These (see Scheme 1, left) are biomimetic structures which replicate the reactivity of the retinal chromophore of visual pigments. For instance, NAIPs (in the following, we use NAIP to refer, in general terms, to both NAIP

Scheme 1. Molecular Framework of the Cationic Retinal Protonated Schiff Base Mimics MeO-NAIP (R = R′ = CH_3) and MeO-NHIP (R = H, R′ = CH_3) Compared with the Molecular Framework of the GFP Fluorophore *p*-HBDI Anion[a]

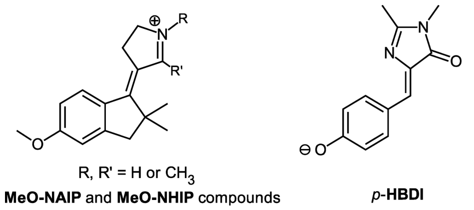

[a]The moiety of dMe-MeO-NAIP with R = CH_3, R′ = H is also discussed in the next sections.

Received: October 21, 2015

and NHIP) have been shown to undergo a regioselective subpicosecond double bond photoisomerization similar to that observed for the protein embedded chromophore of animal and microbial rhodopsins.[13,14,16,17] Due to their cationic nature, NAIPs provide opportunities for achieving systems with repositioning or rotating positively charged rotors with promising applications in materials science, synthetic biology, and nanotechnology.[19,20]

In spite of the results described above, it was not obvious until now that a biomimetic strategy could be successfully employed for achieving rotary devices beyond the current biological mimics. In the present report, we show that this is indeed the case by preparing a novel light driven switch bearing a negatively charged, rather than neutral or positively charged, rotor. More specifically, our biomimetic strategy has been reemployed to design and prepare a molecular switch mimicking the radiationless photoisomerization of the green fluorescent protein (GFP) fluorophore: the *para*-4-hydroxybenzylidene-2,3-dimethylimidazolinone (*p*-HBDI) anion (see Scheme 1, right).

GFP, originally from the jellyfish *Aequorea victoria*, can be readily expressed in a range of other organisms from microbes to mammals,[21] and it is widely used as a genetically encodable fluorescent probe due to its high fluorescence quantum yield, relatively small size, and spectroscopic features which can be tuned via mutation.[22] The *p*-HBDI fluorophore of GFP is hosted in a tight β-barrel cavity, which locks its central double bond and the adjacent single bond, yielding a photochemically nonreactive molecule and, consequently, an efficient emitter.[21,23,24] This conclusion is supported by the extreme loss of fluorescence displayed by *p*-HBDI in solution.[25] In fact, it has been shown both computationally[26] and experimentally[27] (both in isolated conditions[28] and in solution[29]) that a rapid twisting of the *p*-HBDI central bond[30] leads to radiationless deactivation via decay at a conical intersection between the first singlet excited state (S_1) and the ground state (S_0) of the molecule.[31]

The behavior described above has prompted us to look for *p*-HBDI mimics which could undergo the type of regioselective double bond isomerization required for the construction of rotary switches and motors but that, at the same time, could be efficiently prepared. Accordingly, we report on the computational design, preparation, and spectroscopic characterization of a synthetic *p*-HBDI mimic featuring a single exocyclic and photoisomerizable double bond connecting two rigid units. We show that the new switch not only offers features complementary to NAIPs (e.g., it is *negatively* rather than *positively* charged) but can also be prepared more efficiently, which is highly beneficial for its future applications.

■ RESULTS AND DISCUSSION

Design and Modeling. Only few studies pointed to the development of molecular switching functions based on *p*-HBDI mimics. Specific mutations of GFP or GFP-like proteins yielded chromophores capable of undergoing *E*/*Z* isomerization, making the protein fluorescence switchable via irradiation at specific wavelengths.[32] A synthetic *p*-HBDI mimicking switch has been proposed by Sampedro and co-workers;[33,34] however, its rotor is conformationally flexible due to the conservation of the exocyclic single bond present in the native *p*-HBDI framework (see Scheme 1) and does not contain the phenolic group needed to generate the corresponding anion. In order to design a *p*-HBDI-like framework with locked stator and rotor orientations, we decided to restrain the *p*-HBDI aromatic ring twisting by adding an ethylene (—CH_2—CH_2—) bridge to the structure (compare left and right structures in Figure 1). The bridge would prevent dissipation of the absorbed photon energy through rotation about the single aryl—alkene bond. We also decided to replace the imidazolone with a pyrrolidone moiety mainly to enable a facile synthesis (as detailed below) but also to enhance the translocation of the indanylidene negative charge along the molecular framework upon light absorption. This would facilitate the S_1 isomerization (i.e., the spectroscopic state S_1 is expected to have charge transfer character and its electronic structure is dominated by the resonance formula at the bottom right of Figure 1).

Before describing the synthesis and kinetic characterization (next subsection) of the anionic *p*-HBDI-like switch (from now on, "*p*-HBDI-like" will refer exclusively to the anionic form), it is useful to analyze its intrinsic (i.e., gas-phase) spectroscopy and reactivity computationally. Since the switch is designed to work

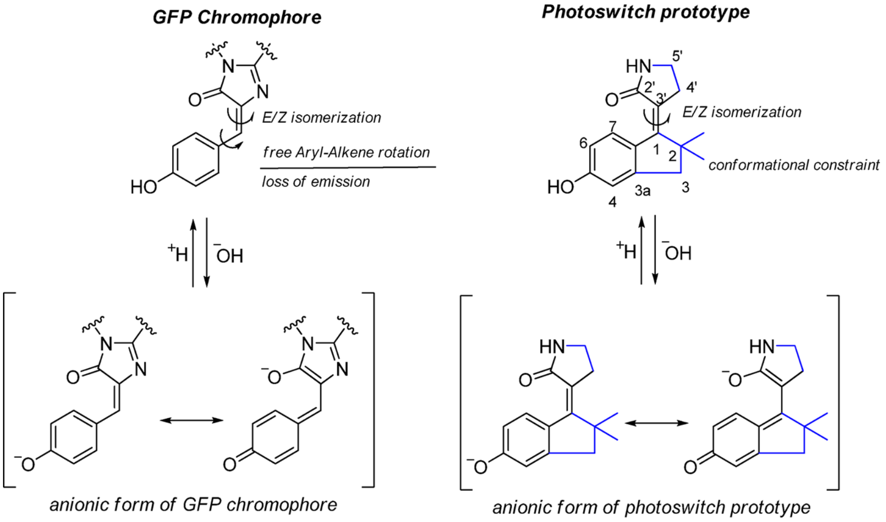

Figure 1. Structure of GFP chromophore (left), whose fluorescent anionic form corresponds to an alkyl derivative of *p*-HBDI, compared with the structure of the *Z* isomer of our designed *p*-HBDI-like switch (right). Both the neutral and anionic forms are displayed. The bonds in blue represent the points of modification with respect to the native *p*-HBDI structure.

in a polar solution environment, we do not deal here with the possibility of spontaneous electron detachment which may compete with the production of a bound excited state when an anion is in isolated conditions.[35,36] Accordingly, the *p*-HBDI-like S_0 and S_1 potential energy surfaces (PESs) were mapped both via density functional theory computations employing the REKS and SI-SA-REKS methods[37] and via wave function based computations employing the CASPT2//CASSCF protocol (see the Materials and Methods section for details). The S_0 equilibrium structures of the *E* and *Z* isomers of the switch are found to exist in conformations with P and M helicities and pyramidalized nitrogens, yielding two pairs of enantiomers (i.e., the P,R and M,S pair and the M,R and P,S pair) in a diastereomeric relationship with each other. Figure 2 displays the detailed *E*-P,R and *Z*-P,R diastereoisomers featuring P helicity and a R configuration of the nitrogen. As changing the N configuration did not seem to be relevant for studying the double bond isomerization, the N-inversion process was not investigated.

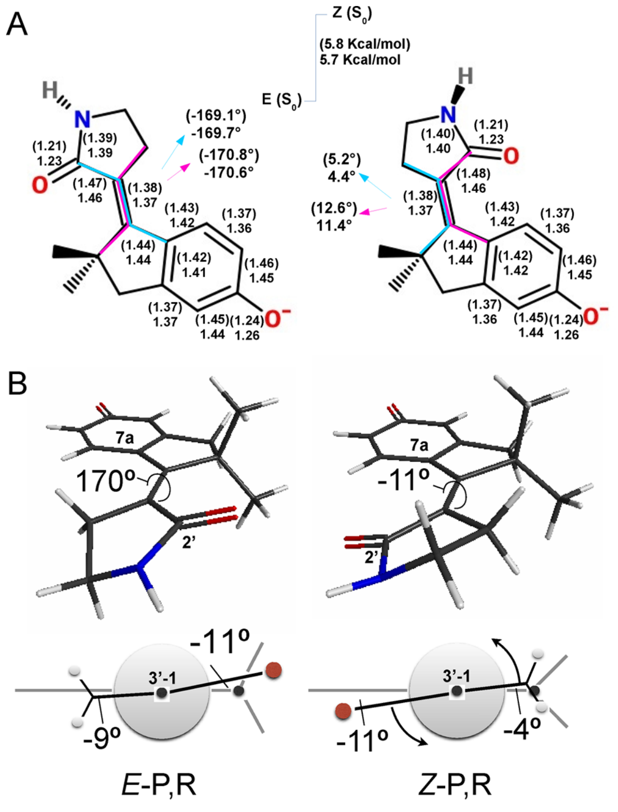

Figure 2. Computed gas-phase S_0 equilibrium structures of the designed *p*-HBDI-like switch. (A) Comparison between the relative energy and main geometrical parameters computed at the REKS and CASSCF (in parentheses) levels for the *E* (left) and *Z* (right) isomers in the P,R configuration: both computational methods yield similar results. (B) Perspective representation and Newman projections of the same *E*-P,R and *Z*-P,R structures.

Figure 3 reports the energies of the located minima and transition states along schematic S_0 and S_1 REKS energy profiles as a function of the C2′−C3′−C1−C7a dihedral angle (see Figure 1 for the numbering) describing the progression along the reaction coordinate. On the S_0 PES, the *E*-P,R stereoisomer, which is found to be the lowest in energy, does not feature a stable M,R diastereoisomer possibly because inversion of the pyrrolidone ring with R nitrogen disfavors the M helicity. However, both *Z*-P,R and *Z*-M,R could be located with the former lying 6.0 kcal/mol above *E*-P,R and the latter being 2.1 kcal/mol less stable. These diastereoisomers are connected by a shallow transition state with an activation barrier of 1.8 kcal/mol controlling the conversion from M to P leading to a change in helicity.

As shown in Figure 3, when starting from *E*-P,R, the thermal *E* → *Z* isomerization would directly produce the *Z*-M,R diastereomer by overcoming a large barrier. *Z*-M,R is then converted to *Z*-P,R via a shallow but distinct transition state. On the other hand, *Z*-P,R is connected to the original *E*-P,R structure through a second high energy transition state located 26.8 kcal/mol higher. If the ca. 30 kcal/mol computed *E* → *Z* and *Z* → *E* activation barriers are conserved in solution, one would predict a very slow thermal isomerization at room temperature with the system reaching the thermal equilibrium only at higher temperatures.

The vertical excitation energies calculated for the most stable *E*-P,R and *Z*-P,R *p*-HBDI-like diastereomers were obtained using the SSR-LC-ωPBE/6-31+G* method (see the Materials and Methods section for details). As shown in Figure 3, these correspond to 347 nm for *E*-P,R and 368 nm for *Z*-P,R, respectively. The difference between these values is suitable for modulating the photostationary state composition if, again, such a difference is maintained in solution. Using the SSR-LC-ωPBE/6-31+G* method, we located two minimum energy conical intersections (MECIs), which correspond to real crossings between the S_1 and S_0 PESs. These MECIs lie below the FC points by 18.9 kcal/mol ($MECI_{270}$ connecting *E*-P,R to *Z*-M,R) and 19.6 kcal/mol ($MECI_{90}$, connecting *Z*-P,R to *E*-P,R). The MECI geometries are shown in Figure 4A along with the corresponding branching plane (BP) vectors.

As apparent from Figure 3, the S_1 PES near the *E*-P,R and *Z*-P,R Franck−Condon (FC) points is rugged but flat (with energy barriers below 2.3 kcal/mol). The energy profile shows only a modest initial relaxation along the bond length alternation (BLA) displacement inverting skeletal double and single bonds (the BLA value is calculated as the difference between the average length of the single bonds and the average length of the double bonds in the O=C2′—C3′=C1—C7a=C7—C6=C5—O framework). In contrast, along the reactive double bond twisting coordinate (described by the C2′—C3′—C1—C7a dihedral angle), the flatness of the PES implies a nearly barrierless double bond twist. However, beyond ca. 40° twisting, the energy decreases sharply and distinct S_1 energy minima (not shown in Figure 3) are reached at ca. 90° twisting. These minima are only slightly (ca. 1 kcal/mol) below the corresponding MECIs, suggesting rapid decay to S_0 in spite of the weakly sloped rather than peaked topography[38] of the located MECIs. Such topography will be further discussed below.

It is noteworthy that the *E*-P,R conformation is pretwisted through ca. 10° in the counterclockwise (CCW) sense. This suggests that reaching $MECI_{270}$ from the *E*-P,R FC point is expected to be preferred, which implies a preference for CCW twisting. However, the flatness of the S_1 PES makes this prediction uncertain and dynamic simulations are needed to prove this conjecture. The same conjecture applies to *Z*-P,R that also features a CCW pretwisted structure prompting the isomerization motion toward $MECI_{90}$. Of course, a preferential CCW twisting of both *E*-P,R and *Z*-P,R would accomplish a complete *E* → *Z* → *E* rotation relative to the *E*-P,R isomer fueled by the sequential absorption of two photons. Symmetry considerations lead to the conclusion that the *E*-M,S enantiomer of *E*-P,R would undergo a complete rotation in the opposite CW direction.

DOI: 10.1021/jacs.5b10812
J. Am. Chem. Soc. XXXX, XXX, XXX−XXX

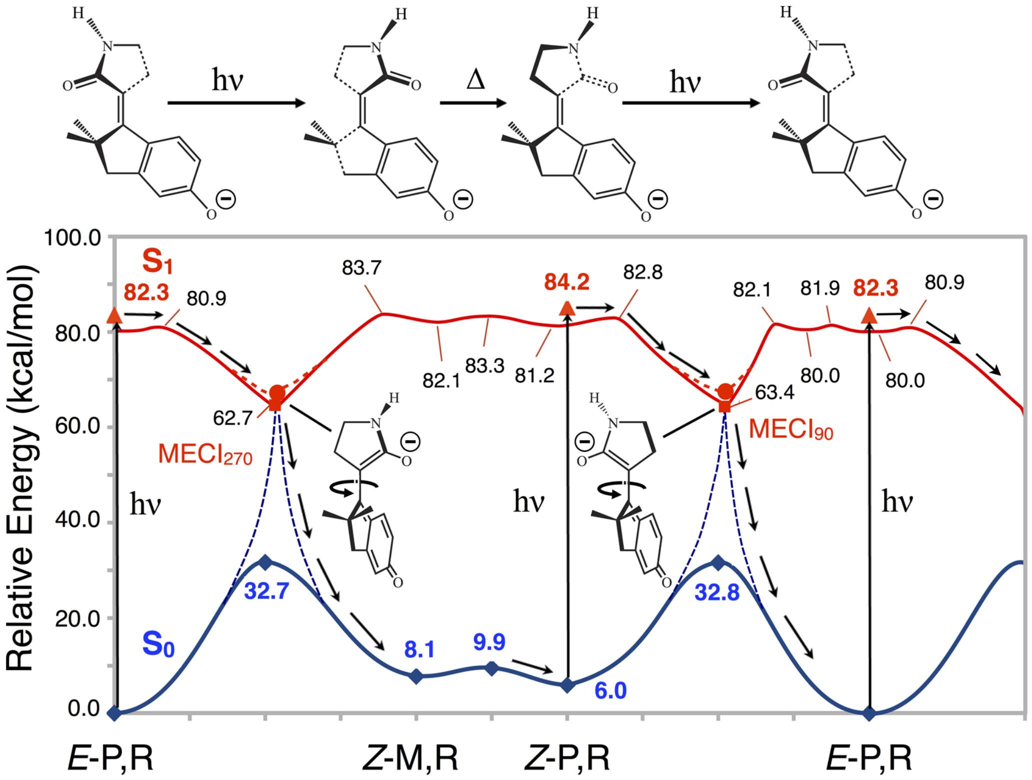

Figure 3. Schematic S_0 (blue) and S_1 (red) energy profiles along the isomerization paths of the *p*-HBDI-like switch. The reaction coordinate describes the counterclockwise twisting of the pyrrolidone moiety with respect to the indanylidene moiety, and the stream of arrows illustrates two sequential photochemical isomerization events. The energy profiles are computed at the SI-SA-REKS level of theory. The S_0 stationary points are shown as blue diamonds. The red triangles mark the vertical excitations at the optimized *E*-P,R and *Z*-P,R S_0 structures (i.e., the Franck−Condon points). The equilibrium S_1 minima are represented by red squares. The optimized MECIs where S_0 and S_1 energies are degenerate are marked with red circles. The energy profiles describing the relaxation paths through the MECI points along S_1 and S_0 are pictorially represented by dashed lines.

For a reaction occurring through a CI*nt*, the BP vectors play a role similar to the transition vector at a transition state driving a thermal reaction.[38,39] Thus, the BP analysis provides information on the atomic displacements leading away from the nonadiabatic coupling (i.e., from the MECI structures or from other nearby intersection seams and avoided crossing points) and, in turn, on the isomerization mechanism.[40−42] The BP vectors of the two MECIs of the *p*-HBDI-like switch are found to correspond, roughly, to the twisting about the exocyclic double bond and to the BLA mode (X_1 and X_2 in Figure 4A, respectively). Interestingly, these are the same BP displacements documented for NAIP molecular switches.[42] Such a similarity is consistent with a recent study[42] showing that switches undergoing a predominantly heterolytic breaking of a π-bond are likely to have S_1/S_0 MECI characterized by a twisting/BLA BP as opposed to the twisting/pyramidalization BP typical of molecules undergoing a predominantly homolytic π-bond breaking (e.g., polyenes). Indeed, the two electronic configurations representing the intersecting S_0 and S_1 states of the designed switch have charge-transfer (CT) closed-shell character and diradical (DIR) open-shell character, respectively (see Figure 4B). As we will now discuss, these electronic structures play an important role in determining the reactivity and S_1 dynamics of the system.

To test the possible involvement of triplet states in the switch photoisomerization, we have searched for minimum energy crossing points (MECPs) between the ground triplet state (T_0) and the S_0 and S_1 states. No T_0/S_1 MECP could be located within the energy range covered in Figure 3. Two T_0/S_0 MECPs were instead located in the proximity of each S_1/S_0 MECI point. Although these MECPs lie within 3 kcal/mol and are geometrically (RMSD ca. 0.034−0.036 Å) close to the MECIs, the S_1−S_0 energy gap at the position of these MECPs is in the range of 13 kcal/mol. Taken together, these results suggest that the T_0 population is not likely within the energy range achieved in the experiments, and that $S_1 \rightarrow S_0 \rightarrow T_0$ is unfeasible due to the wide S_1−S_0 energy gap at MECPs.

The SI-SA-REKS computations above provide reliable information on the PES structure of the bound S_1 state driving the switch photoisomerization.[43] However, the simulation of the dynamics of nonadiabatic processes at the SI-SA-REKS level is still impractical. For this reason, the gas-phase S_1 evolution and lifetime of the *p*-HBDI-like switch have been investigated using scaled-CASSCF semiclassical trajectories.[44] These are single surface-hop trajectories released from the FC point with no initial kinetic energy (from now on called FC trajectories) and employed for mechanistic studies of events falling in the sub-picosecond regime. Generally, there is a good agreement between the geometries, relative energies, and charge distributions of the species calculated by the SI-SA-REKS and the scaled-CASSCF methods (see the Supporting Information for more detail); hence, the latter method can be used in lieu of the former in the dynamics simulations.

The comparison of the S_0 equilibrium structures computed at the CASSCF and SI-SA-REKS levels (see Figure 2) and the comparison of the structures of the minima located along the flat CASPT2//CASSCF minimum energy path (MEP) S_1 energy

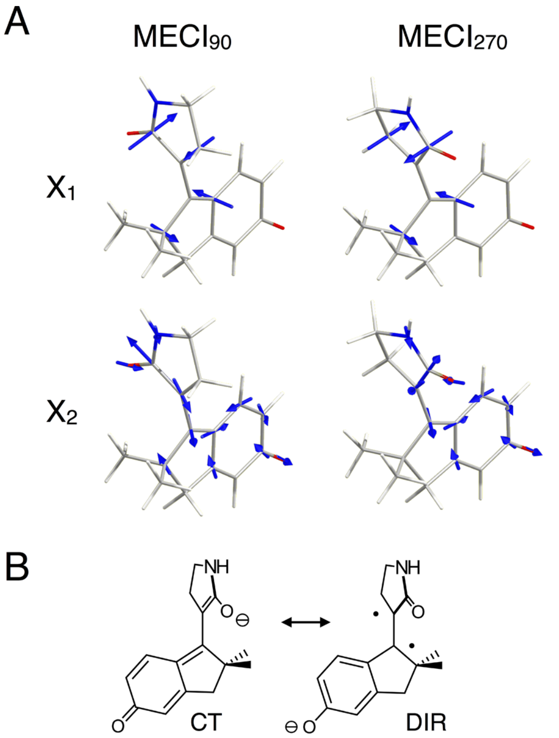

Figure 4. MECIs of the *p*-HBDI-like switch. (A) Geometries of the switch at the intersection connecting the *E*-P,R and *Z*-M,R stereoisomers (left) and the intersection connecting *Z*-P,R to *E*-P,R stereoisomers (right). The blue arrows, representing the atomic displacements in the BP vectors of both structures, correspond to double bond twisting (X_1) and BLA (X_2) distortions. (B) Lewis resonance structures dominating the intersecting S_0 and S_1 wave functions at the MECIs.

profiles (see Figure 5A and B) and the corresponding SI-SA-REKS S_1 minima of Figure 3 indicate a structural consistency between the two levels of theory. The energy difference between the equilibrium *E*-P,R and *Z*-P,R forms is also consistent (6.0 and 6.1 kcal/mol at the SI-SA-REKS and CASPT2//CASSCF levels, respectively), as it is for the charge distribution (see Table 1) for the FC structures and structures closest to the MECIs (indicated as "AC" in both Figure 5 and Table 1). On the other hand, the CASPT2//CASSCF excitation energies appear ca. 5 and 7 kcal/mol red-shifted with respect to the SI-SA-REKS values when using the 6-31G* and 6-31+G* basis sets, respectively, although all levels of theory consistently predict that the λ_{max} of *E*-P,R is blue-shifted compared to that of *Z*-P,R (see also the next subsection). Such excitation energy differences are assumed not to affect significantly the mechanistic information provided by the *E*-P,R and *Z*-P,R FC trajectories of Figure 5C.

It is apparent that, consistently with the MEP results of Figure 5A, the initial S_1 dynamics of the *p*-HBDI-like switch is, in general, dominated by a stretching relaxation (this is described by the bond length *L* defined in Figure 5C) followed by the central bond twisting relaxation along a flat S_1 potential energy region. Progression along a twisting (i.e., isomerization) coordinate is best reflected by the evolution of the value of the τ angle (the τ angle defined in Figure 5B reflects, approximately, the magnitude of the overlap between the π-systems of the indanylidene and pyrrolidone units) rather than the C2′−C3′−C1−C7a dihedral, and it confirms that, for the specific case of the *E*-P,R and *Z*-P,R diastereomers, the rotation proceeds in a CCW direction. Both diastereomers then reach an avoided crossing (AC) region in ca. 500 fs and continue their S_1 motion without decay to S_0. This suggests that a sub-picosecond decay may occur either via vibrational excitation or, as we will show below, via a solvent effect changing the topology of the PES in the decay region (e.g., changing an AC into a CI*nt* point). Indeed, as we will document below, an AC region is also detected in the gas-phase FC trajectory of the homologue MeO-NHIP switch of Scheme 1, while the corresponding condensed-phase FC trajectories (i.e.,, in a box of explicit MeOH solvent molecules) have been shown to intercept a region with much smaller S_1-S_0 energy gap, directly at a CI*nt* point, on a shorter time scale.[13]

A different property of the computed S_1 trajectories is revealed by the analysis of the charge translocation along the switch backbone. This analysis reflects the character of the S_1 electronic structure (i.e., the electronic wave function) in terms of the weight of CT or DIR resonance Lewis structure/electronic configuration (see Figure 4B). As displayed in Table 1, it turns out that (i) at the S_0 equilibrium structure (FC) the character of the S_0 wave function is mixed but dominated by the DIR/COV character (COV stands for covalent; DIR/COV indicates that the COV character smoothly turns into a DIR character at highly twisted double bond geometries where a homolytic π-bond breaking is accomplished); (ii) at the same FC structure the character of the S_1 wave function is mixed and contains both CT and DIR characters; (iii) after ca. 400 fs dynamics and in a situation where the twisting double bond is ca. 40° twisted, the S_1 electronic configuration dominating the reacting system turns to be completely DIR. Point iii indicates that the system is moving along a region of the S_1 PES which better correlates with the S_0, rather than S_1 wave function at the reactant structure. As we will detail in a comparative analysis below, such a region also appears in the MeO-NHIP switches but closer to the AC point, while a modestly dominating CT character is maintained along the twisting.

By definition, the CT and DIR character of the S_1 wave function are interchanged at a CI*nt* point.[45] Therefore, in order to provide an explanation for the fact that the *p*-HBDI-like switch intercepts an AC rather than a CI*nt* and for the fact that a large region of the S_1 PES has an electronic structure dominated by a DIR character, we have explored the MECI topography. As shown in Figure 6, it is found, at all levels of theory and for both the $MECI_{90°}$ and $MECI_{270°}$, that the intersection does not display a peaked topography but a slightly sloped topography along the X_2 vector dominated by the BLA coordinate. The S_1 energy profile correctly displays, for both *E*-P,R and *Z*-P,R, a minimum located slightly lower than the MECI point, as also found via geometry optimization (see above). Such a minimum has an electronic structure corresponding to the DIR character. The stationary point energies of Figure 3, the energy profiles of Figure 5A and C, and the energy profiles along X_2 in Figure 6A converge in the schematic representation of Figure 6B which summarizes the computational characterization of the designed molecule as well as the possible S_1 evolution.

Synthesis and Photochemistry. The designed *p*-HBDI-like switch was synthesized starting from 5-methoxy-1-indanone. Following the synthetic route shown in Scheme 2, the starting material was bismethylated in position C2 to obtain the indanone **1** which was then reacted with *N*-Boc-pyrrolidinone to obtain **2** through dehydration of the aldol condensation intermediate. The bis methyl substitution on the C2 of the 5-methoxy-1-indanone was performed to prevent the possible competition between the *endo* and *exo* cyclic dehydration of the intermediate alcohol.

DOI: 10.1021/jacs.5b10812
J. Am. Chem. Soc. XXXX, XXX, XXX−XXX

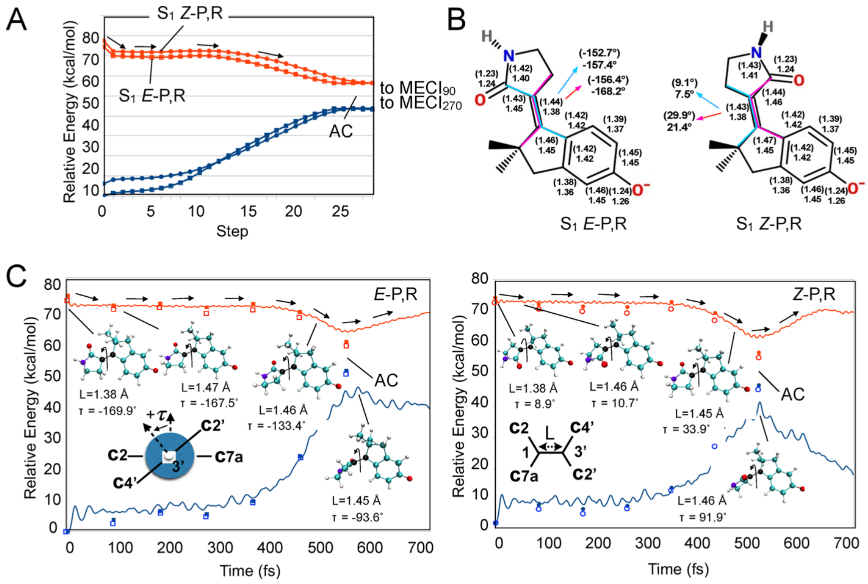

Figure 5. S_1 evolution of the *p*-HBDI-like switch. (A) S_1 (red) and S_0 (blue) energy profiles computed along the MEP (CASPT2//CASSCF/6-31G* level with a radius of 0.07 Å·(amu)$^{1/2}$) starting from both the *E*-P,R (circles) and *Z*-P,R (square) FC points and leading to the MECI$_{270}$ and MECI$_{90}$, respectively (see Figure 3). (B) Comparison between the located SI-SA-REKS *E*-P,R and *Z*-P,R S_1 energy minima of Figure 3 and the structures located at the center of the two S_1 shallow valleys found along the *E*-P,R and *Z*-P,R MEPs. The values in parentheses (Å and deg) refer to the CASSCF geometry. (C) Scaled-CASSCF/6-31G* S_1 FC trajectories for *E*-P,R and *Z*-P,R. The full circles and full squares refer to the single point CASPT2/6-31G* computations performed along the unscaled-CASSCF trajectories and used for scaling the CASSCF energy gaps and time scales (see the Supporting Information for details) given by the full lines. The corresponding open square points refer to the 6-31+G* basis set which does not seem to have a significant effect on the energy profile in spite of the additional diffuse functions. This is more probably due to the rather delocalized nature of the anionic charge. The structures along the trajectories provide information on the main geometrical evolution of the isomers (parameters in Å and deg). The definitions of the angle *τ* and bond length *L* are given as insets.

Table 1. Charge Evolution along the Trajectories of Figure 5C[a]

	E-P,R charges		*Z*-P,R charges	
	indanylidene frag.[b]	pyrrolidone frag.[b]	indanylidene frag.[b]	pyrrolidone frag.[b]
S_0 FC	−0.62 (−0.56)	−0.38 (−0.44)	−0.61 (−0.58)	−0.39 (−0.42)
S_1 FC	−0.51 (−0.58)	−0.49 (−0.42)	−0.51 (−0.58)	−0.49 (−0.42)
S_1 90 fs	−0.50	−0.50	−0.49	−0.51
S_1 180 fs	−0.52	−0.48	−0.50	−0.50
S_1 270 fs	−0.51	−0.49	−0.50	−0.50
S_1 360 fs	−0.56	−0.44	−0.56	−0.44
S_1 450 fs	−0.73	−0.27	−0.71	−0.29
S_1 AC	−0.98 [−0.96]	−0.02 [−0.04]	−0.98	−0.02
S_0 360 fs	−0.50	−0.50		
S_0 450 fs	−0.31	−0.69		
S_0 AC	−0.07 [−0.05]	−0.93 [−0.95]		

[a] We set the CT character dominating when the indanylidene fragment has charge ≥ −0.5 and the COV/DIR character dominating when the indanylidene fragment has charge < −0.5. [b] Numbers in parentheses indicate the corresponding values for the REKS optimized structures, and those in the square brackets, the values corresponding to the optimized MECIs (see Figure 3).

The methoxy group of **2** was then deprotected with BBr_3 to get the final phenolic compound **3** as an *E*/*Z* mixture (8:2). In compound **3**, the phenolic group is placed in the *para* position with respect to the double bond similarly to *p*-HBDI fluorophore, while carbons C2 and C3 (see Figure 1 for the numbering) provide the conformational locking of the final molecule. In conclusion, **3** was prepared in only three steps (compared to six required for the synthesis of the homologue NAIP compound in Scheme 2) and a total yield of 58% (versus ∼43% for the NAIP).[46,14]

Compounds **2** and **3** have been characterized by homonuclear and heteronuclear NMR analysis. In particular, NOE experiments on both compounds evidence contacts between H-4′ and H-7 for a dominant form and between H-4′ and H-A for a minor form, attributed to *E* and *Z* configurations, respectively. Moreover, the chemical structures and the configurations of *E*-**2** and *E*-**3** were also confirmed by crystallography and reported in Figures S1 and S2 of the Supporting Information.

The absorption spectrum of *E*-**3** depends significantly on the pH and the solvent.[47] The absorption maxima (λ_{max}) and spectra of **3** in different solvents and at neutral or strongly basic pH (i.e., after adding an excess of KOH to generate the target anionic form of the phenol) are reported in Table 2 and Figure 7. The neutral form of the *E*-**3** and *Z*-**3** isomers does not display significant solvatochromism, with λ_{max} values remaining in the 318−320 and 319−324 nm ranges, respectively. By contrast, the anion corresponding to the designed *p*-HBDI-like switch not

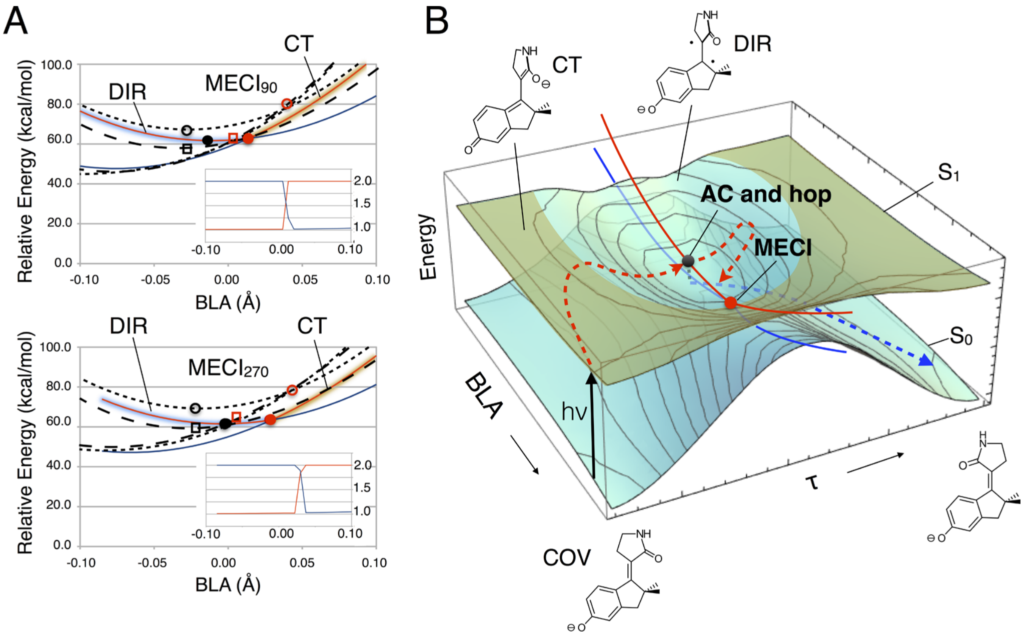

Figure 6. Structure of the PES driving *p*-HBDI-like photoisomerizations. (A) S_0 and S_1 energy profiles along cross sections corresponding to the X_2 vector of Figure 4A for the located MECIs. SI-SA-REKS (full line), unscaled CASSCF (dotted line), and CASPT2 (dashed line). The locations of the REKS (full black circle), CASSCF (open black circle), and CASPT2 (open black square) energy minima correspond to avoided crossings (ACs). For the corresponding CI*nt*'s, the corresponding symbols are in red. The insets show the occupation of a stronger occupied active orbital of SSR; the occupation close to 1.0 indicates the COV and/or DIR electronic configuration (see text) which are shaded in blue on the energy profiles; the occupation close to 2.0 indicates the closed-shell CT electronic configuration shaded in brown. (B) Schematic representation of the structure of the S_1 PES driving the photoisomerization of the switch. The photochemical reaction path for the *E*-P,R diastereomer is marked with dashed red (S_1 relaxation) and blue (S_0 relaxation) curves. The angle τ defined in Figure 5C reflects, approximately, the magnitude of the overlap between the π-systems of the indanylidene and pyrrolidone units. The BLA displacement is inverting skeletal double and single bonds along the O=C2′—C3′=C1—C7a=C7—C6=C5—O framework.

Scheme 2. Synthesis of 3 (*p*-HBDI-Like Compound) and Comparison with NAIP Compounds[a]

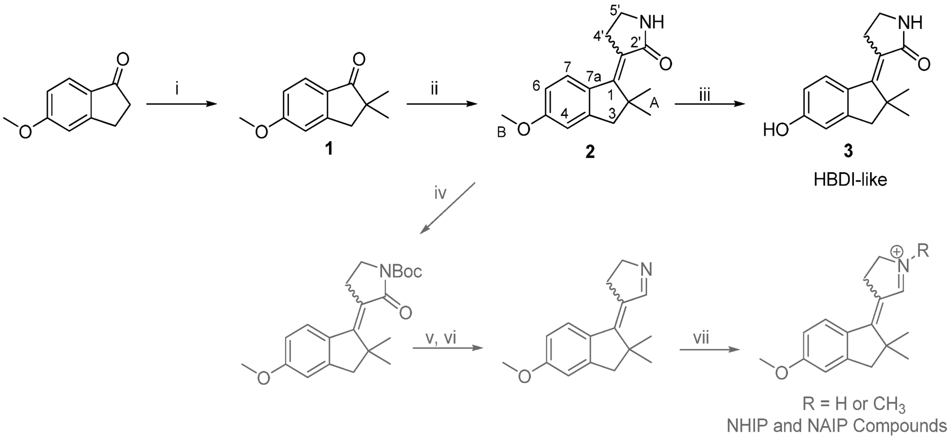

[a]Reagents: (i) MeI, *t*-BuOK, *t*-BuOH, Et_2O; (ii) *N*-Boc-pyrrolidinone, LiHDMS, $BF_3(Et)_2O$, THF, TFA; (iii) BBr_3, DCM; (iv) di-*tert*-butyl dicarbonate, DMAP, TEA, DCM; (v) CH_3MgBr, THF; (vi) TFA, DCM; (vii) MeOTf or HCl, benzene.

only features a significant red shift of the λ_{max} values with respect to the neutral form but also displays solvatochromism. (Notice that the *E*-**3** anion is a racemic mixture of *E*-P,R and *E*-M,S enantiomers while the *Z*-3 anion is a racemic mixture of *Z*-P,R and *Z*-M,S enantiomers).

The computed gas-phase *p*-HBDI-like switch λ_{max} values (also reported in Table 2) fall either relatively close to the observed quantities (SI-SA-REKS) or ca. 5 kcal/mol red-shifted (CASPT2//CASSCF). This may be compared with the NHIP behavior showing gas-phase λ_{max} values significantly, ca. 10 kcal/mol, red-shifted with respect to methanol solution. In NHIP, this is explained by the solvent stabilization of the S_0 charge distribution with respect to the S_1 translocated charge distribution. In fact, the λ_{max} of the close NAIP compound of Scheme 1 (with R = Me) is computed to be 452 nm (*E*) and 449 nm (*Z*) at the CASPT2//CASSCF level[48] and confirmed by a measured gas-phase value of 447 nm for the *Z* isomer, while the observed values in methanol are 377 nm (*E*) and 385 nm (*Z*).[16] The difference between NAIP and *p*-HBDI-like switches can be, in part, explained by the fact that upon vertical excitation NAIP

Table 2. λ_{max} Value of the *E*-3 and *Z*-3 Neutral and Anionic Forms in Different Solvents

solvent (dipole moment)	*E*-3 (nm) neutral	*E*-3 (nm) anionic[a]	*Z*-3 (nm) neutral	*Z*-3 (nm) anionic[a]
water (1.85)	319	348	321	351
methanol (1.70)	320	351	324	359
ethanol (1.69)	320	356	322	360
DMSO (3.96)	320	381	322	386
DMF (3.82)	318	383	319	386
gas phase (computed)		347 (384)[b]		368 (402)[b]
methanol (computed)[c]		375		397

[a] Generated by addition of KOH to the neutral solutions. [b] SI-SA-REKS and CASPT2//CASSCF (in brackets) values. [c] CASPT2//CASSCF/6-31G*/AMBER computations (see last subsection).

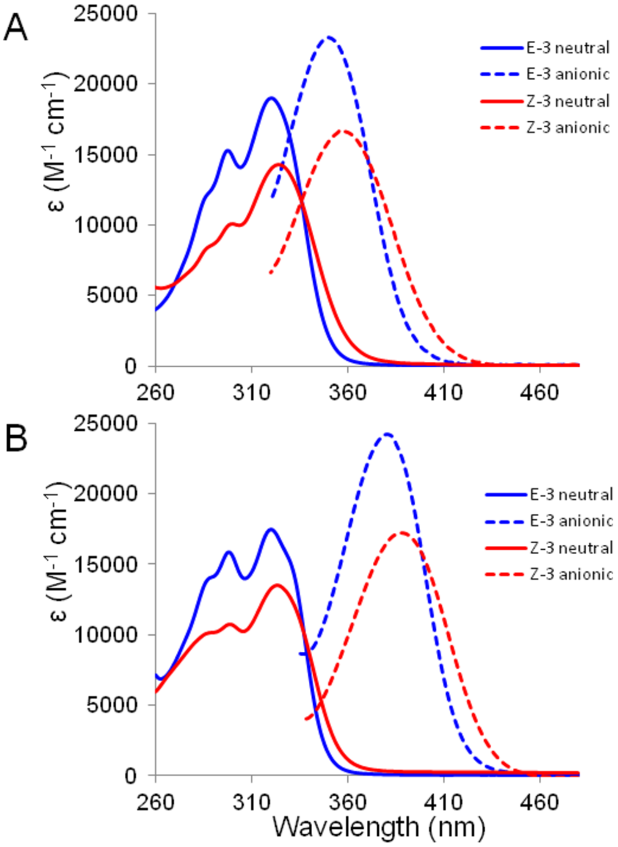

Figure 7. UV–vis absorption spectra of *E*-**3** and *Z*-**3**. The anionic forms are obtained by addition of KOH. (A) Methanol solution. (B) DMSO solution. While the S_0 to S_1 absorption spectrum of the neutral form is structured, that of the anionic form is not. We argue that this could result from the much stronger interaction of the anionic form with polar solvents. The enhanced solute–solvent interaction would damp the observed structure because of enhanced inhomogeneous broadening.

displays a 30% charge transfer between the indanylidene and pyrrolinium moieties[15] while Table 1 shows that our *p*-HBDI-like switch displays a much weaker ca. 10% charge translocation. With a smaller charge translocation occurring upon excitation to S_1, the solvent effect is expected to be of a lesser extent. This is supported by additional TD-DFT calculations performed with and without PCM solvent environment, which show a ca. 10 nm solvent induced blue-shift. As we will discuss below, the use of an explicit solvent model (i.e., a box of methanol molecules described at the molecular mechanics level) predicts, consistently, a 10 and 5 nm solvent induced blue-shift for the *E* and *Z* isomers, respectively.

While it has been reported that the counterions form solvent separated ion pairs in methanol,[16] less separated ion pairs and other factors may be involved in determining the ca. 30 nm red-shift observed in the aprotic DMSO or DMF solvents with respect to methanol. These solvents appear to provide a better stabilization of S_1 with respect to S_0 or, alternatively, a lesser stabilization of the S_0 with respect to S_1 in comparison with protic solvents (e.g., through formation of solvent–solute adducts).

The photoisomerization of **3** was investigated by irradiation in a Pyrex NMR tube at room temperature (ca. 5.0 mg in 0.5 mL of CD_3OD or DMSO-d_6) at three different wavelengths across the absorption bands for each solvent in neutral or anionic form. The isomer composition of the corresponding photostationary states is given in Table 3 and was determined using ^{1}H NMR spectroscopy by computing the area ratio of the signal attributable to H-7. Distinct photostationary states were reached upon irradiation at different wavelengths, demonstrating that it is possible to modulate the isomeric equilibrium in line with the differences in λ_{max} of the two forms.

Table 3. Analysis of the Photostationary States Composition of the Neutral and Anionic Forms of 3 in Methanol and DMSO, at Different Irradiation Wavelengths

irradiation λ_{max} (nm)	solvent	*E*/*Z* composition (±0.1)	$\varepsilon_E/\varepsilon_Z$[b]	η_{ZtoE}/η_{EtoZ}[c]
		Neutral Form		
290	CD_3OD	1/1.40	1/0.68	1/0.95
290	DMSO-d_6	1/1.35	1/0.71	1/0.96
320	CD_3OD	1/1.07	1/0.73	1/0.78
320	DMSO-d_6	1/1.05	1/0.75	1/0.79
360	CD_3OD	1/0.19	1/4.6	1/0.87
360	DMSO-d_6	1/0.21	1/3.1	1/0.66
		Anionic Form[a]		
320	CD_3OD	1/1.48	1/0.57	1/0.84
350	DMSO-d_6	1/1.35	1/0.55	1/0.74
350	CD_3OD	1/1.29	1/0.68	1/0.88
380	DMSO-d_6	1/1.32	1/0.69	1/0.91
410	CD_3OD	1/0.11	1/5.3	1/0.58
440	DMSO-d_6	1/0.10	1/5.3	1/0.53

[a] Generated by addition of a drop of 40% NaOD in D_2O. [b] *E*/*Z* ratio of the extinction coefficients ε given in Figure 7. [c] Ratio of the photoisomerization yields calculated as a product of the *E*/*Z* composition of the PSSs by the *E*/*Z* ratio of the extinction coefficients (see text).

After irradiation, the resulting mixtures were stored at room temperature in the dark for a few days without displaying a significant change in composition. In line with the ca. 30 kcal/mol S_0 energy barriers computed for double bond isomerization (see Figure 3), the lack of thermal return indicates that the energy barrier for S_0 (i.e., thermal) *Z*/*E* isomerization is high enough to restrain such a process at room temperature. Conversely, upon heating at 100 °C for 24 h in DMSO-d_6, pure *E*-**3** (isolated by flash chromatography) and *E*/*Z* mixtures of **3** in both the neutral and anionic forms yielded an *E*/*Z* ratio of 1/0.1. Under these conditions, no decomposition was observed, confirming the compound chemical stability.

In the absence of thermal isomerization and photodegradation, the relative concentrations [*E*]/[*Z*] of both isomers in the PSSs at a given illumination wavelength are only controlled by the relative excitation probabilities (given by the extinction coefficients ε_E and ε_Z) and the photoisomerization quantum yields (QYs, η_{EtoZ} and η_{ZtoE}) of both isomers at this wavelength. More precisely, from the spectra displayed in Figure 7 and the PSS E/Z compositions given in Table 3, we can infer the ratio of QYs of both isomers as $\eta_{ZtoE}/\eta_{EtoZ} = [E]/[Z] \times (\varepsilon_E/\varepsilon_Z)$ also reported in Table 3. This reveals that, for both anion and neutral forms, in MeOH or DMSO, the QYs of both isomers differ by no more than 20% when illuminating at the maximum or high energy side of the absorption spectra. Upon illumination in the red most part of the spectra where the extinction coefficients are much weaker, the QY ratio become inaccurate but remains similar to at most a 50% difference between both isomer QYs. Then, we conclude that the PSS compositions are essentially determined by the relative extinction coefficients of both isomers. This explains why the *Z* isomer cannot be accumulated as much as the *E* isomer, since there is no wavelength where *Z* has a significantly weaker absorption than *E*.

The absolute photoisomerization quantum yield of the *E* isomer of the neutral compound in methanol was determined to be 0.19, by HPLC analysis upon irradiation at 315 nm. For the anionic *E*-**3** compound, a quantum yield of 0.16 was determined by spectrophotometric analysis upon 350 nm irradiation. See the Materials and Methods for details. According to Table 3, the *Z* isomers have similar or slightly higher (by ~20%) photoisomerization quantum yields. These values are in the same range as or slightly lower than those of the cationic MeO-NAIP (see Scheme 1: R = R′ = CH_3), which were reported to be 0.34 and 0.19 for the *E* and *Z* isomers, respectively,[15] or of *E*-dMe-MeO-NAIP (see Scheme 1: R = CH_3, R′ = H), reported to be 0.25.[14]

Photoisomerization Dynamics. The computational investigation of the *p*-HBDI-like switch indicates that the system may undergo light induced isomerization on a sub-picosecond time scale in solution and at room temperature. The synthesis of **3** allowed for an experimental verification of the energy landscape and dynamics summarized in Figure 6B. Accordingly, a methanol solution of pure *E*-**3** (that is containing <3% of *Z*-**3**) with an excess of KOH generating the anionic form was investigated by femtosecond transient absorption (TA) spectroscopy in two distinct experiments allowing photoexcitation at two different wavelengths (see the Materials and Methods). First, a 350 nm femtosecond pump, tuned at the S_0 to S_1 absorption maximum, was used to excite the system. Second, a 400 nm pump was used to prepare the system in a different Franck–Condon state minimizing the initial excess of vibrational energy in S_1. Both experiments deliver very similar TA data, and Figure 8 displays an overview of the data obtained upon 350 nm excitation in the form of a 2D map (the same 2D map obtained upon 400 nm excitation is disclosed in Figure S3). Ground state bleach (GSB) is expected as a negative signal (blue coded) at wavelengths where S_0 *E*-**3** absorbs, and is indeed observed at probing wavelengths shorter than 375 nm. S_1 signatures are observed at early times and are composed of (i) an excited state absorption (ESA) which partially overlaps with the GSB and appears as a positive signal (red coded) in the range 375–440 nm and (ii) a stimulated emission (SE) band appearing as a negative signal (blue to violet) at wavelengths >440 nm. Within the first 1 ps, the early SE and ESA signatures have decayed, to reveal a longer lived (positive, yellow) band centered at 400 nm which further decays and spectrally narrows on the ps time scale to eventually form the relaxed ground state photoproduct absorption (PA) signature, as will be clearly identified below.

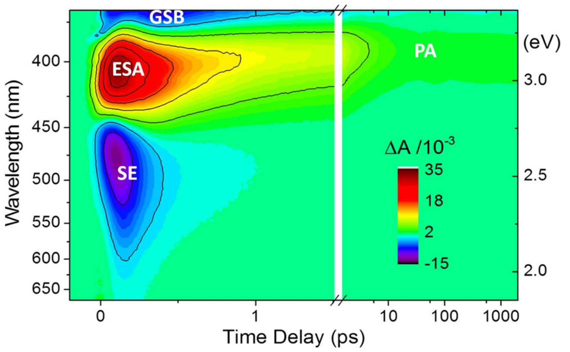

Figure 8. False color 2D map of the TA data (Δ*A*) measured upon 350 nm excitation of the anionic *E*-**3** in methanol, as a function of probe wavelength (nm) or energy (eV) and pump–probe time delay (ps).

Figure 9 displays detailed insight into the TA data obtained with *E*-**3** in methanol upon 350 nm (same data set as in Figure 8) and 400 nm excitations. Parts A and B of Figure 9 compare a selection of TA spectra recorded in both experiments. The various spectral signatures introduced above appear very similar in both experiments, with a somewhat broader ESA band, extending about 20 nm further to the red, when a 350 nm excitation pulse is used, populating higher-lying vibrational levels in the S_1 state. In the 175 fs spectra in both experiments, the SE has already decayed around 450–470 nm, while it has increased at wavelengths λ > 500–550 nm. This indicates spectral relaxation in the S_1 state, attributed to vibrational and possibly very fast polar solvent relaxations.[49] In the 400 fs spectrum, both SE and ESA have decayed significantly while the GSB (λ < 375 nm) remains deep (see in particular Figure 9B). At 1.5 ps, the SE has completely vanished and the GSB has partially recovered, as best seen in the 400 nm pumped experiment where probing wavelengths extend further in the UV (Figure 9B). This spectral shape further evolves on the several ps time scale until a stationary spectrum is observed (Figure 9C), which overlaps with the difference between the *Z*-**3** and *E*-**3** steady-state absorption spectra. This is the definitive evidence that the final product is *Z*-**3** (i.e., a racemic *Z*-P,R + *Z*-M,S). Knowing the pure *Z*-**3** and *E*-**3** extinction coefficients (Figure 7A), the relative intensity of the final difference spectrum with respect to that of the initial GSB (~3 mOD at 350 nm, see Figure 9B) allows us to estimate the *E* to *Z* photoisomerization quantum yield to be ~0.22. This estimate is however uncertain due to the overlap of the GSB with the initial strong ESA (i.e., the initial GSB is possibly larger than 3 mOD). Hence, this value should be considered as an upper boundary, in agreement with the reference value of 0.16 obtained by HPLC analysis (see above).

Figure 9D compares a selection of kinetic traces recorded in the SE spectral window with 350 or 400 nm excitation. The traces, which are remarkably similar in both experiments, display a marked (i.e., time-resolved) rise, and the SE signal maximum is observed at a time delay which increases with the wavelength, from ~100 fs at 463 nm to ~185 fs at 675 nm (see small vertical arrows in Figure 9D and the more detailed analysis in Figure S4). Whether this behavior reflects a wavelength dependence of the SE signal onset or is due to an overlapping, very short-lived, red to infrared ESA band (as, for instance, observed in the NAIPs[13,17]) is uncertain. In any case, this delayed onset indicates motion/relaxation (or solvation) away from the FC region on the ~150 fs time scale. Interestingly, in the red-most part of the probing window (see the traces at 675 nm), this motion out of the FC region appears somewhat slower (by ~50 fs, with an accuracy of ±30 fs) in the 400 nm pump experiment characterized by a minimal excess of vibrational energy. Figure 9E displays the ESA, GSB, and PA kinetics at UV probing wavelengths, a spectral window which is best covered by

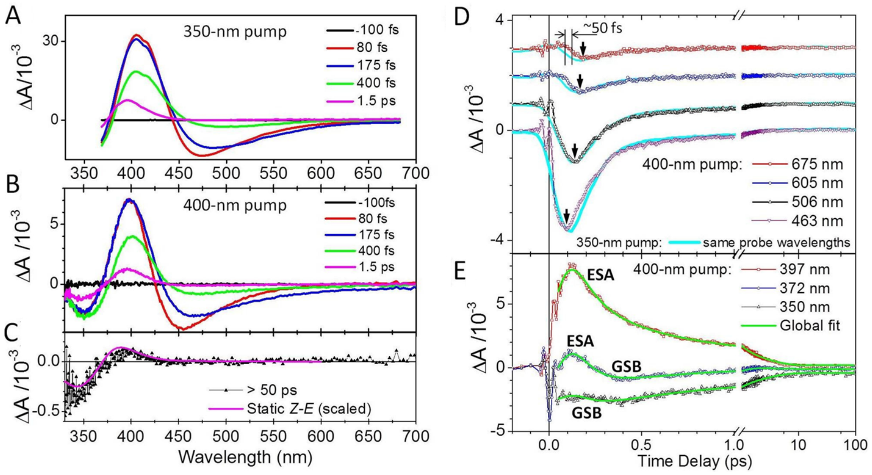

Figure 9. Selection of TA spectra of *E*-**3** in methanol in excess of KOH, obtained upon 350 nm (see panel A) and 400 nm (see panel B) excitation wavelengths. (C) Final (>50 ps) TA spectrum obtained upon 400 nm excitation, overlapped with the difference between static *Z*-**3** and *E*-**3** absorption spectra. (D) Comparison between the kinetic traces observed at a selection of probing wavelengths in the SE band upon 350 and 400 nm excitation. The arrows indicate the maximum of the SE signal amplitude occurring at later times for increasing probing wavelengths. At the 675 nm probing wavelength, there is an indication of a 50 fs larger delay in the SE signal rise when exciting at 400 nm as compared to 350 nm. (E) ESA decay kinetics probed in the UV region upon 400 nm excitation and global fit. The early oscillations observed in the range −50 fs to +50 fs in panels D and E are an artifact resulting from the imperfect cancellation of the intense solvent signal in the 400 nm pumped experiment (see Figures S3 and S4).

the experiment performed with the 400 nm pump, even if imperfect solvent artifact correction causes spurious residual oscillations in the range from −50 to +50 fs. The 396 nm kinetic trace is a simultaneous contribution of the overlapping ESA decay and PA rise and further thermalization. At 372 nm, the decay of the (positive) ESA signal within ~400 fs reveals the underlying (negative) GSB, while, at 350 nm, the signal remains nearly constant over the first 500 fs, most likely as a result of the compensating time evolutions of both ESA and GSB overlapping at this wavelength.

Quantitative analysis of TA data is commonly done by global fitting, which assumes that spectral (λ) and time (t) variables are separable[50] and is therefore ideally suited to recover exponentially decaying populations characterized by time-independent (i.e., vibrationally relaxed) spectra. In the present case of dynamic spectral shifts, as illustrated above, this assumption becomes questionable and the decay kinetics may deviate, especially at early times, from the multiexponential decay expected from a rate equation modeling of population kinetics. To account for that, we use as a fitting function the sum of a multiexponential decay and of a Gaussian function of standard deviation σ, centered on the time origin, a priori accounting for the instrument response function (see details in the Supporting Information). In the general case, the amplitude of that Gaussian function would account for a nonresolved kinetics (in which case the detected time evolution is indeed that of the IRF). Here, it may also account for the wavelength dependence of the signal onset due, e.g., to dynamic spectral shifts, in which case the parameter σ is no longer solely related to the experimental time resolution. This choice of fitting function is a practical way to significantly improve the quality of the fitting at early times, and therefore also at later times due to the interdependence of the time scales extracted from multiexponential global fitting.

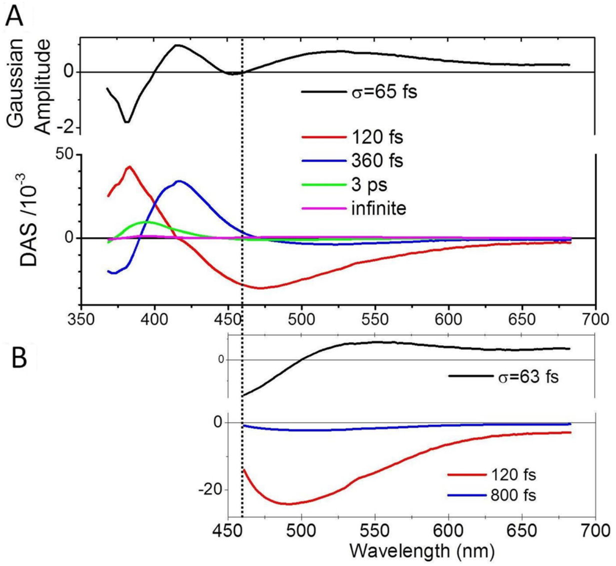

Figure 10. Global analysis of the TA data of *E*-**3** upon 350 nm excitation. (A) Gaussian-associated and Decay-Associated spectra (see details in the Supporting Information) (B) The same analysis performed on the λ > 460 nm portion of the data set enables a more specific characterization of the biexponential decay kinetics of the SE band.

The result of this global fitting of the 350 nm pumped TA data (see details in the Supporting Information, Figure S5) is displayed in Figure 10A in the form of a "Gaussian-associated" spectrum and usual "decay-associated" spectra (DAS). The amplitude of the Gaussian-associated spectrum is low, but still its positive sign at λ > 475 nm and the value of σ = 65 fs (corresponding to a Gaussian fwhm of 2.34 × σ ~ 150 fs) are accounting for the 150 fs delayed onset of the (negative) SE signal in that wavelength range. Also, its positive and negative extrema around 420 and 380 nm, respectively, are in line with an early blue shift of the (positive) ESA signal on the same time scale, which is close to the experimental time resolution. Then, the 120 fs DAS has the same shape as the SE band at λ > 420 nm, and therefore reveals the decay of the SE signal on this time scale. The positive sign of the same DAS for λ < 420 nm is in line with the decay of the short-wavelength portion of the ESA band which overlaps the GSB in that spectral window (Figure 8). This very fast SE and ESA decay is followed by a 400 fs DAS corresponding to the simultaneous recovery of the GSB ($\lambda < 380$ nm) and decay of the band peaking at 420 nm. We attribute this DAS to a second excited state decay component. Subsequently, the 3 ps DAS is attributed to ground state spectral relaxation due to further vibrational and solvent relaxation, in line with what was already observed for the NAIP compounds in the same solvent.[16,17] The final "infinite" DAS accounts for the long-lived differential spectrum already discussed in the 400 nm pumped data, Figure 9C.

The same global analysis is done on the 400 nm data, but time delays shorter than 50 fs are disregarded to avoid complications due to spurious solvent artifact in that data set (see details in the Supporting Information). The result of this global fit is illustrated by a selection of wavelengths in Figure 9E. The corresponding DAS (see Figure S6) appear almost identical to Figure 10A, with two excited state decay components of 100 and 430 fs, followed by a 2.5 ps vibrational/solvent cooling in the ground state. This confirms that the excited state dynamics and decay of compound *E*-**3** is weakly affected by the initial excess of vibrational energy and therefore suggests that the vibrational modes optically excited and responsible for the early fast motion out of the FC region are not immediately coupled to the reaction coordinate responsible for the S_1 decay (e.g., torsion around the isomerizing bond). As computationally documented above, this initial motion is dominated by a stretching relaxation (BLA mode), like in other isomerizing systems including NAIPs[51] and rhodopsins.[44] This relaxation unlocks the torsion motion which in turn is induced by the slope of the S_1 potential surface, shown to be rather flat for *E*-**3** (Figure 5).

p-HBDI-Like versus NAIP Isomerization Mechanisms. Figure 11 compares the room temperature kinetic traces recorded upon 400 nm excitation for *E*-**3**, *E*-dMe-MeO-NAIP[14] (see Scheme 1: R = CH_3, R′ = H), and *E*- and *Z*-MeO-NAIP[13] (R = R′ = CH_3) in methanol solutions, at wavelengths representative of the SE decay kinetics. Table 4 compares the excited state lifetimes of the same four compounds. The SE decay kinetics of anionic *E*-**3** (black trace) appears qualitatively similar to that of the cationic *E*-dMe-MeO-NAIP (red trace, see the TA 2D map in Figure S7A). For both compounds, the SE signal is seen to increase until 100−160 fs, where it reaches its maximum amplitude. After the maximum, both kinetics are correctly fitted with a biexponential function. For *E*-dMe-MeO-NAIP, the dominating (85%) decay component is 300 fs and the second SE decay time is 0.9 ps, while the ESA decays with a 350 fs decay time, similar to the first component of the SE (see fits in Figure S7B).

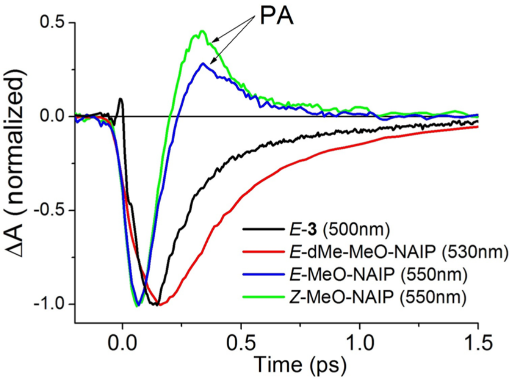

Figure 11. Comparison of the TAS data obtained upon 400 nm excitation for methanol solutions of *E*-**3**, *E*-dMe-MeO-NAIP, and *E*- and *Z*-MeO-NAIP, at a selection of probing wavelengths (in parentheses) representative of the SE decay kinetics of each compound. For both isomers of MeO-NAIP, the rapid SE decay is followed by the impulsive rise of the photoproduct absorption (PA). For the *E*-**3** kinetic trace (black), the very short-lived positive dip around 0 ps is a residual of a solvent-induced signal, not a signature of *E*-**3** dynamics.

In the case of both *E* and *Z* isomers of the cationic MeO-NAIP (R = CH_3, R′ = CH_3), the negative SE signal measured at 550 nm is instead seen to rise instantaneously (i.e., within an experimental time resolution of ~80 fs in these experiments, see blue and green traces in Figure 11). This is in line with the results of fluorescence up-conversion experiments performed on the *Z* isomer (ref 16) and revealing a biphasic decay with a <40 fs time scale indicative of a dynamic Stokes shift due to fast motion out of the FC on this time scale. Also, the photoreactivity of MeO-NAIP is characterized by the peculiar vibrationally coherent motion (see ref 13) of an S_1 population which decays after about 200 fs, resulting in the impulsive onset of the photoproduct absorption (PA) seen in Figure 11. No such impulsive PA signal is seen in the *E*-**3** nor dMe-MeO-NAIP compounds. In MeO-NAIP, this positive PA signal overlaps and masks any putative longer-lived (negative) SE signal and precludes the biexponential fit analysis of the SE kinetics. However, a second, 300 fs decay component observed in the MeO-NAIP fluorescence emission (ref 16) may well correspond to a subpopulation residing in S_1 somewhat longer than the vibrationally coherent population observed to decay to S_0 already after ~200 fs.

Altogether, a biphasic SE or fluorescence decay is observed in all compounds, with in addition evidence for a biphasic ESA decay for *E*-**3** with both time constants associated with two distinct spectral signatures. The spectrally broad, red-shifting, and short-lived SE band of *E*-**3** resembles that of MeO-NAIP[13] even if the relaxation dynamics out of the FC region appears slower in *E*-**3**. However, while in MeO-NAIP this broadband, short-lived SE signal is followed by the impulsive onset of a red-detuned photoproduct signature, in *E*-**3** it is followed by the 360−430 fs decay of the 420 nm band, which we attribute to the ESA of S_1 in conformations where SE is instead much weaker (see the small SE amplitude in the 360 fs DAS, Figure 10). This longer excited state lifetime and the lack of impulsive photoproduct are instead similar to the case of dMe-MeO-NAIP, where the SE band is spectrally narrower, does not show such a short 120 fs decay component, and remains detected during the entire S_1 lifetime dominated by a 300−350 fs time constant also characterizing the ESA decay. We therefore conclude that the S_1 dynamics of *E*-**3** can possibly be interpreted in two ways:

(i) Sequential scenario: The motion out of the FC rapidly drives the sytem, within ~250 fs (~150 fs spectral shift followed by 120 fs decay), in a distinct configurational subspace of S_1, where the SE and the UV side of the ESA band become much weaker, and only the ESA band centered at 420 nm may be detected. The system subsequently decays to S_0 on the 360−430 fs time scale.

(ii) Parallel scenario: Following the early motion out of the FC region, S_1 decays along two distinct pathways (possibly corresponding to distinct conformations already populated in the ground state), one on the 120 fs time scale, characterized by a dynamically shifting UV ESA and red SE, and a second one on the 360 fs time scale characterized by the 420 nm ESA and weaker SE. The analogy with the

Table 4. Comparison of the Excited-State Lifetimes (in fs) Measured in Methanol for the Anionic *p*-HBDI-Like upon 350 or 400 nm Excitation and for the Cationic dMe-MeO-NAIP and MeO-NAIP Compounds upon 400 nm Excitation

anionic *p*-HBDI-like *E*-**3** pumped @ 350 nm	anionic *p*-HBDI-like *E*-**3** pumped @ 400 nm	dMe-MeO-NAIP[c] *E*	MeO-NAIP *E* and *Z*
SE[a]: 120 (90%), 800 (10%)	SE[a]: 100 (90%), 600 (10%)	SE: 300 (85%), 900 (15%)	200[d]
ESA[b]: 120 (380 nm), 360 (420 nm)	ESA[b]: 100 (380 nm), 430 (405 nm)	ESA: 350	

[a] A specific global analysis of the SE decay is performed on the *E*-**3** data set spectrally restricted to the SE band (see Figure 10B and Figure S8). [b] Both ESA decay times correspond to distinct ESA bands (absorption maxima given in parentheses); see Figure 10 and Figure SI-6. [c] See data and fit in Figure SI-7. [d] Lifetime of the vibrationally coherent S_1 population; see text.

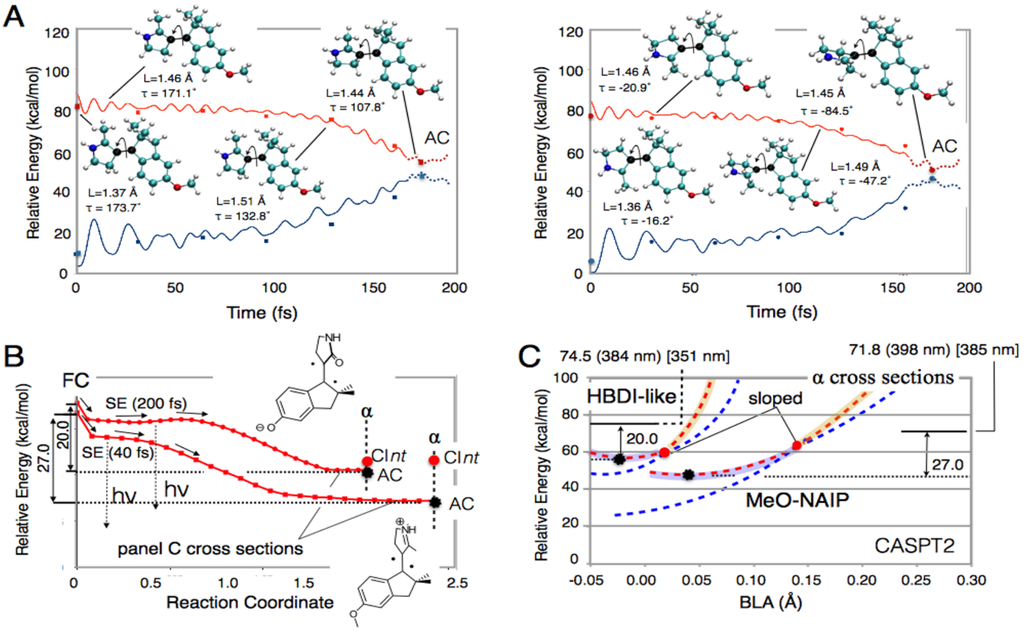

Figure 12. MeO-NHIP FC trajectories and comparison between the *Z* isomer of MeO-NHIP and the *E* isomer of *p*-HBDI-like. (A) Scaled-CASSCF/6-31G* S_1 FC trajectories of *Z*-MeO-NHIP and *E*-MeO-NHIP. The full circles and full squares refer to the single point CASPT2/6-31G* computations performed along the unscaled-CASSCF trajectories and used for scaling the CASSCF energy gaps and time scales (see the Supporting Information for details) given by the full lines. The structures along the trajectories provide information on the main geometrical evolution of the two isomers (parameters in Å and deg). The definitions of the angle τ and bond length *L* are given as insets of Figure 5C. (B) S_1 (red) energy profiles computed along the MEP CASPT2//CASSCF level with a radius of 0.07 and 1.0 Å·(amu)$^{1/2}$ for *p*-HBDI-like and MeO-NHIP, respectively. The dashed vertical segments represent the location of the orthogonal BLA cross sections α in panel C. The energies of the CASPT2 energy minima (AC, black full circle) and CI*nt*'s (red full circle) are also given. (C) Comparison between the S_0 and S_1 energy profiles of the BLA cross sections (see also panel B) for *E*-*p*-HBDI-like and *Z*-MeO-NHIP at the CASPT2 level (dashed line). The locations of the CASPT2 energy minima (AC, black full circle) and CI*nt*'s (red full circle) are also given. Values in parentheses refer to computed values, while values in square brackets refer to experimental values.

case of the NAIP compounds where such a very fast S_1 decay channel results in an impulsive red-detuned photoproduct signature which is not observed here lends credence to the first, sequential scenario.

To rationalize the above comparison between different switches, it is useful to consider the intrinsic structure of their S_1 PESs. This can be done by comparing the three PES elements: the S_1 MEP, the S_1 FC trajectory, and the energy profiles along a BLA scan given in Figure 5A, Figure 5C, and Figure 6A, respectively, for *p*-HBDI-like (*E*-**3** and *Z*-**3**). The corresponding data for MeO-NAIP are instead given in Figure 12. For both switches, the initial motion out of the FC point is initially driven by stretching modes (see initial structures in Figures 5C and 12A which document the *L* expansion) in line with the dashed red line in Figure 6B running, initially, along the "BLA" coordinate. In *p*-HBDI-like, this is followed by slow relaxation along a long energy plateau (this is evident in both the MEP of Figure 5A and the trajectory of Figure 5C) until torsional deformations reach ~40° schematically depicted as the borderline between the brown (CT wave function) and light-blue (COV/DIR wave function) regions (Figure 6B). The same scenario holds for MeO-NAIP switches where the motion out of the FC region is observed both in the SE and ESA signatures[13,17] and it is predicted to occur on a flat but much shorter PES region (see the trajectories in Figure 12A as well as the comparison between the MEP S_1 energy profile in Figure 12B).[16] In fact, MeO-NAIP mimics retinal proteins where a very fast fluorescence relaxation occurs.[52−54]

As evident from the energy profiles in Figure 12B, the differences in the extension and slope of the S_1 plateau indicate that this represents the main cause for the shorter excited-state lifetime of MeO-NAIP (~200 fs in methanol) as compared to that in *p*-HBDI-like (~400 fs for *E*-**3**). The length and slope of the plateau would control the motion toward the decay region. Furthermore, it has been reported that a tiny excited state barrier located along a torsion degree of freedom (which may exist in *E*-**3**) may induce a biexponential decay even if there is only a single decay channel.[55] At the molecular level, the different extension of the S_1 energy plateau can be assigned to the gear conformation of Figure 2 present in the S_0 structure of *E*-**3** (and also found in the *E* form of dMe-MeO-NAIP[14]) which is absent both in *Z*-**3** and in the *Z* isomer of MeO-NHIP.[16] Such an arrangement would lend a greater stability of the transient S_1 planar conformations of *E*-**3**. In fact, TA spectroscopy performed on a 55:45 *Z*/*E* mixture of compound **3** upon 400 nm excitation revealed very similar data (see Figure S3), except that the ESA decay appears slightly faster and the relative weight of the slow SE decay component is weaker than for the pure *E* isomer (see Figure S9). This indicates that the "skewed", nonplanar conformation of *Z*-**3** would display a faster S_1 decay due to impossibility of a geared arrangement as in *E*-**3** (see Figure 2B).

Notice that above we have exclusively related the modeled PESs to the relaxation of the excited state signals (SE or ESA). However, the full reactive process would be affected by the detailed topography of the sloped CI*nt*. The fact that measurements were carried out at room temperature and in polar solvent rather than in the gas phase at 0 K sets a limit in the use of the data of Figures 5 and 12 for interpreting the observed time scales. However, the similarity in the S_1 decay, including the biexponential nature of SE or fluorescence kinetics of all compounds, points to a similar kinetic scenario. Consistently, Figure 12C compares the shape of *E*-**3** and *Z*-MeO-NHIP energy profiles in the gas phase in the corresponding AC regions and along the BLA coordinate and reveals that in both cases one has a sloped CI*nt*. Below, using quantum mechanics/molecular mechanics (QM/MM) calculations, we demonstrate that the presence of a polar solvent affects both CI*nt* topologies (see also discussion in the Conclusions section) in a rather predictable and similar way. This similarity is substantially due to the common charge transfer character of the S_1 states of the anionic *p*-HBDI-like and the cationic MeO-NAIP switches. Such character suggests that the solvent (e.g., methanol) may influence the topologies of CI*nt*'s in a similar fashion in the two switches, thus replicating, in solution, what is described already for the gas phase where very similar topographies have been documented.

More specifically, the similarity between the anionic *p*-HBDI-like switch and the cationic MeO-NAIP switch becomes apparent when examining the CT character of their S_1 states. As discussed above, upon light excitation, in the *p*-HBDI-like switch, the anionic center is formally moving from the indanylidene to the pyrrolidone unit, while in NAIPs the cationic center is shifting from the pyrrolinium to the indanyilidene unit. Therefore, both S_1 processes are characterized by a unidirectional transfer of electron density from the indanylidene ring to the pyrrolidone or pyrrolinium rings. This electron density transfer triggers the S_1 BLA change/relaxation that unlocks the central bond torsional motion. A similarity is therefore also expected and found in the twisting mechanism which, in both switches, is dominated by an axial, rather than precessional, rotor twisting with respect to the axis of the isomerizing double bond.[42] This last property is in line with the optimized geometry of the CI*nt*'s and orientation of the BPs which appear very similar for both switches.[16]

The comparison of Tables 1 and 5 provides more quantitative information on the evolution of the charge transfer with respect to the stator and rotor units (i.e., across the reactive double bond) in *p*-HBDI-like and MeO-NHIP switches in the gas phase. As anticipated in the previous section, in S_0, the MeO-NHIP positive charge is localized in the pyrrolinium unit and it gets displaced toward the indanylidene unit upon photoexcitation (see first two entries in Table 5).[15] Similarly, in S_0, the *p*-HBDI-like negative charge is instead partially distributed between the two cyclic units with ca. 60% of the charge initially residing in the indanylidene moiety. In this case, a lesser amount of charge (see first two entries in Table 1) gets translocated to the pyrrolidone unit upon light absorption. The difference in the computed evolution of the charge distribution along the S_1 isomerization coordinate of the two switches reflects the different magnitude of these initial changes. In MeO-NHIP, the electron density partially returns to the indanylidene unit and then remains more or less constant up to the AC point where 100% of the positive charge is found on the pyrrolinium unit. This is consistent with the DIR character of the wave function at the S_1 AC minimum discussed above. In the *p*-HBDI-like switch, the initially translocated charge also reverts back but on a slower time scale and magnitude until, as for MeO-NAIP, it suddenly reverts back to a fully DIR wave function more similar to the S_0 than S_1 charge distribution. This occurs, again, at a twisted AC structure. Thus, both *p*-HBDI-like and MeO-NHIP display the charge translocation process leading to a diradical structure at AC. These results are consistent with the assignment of the electronic structures along the S_1 and S_0 states along the α cross sections of Figure 12C (i.e., the AC S_1 minimum has a "light-blue" DIR character, while at the same point the S_0 state has a "brown" CT character).

Table 5. Charge Evolution along the Trajectories of Figure 12A[a]

	E-charges		*Z*-charges	
	indanylidene frag.[b]	pyrrolinium frag.[b]	indanylidene frag.[b]	pyrrolinium frag.[b]
S_0 FC	0.34 (0.18)	0.66 (0.82)	0.33 (0.18)	0.67 (0.82)
S_1 FC	0.68 (0.18)	0.32 (0.82)	0.67 (0.18)	0.33 (0.82)
S_1 30 fs	0.58	0.42	0.53	0.47
S_1 60 fs	0.54	0.46	0.57	0.43
S_1 90 fs	0.57	0.43	0.49	0.51
S_1 120 fs	0.52	0.48	0.40	0.60
S_1 150 fs	0.61	0.39	0.29	0.71
S_1 AC	0.05 [0.03]	0.95 [0.97]	0.06	0.94

[a] We set the CT character dominating when the indanylidene fragment has charge ≥0.5 and the COV/DIR character dominating when the indanylidene fragment has charge <0.5. [b] Numbers in parentheses indicate the corresponding values for the REKS optimized structure and the square brackets the values corresponding to the optimized MECI points of Figure 11B.

p-HBDI-Like Isomerization Mechanism in Solution. Figure 13 reports on the FC trajectories computed for *E*-**3** and *Z*-**3** in methanol solution using a QM/MM model (see the Materials and Methods section). The trajectories provide a description of the reactive motion occurring in a solvent glass cavity at 0 K (see Figure 13A). More specifically, the *E*-**3** and *Z*-**3** cavities have been generated via room temperature MD equilibration and are therefore representative of a low temperature solvent glass. The two trajectories describe motion toward the corresponding S_1 minima given in Figure 13B. The S_1 and S_0 energy profiles appear, for both isomers, qualitatively similar to the one obtained in the gas phase. However, when comparing Figure 13C with Figure 5C, the following differences are immediately evident. The first difference is related to the switch λ_{max} values that are slightly blue-shifted with respect to the gas phase (see Table 2). The second difference is related to the time required to reach the S_1 minima that is slightly longer for the switch in solution with respect to the gas phase. The third and more fundamental difference is that the intercepted minima now correspond to degeneracy or near degeneracy regions for *E*-**3** and *Z*-**3**, respectively (i.e., the S_1−S_0 energy gap at the minima

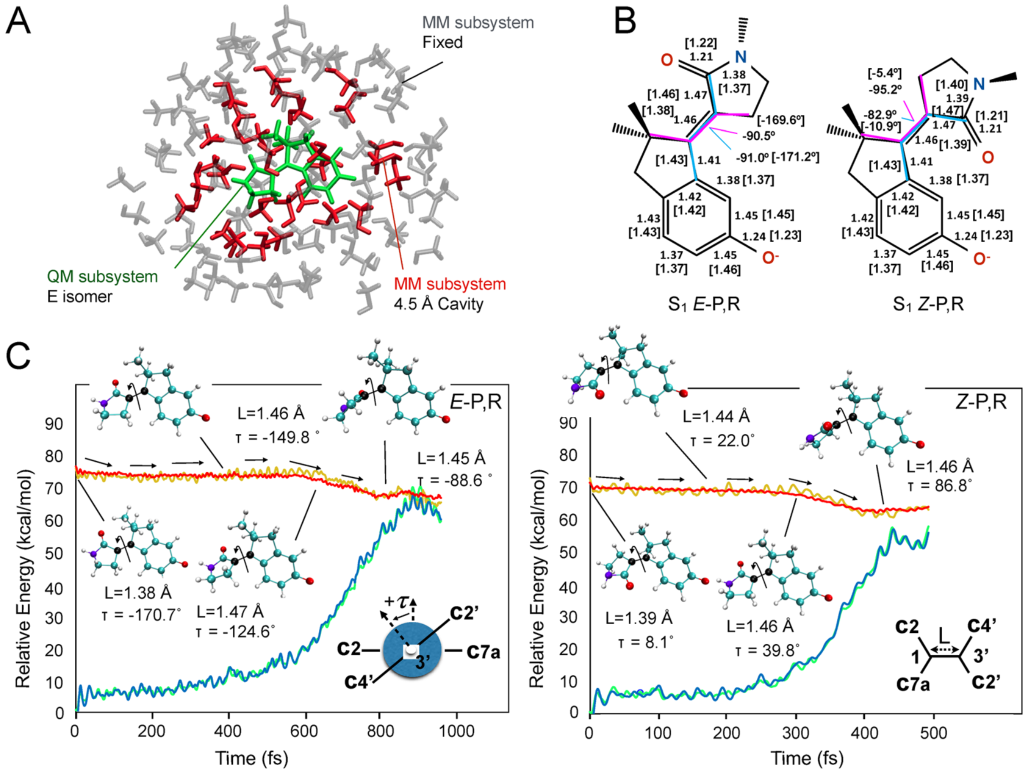

Figure 13. *p*-HBDI-like switch FC trajectories in methanol solution. (A) Structure of the QM/MM model used in the FC trajectory computations in solution. (B) Comparison between the S_0 and S_1 state optimized *E*-P,R and *Z*-P,R structures in methanol solution. The values in square brakets refer to the corresponding S_0 optimized structure. The bond lengths are in Å, and the dihedrals are in deg. (C) Scaled-CASSCF/6-31G* S_1 FC trajectories for *E*-P,R and *Z*-P,R. The red and blue lines represent the S_1 and S_0 scaled-CASSCF energy profiles. The yellow and green lines refer to the S_1 and S_0 energies obtained from single point CASPT2/6-31G* computations performed along the CASSCF trajectories. The structures along the trajectories provide information on the main geometrical evolution of the isomers (parameters in Å and deg). The definitions of the angle τ and bond length L are given as insets.

is <4 kcal/mol and therefore much reduced with respect to the >10 kcal/mol of Figure 5C).

When considering the effect of the temperature, the trajectories seem to be consistent with the experimental observations. In fact, as we will also discuss in the Conclusions, the effect of the methanol environment transforms the AC points of the gas-phase switch into CI*nt* (i.e., the sloped CI*nt*'s become peaked), thus explaining the ultrafast decay of the switch to S_0. Also, by definition, FC trajectories describe a motion where the only source of kinetic energy is coming from the acceleration of the molecule along the S_1 PES. Along the flat S_1 PES of **3**, the relaxation must occur via an almost diffusive motion that is expected to be faster in molecules with nonzero initial kinetic energy (i.e., at room temperature). This would explain the longer computed time required to reach the CI*nt* (~800 fs of *E*-**3**) with respect to the observed S_1 lifetime (~400 fs). Also, notice that the flatter S_1 energy surfaces of *p*-HBDI-like switches with respect to MeO-NHIP switches makes the dynamics of the first ones more sensitive to environmental effects. This would explain why the reported MeO-NAIP FC trajectories in methanol solution reach the corresponding CI*nt*'s on a time scale not too different from those of Figure 12A and of ca. 200 fs,[51] in good agreement with experimental findings (Table 4).

■ CONCLUSIONS

Above, we have reported on the design, preparation, and spectroscopic investigation of a novel *anionic* molecular switch mimicking the electronic structure of the green fluorescent protein chromophore but featuring the same locked framework as *cationic* MeO-NAIP/MeO-NHIP switches. The facile synthesis of **3** has promptly allowed the switch experimental characterization in terms of spectroscopy, photochemistry, and laser-induced ultrafast dynamics. We have shown that the system is photochromic and thermally stable at room temperature and that the anionic form in methanol has *E*-P,R and *Z*-P,R λ_{max} values separated by ca. 10 nm. Furthermore, the photoisomerization of both diastereomers occurs on a sub-picosecond time scale.

The above features have been tentatively rationalized by mapping the intrinsic (i.e., gas-phase) S_0 and S_1 PESs and by running S_1 FC trajectory computations. The effect of the solvent environment has also been investigated by running QM/MM FC trajectory calculations in methanol solution. The results support the schematic mechanism of Figure 14A (also given in Figure 6B) starting with an evolution along a rugged and flat S_1 PES corresponding to a potentially emissive state (i.e., traced by an ~200 fs lived SE signal) of the switch. The corresponding reaction coordinate is initially dominated by a BLA mode and then develops along lower frequency modes including the torsion describing the isomerization of the central double bond until the system reaches a PES region characterized by an AC with ca. 90° twisted structure (i.e., with an orthogonal configuration of the pyrrolidone and indanyilidene rings) and with a DIR electronic character and the negative charge localized on the indanylidene moiety. In the gas phase, a sloped conical intersection (see the inset) is located

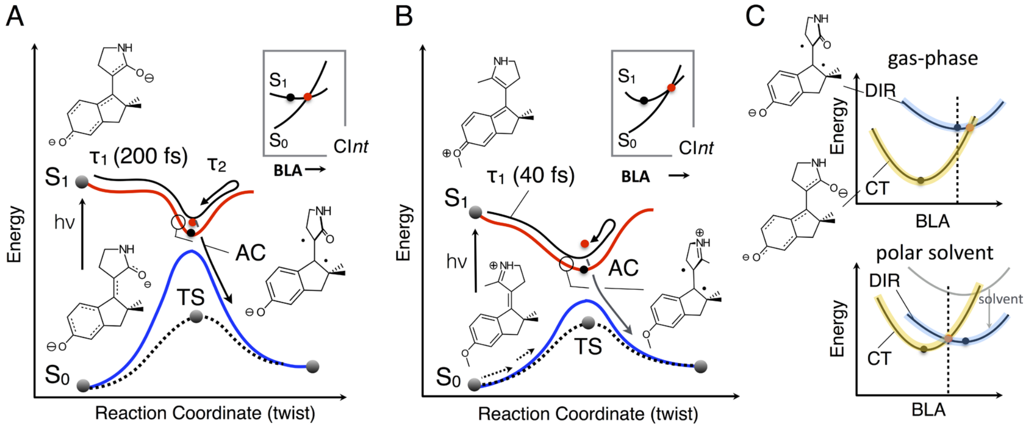

Figure 14. *p*-HBDI-like and MeO-NHIP isomerization mechanisms. (A) Schematic representation of the photochemical reactive trajectories (full black line) for a *p*-HBDI-like switch. A long plateau is entered along the S_1 PES (full red line) restraining the motion toward an AC minimum and a CI*nt* just above it. The CI*nt* has a sloped topography (see inset). The chemical formulas convey the idea that the majority of the S_1 population has initially CT character but along the trajectory a mixed CT/DIR and then almost 100% DIR character develops near the AC minimum (see circled region). (B) The same trajectories for the previously investigated MeO-NHIP switch.[16] In this case, the plateau providing access to the nonadiabatic decay region does not really exist and the progression toward the AC point is faster. The evolution of the electronic character is similar (but of opposite sign) with respect to *p*-HBDI-like. (C) Schematic relationship between the relative stability of the CT and DIR electronic configurations along the BLA coordinate and the topography of the CI*nt* in the gas phase (i.e., for the computed intrinsic *p*-HBDI-like and MeO-NHIP force fields) and in a polar solvent. Notice that along the vertical dashed line the solvent effect turns the S_1 minima into a CI*nt*, as consistently found in Figure 13C. At the same time, a sloped CI*nt* is turned into a peaked CI*nt*.

ca. 1 kcal/mol above the AC point (the same mechanistic picture is obtained when using completely different quantum chemical tools such as DFT and CASPT2//CASSCF methods).

We have also discussed how, remarkably, although compound **3** and the previously investigated MeO-NAIP/MeO-NHIP switches have opposite charges, the photoreactivity is triggered by an electron density translocation occurring in the same direction along the exocyclic reactive double bond. This results in a S_1 dynamics controlled by a qualitatively similar reaction coordinate dominated, sequentially, by BLA and double bond torsion. This is illustrated by the MeO-NHIP mechanistic scheme in Figure 14B where a similar AC and sloped CI*nt* is predicted in the gas phase for both compounds. However, a major difference between the mechanism of Figure 14A and B arises in the FC region where after the stretching relaxation only MeO-NAIP evolves rapidly toward the AC structure with a DIR character. Correspondingly, the lack of an extended S_1 PES would be responsible for a very fast, early spectral relaxation in S_1 in MeO-NAIP, as compared to *E*-**3**.

The reported mapped gas-phase PESs not only inform on the intrinsic S_1 kinetics and reactivity of the two switches but can be useful to estimate the possible effects of the solvent environment allowing to rationalize, on structural bases, the experimental similarity observed between *p*-HBDI-like and NAIPs. Indeed, as illustrated in Figure 14C, a change in the CI*nt* topography from highly sloped to peaked with a consequent disappearance of the AC minima is easily predicted. Such a solvent-induced change would be substantially due to the specific S_0 solvation shell that would create, in a similar way, "effective counterions" surrounding the negatively charged oxygen in *p*-HBDI-like and positively charged nitrogen in NAIP. Assuming that during the measured sub-picosecond S_0 lifetime there is not enough time for the reorganization of the solvation shell, one can predict a stabilization of the DIR electronic structure (where the charges are located close to their S_0 position) with respect to the CT electronic structure. As illustrated in Figure 14C, such stabilization would lead to a change in local topography and, most remarkably, from a "gas-phase" sloped CI*nt* to a "solvated" peaked CI*nt*. Notice that the same effect is predicted to lead to a blue-shift of the λ_{max} with respect to the computed gas-phase quantities.

The qualitative predictions discussed above are found to be consistent with the experimental observations and with the results of our QM/MM FC trajectory computations in methanol solution (see Figure 13C) where (i) the absorption maxima are predicted to be ca. 10 nm blue-shifted with respect to the gas phase, due to the stabilization of the S_0 state with respect to the S_1 state, and (ii) the conical intersection moves at the bottom of the S_1 PES facilitating the decay. Indeed, the difference between the *E*-**3** computed gas-phase λ_{max} value and its corresponding computed λ_{max} values in methanol (as a reference solvent) displays a 10 nm blue-shift due to the stabilization of the S_0 state with respect to the S_1 state. Similarly, for *Z*-MeO-NHIP, one finds even larger blue-shifts of 21 nm when comparing the computed gas-phase λ_{max} (Figure 12C) with the computed quantity in methanol solution (377 nm).[16] In the past, we also reported that the computed S_1 relaxation path for *Z*-MeO-NHIP in methanol intercepted a CI*nt* rather than an AC also consistently with the signatures of coherent motion[17,13] (similar to those reported for bovine rhodopsin and interpreted as the consequences of vibrationally coherent decay at a CI*nt* producing oscillations in the photoproduct PES).[56,57] These data and our FC trajectories in methanol suggest that in polar solvents both *E*-**3** and *Z*-MeO-NHIP intercept peaked CI*nt*'s at the end of their S_1 relaxation paths. These predictions lead us to the expectation that, at room temperature, both compounds may have closer S_1 lifetimes and product appearance times, as actually observed experimentally in methanol.

In conclusion, compound **3** is a new biomimetic molecular switch complementary to NAIP and other retinal chromophore-like switches in terms of charge translocation and S_1 kinetics. Structure **3** can in principle easily be functionalized at the pyrrolidone N atom, thus providing anchor points for linking such a system to a support including a biopolymer (e.g., protein) or a metal surface. A seemingly facile functionalization is also possible for NAIPs but at the level of the indanylidene unit (see Figure 15). Indeed, N-substitution in the *p*-HBDI-like

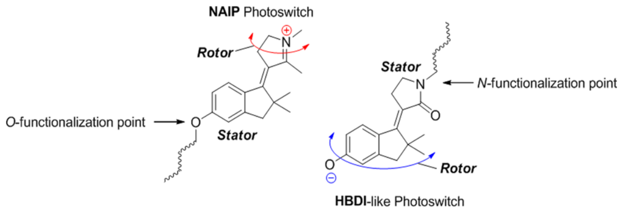

Figure 15. Schematic representation of functionalized complementary NAIP and *p*-HBDI-like photoswitches.

compound and the O-substitution on the indene ring of the NAIPs with clickable alkyl chains are already under scrutiny in our lab. Therefore, *p*-HBDI-like and NAIP photoswitches may realistically form, when combined in a single material, the basis for the production of systems achieving the light-driven rotation of a negatively or positively charged rotor unit respectively leading to light-responsive systems useful in different conditions (e.g., pH, charge, steric hindrance of the rotor, wavelength, etc.).

■ MATERIALS AND METHODS

Synthesis. All chemicals used were of reagent grade. Yields refer to purified products and are not optimized. Merck silica gel 60 (230−400 mesh) was used for column chromatography. Merck TLC plates and silica gel 60 F_{254} were used for TLC. ^{1}H NMR spectra were recorded at 400 MHz (Bruker DRX-400 AVANCE spectrometer) in the indicated solvents (TMS as internal standard): the values of the chemical shifts are expressed in ppm and the coupling constants (J) in Hz. An Agilent 1100 LC/MSD operating with an electrospray source was used in mass spectrometry experiments. The absorption spectra were recorded with a PerkinElmer Lambda 40 in the indicated solvent.

3-(5-Methoxy-2,2-dimethyl-2,3-dihydro-1*H*-inden-1-ylidene)pyrrolidin-2-one (2). To a solution of *N*-Boc-2-pyrrolidinone (6.45 mmol, 1.20 g) dissolved in anhydrous THF (10 mL), a 1 M solution of lithium hexamethyldisilazide (LiHMDS) in anhydrous THF (7.74 mmol, 7.74 mL) was added at −78 °C under a nitrogen atmosphere. After 1 h, a solution of compound **1** (7.74 mmol, 1.47 g) and $BF_3 \cdot Et_2O$ (7.74 mmol, 976 μL) in anhydrous THF (8 mL) was added dropwise. The reaction mixture was stirred at −78 °C for 3 h. Then, NH_4Cl (s.s.) was added, and the crude was extracted with CH_2Cl_2. The combined organic layers were dried over Na_2SO_4 and concentrated under reduced pressure. The oily residue was dissolved in CH_2Cl_2 (15 mL), and trifluoroacetic acid (1.0 mL) was added. The resulting reaction mixture was stirred at room temperature for 30 min. Then, $NaHCO_3$ (s.s.) was added and the crude was extracted with CH_2Cl_2. The residue was purified by flash chromatography on silica gel (1:1, ethyl acetate/petroleum ether) to obtain compound **2** (1.26 g, 76%) as a pale yellow solid (8:2 mixture of *E*/*Z* isomers). For analytical purposes, *E*-**2** and *Z*-**2** isomers were separated by flash chromatography.

(E)-3-(5-Methoxy-2,2-dimethyl-2,3-dihydro-1H-inden-1-ylidene)-pyrrolidin-2-one (E-2). ^{1}H NMR (400 MHz, $CDCl_3$): 1.57 (m, 6H, H_A), 2.95 (s, 2H, H_3), 3.19 (t, 2H, J = 6.6, $H_{4'}$), 3.48 (t, 2H, J = 6.6, $H_{5'}$), 3.84 (s, 3H, H_B), 6.77−6.88 (m, 2H, H_4 and H_6), 7.44 (d, 1H, J = 8.4, H_7). ^{13}C NMR (100 MHz, $CDCl_3$): 27.4 (C_A), 32.2 ($C_{4'}$), 39.5 ($C_{5'}$), 45.1 (C_2), 50.9 (C_3), 55.3 (C_B), 109.5 (C_4), 113.2 (C_6), 120.1 ($C_{3'}$), 127.5 (C_7), 133.9 (C_{7a}), 149.6 (C_{3a}), 156.9 (C_1), 160.8 (C_5), 172.4 ($C_{2'}$). NOE experiments showed contacts between $H_{4'}$ (t, δ = 3.19) and H_7 (d, δ = 7.44). MS (ESI): m/z 280.0 (M + Na^+).

(Z)-3-(5-Methoxy-2,2-dimethyl-2,3-dihydro-1H-inden-1-ylidene)-pyrrolidin-2-one (Z-2). ^{1}H NMR (400 MHz, $CDCl_3$): 1.31 (m, 6H, H_A), 2.82 (s, 2H, H_3), 3.08 (t, 2H, J = 6.6, $H_{4'}$), 3.44 (t, 2H, J = 6.7, $H_{5'}$), 3.81 (s, 3H, H_A), 6.69 (s, 1H, H_4), 6.75 (dd, 1H, J = 2.4, 8.9, H_6), 8.61 (d, 1H, J = 8.9, H_7). ^{13}C NMR (100 MHz, $CDCl_3$): 26.6 (C_A), 28.3 ($C_{4'}$), 39.6 ($C_{5'}$), 47.1 (C_2), 49.3 (C_3), 55.2 (C_B), 108.8 (C_4), 112.3 (C_6), 119.8 ($C_{3'}$), 130.9 (C_{7a}), 131.1 (C_7), 148.4 (C_{3a}), 155.9 (C_1), 160.6 (C_5), 173.0 ($C_{2'}$). NOE experiments showed contacts between $H_{4'}$ (t, δ = 3.08) and H_A (m, δ = 1.31). MS (ESI): m/z 280.0 (M + Na^+).

3-(5-Hydroxy-2,2-dimethyl-2,3-dihydro-1*H*-inden-1-ylidene)pyrrolidin-2-one (3). To a solution of compound **2** (0.10 g, 0.39 mmol) in dichloromethane (10 mL) cooled to 0 °C was added dropwise a solution (1 M in CH_2Cl_2) of BBr_3 (3.9 mL, 3.9 mmol). The resulting mixture was stirred for 3 h at room temperature. Then, a saturated $NaHCO_3$ solution was added until the gas evolution ceased. The reaction mixture was extracted with dichloromethane, and the organic layer was dried over sodium sulfate and evaporated under reduced pressure. Purification of residue by flash chromatography with petroleum ether-ethyl acetate (1:1) as the eluent gave pure compound **3** (0.90 g, yield 89%) as a pale yellow solid (8:2 mixture of *E*/*Z* isomers). *E*-**3** and *Z*-**3** isomers were separated by flash chromatography using petroleum ether-ethyl acetate (8:2) as the eluent. The fast concentration under reduce pressure at 45 °C of the column fraction containing *E*-**3** provided the pure (>97%) compound which was crystallized from a mixture of CH_2Cl_2/methanol (9:1). Instead, concentration under reduced pressure at 45 °C of the column fraction containing *Z*-**3** provided the *Z*/*E* mixture (55/45) used in the TAS study. For analytical purposes, a pure (>97%) sample of *Z*-**3** was obtained by evaporating the column fractions with a gentle stream of nitrogen.

(E)-3-(5-Hydroxy-2,2-dimethyl-2,3-dihydro-1H-inden-1-ylidene)-pyrrolidin-2-one (E-3). ^{1}H NMR (400 MHz, CD_3OD): 1.51 (m, 6H, H_A), 2.86 (s, 2H, H_3), 3.12 (t, 2H, J = 6.7, $H_{4'}$), 3.42 (t, 2H, J = 6.7, $H_{5'}$), 6.68 (s, 1H, H_4), 6.70 (dd, 1H, J = 2.2, 8.6, H_6), 7.40 (d, 1H, J = 8.6, H_7). ^{1}H NMR (400 MHz, DMSO-d_6): 1.45 (m, 6H, H_A), 2.79 (s, 2H, H_3), 3.00 (t, 2H, J = 6.4, $H_{4'}$), 3.27 (t, 2H, overlap with H_2O, $H_{5'}$), 6.60−6.74 (m, 2H, H_4 and H_6), 7.33 (d, 1H, J = 8.4, H_7), 7.71 (brs, 1H, OH), 9.70 (br s, 1H, NH). ^{13}C NMR (100 MHz, CD_3OD): 28.0 (C_A), 32.2 ($C_{4'}$), 40.8 ($C_{5'}$), 46.0 (C_2), 51.9 (C_3), 112.3 (C_4), 115.3 (C_6), 121.0 ($C_{3'}$), 129.1 (C_7), 133.9 (C_{7a}), 150.7 (C_{3a}), 158.6 (C_1), 160.4 (C_5), 174.5 ($C_{2'}$). NOE experiments showed contacts between $H_{4'}$ (t, δ = 3.12) and H_7 (d, δ = 7.40). MS (ESI): 266.0 m/z (M + Na^+).

(Z)-3-(5-Hydroxy-2,2-dimethyl-2,3-dihydro-1H-inden-1-ylidene)-pyrrolidin-2-one (Z-3). ^{1}H NMR (400 MHz, CD_3OD): 1.30 (m, 6H, H_A), 2.77 (s, 2H, H_3), 3.07 (t, 2H, J = 6.6, $H_{4'}$), 3.40 (t, 2H, J = 6.6, $H_{5'}$), 6.56 (dd, 1H, J = 2.4, 8.7, H_6), 6.60 (s, 1H, H_4), 8.32 (d, 1H, J = 8.7, H_7). ^{1}H NMR (400 MHz, DMSO-d_6): 1.22 (m, 6H, H_A), 2.70 (s, 2H, H_3), 2.93 (t, 2H, J = 6.6, $H_{4'}$), 3.24 (t, 2H, J = 6.5, $H_{5'}$), 6.49 (dd, 1H, J = 2.2, 8.7, H_6), 6.55 (s, 2H, H_4), 7.73 (br s, 1H, OH),8.54 (d, 1H, J = 8.7, H_7), 9.53 (br s, 1H, NH). ^{13}C NMR (100 MHz, CD_3OD): 27.0 (C_A), 29.4 ($C_{4'}$), 40.9 ($C_{5'}$), 48.3 (C_2), 50.2 (C_3), 111.5 (C_4), 114.3 (C_6), 120.7 ($C_{3'}$), 131.1 (C_{7a}), 132.0 (C_7), 150.0 (C_{3a}), 158.0 (C_1), 159.9 (C_5), 175.1 ($C_{2'}$). NOE experiments showed contacts between $H_{4'}$ (t, δ = 3.07) and H_A (m, δ = 1.30). MS (ESI): 266.0 m/z (M + Na^+).

Photoisomerization Quantum Yields. Absorption spectra were recorded on a PerkinElmer - Lambda 800 spectrophotometer. The sample was irradiated using a xenon lamp equipped with a monochromator for the selection of the excitation wavelength (315 or 350 nm). A potassium ferrioxalate solution was used as an actinometer to determine the light source intensity at the different excitation wavelengths. The chromatographic analysis was performed using a Waters apparatus equipped with a Lux cellulose 1 column and a UV−vis diode array detector. The protocols followed for the quantum yield measurement of the neutral and anionic forms of *E*-**3** are also reported in refs 58 and 46, respectively.

Transient Absorption Spectroscopy. Transient absorption spectroscopy (TAS) was performed at two distinct excitation wavelengths of 350 nm (at the maximum of the absorption band) and of 400 nm (for minimum excess vibrational energy). The 350 nm pump pulse is produced by a commercial OPA followed by a frequency mixing stage (TOPAS, Light conversion) and pumped by the fundamental 800 nm pulse of an amplified laser system (Amplitude Technologies) operating at 5 kHz. This TA experiment achieves an ~80 fs time resolution. Another TA experiment is performed with a recently built setup[59] producing a broadband 400 nm pulse. Another amplified Ti:Sa laser system (Amplitude Technologies) is used, generating 40 fs, 3 mJ pulses centered at 810 nm with a repetition rate of 1 kHz. In short, nonlinear propagation of about 1 mJ of that fundamental pulse inside a hollow fiber filled in with neon (commercial system by Imperial College Consultants) induces large spectral broadening and yields a red to infrared, sub-7 fs pulse after recompression with a set of chirped mirrors. Type II sum frequency mixing of the sub-7 fs pulse with the fundamental 40 fs pulse yields the 400 nm pulse displayed in Figure S10. This 400 nm pulse is used without any further recompression as a pump beam and provides TA data with sub-30 fs time resolution. In both experiments, the probe pulse is a white light supercontinuum generated in CaF_2 with the 800 nm fundamental pulse (at 5 or 1 kHz, in either setup).

Both pump and probe beams are focused into a 0.2 mm thick quartz flow cell containing the sample in solution. A peristaltic pump is used to circulate the sample so as to refresh it between successive excitation laser shots. TAS is performed on methanol solutions of compound **3** in excess of KOH. Three experiments are performed, on the >97% pure E isomer with (i) 400 nm and (ii) 350 nm excitation wavelength and (iii) on a 55% *Z*/45% *E* mixture of both isomers, with 400 nm excitation wavelength. The sample absorbance at 350 nm is 0.6 over the 0.2 mm thickness of the flow cell in all TAS experiments. Taking into account the spectral overlap between the 400 nm pump laser spectrum and the absorption spectrum of each isomer (see Figure S8), we conclude that, in a mixture of both isomers, the excitation probability of the *Z* isomer is about twice as much as that of the *E* isomer.

All TAS data presented here (see 2D maps in the Supporting Information) are postprocessed in order to compensate for the group velocity dispersion in the probe beam so as to define accurately the time zero (within ±20 fs) at all wavelengths. At very early times, the nonlinear interaction of pump and probe beams in the solvent and cuvette generates a time- and wavelength-dependent signal (see ref 60), sometimes called "coherent artifact". The latter is recorded separately in pure solvent and subtracted to the data recorded on solutions of compound **3**. With the more intense 400 nm pump pulse (see next paragraph), the artifact does not perfectly cancel out, and kinetic traces remain spoiled at very early times by that "solvent" signal. Therefore, the fits of kinetic traces only start after 50 fs.

All experiments are performed within the linear regime of excitation. More precisely, in the 350 nm pumped experiment, the probe beam diameter is ∼60 μm, while the pump is ∼100−120 μm in diameter and 36 nJ in pulse energy (180 μW at 5 kHz repetition rate). With the extinction coefficient of *E*-**3** being ∼23 000/M/cm (see Figure 7A), the Beer−Lambert law predicts that the maximum excitation probability is therefore ∼5%. With the 400 nm pumped experiment, the pump and probe beam diameters are, respectively, ∼250 and ∼140 μm. The column-averaged excitation probabilty is ≤1%, given by the ratio between the early bleach signal at 350 nm, estimated in Figure 9B to be 3−5 mOD (uncertain because of the ESA band partial overlap), and the absorbance of 600 mOD of the sample in the flow cell. This second estimate confirms the ∼5 times higher excitation propobability estimated with the 350 nm pump, since the TA signal is indeed 4−5 times larger in Figure 9A. Finally, since the absorbance of compound *E*-**3** is ∼25 times stronger at 350 nm than at 400 nm, the 400 nm pulse fluence must be ∼5 times larger to achieve 5 times weaker excitation probability, resulting in a much more intense coherent artifact, relative to the compound signal.

Computations. Computational work was performed using the REKS and SI-SA-REKS methods (see ref 37 and references cited therein). The methods employ ensemble density functional theory and are capable of delivering results matching the accuracy of high-level multireference *ab initio* wave function methods, such as MRCISD and XMCQDPT2, when describing ground (REKS) and excited (SI-SA-REKS) state PESs and conical intersections of large molecular systems. The capabilities of the SI-SA-REKS method were demonstrated in direct comparison with the results of the most accurate multireference *ab initio* wave function method, MRCISD, carried out for a wide range of organic and biological chromophores and conical intersections.[61,62]

In the present work, the REKS and SI-SA-REKS (in the following, abbreviated to SSR) methods are employed in connection with the long-range corrected LC-ωPBE[63−65] density functional and the 6-31G* basis set[66] augmented by the diffuse functions on the N and O atoms. The SSR-LC-ωPBE/6-31(+)G* and RE-LC-ωPBE/6-31(+)G* calculations were carried out in the gas phase.

In the ground electronic state, the geometries of all stationary points were located using the RE-LC-ωPBE/6-31(+)G* method. The vertical excitation energies at the optimized S_0 geometries were subsequently calculated using the SSR-LC-ωPBE/6-31(+)G* method (see the FC points in Figure 3). This computational protocol yields accurate vertical excitation energies consistent with correlated methods such as MRCISD+Q, as was demonstrated in previous works,[62,67] Mapping of the ground and excited state PESs along the torsional reaction coordinate was carried out by a relaxed scan along the C2′−C3′−C1−C7a dihedral angle using the SSR-LC-ωPBE/6-31(+)G* method. During the scan, the geometries were optimized for the averaged (i.e., S_0 + S_1) state by constraining the C2′−C3′−C1−C7a dihedral angle to specific values incremented through steps of 10°. The energies of the S_0 stationary points obtained in the scan match the respective energies obtained in the ground state RE-LC-ωPBE/6-31(+)G* geometry optimizations within less than 2 kcal/mol.

The MEP and excited state trajectories necessary to investigate the isomerization mechanism are computed at the CASSCF level of theory with a 12 electrons in 11 π-orbitals active space (the nitrogen lone pair is excluded) similar to the active space adopted for other HBDI-like chromophores.[38,39] In order to check for consistency with the SI-SA-REKS level, CASPT2//CASSCF/6-31G* single point computations have been carried out along both the MEPs and the trajectories to reevaluate the energy profiles. As originally done for the NAIP photoswitches, the CASPT2 calculations have been carried out using a three-root state average zero-order CASSCF wave function (with the IPEA = 0 parameter). The SI-SA-REKS level computations have been carried out with the COLOGNE12 suite of programs.[68] The CASSCF and CASPT2 computations have been carried out with MOLCAS 7.8.

The study of the molecular switch in a solvent environment was performed following a procedure presented in Melloni and co-workers[51] and is described here. To construct the model of the switch in a solvent, the ground state optimized chromophore in the gas phase was embedded in the center of a cubic box of size 39.75 × 39.75 × 39.75 Å^3 containing methanol. The chromophore was kept frozen, and the solvent system was minimized at the molecular mechanics (MM) level by 1000 conjugate-gradient minimization steps with periodic boundary conditions. The nuclear charges of the chromophore atoms for this purpose were computed using the electrostatic potential fitted method (ESPF) at the CASSCF 6-31G* level of theory using MOLCAS computer software.[69] The minimized solvent system was relaxed using a molecular dynamic simulation while keeping the chromophore fixed. This was done within the isothermal−isobaric NPT ensemble at 1 atm pressure and 298 K temperature. The construction of the solvent box, solvent minimization, and the relaxation were performed using the GROMACS computer package.[70,71] The generalized Amber force field (GAFF) parameters for the chromophore were generated using the ANTECHAMBER software package[72,73] and were used for the molecular mechanics calculations throughout this work. Then, a QM/MM model was defined for the solvent system (see Figure 12). In this model, the chromophore and the solvent are treated at the QM and MM levels, respectively. The solvent molecules located within 4.5 Å of any QM atom were allowed to move during the computations, and the rest was kept frozen. The chromophore was reoptimized in its ground and excited states employing a CASSCF/6-31G*/AMBER protocol with an active space comprised of 12 electrons in 11 orbitals. A Franck−Condon trajectory was also propagated for 1 ps. All the QM/MM calculations were carried out by coupling MOLCAS to the TINKER software package.[74]

■ ASSOCIATED CONTENT

Ⓢ Supporting Information

The Supporting Information is available free of charge on the ACS Publications website at DOI: 10.1021/jacs.5b10812.

Spectroscopic and computational details and Cartesian coordinates of the computed stationary points and conical intersections (PDF)

Crystallographic structure of compound *E*-**2** (CIF)

Crystallographic structure of compound *E*-**3** (CIF)

AUTHOR INFORMATION

Corresponding Authors

*paomar@oneonline.it
*mike.filatov@gmail.com
*Jeremie.Leonard@ipcms.unistra.fr
*molivuc@bgsu.edu

Author Contributions

¶These authors contributed equally to this work.

Notes

The authors declare no competing financial interest.

ACKNOWLEDGMENTS

This work was supported mainly by the Italian MIUR for funding (PRIN 2010-2011) and, in part, by the National Science Foundation under grant nos. CHE-1152070 and CHE-1151416, the Human Frontier Science Program Organization under grant RGP0049/2012CHE09-56776, and the EU FP7 Marie Curie fellowship PIOF-GA-2012-332233 granted. M.O. is grateful to NSF-XSEDE and Ohio Supercomputer Center for granted computer time. M.F. is grateful to the Korean Ministry of Science for support within the framework of the Brain Pool program. M.G. and J.L. acknowledge support from the Région Alsace (contrat doctoral, # 607-12-C31) and from the French Agence Nationale de la Recherche via the ANR-11-JS04-010-01 "IPQCS" grant, and via the "Investissement d'Avenir" program: Labex NIE ANR-11-LABX-0058_NIE, Labex CSC ANR-10-LABX-0026_CSC, Equipex UNION ANR-10-EQPX-52-01.

REFERENCES

(1) Browne, W. R.; Feringa, B. L. *Nat. Nanotechnol.* **2006**, *1*, 25–35.

(2) Balzani, V.; Credi, A.; Venturi, M. *Chem. Soc. Rev.* **2009**, *38*, 1542–550.

(3) Pollard, M. M.; Klok, M.; Pijper, D.; Feringa, B. L. *Adv. Funct. Mater.* **2007**, *17*, 718–729.

(4) Tahara, R.; Morozumi, T.; Nakamura, H.; Shimomura, M. *J. Phys. Chem. B* **1997**, *101*, 7736–7743.

(5) Collins, G. E.; Choi, L.-S.; Ewing, K. J.; Michelet, V.; Bowen, C. M.; Winkler, J. D. *Chem. Commun.* **1999**, 321–322.

(6) Lemieux, V.; Spantulescu, M. D.; Baldridge, K. K.; Branda, N. R. *Angew. Chem., Int. Ed.* **2008**, *47*, 5034–5037.

(7) Blanco-Lomas, M.; Samanta, S.; Campos, P. J.; Woolley, G. A.; Sampedro, D. *J. Am. Chem. Soc.* **2012**, *134*, 6960–6963.

(8) Kienzler, M. a.; Reiner, A.; Trautman, E.; Yoo, S.; Trauner, D.; Isacoff, E. Y. *J. Am. Chem. Soc.* **2013**, *135*, 17683–17686.

(9) Quandt, G.; Höfner, G.; Pabel, J.; Dine, J.; Eder, M.; Wanner, K. T. *J. Med. Chem.* **2014**, *57*, 6809–6821.

(10) Greb, L.; Lehn, J. *J. Am. Chem. Soc.* **2014**, *136*, 13114–13117.

(11) Guo, X.; Zhou, J.; Siegler, M. a.; Bragg, A. E.; Katz, H. E. *Angew. Chem., Int. Ed.* **2015**, *54*, 4782–4786.

(12) Zanirato, V.; Pollini, G. P.; De Risi, C.; Valente, F.; Melloni, A.; Fusi, S.; Barbetti, J.; Olivucci, M. *Tetrahedron* **2007**, *63*, 4975–4982.

(13) Léonard, J.; Schapiro, I.; Briand, J.; Fusi, S.; Paccani, R. R.; Olivucci, M.; Haacke, S. *Chem. - Eur. J.* **2012**, *18*, 15296–15304.

(14) Dunkelberger, A. D.; Kieda, R. D.; Shin, J. Y.; Rossi Paccani, R.; Fusi, S.; Olivucci, M.; Fleming Crim, F. *J. Phys. Chem. A* **2012**, *116*, 3527–3533.

(15) Lumento, F.; Zanirato, V.; Fusi, S.; Busi, E.; Latterini, L.; Elisei, F.; Sinicropi, A.; Andruniów, T.; Ferré, N.; Basosi, R.; Olivucci, M. *Angew. Chem., Int. Ed.* **2007**, *46*, 414–420.

(16) Sinicropi, A.; Martin, E.; Ryazantsev, M.; Helbing, J.; Briand, J.; Sharma, D.; Léonard, J.; Haacke, S.; Cannizzo, A.; Chergui, M.; Zanirato, V.; Fusi, S.; Santoro, F.; Basosi, R.; Ferré, N.; Olivucci, M. *Proc. Natl. Acad. Sci. U. S. A.* **2008**, *105*, 17642–17647.

(17) Briand, J.; Braem, O.; Rehault, J.; Leonard, J.; Cannizzo, A.; Chergui, M.; Zanirato, V.; Olivucci, M.; Helbing, J.; Haacke, S. *Phys. Chem. Chem. Phys.* **2010**, *12*, 3178–3187.

(18) Léonard, J.; Briand, J.; Fusi, S.; Zanirato, V.; Olivucci, M.; Haacke, S. *New J. Phys.* **2013**, *15*, 105022.

(19) Mayer, G.; Hechel, A. *Angew. Chem., Int. Ed.* **2006**, *45*, 4900–4921.

(20) Zhang, J. L.; Zhong, J. Q.; Lin, J. D.; Hu, W. P.; Wu, K.; Xu, G. Q.; Wee, A. T. S.; Chen, W. *Chem. Soc. Rev.* **2015**, *44*, 2998–3022.

(21) Zimmer, M. *Chem. Rev.* **2002**, *102*, 759–781.

(22) Subach, F. V.; Verkhusha, V. V. *Chem. Rev.* **2012**, *112*, 4308–4327.

(23) Baldridge, A.; Solntsev, K. M.; Song, C.; Tanioka, T.; Kowalik, J.; Hardcastle, K.; Tolbert, L. M. *Chem. Commun.* **2010**, *46*, 5686–5688.

(24) Stavrov, S. S.; Solntsev, K. M.; Tolbert, L. M.; Huppert, D. *J. Am. Chem. Soc.* **2006**, *128*, 1540–1546.

(25) Follenius-Wund, A.; Bourotte, M.; Schmitt, M.; Iyice, F.; Lami, H.; Bourguignon, J.-J.; Haiech, J.; Pigault, C. *Biophys. J.* **2003**, *85*, 1839–1850.

(26) Voityuk, A.; Michel-Beyerle, M.-E.; Rösch, N. *Chem. Phys. Lett.* **1998**, *296*, 269–276.

(27) Niwa, H.; Inouye, S.; Hirano, T.; Matsuno, T.; Kojima, S.; Kubota, M.; Ohashi, M.; Tsuji, F. I. *Proc. Natl. Acad. Sci. U. S. A.* **1996**, *93*, 13617–13622.

(28) Dickson, R. M.; Cubitt, a B.; Tsien, R. Y.; Moerner, W. E. *Nature* **1997**, *388*, 355–358.

(29) Kummer, A. D.; Kompa, C.; Niwa, H.; Hirano, T.; Kojima, S.; Michel-Beyerle, M. E. *J. Phys. Chem. B* **2002**, *106*, 7554–7559.

(30) Olsen, S.; Lamothe, K.; Martínez, T. J. *J. Am. Chem. Soc.* **2010**, *132*, 1192–1193.

(31) Weber, W.; Helms, V.; McCammon, J. a; Langhoff, P. W. *Proc. Natl. Acad. Sci. U. S. A.* **1999**, *96*, 6177–6182.

(32) Moeyaert, B.; Nguyen Bich, N.; De Zitter, E.; Rocha, S.; Clays, K.; Mizuno, H.; Van Meervelt, L.; Hofkens, J.; Dedecker, P. *ACS Nano* **2014**, *8* (2), 1664–1673.

(33) Blanco-Lomas, M.; Campos, P. J.; Sampedro, D. *Org. Lett.* **2012**, *14*, 4334–4337.

(34) Martínez-López, D.; Yu, M.-L.; García-Iriepa, C.; Campos, P. J.; Frutos, L. M.; Golen, J. A.; Rasapalli, S.; Sampedro, D. *J. Org. Chem.* **2015**, *80*, 3929–3939.

(35) Toker, Y.; Rahbek, D. B.; Klærke, B.; Bochenkova, A. V.; Andersen, L. H. *Phys. Rev. Lett.* **2012**, *109*, 128101.

(36) Gromov, E. V.; Burghardt, I.; Köppel, H.; Cederbaum, L. S. *J. Am. Chem. Soc.* **2007**, *129*, 6798–6806.

(37) Filatov, M. *WIREs Comput. Mol. Sci.* **2015**, *5*, 146–167.

(38) Atchity, G. J.; Xantheas, S. S.; Ruedenberg, K. *J. Chem. Phys.* **1991**, *95*, 1862–1876.

(39) Sellner, B.; Barbatti, M.; Lischka, H. *J. Chem. Phys.* **2009**, *131*, 024312.

(40) Bernardi, F.; Olivucci, M.; Robb, M. A. *Chem. Soc. Rev.* **1996**, *25*, 321–328.

(41) Migani, A.; Olivucci, M. In *Conical Intersections: Electronic Structure, Dynamics and Spectroscopy*; Domcke, W., Yarkony, D. R., Köppel, H., Eds.; Advanced Series in Physical Chemistry; World Scientific: Singapore, 2004; Vol. *15*, pp 271–322.

(42) Filatov, M.; Olivucci, M. *J. Org. Chem.* **2014**, *79*, 3587–3600.

(43) Huix-Rotllant, M.; Filatov, M.; Gozem, S.; Schapiro, I.; Olivucci, M.; Ferré, N. *J. Chem. Theory Comput.* **2013**, *9*, 3917–3932.

(44) Frutos, L. M.; Andruniów, T.; Santoro, F.; Ferré, N.; Olivucci, M. *Proc. Natl. Acad. Sci. U. S. A.* **2007**, *104*, 7764–7769.

(45) Zilberg, S.; Haas, Y. *Photochem. Photobiol. Sci.* **2003**, *2*, 1256−1263.
(46) Rossi Paccani, R.; Donati, D.; Fusi, S.; Latterini, L.; Farina, G.; Zanirato, V.; Olivucci, M. *J. Org. Chem.* **2012**, *77*, 1738−1748.
(47) Dong, J.; Solntsev, K. M.; Tolbert, L. M. *J. Am. Chem. Soc.* **2006**, *128*, 12038−1239.
(48) Pieri, E. Force Fields and non-Adiabatic Dinamics of Biomimetic Molecular Rotors. MSc Thesis, Università degli Studi di Siena, Italy, 2014.
(49) Horng, M. L.; Gardecki, J. A.; Papazyan, A.; Maroncelli, M. *J. Phys. Chem.* **1995**, *99*, 17311−17337.
(50) Van Stokkum, I. H. M.; Larsen, D. S.; Van Grondelle, R. *Biochim. Biophys. Acta, Bioenerg.* **2004**, *1657*, 82−104.
(51) Melloni, A.; Rossi Paccani, R.; Donati, D.; Zanirato, V.; Sinicropi, A.; Parisi, M. L.; Martin, E.; Ryazantsev, M.; Ding, W. J.; Frutos, L. M.; Basosi, R.; Fusi, S.; Latterini, L.; Ferré, N.; Olivucci, M. *J. Am. Chem. Soc.* **2010**, *132*, 9310−9319.
(52) Kandori, H.; Furutani, Y.; Nishimura, S.; Shichida, Y.; Chosrowjan, H.; Shibata, Y.; Mataga, N. *Chem. Phys. Lett.* **2001**, *334*, 271−276.
(53) Kochendoerfer, G. G.; Mathies, R. A. *J. Phys. Chem.* **1996**, *100*, 14526−14532.
(54) Schmidt, B.; Sobotta, C.; Heinz, B.; Laimgruber, S.; Braun, M.; Gilch, P. *Biochim. Biophys. Acta, Bioenerg.* **2005**, *1706*, 165−173.
(55) Olivucci, M.; Lami, A.; Santoro, F. *Angew. Chem., Int. Ed.* **2005**, *44*, 5118−5121.
(56) Polli, D.; Altoe, P.; Weingart, O.; Spillane, K. M.; Manzoni, C.; Brida, D.; Tomasello, G.; Orlandi, G.; Kukura, P.; Mathies, R. A.; Garavelli, M.; Cerullo, G. *Nature* **2010**, *467*, 440−443.
(57) Wang, Q.; Schoenlein, R. W.; Peteanu, L. A.; Mathies, R. A.; Shank, C. V. *Science* **1994**, *266*, 422−424.
(58) Sampedro, D.; Migani, A.; Pepi, A.; Busi, E.; Basosi, R.; Latterini, L.; Elisei, F.; Fusi, S.; Ponticelli, F.; Zanirato, V.; Olivucci, M. *J. Am. Chem. Soc.* **2004**, *126*, 9349−9359.
(59) Gueye, M.; Nillon, J.; Crégut, O.; Léonard, J. *Rev. Sci. Inst.* **2016**, under review.
(60) Kovalenko, S.; Dobryakov, A.; Ruthmann, J.; Ernsting, N. *Phys. Rev. A: At., Mol., Opt. Phys.* **1999**, *59*, 2369−2384.
(61) Filatov, M. *J. Chem. Theory Comput.* **2013**, *9*, 4526−4541.
(62) Nikiforov, A.; Gamez, J. A.; Thiel, W.; Huix-Rotllant, M.; Filatov, M. *J. Chem. Phys.* **2014**, *141*, 124122.
(63) Vydrov, O. A.; Heyd, J.; Krukau, A.; Scuseria, G. E. *J. Chem. Phys.* **2006**, *125*, 074106.
(64) Vydrov, O. A.; Scuseria, G. E. *J. Chem. Phys.* **2006**, *125*, 234109.
(65) Vydrov, O. A.; Scuseria, G. E.; Perdew, J. P. *J. Chem. Phys.* **2007**, *126*, 154109.
(66) Krishnan, R.; Binkley, J. S.; Seeger, R.; Pople, J. A. *J. Chem. Phys.* **1980**, *72*, 650−654.
(67) Filatov, M.; Huix-Rotllant, M. *J. Chem. Phys.* **2014**, *141*, 024112.
(68) Kraka, E.; Filatov, M.; Zou, W.; Gräfenstein, H.; Izotov, D.; Gauss, J.; He, Y.; Wu, A.; Polo, V.; Olsson, L.; Konkoli, Z.; He, Z.; Cremer, D. *COLOGNE2012*; Southern Methodist University: Dallas, TX, 2012.
(69) Aquilante, F.; De Vico, L.; Ferré, N.; Ghigo, G.; Malmqvist, P.-Å.; Neogrády, P.; Pedersen, T. B.; Pitoňák, M.; Reiher, M.; Roos, B. O.; Serrano-Andrés, L.; Urban, M.; Veryazov, V.; Lindh, R. *J. Comput. Chem.* **2010**, *31*, 224−247.
(70) Lindahl, E.; Hess, B.; van der Spoel, D. *J. Mol. Model.* **2001**, *7*, 306−317.
(71) Berendsen, H. J. C.; van der Spoel, D.; van Drunen, R. *Comput. Phys. Commun.* **1995**, *91*, 43−56.
(72) Wang, J.; Wang, W.; Kollman, P. A.; Case, D. A. *J. Mol. Graphics Modell.* **2006**, *25*, 247−260.
(73) Wang, J.; Wolf, R. M.; Caldwell, J. W.; Kollman, P. A.; Case, D. A. *J. Comput. Chem.* **2004**, *25*, 1157−1174.
(74) Ponder, J. W.; Richards, F. M. *J. Comput. Chem.* **1987**, *8*, 1016−1024.
(75) Liu, X. Y.; Chang, X. P.; Xia, S. H.; Cui, G.; Thiel, W. *J. Chem. Theory. Comput.* **2016**, *12*, 753−764.
(76) Hsu, Y. H.; Chen, Y. A.; Tseng, H. W.; Zhang, Z.; Shen, J. Y.; Chuang, W. T.; Lin, T. C.; Lee, C. S.; Hung, W. Y.; Hong, B. C.; Liu, S. H.; Chou, P. T. *J. Am. Chem. Soc.* **2014**, *136*, 11805−11812.

■ NOTE ADDED IN PROOF

At the reviewing stage a computational work[75] by Thiel and coworkers was published on-line. The work describes a 5-(4-*para*-hydroxybenzylidene)-2,3-dimethyl-3,5-dihydro-4*H*-imidazol-4-one (*p*-LHBDI) molecular switch more directly related to the GFP fluorophore than our *p*-HBDI-like switch. However, the paper only concerns the neutral form of the switch (not the ionic form) and focuses on the *o*-LHBDI regio-isomer. The synthesis of *p*-LHBDI was reported earlier[76] and is different from the one reported here for *p*-HBDI-like. On the other hand, we note that the spectroscopic characterization of both the neutral and anion forms of *o*-LHBDI[76] in ethanol and *p*-HBDI-like in methanol show similar absorption properties but a longer excited state lifetime of the *o*-LHBDI anion.

Supporting Information for

Design, synthesis and Dynamics of a GFP Fluorophore Mimic with an Ultrafast Switching Function

Marco Paolino[‡,*], Moussa Gueye[†], Elisa Pieri[‡], Madushanka Manathunga[¶], Stefania Fusi[‡], Loredana Latterini[¶¶], Danilo Pannacci[¶¶], Michael Filatov[#,*], Jérémie Léonard[†,*] and Massimo Olivucci[‡,¶,‡‡*]

‡ Dipartimento di Biotecnologie, Chimica e Farmacia, Università di Siena, Via A. Moro 2, 53100 Siena, Italy; † Institut de Physique et Chimie des Matériaux de Strasbourg & Labex NIE, Université de Strasbourg, CNRS UMR 7504, Strasbourg, France; ¶ Chemistry Department, Bowling Green State University, USA; ¶¶ Dipartimento di Chimica, Biologia e Biotecnologie, Università di Perugia, Via Elce di Sotto, 8, 06123 Perugia, Italy; # Department of Chemistry, School of Natural Sciences, Ulsan National Institute of Science and Technology (UNIST), Ulsan 689-798, Korea; ‡‡ University of Strasbourg Institute for Advanced Studies, 5, allée du Général Rouvillois F-67083 Strasbourg, France.

E-mail: paomar@oneonline.it, mike.filatov@gmail.com, Jeremie.Leonard@ipcms.unistra.fr, molivuc@bgsu.edu

Content of supporting information

X-Ray crystallography

Single crystals of *E*-**2** and *E*-**3** were submitted to X-ray data collection on an Oxford-Diffraction Xcalibur Sapphire 3 diffractometer with a graphite monochromated Mo-Ka radiation (λ = 0.71073Å) at 293 K. The structures were solved by direct methods implemented in SHELXS-97 program.[1] The refinements were carried out by full-matrix anisotropic least squares on F^2 for all reflections for non-H atoms by means of the SHELXL-97 program.[1] Crystallographic data (excluding structure factors) for the structure in this paper have been deposited with the Cambridge Crystallographic Data Centre as supplementary publication no. CCDC 1062457 (*E*-**2**) and CCDC 1062459 (*E*-**3**). Copies of the data can be obtained, free of charge, on application to CCDC, 12 Union Road, Cambridge CB2 1EZ, UK; (fax: +44 (0) 1223 336 033; or e-mail: deposit@ccdc.cam.ac.uk).

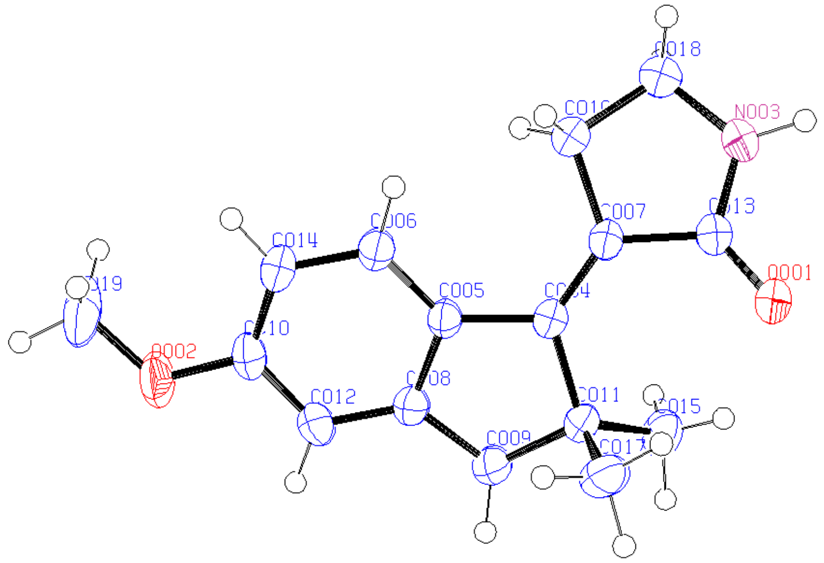

Figure SI-1. Crystallographic structure of compound E-**2**. Ellipsoids enclose 50% probability.

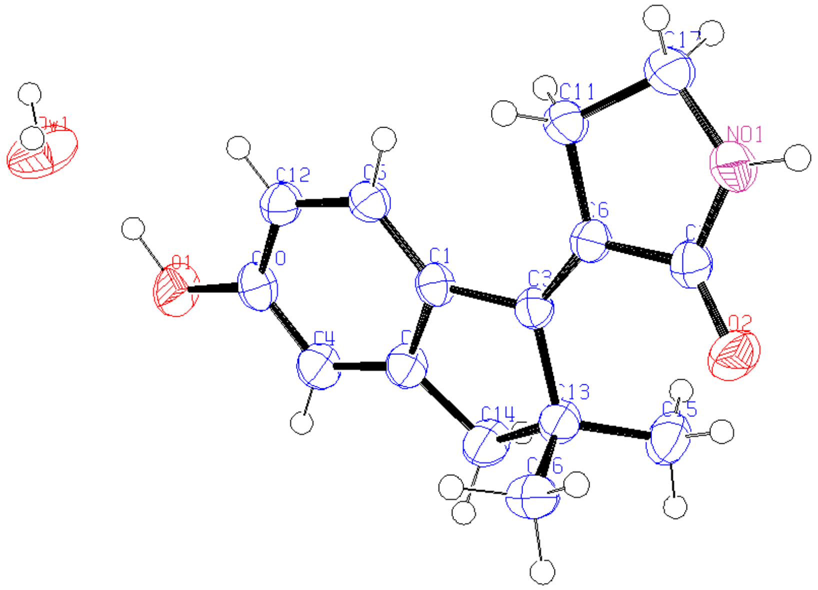

Figure SI-2. Crystallographic structure of compound E-**3**. Ellipsoids enclose 50% probability.

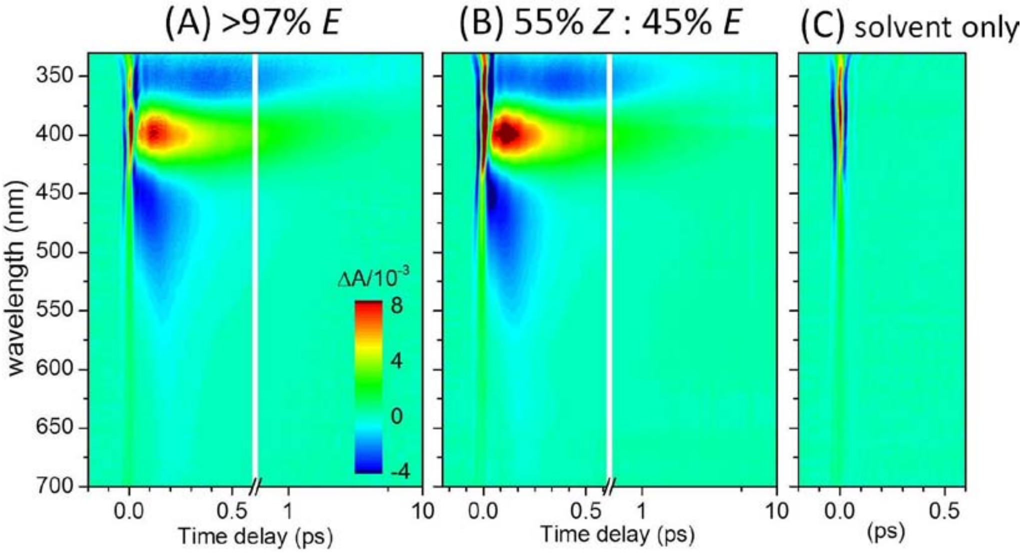

Figure SI-3. 400-nm-pumped TA 2D map in false color code as a function of probe wavelength (in nm) and time delay (in ps) between pump and probe pulses of (A) the >97% pure *E*-**3** isomer and (B) a 55% *Z*-**3** - 45% *E*-**3** mixture of both isomers in MeOH in the presence of large concentration of KOH. (C) TA signal recorded in the same conditions for the pure solvent (MeOH + KOH) with the same color code. All datasets have been post-processed ("chirp" correction) in order to display a common time origin for all probe wavelengths.

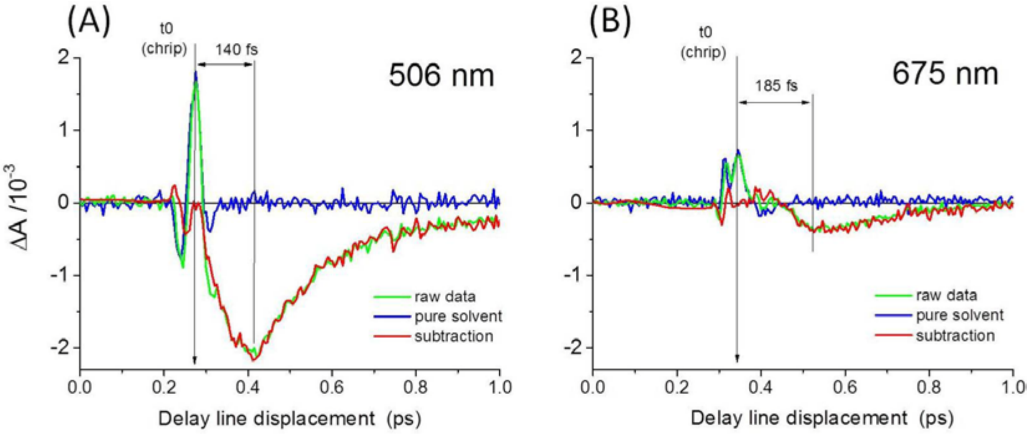

Figure SI-4. Illustration, with the 400-nm pumped TA data for pure *E*-**3**, of the data processing for solvent artifact subtraction and chirp correction at two probing wavelengths corresponding to two kinetic traces displayed in Figure 9D of the paper, i. e. (A) 506nm and (B) 675nm. The data are acquired on *E*-**3** in methanol (in excess of KOH) yielding the green traces and immediately after, on the pure solvent (i. e. methanol + KOH), resulting in the blue traces. The pure solvent signal (the so-called artifact) is used to pinpoint the delay line position for pump-probe temporal overlap (i. e. time zero), which is probe-wavelength dependent due to the chirp in the probe pulse. The signal attributable to *E*-**3** only (red traces) and displayed in Figure 9D is computed as the difference between the raw data and the solvent signal. Residual oscillations close to the time origin are due to imperfect solvent artifact subtraction.

Global analysis of the 350-nm-pumped TA data disclosed in Figure 8 of the paper.

Global analysis starts with data reduction (i. e. noise filtering) by singular value decomposition (SVD) of the entire data set. SVD may be used to decompose any 2D matrix in a set of singular transients associated to singular spectra and characterized by their relative weight, i. e. the singular values (SV). Global fitting is then performed by the simultaneous fitting of the singular kinetics characterized by the dominant few singular values. The information contained in the other terms of the decomposition (weaker singular values and singular kinetics) are disregarded as being representative of the noise in the data.

For the TA 2D dataset obtained upon 350-nm excitation of E-**3**, the singular values are illustrated in the inset of Figure SI-5A, and we fit "globally" the 4 first singular transients (see Figure SI-5A). This global fitting means that the same function is used to fit simultaneously all 4 singular transients, while sharing the same time constants in all 4 traces, but enabling the fitting routine (non-linear least-square fitting method, "Origin" software) to adjust independently the corresponding pre-exponential factors in each individual singular transients.

A usual fitting function for TA data analysis is the convolution $G(t) = P(t) \otimes I(t)$, of a sum of exponentially decaying functions, $P(t)$, with the instrument response function $I(t)$, assumed to be a Gaussian function of standard deviation σ:

$$G(t) = P(t) \otimes I(t), \text{ with}$$
$$P(t) = \sum_i H(t) \times A_i \exp\left(-\frac{t}{\tau_i}\right), \quad (H(t) = 0 \text{ for t} < 0; H(t) = 1 \text{ for t} \geq 0.)$$
$$I(t) = \frac{1}{\sigma\sqrt{2\pi}} exp\left(-\frac{(t-t_0)^2}{2\sigma^2}\right), \quad (t_0\text{, the time origin as determined as e. g. in Fig. SI-4)}$$

In the case a time constant τ_i is significantly shorter than the experimental time resolution σ, then the convolution yields the nearly unaltered shape of the Gaussian $I(t)$. In the end, as a general fitting function $F(t)$ for global analysis we use:

$$F(t) = G(t) + A_0 \times I(t),$$

While the A_i's appearing in $P(t)$, are directly proportional to the populations decaying with time constant τ_i, the amplitude A_0 corresponding to the "non-resolved" component is also affected by the experimental time-resolution, and cannot be quantitatively compared to the A_i's.

The global fitting, using this function $F(t)$, of the 350-nm TA data is illustrated in Figure SI-5. Importantly, in the present case where the signal rise is non-instantaneous (see e. g. the delayed rise of the SE in Figure 9D in the paper), the component $A_0 \times I(t)$ may not account for a non-resolved signal, but may advantageously enable the fitting of that delayed onset. In this case the result of the fitting for the parameter σ, is also affected by this molecular time scale over which dynamic spectral shifts may occur, and is no longer strictly representative of the time resolution.

The same function F(t) is used to fit simultaneously the four dominant singular transients, with shared values for the parameters t_0, σ, the three finite time constants τ_i's (i=1,2,3), and one infinite time constant (τ_4 which accounts for the long-lived photoproduct signature and is not a free parameter). Only the 5 corresponding amplitudes A_i's and A_0 are optimized independently for the four singular transients.

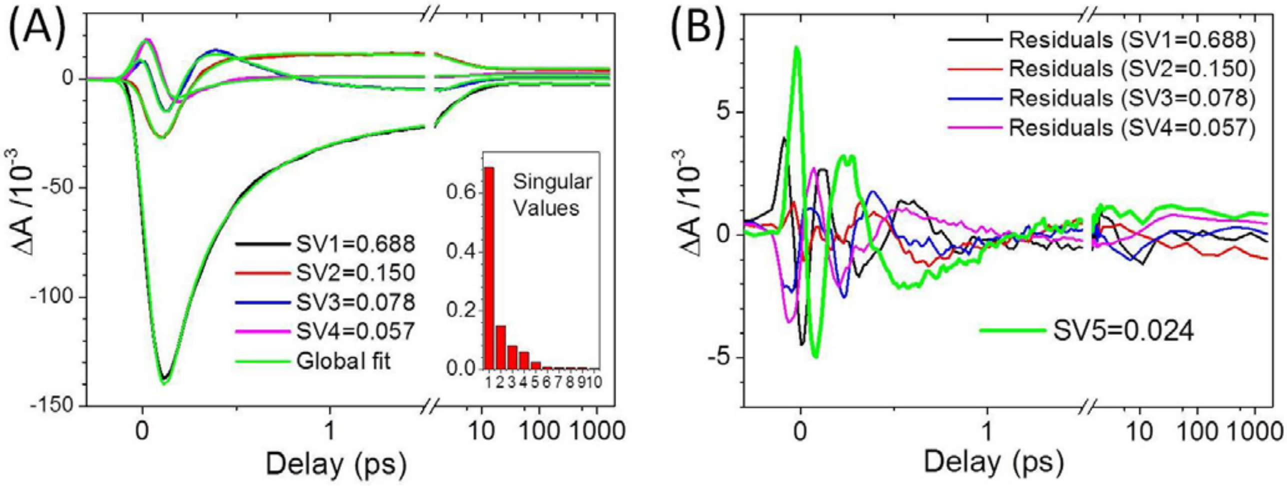

Figure SI-5: Global analysis of the entire 2D map displayed in Figure 8: A) The four dominant singular transients and their fit by the fitting function $F(t)$ introduced above. The inset displays the values of the ten dominant singular values. B) The residuals corresponding to the simultaneous fitting of the four singular kinetics of panel A, compared to the first neglected singular transient corresponding to the fifth singular value SV5.

Figure SI-5B displays the 4 residuals obtained by this global fitting and shows that their amplitudes are smaller than the first neglected singular transient (SV5). Noticeably the latter displays an oscillatory behavior at early times with can obviously not be fitted by a sum of exponential functions and a gaussian function. This is characteristic of data sets where all kinetics do not start simultaneously at the time origin, as is the case here e. g. with the SE signal rising later and later while probing further and further to the red.

We conclude that even if the fitting function $F(t)$ is not optimum (it cannot fit the SV5 singular transient although it remains larger than the amplitude of the residuals of the first 4 fits), it works remarkably well in the present case of non-exponential early dynamics.

Using the same SVD mathematical transformation, one can reconstruct the so-called decay associated spectra from the set of A_i's obtained as a result of the fitting routine for the four singular transients. These DAS are displayed in Figure 10A of the paper: they represent the wavelength-dependent weight of each decaying component τ_i throughout the data set. With the present choice of fitting function, the wavelength dependence of the non-resolved Gaussian component may be retrieved similarly in the form of a “Gaussian-associated” spectrum which is also displayed in Figure 10A.

Global analysis of the 400-nm-pumped TA data disclosed in Figure SI-3A.

Before performing global analysis, the solvent artifact signal (Figure SI-3C) is subtracted as illustrated in Figure SI-4. However, in that experiment, the solvent signal is particularly intense relative to the solute signal and the result is not perfect: spurious solvent signals remain as seen in Figure SI-4 or Figures 9D and 9E. For this reason we apply the SVD and global analysis only for time delays > 50 fs, where this artifact signal is essentially over. We fit globally the four dominant singular transient by the same fitting function F(t) as above, but we simply force t0=0. The result of the analysis is displayed in Figure SI-6. The fit is very good. The first neglected singular transient is weaker that the residuals of the global fitting, which justifies neglecting all singular values beyond the four first. The comparison between the fitted 2D map and the original data is displayed in Figure 9E at a selection of wavelengths.

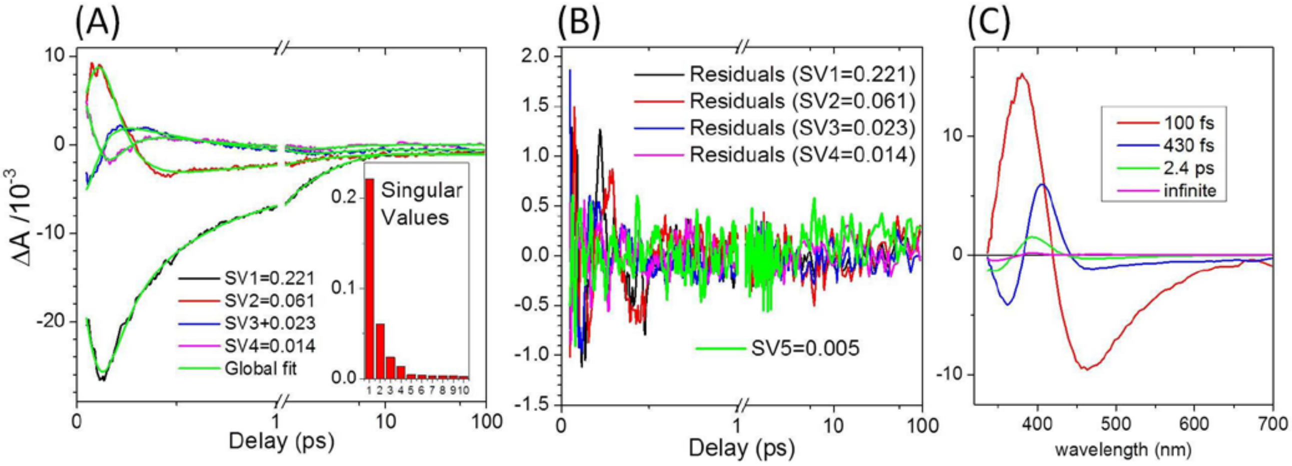

Figure SI-6: Global analysis of the solvent corrected data obtained upon 400-nm excitation: (A) The four first singular transients and their global fit for t > 50 fs. (B) Residuals of the four fits and comparison with the first neglected singular transient (SV5). (C) Corresponding DAS.

Analysis of the Excited state decay kinetics of E-dMe-MeO-NAIP upon 400-nm excitation.

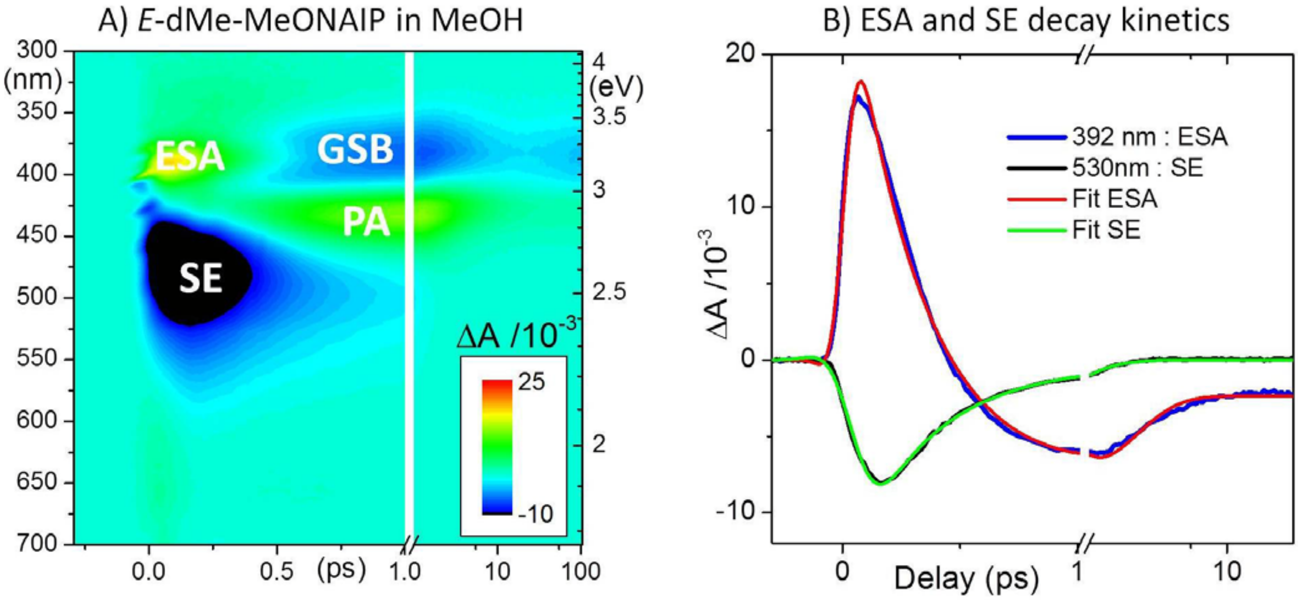

Figure SI-7. A) 400-nm-pumped TA 2D map of *E*-dMe-MeO-NAIP in MeOH, represented in false color code as a function of probe wavelength (in nm or eV) and time delay (in ps) between pump and probe pulses. SE=Stimulated emission, ESA=Excited state absorption, GSB = Ground State Bleach, PA= Photoproduct Absorption. B) Kinetic traces at 392nm, representative of the ESA decay and gSB recovery, and 530nm representative of the SE decay. Both traces are fitted by the function *F(t)* introduced above. The ESA decay (red line) occurs on the time scale τ1= 350 fs, revealing the underlying GSB signal which reduces on the ~1.5ps time scale due to ground state vibrational cooling. The SE decays with τ1= 300 +/- 20 fs (85%) and τ2= 0.9 +/- 0.1ps (15%) (green line).

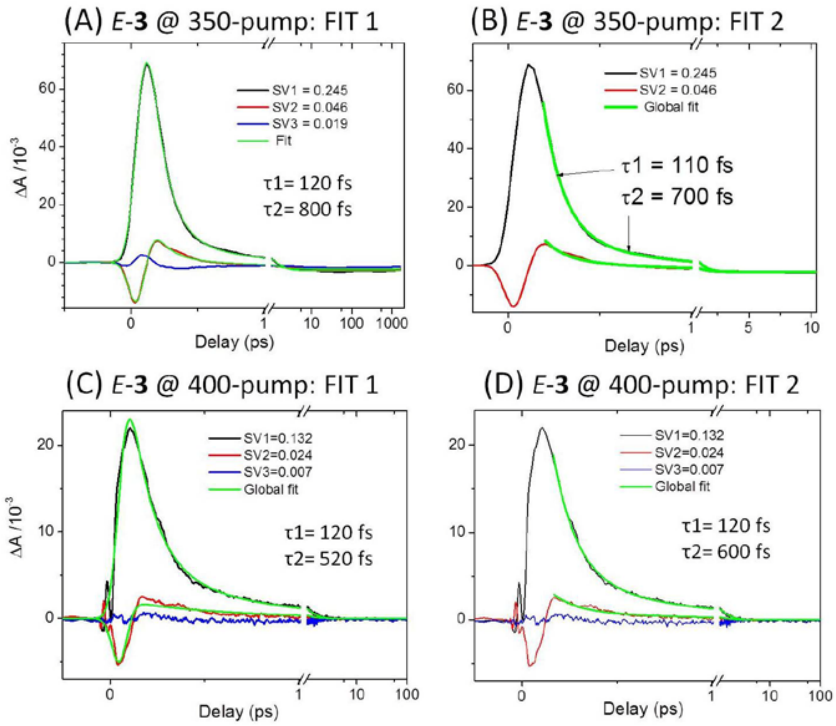

Figure SI-8. Analysis of the SE decay kinetics of the *E*-**3** upon 350-nm excitation (A,B: SVD on dataset restricted to λ>460nm) and 400-nm excitation (C,D: SVD on dataset restricted to λ>445nm). Two different types of global fits are performed on the first two singular kinetics: either the entire kinetics are fitted by F(t) (A,C) or the kinetics are fitted only after t=200fs, to disregard the early times where the fitting function is expected to be less performing due to the dynamic spectral shift of the SE. The 400-nm-pumped data are in particular not well fitted in the first 200 fs (see C). The gaussian- and decay- associated spectra reconstructed from the analysis of panel A are displayed in Figure 10B.

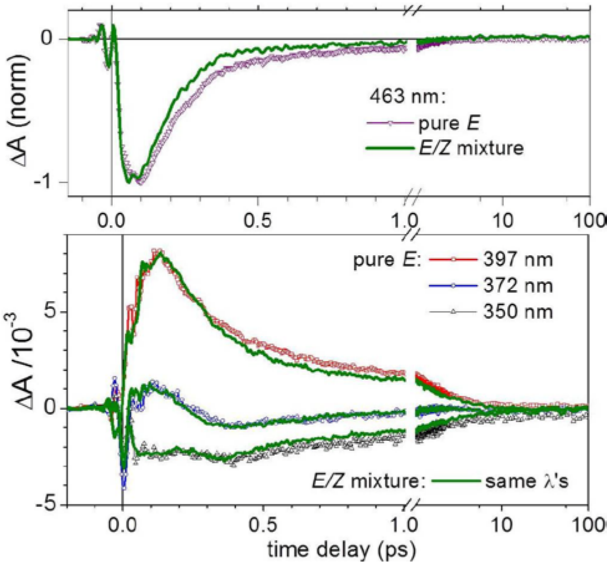

Figure SI-9: Comparison of the kinetic traces of the 97% pure *E* and the 55:45 *Z/E* mixtures upon 400-nm excitation at a selection of wavelengths representative of the SE decay (463nm, top), the ESA decay and GSB recovery (bottom).

400-nm excitation pulse spectrum

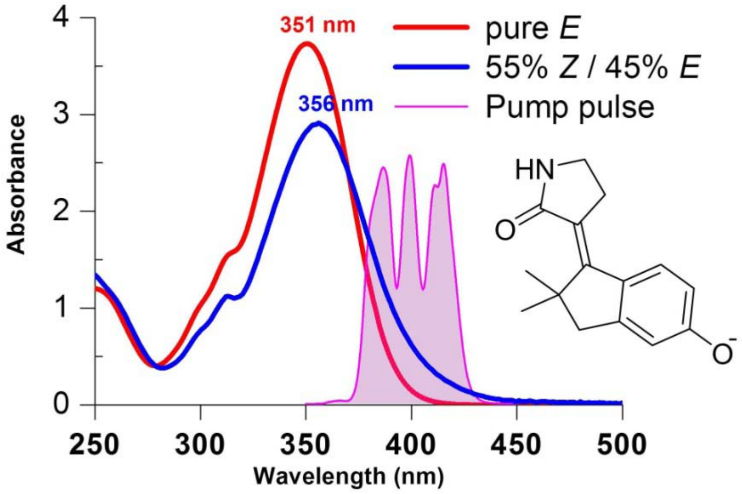

Figure SI-10. Chemical structure and absorption spectra of compound **3** in its anionic form: >97% pure *E (red)* 55% Z / 45% E mixture (blue) in MeOH in the presence of large concentration of KOH. The power spectrum of the 400-nm pump laser used for transient absorption spectroscopy is represented in pink.

Part V.

General conclusion and outlook

The elucidation and understanding of photoisomerization dynamics in molecular photoswitches is crucial for application and engineering. As these processes happen on time scales down to sub-picoseconds, pump-probe spectroscopy is one versatile optical method granting experimental access to such ultrafast spectro-temporal dynamics. For that purpose, a femtosecond transient absorption spectrometer setup has been use ("historical setup"). It allows us to measure, over a broadband spectral range (300-800 nm) and a large time window (up to 6 ns), pump-induced absorption changes with a time resolution of 70 fs and a high signal-to-noise ratio, enabling to investigate the electronic populations dynamics of the investigated isomerizing compounds (Chapter 2).

A key point for understanding the photoreaction dynamics is to consider the movement of the nuclei on the potential energy surface, which can, depending on its specific topology, enhance or disadvantage the quantum yield of the photoisomerization. Because the motion on the potential surface corresponds to a variation in the electronic energy, this movement can be observed spectroscopically. However, as the wavepacket oscillations may occur on a very short time scale, the temporal resolution of this vibrational coherence demands for a high experimental accuracy. To reach this range of temporal resolution, a new setup for ultrafast spectroscopy has been built. This experimental set-up records time-domain Raman spectroscopy by so-called vibrational coherence spectroscopy (VCS), with broadband UV-Vis detection and sub-8 fs excitation pulses centred at 400 nm and 800 nm enabling excitation of the compounds of interest. Upon Fourier transformation of the oscillatory residuals on the signal recorded by transient absorption spectroscopy with this set-up, we recover the Raman spectrum of the ground state and of the transient, excited (Franck-Condon) state. Up to 3000 cm^{-1} vibrational signatures are demonstrated in pure acetonitrile, with $< 20\ \mu OD$ noise floor (Chapter 3).
As a next experimental development three-pulse experiment using the 400 nm pulse as a "pump" pulse to trigger the photodynamic and the 800 nm pulse as a subsequent "VCS" pulse will also be implemented to trigger coherent vibrational motion along the course of the photoreaction, and in particular when the molecular system evolves in the vicinity of the CI, where the 800 nm pulse transiently becomes resonant. This work aims at implementing Quantum Control Spectroscopy (QCS) as a powerful tool to unravel and control the mechanisms that govern the dynamics and yield of ultrafast photoreactions involved in photomechanical or photoelectrical energy transduction at the molecular scale in condensed phase.

The main the goal of this work has been the investigation of the different characteristics of biologically inspired synthetic photoswitches by means of ultrafast transient absorption spectroscopy. These investigations aim for instance

at mimicking the photocatalytic environment of the rhodopsin cavity by molecular engineering, with central questions, about the parameters governing the dynamics and the yield of such photoreaction. In this context,we investigated the photoisomerization dynamics of IP compounds expected to mimic the ultrafast photoisomerization dynamics of the retinal chromophore in rhodopsin in Chapter 4. Two types of reaction scenarios described as coherent or non-coherent photoisomerization qualifie the IP family. The first one concerns the molecules which display a fast photoisomerization dynamics, with indication of vibrational coherence reactive motion on the photoproduct ground state and the second one concerns the molecules which display an ultrafast, mostly rate-equation-like, isomerization reaction. The difference in IP photoisomerization dynamics is identified by considering the substitution effects on the ground state structure of the molecule. The occurrence of vibrationally-coherence reactive motion requires fast decay favored by the pre-twisting geometry caused by the presence of methyl group in C5 carbon. Removing the methyl substituent in C5 (so-called "demethylated") stabizes a so-called "geared arrangement of the E isomer, which seems to initiate fast, coherent motion on S_1 and thus through the CI.
we used the IP family as a model system to investigate the influence of the reactive nuclear motion on the photoreaction yield. Rather than absolute quantum yield determination we determine more accurately the relative quantum yield of different IP compounds and their excited state lifetime is determined. By comparing all the IP together, no clear correlation is observed between the excited state lifetime or the observation of vibrationally-coherent reactive motion and the photoisomerization quantum yield unlike in Rho.
The dynamics of these photoreactions, as well as the isomerization QY are critically influenced by the shape of the electronic potential energy surfaces (PES) of the involved ground and excited states, the topology of the CI (it self influenced by the interaction with the environment in the condensed phase), and the vibrational dynamics of the system through these intersections. The complex configuration of these multi-dimensional surfaces makes the difficulty to explore them experimentally with conventional TAS. Thus it is possible to explore the PES by VCS.

We reported in chapter 5 the first application of VCS in IP compounds by combining on- and off-resonant experiments. With this combination of VCS schemes, we have been able to decipher the vibrational modes which are signatures of the ground or excited state, or those which are excited optically or by the reactive motion itself and contribute to the reaction coordinate. The measurements revealed that the parent MeO-NAIP switch isomerizes in a vibrationally-coherent fashion with the transfer of coherence activities of low-frequency vibrational modes from the excited state to the photoproduct ground state upon internal conversion through the CI like in Rho. The comparison of the vibrational dynamics of the parent MeO-NAIP and the dMe-MeO-NAIP where the methyl group on C5 is replaced by a hydrogen atom, confirmed that the methyl group on C5 is necessary to trigger and preserve the vibrational coherence observed along the reaction coordinate in MeO-NAIP. This qualitative difference in both photoreaction dynamics is also characterized by vibrational modes in both the ground and excited states.

Following a rational, theory-guided strategy, the effect of various simple Quantum Control strategies on the vibrational dynamics and on the quantum yield of ultrafast photoreactions will be investigated. The approach will first be applied to molecular photoswitches, which exhibit outstanding vibrationally coherent photoisomerization and are computationally tractable with state-of-the-art theoretical approaches.
Thus the family based on the IP structure appears to be a very good model system to study the parameters governing the coherent photoisomerization dynamics, combining theoretical and experimental investigations.

Unraveling the mechanisms of this conformational change would open a wide applicability of synthetic molecules mimicking the photoreaction of rhodopsin. In the context of photocontrolling peptides conformations and therefore biological functions, computational investigations performed on a number of retinal analogues expected to act as photoswitches in solution have shown that some of these molecules may work as efficient photoswitches for peptides [86] . In Chapter 6, we presented the photocontrol dynamics of a peptide conformation with a benzylidene-pyrroline chromophore that mimics the PSBR and can be used to introduce light-switchable intramolecular cross-links in peptides. We presented a detailed experimental and computational study to investigate the electronic and conformational dynamics of a peptide cross-linked with the retinal-like switch. By combining temperature-dependent, femtosecond UV-Vis transient absorption spectroscopy, high-level hybrid quantum mechanics/molecular mechanics and extensive classical molecular dynamics, we compared the photoisomerization dynamics and mechanisms of the molecular switch free in solution or covalently bound to the peptide. We concluded that the photoisomerization occurs through a conical intersection after thermal activation over an S_1 potential energy barrier, the magnitude of which depends on the ground state (S_0) conformation of the cross-linked peptide. We have been able to rationalize the effect of the peptide linkage on the switch photoisomerization, and propose the underlying mechanism. This work can thus be seen as an approach where, starting from the bare synthetic, biomimetic chromophore, we have considered the effect of its linking to a peptide on the photoisomerization reaction dynamics. That has to be carefully explored in the view of designing synthetic chromophores for the efficient photoswitching of molecular functions.

Finally, we have also reached the spectroscopic properties and the reaction mechanism of a new IP neighboring molecular switch, but designed as a model of anion HBDI chromophore of GFP, and much easier synthesis (Chapter 7). Together with the theoretical studies, we have shown that the new anionic switch has a dynamic photo-reaction similar to the dMe-MeO-NAIP and the MeO-NAIP cationic switches, which is explained by a nearby structure and similar charge translocation in the excited state (an opposite charge moves in the opposite direction).

The results brought by this experimental work and other computational techniques (QM/MM) strongly support the idea that the biomimetic molecular switches are good candidates for both theoretical and experimental investigation of photoisomerization dynamics through the CI.

Part VI.

Appendix

A. Sum frequency Generation: Conversion efficiency

To estimate the conversion efficiency of a SFG process, it is reasonable to reduce the problem to a simpler model of three monochromatic waves of infinite expansion and linear polarisation, propagating not necessarily collinearly, but at least in paraxial approximation along an z axis through a second-order nonlinear material. Assuming a pulse envelope A(z, t) evolving slowly in time on scales of the nonlinear response and in space on scales of the wavelength, the nonlinear polarisation caused by the three waves k_1, k_2 and k_3 can be written as

$$\begin{aligned} P^{NL} &= \frac{\varepsilon_0\chi^{(2)}}{4}\left(\sum_{i=1}^{3}(\mathcal{E}_i+\mathcal{E}_i^*)\right)^2 && \text{(A.1)}\\ &\approx \frac{\varepsilon_0\chi^{(2)}}{2}((\mathcal{E}_1\mathcal{E}_2+\mathcal{E}_1^*\mathcal{E}_3+\mathcal{E}_2^*\mathcal{E}_3)+c.c.), && \text{(A.2)}\end{aligned}$$

where we have neglected the terms far from the phase matching condition $\Delta k = k_3 - k_2 - k_1 \approx 0$, i.e. all but the terms corresponding to the processes $\omega_1 + \omega_2 \rightarrow \omega_3$, $\omega_3 - \omega_1 \rightarrow \omega_2$ or $\omega_3 - \omega_2 \rightarrow \omega_1$ in the second step. Therefore, the coupled nonlinear polarisations for each of the three waves are (in complex-field notation):

$$\left\{\begin{array}{lcl} \mathcal{P}_1^{NL} &=& \varepsilon_0\chi^{(2)}\mathcal{A}_2^*\mathcal{A}_3\exp i(k_3-k_2)z\\ \mathcal{P}_2^{NL} &=& \varepsilon_0\chi^{(2)}\mathcal{A}_1^*\mathcal{A}_3\exp i(k_3-k_1)z\\ \mathcal{P}_3^{NL} &=& \varepsilon_0\chi^{(2)}\mathcal{A}_1\mathcal{A}_2\exp i(k_1+k_2)z, \end{array}\right. \tag{A.3}$$

With help of expression which arises from the propagation equation in a second-order nonlinear medium [88], we can write down the coupled differential equations for the wave envelopes $\mathcal{A}_i = \mathcal{A}_i(z)$:

$$\left\{\begin{array}{lcl} \frac{\mathrm{d}\mathcal{A}_1}{\mathrm{d}z} &=& \frac{i\omega_1\chi^{(2)}}{2n_1c}\mathcal{A}_2^*\mathcal{A}_3\exp i(\Delta kz)\\ \frac{d\mathcal{A}_2}{dz} &=& \frac{i\omega_2\chi^{(2)}}{2n_2c}\mathcal{A}_1^*\mathcal{A}_3\exp i(\Delta kz)\\ \frac{d\mathcal{A}_3}{dz} &=& \frac{i\omega_3\chi^{(2)}}{2n_3c}\mathcal{A}_1\mathcal{A}_2\exp i(\Delta kz) \end{array}\right. \tag{A.4}$$

If we assume weak conversion efficiency, i.e $\mathcal{A}_3 << \mathcal{A}_1, \mathcal{A}_2 \forall z$, the third of these equations decouples. In the case where the distance covered in the crystal is short enough that the shape of the envelopes stays approximately constant, $\partial_z \mathcal{A}_1 \approx 0 \approx \partial_z \mathcal{A}_2$, the third equation can be integrated to a compact form, using the boundary condition $\mathcal{A}_3(z=0)=0$ (no sum-frequency wave before the crystal). This yields

$$\begin{aligned} \mathcal{A}_3(z^{'}) &= \frac{i\omega_3\chi^{(2)}}{2n_3c}\mathcal{A}_1\mathcal{A}_2\int_0^{z'}\exp(-i\Delta k_z)dz && \text{(A.5)} \\ &= -\frac{i\omega_3\chi^{(2)}}{2n_3c}\mathcal{A}_1\mathcal{A}_2\exp(-\frac{1}{2}i\Delta kz')\frac{1}{i\Delta k}\left(\exp(-\frac{1}{2}i\Delta z')-\exp(\frac{1}{2}i\Delta z')\right) \\ &= -\frac{i\omega_3\chi^{(2)}}{2n_3c}\mathcal{A}_1\mathcal{A}_2\exp(-\frac{1}{2}i\Delta kz')sinc\left(\frac{\Delta kz'}{2}\right) && \text{(A.6)} \end{aligned}$$

for the envelope of the sum-frequency pulse and hence

$$\begin{aligned} I_3(z') &= \frac{1}{2}n_3\varepsilon_0c|\mathcal{A}_3|^2 && \text{(A.7)} \\ I_3(z') &= \frac{1}{2\varepsilon_0c^3}\frac{|\chi^2|^2}{n_1n_2n_3}\omega_3^2I_1I_2z'^2sinc^2\left(\frac{\Delta kz'}{2}\right) && \text{(A.8)} \end{aligned}$$

for the intensity. The conversion efficiency thus depends in particular on the thickness of the crystal ($I_3 \propto z^2$) and is severely limited by the phase mismatch Δk. In the case where all other parameters are fixed, we can for reasons of convenience define the relative conversion efficiency η as

$$\eta = sinc^2\left(\frac{\Delta kz}{2}\right) \tag{A.9}$$

Factor limiting the conversion yield

To generate high intensities of sum-frequency pulses, the applied nonlinear crystal has to be as thick as possible. The maximum thickness, however, is limited by the following factors:

- As already shown (fig. 3.6.B), a thick crystal reduces the spectral acceptance.
- By traversing the crystal, the pulses gather chirp and are enlarged temporarily.
- Due to the different refractive indices (*no* resp. *ne*) the two fundamental rays see traversing the crystal (for phase matching type II), the two pulses travel at different speed and therefore overlap only over a limited distance. This effect is known as group velocity mismatch (GVM). The cause for GVM is the disparate group velocity of ordinary and extraordinary beam. The group velocity v_g of

a wave packet with central wavelength λ (in air) in a medium with refractive index n is

$$v_g = \frac{\partial\omega}{\partial k} = \frac{c}{n(\lambda)}\left(1 + \frac{\lambda}{n(\lambda)}\frac{\partial n}{\partial\lambda}(\lambda)\right) \qquad \text{(A.10)}$$

where the n has to be replaced by the adequate expression (Sellmeier equations and optionally Eq.**??**) for the nonlinear crystal. The maximum thickness that still admits a sufficient overlap of the two pulses despite GVM on the one hand, and involves a tolerable pulse prolongation on the other hand, was calculated numerically. Following scenario (Fig.A.1) was taken as basis for the calculation: In BBO, negative uniaxial crystals, the extraordinary beam travels faster than the ordinary one, $v_g(e) > v_g(o)$. In our case, the pulse on the ordinary axis (k_2) is shorter and has the larger spectrum than the pulse on the extraordinary axis (k_1). The maximum overlap distance can therefore be reached, if the faster pulse k_1 overtakes k_2 inside the crystal. The criterion to rate the overlap between the two pulses was, that the distance between the two maxima should never be greater than the mean value of the two pulses' spatial spread,

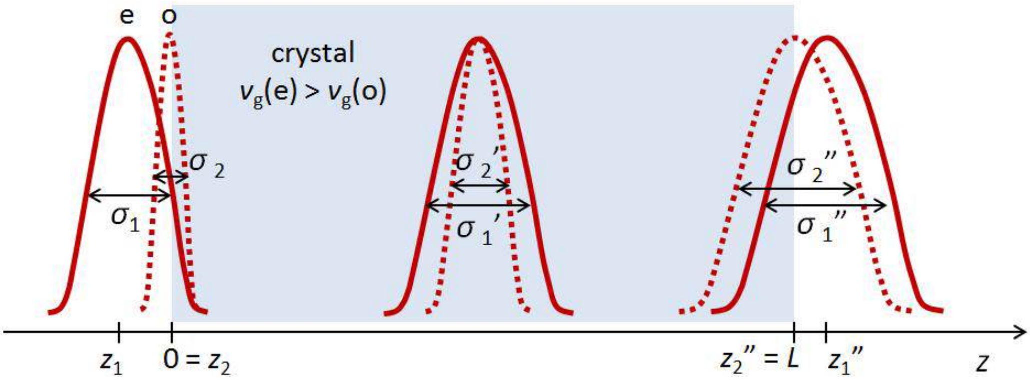

Figure A.1.: The scenario taken as basis for the calculation of the maximum crystal thickness

$$z_1 - z_2 < \frac{1}{2}|v_g(e)\Delta_{(1/2)}t(k_1) + v_g(o)\Delta_{(1/2)}t(k_2)|. \qquad \text{(A.11)}$$

For our computations, we shall assume a longer pulse k_1 with a duration $\Delta_{(1/2)}t(\lambda_1) = 40fs$ and a shorter pulse k_2 with $\Delta_{(1/2)}t(k_2) = 7fs$ (FWHM). The acceptance limit for the maximal pulse prolongation of the shorter pulse k_2 was set to $\Delta_{(1/2)}t(k_2) = 10fs$.

This calculation reveals that the maximum thickness for a BBO crystal is limited by the criterion of the pulse duration not becoming too long due to GVD, delivering a pulse k_2 of $\Delta_{(1/2)}t(k_2) \sim 10fs$ for $L \sim 240\mu m$.

Bibliography

[1] W. E. Moerner and Michel Orrit. Illuminating single molecules in condensed matter. *Science*, 283(5408):1670–1676, 1999.

[2] Rudi Berera, Rienk van Grondelle, and JohnT.M. Kennis. Ultrafast transient absorption spectroscopy: principles and application to photosynthetic systems. *Photosynthesis Research*, 101(2-3):105–118, 2009.

[3] Stoichko D. Dimitrov and James R. Durrant. Materials design considerations for charge generation in organic solar cells. *Chemistry of Materials*, 26(1):616–630, 2014.

[4] T. Nägele, R. Hoche, W. Zinth, and J. Wachtveitl. Femtosecond photoisomerization of cis-azobenzene. *Chemical Physics Letters*, 272(5–6):489 – 495, 1997.

[5] Ben L. Feringa. The art of building small:from molecular switches to molecular motors. *The Journal of Organic Chemistry*, 72(18):6635–6652, 2007. PMID: 17629332.

[6] George Zimmerman, Lue-Yung Chow, and Un-Jin Paik. The photochemical isomerization of azobenzene1. *Journal of the American Chemical Society*, 80(14):3528–3531, 1958.

[7] Remedios González-Luque, Marco Garavelli, Fernando Bernardi, Manuela Merchán, Michael A. Robb, and Massimo Olivucci. Computational evidence in favor of a two-state, two-mode model of the retinal chromophore photoisomerization. *Proceedings of the National Academy of Sciences*, 97(17):9379–9384, 2000.

[8] M. Klessinger and J. Michl. Excited states and photochemistry of organic molecules. *VCH*, 1995.

[9] Marcos Dantus, Mark J. Rosker, and Ahmed H. Zewail. Realtime femtosecond probing of “transition states” in chemical reactions. *The Journal of Chemical Physics*, 87(4), 1987.

[10] R.W. Schoenlein L.A. Peteanu R.A. Mathies Wang, Q. and C.V. Shank. Vibrationally coherent photochemistry in the femtosecond primary event of vision. *Science*, 1994.

[11] H. Kandori, Y. Shichida, and T. Yoshizawa. Photoisomerization in rhodopsin. *Biochemistry (Moscow)*, 66(11):1197–1209, 2001.

[12] Ralph S. Becker and Kenn Freedman. A comprehensive investigation of the mechanism and photophysics of isomerization of a protonated and unprotonated schiff base of 11-cis-retinal. *Journal of the American Chemical Society*, 107(6):1477–1485, 1985.

[13] F. Lumento, V. Zanirato, S. Fusi, E. Busi, L. Latterini, F. Elisei, A. Sinicropi, T. Andruniów, N. Ferré, Basosi, and R. M. Olivucci. Quantum chemical modelling and preparation of a biomimetic photochemical switch. *Angewandte Chemie*, (414):46, 2007.

[14] Adalgisa Sinicropi, Elena Martin, Mikhail Ryazantsev, Jan Helbing, Julien Briand, Divya Sharma, Jérémie Léonard, Stefan Haacke, Andrea Cannizzo, Majed Chergui, Vinicio Zanirato, Stefania Fusi, Fabrizio Santoro, Riccardo Basosi, Nicolas Ferré, and Massimo Olivucci. An artificial molecular switch that mimics the visual pigment and completes its photocycle in picoseconds. *Proceedings of the National Academy of Sciences*, 105(46):17642–17647, 2008.

[15] Julien Briand, Olivier Bram, Julien Rehault, Jeremie Leonard, Andrea Cannizzo, Majed Chergui, Vinizio Zanirato, Massimo Olivucci, Jan Helbing, and Stefan Haacke. Coherent ultrafast torsional motion and isomerization of a biomimetic dipolar photoswitch. *Phys. Chem. Chem. Phys.*, 12:3178–3187, 2010.

[16] Jérémie Léonard, Igor Schapiro, Julien Briand, Stefania Fusi, Riccardo Rossi Paccani, Massimo Olivucci, and Stefan Haacke. Mechanistic origin of the vibrational coherence accompanying the photoreaction of biomimetic molecular switches. *Chemistry – A European Journal*, 18(48):15296–15304, 2012.

[17] Luis Manuel Frutos, Tadeusz Andruniów, Fabrizio Santoro, Nicolas Ferré, and Massimo Olivucci. Tracking the excited-state time evolution of the visual pigment with multiconfigurational quantum chemistry. *Proceedings of the National Academy of Sciences*, 104(19):7764–7769, 2007.

[18] Alfonso Melloni, Riccardo Rossi Paccani, Donato Donati, Vinicio Zanirato, Adalgisa Sinicropi, Maria Laura Parisi, Elena Martin, Mikhail Ryazantsev, Wan Jian Ding, Luis Manuel Frutos, Riccardo Basosi, Stefania Fusi, Loredana Latterini, Nicolas Ferré, and Massimo Olivucci. Modeling, preparation, and characterization of a dipole moment switch driven by z/e photoisomerization. *Journal of the American Chemical Society*, 132(27):9310–9319, 2010.

[19] Marina Blanco-Lomas, Subhas Samanta, Pedro J. Campos, G. Andrew Woolley, and Diego Sampedro. Reversible photocontrol of peptide conformation with a rhodopsin-like photoswitch. *Journal of the American Chem-*

ical Society, 134(16):6960–6963, 2012. PMID: 22482865.

[20] W. Thomas Pollard, SooY. Lee, and Richard A. Mathies. Wave packet theory of dynamic absorption spectra in femtosecond pump–probe experiments. *The Journal of Chemical Physics*, 92(7), 1990.

[21] C. Ruckebusch, M. Sliwa, P. Pernot, A. de Juan, and R. Tauler. Comprehensive data analysis of femtosecond transient absorption spectra: A review. *Journal of Photochemistry and Photobiology C: Photochemistry Reviews*, 13(1):1 – 27, 2012.

[22] S. A. Kovalenko, J. Ruthmann, and N. P. Ernsting. Femtosecond hole-burning spectroscopy with stimulated emission pumping and supercontinuum probing. *The Journal of Chemical Physics*, 109(5), 1998.

[23] S. A. Kovalenko, A. L. Dobryakov, J. Ruthmann, and N. P. Ernsting. Femtosecond spectroscopy of condensed phases with chirped supercontinuum probing. *Phys. Rev. A*, 59:2369–2384, Mar 1999.

[24] Todd S. Rose, Mark J. Rosker, and Ahmed H. Zewail. Femtosecond realtime probing of reactions. iv. the reactions of alkali halides. *The Journal of Chemical Physics*, 91(12), 1989.

[25] S. Ruhman, A.G. Joly, and K.A. Nelson. Coherent molecular vibrational motion observed in the time domain through impulsive stimulated raman scattering. *Quantum Electronics, IEEE Journal of*, 24(2):460–469, Feb 1988.

[26] H.L. Fragnito, J.-Y. Bigot, P.C. Becker, and C.V. Shank. Evolution of the vibronic absorption spectrum in a molecule following impulsive excitation with a 6 fs optical pulse. *Chemical Physics Letters*, 160(2):101 – 104, 1989.

[27] W.T. Pollard, H.L. Fragnito, J.-Y. Bigot, C.V. Shank, and R.A. Mathies. Quantum-mechanical theory for 6 fs dynamic absorption spectroscopy and its application to nile blue. *Chemical Physics Letters*, 168(3):239 – 245, 1990.

[28] Lisa Dhar, John A. Rogers, and Keith A. Nelson. Time-resolved vibrational spectroscopy in the impulsive limit. *Chemical Reviews*, 94(1):157–193, 1994.

[29] S.L. Dexheimer, Q. Wang, L.A. Peteanu, W.T. Pollard, R.A. Mathies, and C.V. Shank. Femtosecond impulsive excitation of nonstationary vibrational states in bacteriorhodopsin. *Chemical Physics Letters*, 188(1):61 – 66, 1992.

[30] Anat Kahan, Omer Nahmias, Noga Friedman, Mordechai Sheves, and Sanford Ruhman. Following photoinduced dynamics in bacteriorhodopsin with 7-fs impulsive vibrational spectroscopy. *Journal of the American Chemical Society*, 129(3):537–546, 2007. PMID: 17227016.

[31] David W. McCamant, Philipp Kukura, Sangwoon Yoon, and Richard A. Mathies. Femtosecond broadband stimulated raman spectroscopy: Appa-

ratus and methods. *Review of Scientific Instruments*, 75(11):4971–4980, 2004.

[32] Philipp Kukura, David W. McCamant, Sangwoon Yoon, Daniel B. Wandschneider, and Richard A. Mathies. Structural observation of the primary isomerization in vision with femtosecond-stimulated raman. *Science*, 310(5750):1006–1009, 2005.

[33] David W. McCamant, Philipp Kukura, Sangwoon Yoon, and Richard A. Mathies. Femtosecond broadband stimulated raman spectroscopy: Apparatus and methods. *Review of Scientific Instruments*, 75(11), 2004.

[34] S. A. Kovalenko, A. L. Dobryakov, and N. P. Ernsting. An efficient setup for femtosecond stimulated raman spectroscopy. *Review of Scientific Instruments*, 82(6), 2011.

[35] Renee R. Frontiera, Chong Fang, Jyotishman Dasgupta, and Richard A. Mathies. Probing structural evolution along multidimensional reaction coordinates with femtosecond stimulated raman spectroscopy. *Phys. Chem. Chem. Phys.*, 14:405–414, 2012.

[36] Satoshi Takeuchi, Sanford Ruhman, Takao Tsuneda, Mahito Chiba, Tetsuya Taketsugu, and Tahei Tahara. Spectroscopic tracking of structural evolution in ultrafast stilbene photoisomerization. *Science*, 322(5904):1073–1077, 2008.

[37] Matz Liebel and Philipp Kukura. Broad-band impulsive vibrational spectroscopy of excited electronic states in the time domain. *The Journal of Physical Chemistry Letters*, 4(8):1358–1364, 2013. PMID: 26282153.

[38] Jan Philip Kraack, Amir Wand, Tiago Buckup, Marcus Motzkus, and Sanford Ruhman. Mapping multidimensional excited state dynamics using pump-impulsive-vibrational-spectroscopy and pump-degenerate-four-wave-mixing. *Phys. Chem. Chem. Phys.*, 15:14487–14501, 2013.

[39] Satoshi Takeuchi Satoru Fujiyoshi and Tahei Tahara. Time-resolved impulsive stimulated raman scattering from excited-state polyatomic molecules in solution. *The Journal of Physical Chemistry A*, 107(4):494–500, 2003.

[40] Torsten Wende, Matz Liebel, Christoph Schnedermann, Robert J. Pethick, and Philipp Kukura. Population-controlled impulsive vibrational spectroscopy: Background- and baseline-free raman spectroscopy of excited electronic states. *The Journal of Physical Chemistry A*, 118(43):9976–9984, 2014. PMID: 25244029.

[41] S. A. Kovalenko, A. L. Dobryakov, J. Ruthmann, and N. P. Ernsting. Femtosecond spectroscopy of condensed phases with chirped supercontinuum probing. *Phys. Rev. A*, 59:2369–2384, Mar 1999.

[42] Oliver Weingart Katelyn M. Spillane Cristian Manzoni Daniele Brida Gaia

Tomasello Giorgio Orlandi Philipp Kukura Richard A. Mathies Marco Garavelli Giulio Cerullo Dario Polli, Piero Altoe. Conical intersection dynamics of the primary photoisomerization event in vision. *Nature*, 467(440), 2010.

[43] M. Liebel, C. Schnedermann, G. Bassolino, G. Taylor, A. Watts, and P. Kukura. Direct observation of the coherent nuclear response after the absorption of a photon. *Phys. Rev. Lett.*, 112:238301, Jun 2014.

[44] M. Liebel, C. Schnedermann, T. Wende, and P. Kukura. Principles and applications of broadband impulsive vibrational spectroscopy. *The Journal of Physical Chemistry A*, 119(36):9506–9517, 2015. PMID: 26262557.

[45] Christoph Schnedermann, Matz Liebel, and Philipp Kukura. Mode-specificity of vibrationally coherent internal conversion in rhodopsin during the primary visual event. *Journal of the American Chemical Society*, 137(8):2886–2891, 2015. PMID: 25647020.

[46] M. Nisoli, S. De Silvestri, and O. Svelto. Generation of high energy 10 fs pulses by a new pulse compression technique. *Applied Physics Letters*, 68(20):2793–2795, 1996.

[47] Tobias Witting, Felix Frank, Christopher A. Arrell, William A. Okell, Jonathan P. Marangos, and John W. G. Tisch. Characterization of high-intensity sub-4-fs laser pulses using spatially encoded spectral shearing interferometry. *Opt. Lett.*, 36(9):1680–1682, May 2011.

[48] C. Vozzi, M. Nisoli, G. Sansone, S. Stagira, and S. De Silvestri. Optimal spectral broadening in hollow-fiber compressor systems. *Applied Physics B*, 80(3), 2005.

[49] Jun Liu, Yuichiro Kida, Takahiro Teramoto, and Takayoshi Kobayashi. Generation of stable sub-10 fs pulses at 400 nm in a hollow fiber for uv pump-probe experiment. *Opt. Express*, 18(5):4664–4672, Mar 2010.

[50] Jun Liu, Atsushi Yabushita, Seiji Taniguchi, Haik Chosrowjan, Yasushi Imamoto, Keiichi Sueda, Noriaki Miyanaga, and Takayoshi Kobayashi. Ultrafast time-resolved pump–probe spectroscopy of pyp by a sub-8 fs pulse laser at 400 nm. *The Journal of Physical Chemistry B*, 117(17):4818–4826, 2013. PMID: 23534531.

[51] Rocio Borrego Varillas, Alessia Candeo, Daniele Viola, Marco Garavelli, Sandro De Silvestri, Giulio Cerullo, and Cristian Manzoni. Microjoule-level, tunable sub-10 fs uv pulses by broadband sum-frequency generation. *Opt. Lett.*, (13):3849–3852.

[52] Atsushi Yabushita, Yu-Hsien Lee, and Takayoshi Kobayashi. Development of a multiplex fast-scan system for ultrafast time-resolved spectroscopy. *Review of Scientific Instruments*, 81(6):–, 2010.

[53] Donna Strickland and Gerard Mourou. Compression of amplified chirped

optical pulses. *Optics Communications*, 55(6):447 – 449, 1985.

[54] J.S. Robinson, C.A. Haworth, H. Teng, R.A. Smith, J.P. Marangos, and J.W.G. Tisch. The generation of intense, transform-limited laser pulses with tunable duration from 6 to 30 fs in a differentially pumped hollow fibre. *Applied Physics B*, 85(4):525–529, 2006.

[55] A.K. Dharmadhikari, F.A. Rajgara, and D. Mathur. Systematic study of highly efficient white light generation in transparent materials using intense femtosecond laser pulses. *Applied Physics B*, 80(1):61–66, 2004.

[56] Dario Polli, Larry Lüer, and Giulio Cerullo. High-time-resolution pump-probe system with broadband detection for the study of time-domain vibrational dynamics. *Review of Scientific Instruments*, 78(10), 2007.

[57] C. Riedle, S. Lochbrunner, E. Riedle, and D. J. Nesbitt. Ultrasensitive ultraviolet-visible 20fs absorption spectroscopy of low vapor pressure molecules in the gas phase. *Review of Scientific Instruments*, 79(1), 2008.

[58] A. L. Dobryakov, S. A. Kovalenko, A. Weigel, J. L. Pérez-Lustres, J. Lange, A. Müller, and N. P. Ernsting. Femtosecond pump/supercontinuum-probe spectroscopy: Optimized setup and signal analysis for single-shot spectral referencing. *Review of Scientific Instruments*, 81(11), 2010.

[59] M. J. Feldstein, P. Vöhringer, and N. F. Scherer. Rapid-scan pump–probe spectroscopy with high time and wave-number resolution: optical-kerr-effect measurements of neat liquids. *J. Opt. Soc. Am. B*, 12(8):1500–1510, Aug 1995.

[60] John C. Deàk, Lawrence K. Iwaki, , and Dana D. Dlott*. Vibrational energy redistribution in polyatomic liquids: ultrafast irraman spectroscopy of acetonitrile. *The Journal of Physical Chemistry A*, 102(42):8193–8201, 1998.

[61] Giovanni Bassolino, Tina Sovdat, Matz Liebel, Christoph Schnedermann, Barbara Odell, Timothy D.W. Claridge, Philipp Kukura, and Stephen P. Fletcher. Synthetic control of retinal photochemistry and photophysics in solution. *Journal of the American Chemical Society*, 136(6):2650–2658, 2014. PMID: 24479840.

[62] J Léonard, J Briand, S Fusi, V Zanirato, M Olivucci, and S Haacke. Isomer-dependent vibrational coherence in ultrafast photoisomerization. *New Journal of Physics*, 15(10):105022, 2013.

[63] Igor Schapiro, Stefania Fusi, Massimo Olivucci, Tadeusz Andruniów, Swaroop Sasidharanpillai, and Glen R. Loppnow. Initial excited-state dynamics of an n-alkylated indanylidene–pyrroline (naip) rhodopsin analog. *The Journal of Physical Chemistry B*, 118(42):12243–12250, 2014. PMID: 25255466.

[64] Diego Sampedro, Annapaola Migani, Alessandra Pepi, Elena Busi, Ric-

cardo Basosi, Loredana Latterini, Fausto Elisei, Stefania Fusi, Fabio Ponticelli, Vinicio Zanirato, , and Massimo Olivucci. Design and photochemical characterization of a biomimetic light-driven z/e switcher. *Journal of the American Chemical Society*, 126(30):9349–9359, 2004. PMID: 15281826.

[65] Gabriel Marchand, Julien Eng, Igor Schapiro, Alessio Valentini, Luis Manuel Frutos, Elisa Pieri, Massimo Olivucci, Jérémie Léonard, and Etienne Gindensperger. Directionality of double-bond photoisomerization dynamics induced by a single stereogenic center. *The Journal of Physical Chemistry Letters*, 6(4):599–604, 2015. PMID: 26262473.

[66] Vlasta Bonačić-Koutecký, Jutta Köhler, and Josef Michl. Prediction of structural and environmental effects on the s1-s0 energy gap and jump probability in double-bond cis—trans photoisomeriz. *Chemical Physics Letters*, 104(5):440 – 443, 1984.

[67] M. Garavelli, P. Celani, F. Bernardi, M. A. Robb, , and M. Olivucci. The c5h6nh2+ protonated shiff base: an ab initio minimal model for retinal photoisomerization. *Journal of the American Chemical Society*, 119(29):6891–6901, 1997.

[68] R Mathies and L Stryer. Retinal has a highly dipolar vertically excited singlet state: implications for vision. *Proceedings of the National Academy of Sciences*, 73(7):2169–2173, 1976.

[69] Tadeusz Andruniów, Nicolas Ferré, and Massimo Olivucci. Structure, initial excited-state relaxation, and energy storage of rhodopsin resolved at the multiconfigurational perturbation theory level. *Proceedings of the National Academy of Sciences*, 101(52):17908–17913, 2004.

[70] Robert R. Birge. Nature of the primary photochemical events in rhodopsin and bacteriorhodopsin. *Biochimica et Biophysica Acta (BBA) - Bioenergetics*, 1016(3):293 – 327, 1990.

[71] Jérémie Léonard, Erwin Portuondo-Campa, Andrea Cannizzo, Frank van Mourik, Gert van der Zwan, Jörg Tittor, Stefan Haacke, and Majed Chergui. Functional electric field changes in photoactivated proteins revealed by ultrafast stark spectroscopy of the trp residues. *Proceedings of the National Academy of Sciences*, 106(19):7718–7723, 2009.

[72] T P Sakmar, R R Franke, and H G Khorana. Glutamic acid-113 serves as the retinylidene schiff base counterion in bovine rhodopsin. *Proceedings of the National Academy of Sciences*, 86(21):8309–8313, 1989.

[73] Minoru Sugihara, Volker Buss, Peter Entel, , and Jürgen Hafner. The nature of the complex counterion of the chromophore in rhodopsin. *The Journal of Physical Chemistry B*, 108(11):3673–3680, 2004.

[74] Alessandro Cembran, Fernando Bernardi, Massimo Olivucci, and Marco

Garavelli. The retinal chromophore/chloride ion pair: Structure of the photoisomerization path and interplay of charge transfer and covalent states. *Proceedings of the National Academy of Sciences of the United States of America*, 102(18):6255–6260, 2005.

[75] Tina Sovdat, Giovanni Bassolino, Matz Liebel, Christoph Schnedermann, Stephen P. Fletcher, and Philipp Kukura. Backbone modification of retinal induces protein-like excited state dynamics in solution. *Journal of the American Chemical Society*, 134(20):8318–8320, 2012. PMID: 22536821.

[76] R. W. Schoenlein, L. A. Peteanu, Q. Wang, R. A. Mathies, and C. V. Shank. Femtosecond dynamics of cis-trans isomerization in a visual pigment analog: isorhodopsin. *The Journal of Physical Chemistry*, 97(46):12087–12092, 1993.

[77] Oliver Weingart*. The twisted c11c12 bond of the rhodopsin chromophorea photochemical hot spot. *Journal of the American Chemical Society*, 129(35):10618–10619, 2007. PMID: 17691730.

[78] Adam D. Dunkelberger, Ryan D. Kieda, Jae Yoon Shin, Riccardo Rossi Paccani, Stefania Fusi, Massimo Olivucci, and F. Fleming Crim. Photoisomerization and relaxation dynamics of a structurally modified biomimetic photoswitch. *The Journal of Physical Chemistry A*, 116(14):3527–3533, 2012. PMID: 22409209.

[79] P. Altoe O. Weingart K.M. Spillane C. Manzoni D. Brida G. Tomasello G. Orlandi P. Kukura R.A. Mathies M. Garavelli Polli, D. and G. Cerullo. Conical intersection dynamics of the primary photoisomerization event in vision. *Nature*, 2010.

[80] Deping Hu, Jing Huang, Yu Xie, Ling Yue, Xuhui Zhuang, and Zhenggang Lan. Nonadiabatic dynamics and photoisomerization of biomimetic photoswitches. *Chemical Physics*, 463:95 – 105, 2015.

[81] Gerd G. Kochendoerfer and Richard A. Mathies. Ultrafast spectroscopy of rhodopsins — photochemistry at its best! *Israel Journal of Chemistry*, 35(3-4):211–226, 1995.

[82] Samer Gozem, Mark Huntress, Igor Schapiro, Roland Lindh, Alexander A. Granovsky, Celestino Angeli, and Massimo Olivucci. Dynamic electron correlation effects on the ground state potential energy surface of a retinal chromophore model. *Journal of Chemical Theory and Computation*, 8(11):4069–4080, 2012. PMID: 26605574.

[83] Christoph Schnedermann, Matz Liebel, and Philipp Kukura. Mode-specificity of vibrationally coherent internal conversion in rhodopsin during the primary visual event. *Journal of the American Chemical Society*, 137(8):2886–2891, 2015. PMID: 25647020.

[84] Igor Schapiro, Mikhail Nikolaevich Ryazantsev, Luis Manuel Frutos, Nicolas Ferré, Roland Lindh, and Massimo Olivucci. The ultrafast photoisomerizations of rhodopsin and bathorhodopsin are modulated by bond length alternation and hoop driven electronic effects. *Journal of the American Chemical Society*, 133(10):3354–3364, 2011. PMID: 21341699.

[85] Luckner Ulysse, Juanita Cubillos, and Jean Chmielewski. Photoregulation of cyclic peptide conformation. *Journal of the American Chemical Society*, 117(32):8466–8467, 1995.

[86] Adalgisa Sinicropi, Caterina Bernini, Riccardo Basosi, and Massimo Olivucci. A novel biomimetic photochemical switch at work: design of a photomodulable peptide. *Photochem. Photobiol. Sci.*, 8:1639–1649, 2009.

[87] Marina Blanco-Lomas, Subhas Samanta, Pedro J. Campos, G. Andrew Woolley, and Diego Sampedro. Reversible photocontrol of peptide conformation with a rhodopsin-like photoswitch. *Journal of the American Chemical Society*, 134(16):6960–6963, 2012. PMID: 22482865.

[88] M. Joffre. Optique non-linéaire en régimes continu et femtoseconde. *Unpublished Work*.